

IMPROVEMENTS TO OUR UNDERSTANDING OF TORONTO-AREA
ATMOSPHERIC COMPOSITION

by

Cynthia Whaley

A thesis submitted in conformity with the requirements
for the degree of Doctor of Philosophy
Graduate Department of Physics
University of Toronto

Copyright © 2014 by Cynthia Whaley

Abstract

Improvements to our Understanding of Toronto-Area Atmospheric Composition

Cynthia Whaley

Doctor of Philosophy

Graduate Department of Physics

University of Toronto

2014

Using eleven years of trace gas column measurements at the University of Toronto Atmospheric Observatory (TAO), along with data from complementary sources, such as satellites, surface in situ measurements, and nearby rural column measurements, this thesis aims to improve our understanding of the sources of air pollution and the causes of variability in atmospheric composition over the Toronto area.

The relative influence of chemical production and direct emissions on Toronto-area O_3 and CO were determined using GEOS-Chem model simulations. 28 pollution events (defined as enhanced O_3 or CO lower-tropospheric (0-5 km) columns that coincided with surface O_3 exceedances) were found in the TAO dataset between 2002 and 2010. O_3 columns over Toronto during pollution events are influenced by urban and industrial anthropogenic NO_x emissions, biogenic isoprene emissions from the eastern United States, and soil NO_x emissions from the mid- and western United States. During pollution events, Toronto CO columns are greatly influenced by nearby fossil fuel emissions and isoprene oxidation. C_2H_6 columns are often enhanced during pollution events, as the sources of C_2H_6 are similar to those of O_3 and CO. HCN columns are assumed to be enhanced in biomass burning plumes, and thus, aid in identifying transport of biomass burning emissions over Toronto. Sensitivity to meteorological conditions was examined as well, and five case studies were presented in detail.

Passage of the polar vortex over the Toronto area was determined by increases in

scaled potential vorticity (PV) that coincide with outliers in the HF stratospheric time series. Confirmed with polar PV maps and reductions in N₂O stratospheric columns, 53 polar intrusion events were identified in the 2002 to 2013 TAO time series. The effect on HF, HCl, O₃, and N₂O was studied, and we found these events caused a significant increase in HF-column winter/spring variability, and a small increase (on average) in stratospheric O₃ columns.

The results of this thesis have contributed to improving our understanding of the causes and variability of ozone air quality and stratospheric ozone over a major metropolitan area.

Dedication

I dedicate this thesis to my best friend, my companion of fourteen years (twelve of which were at University), my wonderful husband, Vincent Piette. Thank you for your love, support, and encouragement.

Acknowledgements

I will start by thanking my supervisor, Professor Kimberly Strong, who has guided and supervised this research. She has generously given her time and expertise to help me with my work for many years and was a joy to work for. She also encouraged me to travel to workshops and conferences around the world, and I thank her very much for giving me the best possible graduate studies experience I can imagine.

I also want to thank Professor Dylan Jones for unofficially becoming my co-supervisor. He established the GEOS-Chem model in the department and has spent a lot of time showing me how to run it, analyze its output and understand the results. He has also been a joy to work for, and his guidance was instrumental in the interpretation of the TAO data set.

I thank the students, post-docs and interns who have taken measurements with TAO since its installation in 2001, without which I would not have the excellent dataset that I had to work with. These people include but are not limited to: Jeffrey Taylor, Aldona Wiacek, Jenny Kliever, Daniel Weaver, Joseph Mendonca, Maryam Akrami, Michael Maurice, Orfeo Colebatch, Anthony Pugliese and Erik Lutsch.

A special thank you to Thomas Walker, Felicia Kolonjari, Cristen Adams, Rebecca Batchelor, Jeffrey Taylor, and Gaetan Baron for their help during my research. They provided me with invaluable technical help, programs and analysis techniques. I picked their brains on numerous occasions, and they were all very generous in relating their wisdom to me.

Finally, I thank my family for their loving support: my incredible life partner, Vincent Piette, my mother Iris Jackson, my father Charles Whaley and my sister Elisabeth Melsom. Additionally, I thank the more recent additions to my family: Alex Weinberger, Ryan and John Melsom. And the most wonderful addition: Théodore Piette. Thank you all for being there through good times and bad.

Contents

1	Introduction and motivation	1
1.1	Science questions and goals	3
1.2	Unique measurements	3
1.3	Methodology	5
1.3.1	Interpretation of Toronto tropospheric composition	5
1.3.2	Interpretation of Toronto stratospheric composition	6
1.4	Contributions of the candidate and collaborators	6
1.5	Thesis outline	8
2	FTIR measurements	9
2.1	Molecular spectroscopy	9
2.1.1	Line shape	11
2.1.2	Line strength	13
2.2	Fourier transform spectroscopy: theory	14
2.3	Fourier transform spectroscopy: implementation at TAO	17
2.3.1	Experimental setup	17
2.3.2	Semi-automated measurements	18
2.3.3	Instrument line shape	20
2.4	Retrievals	22
2.4.1	Optimal estimation method	22

2.4.2	Implementation with SFIT2	24
2.4.3	Averaging kernels	25
2.4.4	Errors	25
2.4.5	Tikhonov regularization	27
2.5	Future work: improvements to TAO	28
3	Trace gases measured at TAO	29
3.1	Retrieval optimization and harmonization	29
3.1.1	Changing microwindows	32
3.1.2	Changing <i>a priori</i> profiles and vertical grid	41
3.1.3	Changing SNR and S_a	53
3.1.4	Quality control	55
3.1.5	Summary of TAO retrievals	56
3.2	Optimized 11-year time series and trends	58
3.2.1	Ozone	58
3.2.2	Carbon monoxide	61
3.2.3	Ethane	61
3.2.4	Hydrogen cyanide	61
3.2.5	Methane	62
3.2.6	Nitrous oxide	63
3.2.7	Hydrogen fluoride	64
3.2.8	Hydrogen chloride	64
3.3	NDACC archiving	64
3.4	Future work	65
4	Tropospheric measurements and model	67
4.1	Background: tropospheric composition and chemistry	68
4.1.1	Health standards for O_3 and CO	68

4.1.2	Ozone and carbon monoxide chemistry	70
4.1.3	Seasonal cycle of lower-tropospheric O ₃	75
4.1.4	O ₃ trends	75
4.2	FTIR sensitivity to the troposphere	76
4.3	Urban versus rural: the CARE FTS dataset	76
4.4	Complementary measurements from space	79
4.4.1	TES	80
4.4.2	MOPITT	83
4.5	Air quality measurements at the surface	84
4.6	Model description	86
4.6.1	Tagged simulations	88
4.6.2	Smoothing the model	89
4.7	Data and model comparisons	89
4.7.1	Ozone	90
4.7.2	Carbon monoxide	93
4.7.3	Ethane	95
5	Sources of Toronto pollution episodes	97
5.1	Background: O ₃ air pollution in eastern North America	98
5.2	How does Toronto pollution vary with wind direction?	100
5.2.1	Pollution roses	100
5.2.2	Wind direction bins	105
5.3	Model adjoint description	112
5.4	HYSPLIT back-trajectories	113
5.5	Enhanced O ₃ and CO columns: Toronto pollution events	113
5.5.1	Pollution events in the annual time series	114
5.5.2	Pollution events and wind direction	120
5.5.3	Do FTIR tropospheric columns capture poor air quality?	121

5.5.4	Sensitivity of Toronto pollution: North American emissions	123
5.5.5	Sensitivity of Toronto pollution: regional analysis	130
5.6	Case studies	136
5.6.1	Case 1: a high-pressure system brings pollution from the northeast U.S. during abnormally high temperatures	138
5.6.2	Case 2: high local temperatures and transport from the southeast U.S.	143
5.6.3	Case 3: westerly transport and stagnant conditions cause almost 100 ppb surface O ₃ in Toronto	146
5.6.4	Case 4: long-range transport from the west coast	149
5.6.5	Case 5: biomass burning causes large CO column increase, but has little effect on Toronto O ₃	153
5.6.6	What do FTIR columns tell us that the surface measurements can't?156	
5.7	Summary of case studies and conclusions	157
5.8	Future work	160
5.8.1	Source attribution over the whole time series	160
5.8.2	Source attribution for other species	162
5.8.3	FTIR data assimilation	164
6	Polar intrusions over Toronto	166
6.1	Background: the stratosphere and the polar vortex	167
6.2	FTIR sensitivity to the stratosphere	171
6.3	Complementary measurements	173
6.3.1	CARE FTIR spectrometer	173
6.3.2	OSIRIS	173
6.4	Models and meteorological analyses	175
6.4.1	Potential vorticity from MIMOSA and MERRA	175
6.4.2	N ₂ O and O ₃ from GMI	176

6.4.3	Derived meteorological products	177
6.5	Results and discussion	178
6.5.1	Identification and frequency of polar intrusion events	178
6.5.2	Effect on trace gases: variability	183
6.5.3	Effect on trace gases: case studies	190
6.5.4	Vertical structure of polar intrusion events	199
6.6	Summary and conclusions	201
6.6.1	Future work	202
7	Conclusions	203
7.1	Summary and conclusions of the interpretation of tropospheric measurements	204
7.1.1	Significance	205
7.1.2	Policy recommendations	205
7.2	Summary and conclusions of the interpretation of stratospheric measurements	207
7.2.1	Significance	208
7.3	Future work	208
A	Retrieval analysis from M.Sc. report	210
A.1	Retrieval Parameters	210
A.2	Microwindow Analysis	212
B	2002-2013 Trends	230
	Bibliography	232

List of Tables

2.1	Spectral coverage of the DA8 FTS filters.	18
3.1	Microwindows tested for HCN.	33
3.2	Microwindows and other settings tested for CH ₄	39
3.3	TAO (and CARE, see Section 4.3) FTIR Retrieval Parameters: species, NDACC filter number, microwindows, interfering species, mean SNR of measurements, diagonal elements of \mathbf{S}_a , partial columns of interest, median DOFS for total/partial columns, total errors for total/partial columns, and random errors on total/partial columns.	59
5.1	Percentage of measurements coming from the three wind-direction bins defined in Figure 5.6. Shown for all FTIR measurements, only enhanced FTIR measurements, and only FTIR measurements that were associated with pollution events, as defined at the beginning of Section 5.5.	122

5.2	Summary of findings for the five pollution event case studies presented in this chapter: date and time of the events, surface O ₃ VMR (if the surface O ₃ criteria were exceeded, ~ if they were not) from MOE, the FTIR column enhancement (factor of sigma above the monthly mean if greater than 1σ, ~ if not, and x if no measurement), the maximum temperature in Toronto on the day of the event from Environment Canada, the average GEOS wind direction and speed over the 2°x2.5° Toronto grid box at the given date/time, and the cause/sources of the pollution event.	161
6.1	Percent increase in 2003–2012 stratospheric column variability and sPV variability over Toronto due to polar intrusion events. O ₃ products are from the 1000 cm ⁻¹ and 3051 cm ⁻¹ microwindows combined. The first set of sPV variability is due to the 53 polar intrusion events during the FTIR measurement days. The second set of sPV variability is due to all polar intrusion days in the sPV time series, not constrained by FTIR measurement days.	186
6.2	Percent change in stratospheric columns of O ₃ over Toronto due to polar intrusion events for the given year, and for the total time series (2002 to 2013). Bold values highlight changes that are greater than the standard error of the mean difference.	190
A.1	Recommended and standard TAO MWs for the retrieval analysis. Interfering species are given in brackets.	212
A.2	Microwindow analysis: biases	218
B.1	Mean annual trends for each species from 2002 to 2013, and, if significant, their 95% confidence limit.	231

List of Figures

2.1	The TAO interferometer (adapted from ABB Bomem Inc. facility schematics). Sunlight enters the system at the top and its path is traced by the black lines [<i>Wiacek</i> , 2006].	15
2.2	Number of measurement days with the TAO-FTS.	19
2.3	Results of two sample TAO FTS instrument line shape tests from 10 April 2013 (blue) and 9 October 2013 (orange): (left) instrument lineshape, (top, right) modulation efficiency, and (bottom, right) phase error.	21
3.1	Typical spectral fits and residuals (from 27 October 2010) of three MWs of the HCN Test 1 case, and the <i>a priori</i> (solid line) and retrieved profiles (crosses) of HCN. Red arrows indicate the location of the HCN absorption lines. Residuals are the measured minus calculated spectra.	35
3.2	Same as Figure 3.1, but for the HCN Test 2 case.	36
3.3	Same as Figure 3.1, but for the HCN Test 3 case. Other large absorption features in the MW are labelled with the interfering species. The 3286.17–3286.48 MW (bottom, left), and the 3301.03–3301.30 MW (top, right) only have water vapour absorption.	37
3.4	TAO HCN total column time series from three sets of MWs: Test 1=green, Test 2=black, and Test 3=purple crosses.	38

3.5	Typical spectral fits and residuals (from 13 December 2005) in the five MWs and the <i>a priori</i> (solid line) and retrieved profiles (crosses) of CH ₄ for Test 1, using Tikhonov regularization. Residuals are the measured minus calculated spectra.	40
3.6	Same as Figure 3.5, but for CH ₄ Test 2.	41
3.7	Same as Figure 3.5, but for CH ₄ Test 3.	42
3.8	TAO CH ₄ total column 2005 time series from Tests 1 (green), 2 (red), and 3 (blue), using Tikhonov regularization.	43
3.9	Typical spectral fits and residuals (measured minus calculated), from 13 December 2005, in the five MWs and the <i>a priori</i> (solid line) and retrieved profiles (crosses) of CH ₄ for Test 1, using OEM.	44
3.10	Same as Figure 3.9, but for CH ₄ Test 2, using OEM.	45
3.11	Original and WACCM <i>a priori</i> profiles (VMR in mol/mol) used for TAO retrievals for (a) O ₃ , (b) CO, (c) C ₂ H ₆ , (d) HCN, (e) CH ₄ , (f) N ₂ O, (g) HF, and (h) HCl. For HCN (d), an optimized <i>a priori</i> profile is also shown (black line). Note that the x-axis is in log-scale for O ₃ , CO, and C ₂ H ₆ to more clearly see the differences.	47
3.12	TAO CO time series for 2005 of (<i>top</i>): total columns (with total error bars), (<i>middle</i>): DOFS, and (<i>bottom</i>): RMS of the residuals of the spectral fits with different <i>a priori</i> profiles.	48
3.13	TAO C ₂ H ₆ time series for 2005 of (<i>top</i>): total columns (with total error bars), (<i>middle</i>): DOFS, and (<i>bottom</i>): RMS of the residuals of the spectral fits with different <i>a priori</i> profiles.	49
3.14	HCN total column time series from retrievals with different <i>a priori</i> profiles.	50

3.15	HCN profiles. Orange, pink, and dark green thin lines are profiles measured during MkIV balloon campaigns. Grey line is typical GEOS-Chem profile over Toronto. Black crosses indicate a typical ACE-FTS profile over Toronto. Thick blue, green, red, and black lines are <i>a priori</i> profiles that were tested.	51
3.16	HF total column time series from retrievals with different <i>a priori</i> profiles.	52
3.17	TAO O ₃ tradeoff curve, showing median RMS residual vs. SNR for a selection of spectra. An SNR of 35 was chosen for O ₃ retrievals based on this plot.	55
3.18	C ₂ H ₆ measurements kept (black), and discarded (red) using various thresholds for quality filtering (see text): (top) threshold from Equation 3.2, (middle) threshold from Equation 3.3, and (bottom) threshold from Equation 3.4.	57
3.19	TAO total column time series for (a) O ₃ (from 1000 cm ⁻¹ MW), (b) CO, (c) C ₂ H ₆ , (d) HCN, (e) CH ₄ , (f) N ₂ O, (g) HF, and (h) HCl.	60
3.20	Typical CH ₄ VMR averaging kernels (coloured lines) from 9 February 2006, total column averaging kernel (thick green line), and sensitivity (thick purple line).	63
4.1	Schematic of reactions involved in CO and CH ₄ oxidation and O ₃ production.	71
4.2	Map of total North American (a) NO _x emissions, and (b) CO sources (including direct emissions and the hydrocarbon source) on a typical summertime day (21 July 2005). (a) Total = sum of fossil fuel, biofuel, aircraft, lightning, soil and fertilizer sources. (b) Total = sum of fossil fuel, biofuel, and monoterpene sources. All sources are from the emission inventories used in the GEOS-Chem model (Section 4.6). NO _x and CO from biomass burning are excluded since its location and amount are more variable than the other sources.	74

4.3	TAO VMR averaging kernels (blue lines, with those for the 0-5 km levels in red lines), total column averaging kernels (green lines), partial (0-5 km) column averaging kernels (purple lines), and sensitivity (orange lines) for tropospheric species: (a) O ₃ , (b) CO, (c) C ₂ H ₆ , and (d) HCN.	77
4.4	Differences between TAO and CARE (a) O ₃ (0-5 km), (b) CO (0-5 km), and (c) CO (0-3 km) partial columns, and (d) C ₂ H ₆ and (e) HCN total columns. Also shown are the mean differences $\pm 1\sigma$	79
4.5	TES median VMR averaging kernels (2004–2010, within 1° of Toronto) for O ₃ . Red lines indicate the 0-5 km levels.	81
4.6	Climatological monthly mean O ₃ 0-5 km partial columns over Toronto from TAO (2002-2013), GEOS-Chem (2002-2010), and TES (2004-2013). TES and GEOS-Chem profiles were smoothed with a median TAO averaging kernel. Error bars are the standard deviation of the monthly means.	82
4.7	MOPITT median VMR averaging kernels for CO (2002–2010, within 1° of Toronto). Red lines indicate the 0-5 km levels.	84
4.8	Monthly mean total and partial (0-5 km) column CO over Toronto from TAO, GEOS-Chem, and MOPITT. GEOS-Chem profiles were smoothed with a median TAO averaging kernel (TAO and MOPITT are both shown unsmoothed here). Error bars are the standard deviation of the monthly means.	85

4.9	Toronto-area tropospheric time series. The smoothed GEOS-Chem model output is shown by the grey lines in panels (a)-(e). (a) Tropospheric columns of O ₃ in molecules/cm ² (TAO=black, CARE=cyan, TES=green crosses), (b) surface O ₃ in ppb (black), and red lines represent the air quality criteria (1-hour is solid, and 8-hour is dashed), (c) Tropospheric columns of CO in molecules/cm ² (TAO=black, CARE=cyan, and MO-PITT=blue crosses), (d) surface CO in ppb (black), (e) total columns of C ₂ H ₆ in molecules/cm ² (TAO=black, CARE=cyan), and (f) total columns of HCN in molecules/cm ² (TAO=black, CARE=cyan).	91
4.10	(a) Same-hour surface vs. (0-5 km) column O ₃ measurements. (b) Same-hour three-hour mean surface O ₃ measurements vs. GEOS-Chem (GC) surface O ₃ (one-to-one line shown). (c) Coincident (closest-in-time) tropospheric O ₃ columns: GEOS-Chem smoothed vs. TAO measurements (one-to-one line shown). Different colours are for the different seasons, and correlation coefficients (R) are listed for each case.	92
4.11	Monthly mean Toronto O ₃ partial columns from GEOS-Chem (GC, smoothed and unsmoothed) versus those from TAO.	93
4.12	(a) Same-hour surface vs. column CO measurements. (b) Same-hour three-hour mean surface CO measurements vs. GEOS-Chem (GC) surface CO (one-to-one line shown). (c) Coincident (closest-in-time) tropospheric CO columns: GEOS-Chem smoothed vs. TAO measurements (one-to-one line shown). Different colours are for the different seasons, and correlation coefficients (R) are listed for each case.	94
4.13	Monthly mean Toronto CO partial columns from GEOS-Chem (GC, smoothed and unsmoothed) versus those from TAO.	95
4.14	Toronto C ₂ H ₆ total columns from GEOS-Chem (GC, smoothed) versus those from TAO.	96

5.1	Pollution rose for 2002-2013 TAO tropospheric O ₃ (0-5 km) in molecules/cm ² , using GEOS-4 and GEOS-5 wind fields. Means of the O ₃ columns for each season are given.	101
5.2	Pollution rose for 2002-2011 surface O ₃ in ppb, using GEOS-4 and GEOS-5 wind fields. Means of the O ₃ VMRs for each season are given.	102
5.3	Pollution rose for 2002-2013 TAO tropospheric CO (0-5 km) in molecules/cm ² , using GEOS-4 and GEOS-5 wind fields. Means of the CO columns for each season are given.	103
5.4	Pollution rose for 2002-2011 surface CO in ppm, using GEOS-4 and GEOS-5 wind fields. Means of the CO VMRs for each season are given.	104
5.5	DOFS rose for 2002-2013 TAO tropospheric O ₃ columns (unitless), using GEOS-4 and GEOS-5 wind fields. Means of the DOFS for each season are given.	105
5.6	North American map showing the three wind bins used to sort the O ₃ and CO data.	106
5.7	Deseasonalized TAO tropospheric columns of CO vs. O ₃ : (a) all data, and separated into three wind bins: (b) from the southeast, (c) from Canada, and (d) from the west.	108
5.8	Toronto surface O ₃ vs. TAO lower-tropospheric O ₃ (a) overall (2002-2010), and separated into three wind bins: (b) from the southeast, (c) from Canada, and (d) from the west. Different colours are shown for the four seasons.	110
5.9	Same as Figure 5.8, but from GEOS-Chem model output.	111
5.10	(top) Average Toronto summertime maximum temperatures, based on monthly mean temperature data from Environment Canada, which were averaged for June, July, and August of each year. (bottom) Number of pollution events (defined in text, Section 5.5) in each year.	115

5.11	Toronto-area tropospheric time series for summer to fall 2002. The smoothed GEOS-Chem model output is shown by the grey lines. (a) Tropospheric columns of O ₃ in molecules/cm ² (TAO=black, CARE=cyan, TES=green crosses starting in 2006), (b) surface O ₃ in ppb, with red lines representing the air quality criteria (solid for the 1-hour criterion, and dashed for the 8-hour criterion), (c) tropospheric columns of CO in molecules/cm ² (TAO=black, CARE=cyan, and MOPITT=blue crosses), (d) surface CO in ppb, (e) surface NO _x in ppb, (f) total columns of C ₂ H ₆ in molecules/cm ² (TAO=black, CARE=cyan), and (g) total columns of HCN in molecules/cm ² (TAO=black, CARE=cyan). Pollution events are defined in the text, and highlighted by orange circles.	117
5.12	Same as Figure 5.11, but for 2003.	118
5.13	Same as Figure 5.11, but for 2004.	118
5.14	Same as Figure 5.11, but for 2005.	119
5.15	Same as Figure 5.11, but for 2006. Red circles highlight a biomass burning event.	120
5.16	Same as Figure 5.11, but for 2007.	121
5.17	Sensitivity of Toronto tropospheric O ₃ columns (0-5 km), on the dates shown, to total North American (top) fossil fuel NO _x emissions, and (bottom) fossil fuel CO emissions.	124
5.18	Sensitivity of Toronto tropospheric O ₃ columns (0-5 km), on the dates shown, to isoprene emissions.	125
5.19	Sensitivity of Toronto tropospheric O ₃ columns (0-5 km), on the dates shown, to (top) lightning NO _x emissions, and (bottom) soil NO _x emissions.	126
5.20	Sensitivity of Toronto tropospheric O ₃ columns (0-5 km), on the dates shown, to biomass burning NO _x emissions (top) and CO emissions (bottom).	127

5.21	Sensitivity of Toronto tropospheric O ₃ columns (0-5 km), on the dates shown, to aircraft NO _x emissions (top) and biofuel emissions (bottom). . .	128
5.22	Sensitivity of Toronto tropospheric CO columns (0-5 km), on the dates shown, to (a) fossil fuels, (b) isoprene oxidation, (c) biomass burning, and (d) biofuels.	129
5.23	Regions selected for further analysis of GEOS-Chem sensitivity results. . .	130
5.24	Sensitivity of Toronto tropospheric O ₃ columns (0-5 km), on the dates shown, to regional fossil fuel emissions of (top) NO _x and (bottom) CO emissions. The colours here correspond to the colours in Figure 5.23. . . .	131
5.25	Sensitivity of Toronto tropospheric O ₃ columns (0-5 km), on the dates shown, to regional isoprene emissions.	132
5.26	Map of total North American isoprene emissions on a typical summertime day (21 July 2005) in the model (from the MEGAN inventory).	133
5.27	Sensitivity of Toronto tropospheric O ₃ columns (0-5 km), on the dates shown, to regional lightning (top) and soil (bottom) NO _x emissions. . . .	134
5.28	Sensitivity of Toronto tropospheric O ₃ columns (0-5 km), on the dates shown, to regional biomass burning emissions of (top) NO _x , and (bottom) CO.	135
5.29	Sensitivity of Toronto tropospheric CO columns (0-5 km), on the dates shown, to each kind of emission, separated by region.	137
5.30	NCEP maps (daily mean composites) on 5 October 2005 of: (left) surface temperature anomaly, and (right) geopotential height anomaly compared to the 30-year climatological means.	139
5.31	HYSPLIT back-trajectories for Toronto, starting on 5 October 2005, 18:00 UT, going back three days with points every 6 hours. Three altitudes are shown, starting at 0.5, 1.0 and 3.0 km over Toronto.	140

5.32	GEOS-Chem modelled O ₃ at 1.3 km altitude on 2, 3, and 5 October (top, middle, and bottom, respectively) at 21:00 UT. We see the transport and evolution of enhanced O ₃ concentrations.	141
5.33	GEOS-Chem adjoint results for 5 October 2005, showing sensitivity of Toronto O ₃ tropospheric columns to (left) anthropogenic NO _x emissions, and (right) isoprene emissions.	142
5.34	GEOS-Chem surface H ₂ O ₂ /HNO ₃ ratios across North America on 5 October 2005. Ratios less than 0.3 may be hydrocarbon-limited for O ₃ production.	142
5.35	NCEP maps on 7 September 2007 of: (left) surface temperature anomaly, and (right) geopotential height anomaly compared to the 30-year climatological means.	144
5.36	HYSPLIT back-trajectories for Toronto, starting on 7 July 2006, 14:00 UT, going back three days with points every 6 hours. Three altitudes are shown, starting at 0.5, 1.0 and 3.0 km over Toronto.	145
5.37	GEOS-Chem adjoint results for 7 September 2007, showing sensitivity of Toronto O ₃ tropospheric columns to: (left) anthropogenic NO _x emissions, and (right) isoprene emissions.	146
5.38	HYSPLIT back-trajectories for Toronto, starting on 21 July 2005, 18:00 UT, going back three days with points every 6 hours. Three altitudes are shown, starting at 0.5, 1.0 and 3.0 km over Toronto.	147
5.39	NCEP maps on 21 July 2005 of: (left) surface temperature anomaly, and (right) geopotential height anomaly compared to the 30-year climatological means.	148
5.40	GEOS-Chem adjoint results for 21 July 2005, showing sensitivity of Toronto O ₃ tropospheric columns to: (left) anthropogenic NO _x emissions, and (right) isoprene emissions.	149

5.41	GEOS-Chem adjoint results for 2 August 2007, showing sensitivity of Toronto O ₃ tropospheric columns to North American emissions separated by regions.	150
5.42	HYSPLIT back-trajectories for Toronto, starting on 2 August 2007, 13:00 UT, going back seven days with points every 6 hours. Three altitudes are shown, starting at 0.5, 1.0 and 3.0 km over Toronto.	150
5.43	NCEP maps on 2 August 2007 of: (left) surface temperature anomaly, and (right) geopotential height anomaly compared to the 30-year climatological mean.	151
5.44	GEOS-Chem adjoint results for 2 August 2007, showing sensitivity of Toronto O ₃ tropospheric columns to (top) anthropogenic NO _x emissions, (middle) soil NO _x emissions, and (bottom) isoprene emissions.	152
5.45	(left) HYSPLIT back-trajectories for Toronto, starting on 21 July 2005, 18:00 UT, going back three days with points every 6 hours. Three altitudes are shown, starting at 1.0, 3.0 and 4.0 km over Toronto. (right) A MODIS fire map for a period from 30 June 2006 to 9 July 2006, showing a cluster of fires in northern Saskatchewan.	154
5.46	GEOS-Chem adjoint results for 7 July 2006, showing sensitivity of Toronto CO tropospheric columns to North American emissions separated by regions.	155
5.47	GEOS-Chem adjoint results for 7 July 2006, showing sensitivity of Toronto CO tropospheric columns to biomass burning emissions.	156
5.48	(left) Sensitivity of Toronto tropospheric column O ₃ and (right) surface O ₃ to anthropogenic NO _x emissions, for three case studies demonstrating (top) short-range, (middle) mid-range, and (bottom) long-range transport.	158

5.49	TAO OSSE using real TAO observation frequency in July 2010. The scale factors are true emissions divided by constrained emissions for an a priori “bad guess” of 50% more anthropogenic NO _x emissions (1.5×). Here scales of 0.5 = no constraint, 1 = get back the true emissions, and >1 = over-constrained.	165
6.1	VMR averaging kernels (thin coloured lines), sensitivity (thick blue lines), and stratospheric partial column (12-50 km) averaging kernels (thick purple lines) for TAO retrievals of (a) HF, (b) HCl, (c) O ₃ (from 3051 cm ⁻¹ microwindow), (d) O ₃ (from 1000 cm ⁻¹ microwindow), and (e) N ₂ O. In panels (c) and (d), the O ₃ partial column averaging kernels for 12-23 km and 23-50 km are shown in orange and green, respectively.	172
6.2	TAO (black), CARE (cyan), and OSIRIS (red) stratospheric partial columns (12-50 km) of (a) HF, (b) HCl, (c) O ₃ (from the 3051 cm ⁻¹ microwindow) and (d) N ₂ O. In the O ₃ panel (c), the grey and blue crosses are retrievals from the 1000 cm ⁻¹ microwindow for TAO and CARE, respectively. Panel (e) is sPV over Toronto at 435 K (green), 475 K (blue), 675 K (orange), and 950 K (cyan), and the inner (sPV=1.6 × 10 ⁻⁴ s ⁻¹) and outer (sPV=1.2 × 10 ⁻⁴ s ⁻¹) vortex edges are indicated by the upper and lower horizontal lines, respectively.	179
6.3	Number of polar intrusion days at four vertical levels (950 K, 675 K, 475 K, and 435 K) over Toronto from January 2002 to March 2013, from the MERRA DMPs, separated by month. sPV given in 10 ⁻⁴ s ⁻¹ . Panel (a) shows the number of intrusions that are within the vortex edge region, and (b) shows the number of intrusions that are within the vortex. Panel (c) shows the number of intrusion days that met the four criteria described in Section 6.5.1.	180
6.4	Same as Figure 6.3, but separated by year.	181

6.5	Same as Figure 6.2, but an expanded view of each year, and 3051 and 1000 O ₃ products are combined into black (TAO) and cyan (CARE) points. Grey and yellow boxes highlight the polar intrusion events (grey showing events that met the four criteria, and yellow showing events that met only three of the four criteria).	184
6.6	Same as Figure 6.5, but later years.	185
6.7	Variance in TAO stratospheric partial columns of (a) HF, (b) HCl, (c) O ₃ , and (d) N ₂ O, and in (e) sPV, as given by the standard deviation from the climatological monthly mean for each month. Circles are for the full time series, and crosses are for the time series without the polar intrusion events. In panel (e), 435 K is green, 475 K is blue, 675 K is orange, and 950 K is cyan, and the crosses are for the time series without the enhanced sPV days.	188
6.8	Polar intrusion event on 20 January 2003. Left panels: MERRA PV (in pvu) at 435 K, 475 K, 675 K, and 950 K. White contours denote the inner and outer vortex edge limits. Right panel: EP TOMS total O ₃ column (note this map is oriented 90° counter-clockwise compared to the MERRA maps). White circles on each map represents the location of Toronto/Egbert.	194
6.9	Polar intrusion event on 6 February 2007. <i>Top row</i> : MIMOSA PV, MERRA PV (both in pvu), and GMI N ₂ O (in ppbv). <i>Bottom row</i> : GMI O ₃ at 475 K, and 575 K (both in ppbv), and OMI total column O ₃ (note the OMI map is oriented 90° counter-clockwise compared to the other maps). White circles denote the location of Toronto/Egbert. White contours denote the inner and outer vortex edge limits.	195

6.10	Polar intrusion event on 25 March 2011. <i>From left to right:</i> MIMOSA and MERRA PV (both in pvu), GMI N ₂ O and O ₃ (both in ppbv), and OSIRIS O ₃ (also in ppbv). At the bottom is OMI O ₃ total column (note the different orientation). <i>From top to bottom:</i> 475 K, 675 K, and 950 K. White circles denote the location of Toronto/Egbert. White contours denote the inner and outer vortex edge limits.	197
6.11	Polar intrusion event on 16 January 2009. <i>From left to right:</i> MIMOSA and MERRA PV (both in pvu), GMI N ₂ O and O ₃ (both in ppbv), and the OMI total O ₃ column map is also shown (note the different orientation). From top to bottom, the intrusion is shown at 435 K, 475 K, 675 K, and 950 K. White circles denote the location of Toronto/Egbert. White contours denote the inner and outer vortex edge limits.	198
6.12	sPV over Toronto during the 53 polar intrusion events derived from MERRA (blue and coloured lines). The grey vertical lines indicate the outer and inner polar vortex edges. The horizontal dashed lines are the four vertical levels at which sPV was sampled in the time series. The thick black line and dashed black lines are the mean sPV profile from all non-intrusion days and its standard deviation, respectively. The coloured lines are sPV profiles from specific days that were discussed in Sections 6.5.2 and 6.5.4: mauve=20 January 2003, red=14 May 2003, dark green=14 December 2004, orange=3 March 2005, pink=16 January 2009, and light green=27 October 2010.	200
A.1	CH ₄ MW analysis. The error bars are not shown for clarity, however they are approximately the same size as the data points.	213
A.2	C ₂ H ₆ MW analysis. The error bars are not shown for clarity, however they are approximately the same size as the data points.	214

A.3	N ₂ O MW analysis. The error bars are not shown for clarity, however they are approximately the same size as the data points.	215
A.4	CO MW analysis. The error bars are not shown for clarity, however they are approximately the same size as the data points.	216
A.5	O ₃ MW analysis. The error bars are not shown for clarity, however they are approximately the same size as the data points.	217
A.6	Typical spectral fits in the IRWG-recommended MWs for CH ₄	219
A.7	Typical spectral fits in the standard TAO MWs for CH ₄	220
A.8	Typical spectral fits in the IRWG-recommended MWs for C ₂ H ₆	222
A.9	Typical spectral fits in the standard TAO MWs for C ₂ H ₆	223
A.10	Typical spectral fits in the IRWG-recommended MWs for N ₂ O.	224
A.11	Typical spectral fit in the standard TAO MW for N ₂ O.	225
A.12	Typical spectral fits in the IRWG-recommended MWs for CO.	226
A.13	Typical spectral fits in the standard TAO MWs for CO.	227
A.14	Two typical spectral fits in the IRWG-recommended MW for O ₃	228
A.15	Typical spectral fit in the standard TAO MW for O ₃	229

Chapter 1

Introduction and motivation

Outdoor air pollution started to become a widespread problem in the industrial age. With many technological advances came emissions of harmful chemicals and particulate matter to the atmosphere. Air pollution has been directly or indirectly responsible for ozone layer depletion [*WMO*, 2011], acid rain [*International Joint Commission*, 2012], global warming [*IPCC, WorkingGroup1*, 2013], smog [*EPA*, 1999], ocean acidification [*IPCC, WorkingGroup1*, 2013], respiratory illness and death in human beings [*EPA*, 1999; *WHO*, 2014], and damage to plants, animals, and ecosystems [*Bell and Treshow*, 2002; *Fishman et al.*, 2010]. Therefore, the importance of controlling emissions and monitoring atmospheric composition globally cannot be understated.

In Canada, pollutants that are monitored regularly and deemed a health risk are: ozone, particulate matter smaller than 2.5 microns (PM2.5), nitrogen oxides, and carbon monoxide. Overall, air quality in Canada has been improving over the last twenty years. Standards for the surface concentrations of these pollutants have been set, and in Ontario, the standards for nitrogen oxides and carbon monoxide have not been exceeded in over two decades [*MOE*, 2012]. Even the standard for PM2.5 has not been exceeded in Ontario since 2008 [*MOE*, 2013]. Only ozone continues to exceed standards in most parts of Ontario every summer. Ozone in the atmosphere is not emitted by anything

directly. Rather it is created by photochemical reactions between hydrocarbons and nitrogen oxides [Jacob, 1999]. The relationship between ozone and its precursors is not linear, and this is what makes it so difficult to control, as emission reductions do not directly result in ozone reductions.

High ultraviolet exposure due to stratospheric ozone loss is also an issue that remains, especially at high latitudes, as the most severe ozone loss is at the poles [WMO, 2011]. Climate change is causing the stratosphere to cool, and this may increase the frequency of conditions that remove polar stratospheric ozone effectively. For example, in spring of 2011, there was unprecedented Arctic ozone loss due to catalytic chemistry on polar stratospheric clouds in a cold, stable polar vortex [Balis *et al.*, 2011; Manney *et al.*, 2011; Adams *et al.*, 2012; Lindenmaier *et al.*, 2012]. At high latitudes, this does not affect a large population, but sometimes polar vortex air can intrude down to midlatitudes through vortex excursions or filaments that break off from the polar vortex. It has been reported that up to 50% of mid-latitude O₃ volume mixing ratio decreases in the lower-stratosphere can be accounted for by intrusions of O₃-poor polar air to midlatitudes [Marchand *et al.*, 2003; Millard *et al.*, 2003].

While atmospheric research can be done with large networks of surface measurements [e.g., Chin *et al.*, 1994; Fiore *et al.*, 2002; Leibensperger *et al.*, 2008; Cooper *et al.*, Zhang *et al.*, 2011; 2012], or global measurements from satellites, Yang *et al.*, 2010; Voulgarakis *et al.*, 2011; Pommier *et al.*, 2013], there is still much to be gained from studying atmospheric composition over a major city like Toronto. Toronto, with 2.8 million people (6.1 million, if the entire Greater Toronto Area is considered) is the largest city in Canada, and the fourth largest city in North America (after Mexico City, 8.9 million; New York, 8.3 million; and Los Angeles, 3.9 million). Any changes in atmospheric composition may affect a very large number of people. Should a polar vortex intrusion bring O₃-poor air over Toronto, people may suffer exposure to higher ultraviolet radiation and increased skin cancer risk. Should highly polluted air be transported, or trapped

in the city regularly, illness and death can result. For example, a Toronto Public Health study estimated that O_3 air pollution caused 700 hospitalizations and 200 deaths per year in Toronto [*Toronto Public Health*, 2014]. Ground-based atmospheric measurements in a large city are also pragmatic, as instrumentation is easily accessible for installation and maintenance.

1.1 Science questions and goals

The first scientific question I will address in this thesis is about finding the important sources of Toronto-area O_3 air pollution, and quantifying those source contributions. This knowledge may help inform why O_3 air pollution remains a problem for Toronto and Ontario in general.

The second scientific question I will address is to determine how often polar vortex intrusions affect the Toronto-area, and whether they are responsible for significant variations in atmospheric composition (including O_3) there.

To answer these questions, we will need long-term measurements of both the troposphere and stratosphere in the Toronto-area. Therefore, I will report on research done at the University of Toronto Atmospheric Observatory (TAO), which houses a Fourier transform infrared (FTIR) spectrometer as its primary instrument (called the “TAO FTS” throughout this thesis). My first goal is to improve measurements with the TAO FTS, as they originally were mainly used for stratospheric measurements, rather than tropospheric measurements. And my second and third goals are to address the science questions above, using the TAO dataset.

1.2 Unique measurements

The TAO FTS measures solar absorption spectra, from which the concentration of many atmospheric trace gases can be retrieved in a vertical column of air over Toronto. I have

focused my research mainly on six trace gases that are important in the troposphere: ozone (O_3), carbon monoxide (CO), ethane (C_2H_6), hydrogen cyanide (HCN), methane (CH_4), and nitrous oxide (N_2O) and on three trace gases that are important in stratospheric dynamics and chemistry: O_3 , hydrogen fluoride (HF), and hydrogen chloride (HCl). I will refer to these gases as the “eight primary species” in this thesis.

TAO was established in 2001-2002, and is one of a few urban sites in the Network for Detection of Atmospheric Composition Change (NDACC) Infrared Working Group (IRWG), which is a global network of ground-based observatories that use FTIR instruments to measure atmospheric composition. The first goal of this thesis is to optimize the retrieval parameters for Toronto and make them consistent with the rest of the IRWG, and to archive TAO measurements in the NDACC database. This thesis will present eleven years (mid-2002 to mid-2013) of TAO measurements of eight trace gases and the analysis of their seasonal and short-term variability.

Measurements of atmospheric composition can take place on many platforms. There are a number of surface *in situ* measurement networks such as the Canadian Air and Precipitation Monitoring Network (CAPMoN), and the National Air Pollution Surveillance Program (NAPS) that measure air pollutants such as O_3 and CO. These measurements have very long continuous time series (e.g., NAPS was established in 1969), and are very precise and accurate, as they can be calibrated with known quantities of gases. They also function in all weather conditions. A disadvantage is that they only measure the surface air where they are located (a point measurement), and do not provide vertical information. To get vertical information, *in situ* instruments can be placed aboard aircraft (e.g., Measurements of OZone, water vapour, carbon monoxide and nitrogen oxides by inservice Airbus airCraft, MOZAIC) and balloons (e.g., ozonesondes). However, these have the disadvantage of only measuring during specific time periods at particular locations. Satellite measurements of atmospheric composition have the advantage of providing global coverage, relatively long time series (on the order of a few years to decades),

and some vertical information (though not as high resolution as aircraft and balloon). However, it is more difficult to maintain the quality of satellite measurements, they often do not have good temporal resolution at each particular location, and they cannot measure when the sky is cloudy. The advantages of ground-based FTIR measurements are: they can provide long time series (> 10 years), good temporal frequency (restricted to daytime, and clear-sky conditions), and some vertical information for multiple species. Ground-based FTIR spectroscopy can provide greater sensitivity to lower in the troposphere for some species than can satellite measurements. Their column measurements are useful for model comparisons, as the columns are more representative of the larger domain of the model resolution than point surface measurements are. Column measurements are also more useful than *in situ* surface measurements when one is interested in calculating surface fluxes. Column measurements are useful for satellite validation and comparison studies as well. However, ground-based FTIR measurements also have the disadvantages of needing a clear sky, and having restricted spatial coverage. Therefore, they are complementary to other measurement techniques.

1.3 Methodology

1.3.1 Interpretation of Toronto tropospheric composition

The tropospheric observations from TAO are interpreted with the chemical transport model (CTM) GEOS-Chem [www.geos-chem.org], which is a global 3-D model of atmospheric composition driven by assimilated meteorological observations from the NASA Global Modeling and Assimilation Office. The second goal of this thesis is to identify and quantify the important sources of tropospheric O_3 and CO for the Toronto area, and thus, the important contributors to our regional air quality. The GEOS-Chem model allows this to be calculated.

For this study, it is advantageous to use a global model, like GEOS-Chem, as non-

North American emissions contribute a significant background to Toronto-area column concentrations of particular species [e.g., *Lin et al.*, 2000; *Fiore et al.*, 2002]. GEOS-Chem also has the option to simulate certain continental regions, such as North America, at higher resolution, which allows one to better model the sources of short-term variability for the Toronto region. GEOS-Chem simulations have been well-validated [*Bey et al.*, 2001a, 2001b; *Henze et al.*, 2007; *Zhang et al.*, 2008; *Chan et al.*, 2009; *Fisher et al.*, 2010], and the model continues to improve and incorporate more species and more chemistry.

1.3.2 Interpretation of Toronto stratospheric composition

HF and N₂O are long-lived trace gases, which act as tracers of transport. For the third goal of the thesis, I aim to show whether or not polar vortex intrusions via filaments or vortex excursions to midlatitudes are a significant source of variability of Toronto-area stratospheric gases (HF, HCl, and O₃). HF is a stratospheric gas, whose columns in the polar vortex are enhanced due to descending air there. Similarly, N₂O columns are reduced in the polar vortex, as N₂O is a tropospheric gas. Therefore, high outliers of HF and low outliers of N₂O in the TAO dataset may be a sign of polar vortex intrusions. In order to determine if that is the case, scaled potential vorticity from derived meteorological products (DMPs) is used to diagnose if the air overhead is inside the polar vortex or the polar vortex edge. Potential vorticity models, reanalyses, and the Global Modeling Initiative (GMI) 3-D CTM are also used to confirm polar vortex intrusions. The 11 years of HF and N₂O measurements at TAO provide a unique opportunity to determine how often polar vortex intrusions affect this mid-latitude location.

1.4 Contributions of the candidate and collaborators

The TAO FTS and many of its analysis programs (retrievals, instrument line shape, etc.) were established by Kimberly Strong and former PhD students, Aldona Wiacek and

Jeffrey Taylor. Measurements at TAO from 2001 to 2008 were done by Aldona Wiacek, Jeffrey Taylor, and a large number of students, interns, and postdoctoral fellows. From September 2008 to May 2012, I was responsible for 40% of TAO measurements, and four Environment Canada Science Horizons interns were responsible for the remaining 60% of measurements. From 2012 onwards, my measurement responsibilities were reduced, as a technical research officer for TAO was hired, though I was still involved in measurements, maintenance, training, and troubleshooting.

Original retrieval and data analysis programs for TAO were provided by Jeffrey Taylor, and updated programs were provided by Felicia Kolonjari, Rebecca Batchelor, and Rodica Lindenmaier. I was responsible for making them compatible with TAO spectra and retrievals and using them for data analysis. All of the TAO data preparation and retrievals in this thesis were carried out by me.

The FTIR measurements from the Centre for Atmospheric Research Experiments (CARE) were conducted by Environment Canada, and the resulting spectra were provided to me by Richard Mittermeier and Hans Fast. All of the CARE retrievals and analysis in this thesis were carried out by me.

The Measurements of Pollution in the Troposphere satellite measurements were provided by Chris McLinden, and data selection routines were provided by Matthieu Pommer. The partial column calculations and smoothing of MOPITT data were done by me. Tropospheric Emission Spectrometer satellite measurements were downloaded from their website, and I did the data selection and partial column calculations. Surface measurements in Toronto were conducted by the Ontario Ministry of the Environment, as a part of the NAPS program, and were downloaded from their website.

The GEOS-Chem model is a community model developed by its users, although most of its development has been undertaken by the Atmospheric Chemistry Modeling Group at Harvard University. It was implemented in the Department of Physics at the University of Toronto by Dylan Jones. The full chemistry nested adjoint was set up and run for one

Toronto pollution event by former PhD student, Thomas Walker, and I ran the rest of the pollution events using his setup.

Derived meteorological products for Toronto were provided by Gloria Manney and William Daffer. The Global Modelling Initiative model results were provided by Susan E. Strahan, and many of its analysis routines were provided by former PhD student, Cristen Adams. Optical Spectrograph and InfraRed Imager System satellite data were provided by Doug Degenstein and Adam Bourassa, and many of its analysis routines were provided by Cristen Adams and summer student, Boris Pavlovic.

1.5 Thesis outline

The outline of this thesis is as follows: Chapter 2 contains information about our primary measurement technique, FTIR spectroscopy, and how it is used to measure atmospheric composition. Chapter 3 describes how trace gas retrievals for the eight primary species were optimized and harmonized with the IRWG, and then presents their eleven-year total column time series. Some of this work was started during my M.Sc. project, so that portion of the retrieval study is located in the first Appendix (A). A preliminary calculation of the 11-year trends are presented in the second Appendix (B). Chapter 4 presents background on tropospheric chemistry, air quality, complementary surface and satellite measurements, and the GEOS-Chem model. The TAO lower-tropospheric (0-5 km) partial columns of O_3 and CO are presented as well. Tropospheric measurements made at TAO continue to be discussed in Chapter 5, where I show how summertime lower-tropospheric columns can be used to assess air quality, and we take a closer look at Toronto pollution episodes (outliers of O_3 and CO), and identify the processes contributing to O_3 levels in Toronto. Chapter 6 presents the interpretation of TAO stratospheric measurements and their variability due to polar vortex intrusions. Finally, Chapter 7 concludes the thesis and highlights the important results of this research.

Chapter 2

FTIR measurements

Many interesting molecules in our atmosphere are radiatively active, absorbing incoming solar radiation selectively. These molecules have specific rotational and vibrational modes that cause them to absorb radiation at specific mid-infrared (MIR) wavelengths. It is thanks to this property that we are able to measure the composition of the atmosphere at varying altitudes without leaving the ground. This chapter will explain how we use the solar absorption spectra measured by a ground-based FTIR spectrometer to retrieve total and partial column concentrations of trace gases.

2.1 Molecular spectroscopy

All atoms and molecules absorb and emit radiation as a result of transitions between energy states. The simplest and most common example of this is when a hydrogen atom absorbs a photon of wavelength 121.6 nm (photon energy, $E = 10.2$ eV); it then has exactly enough energy to move the electron from its lowest energy state, $n = 1$, to the next highest, $n = 2$. When this electron returns to its lower energy state, it emits a photon of the same wavelength. For molecules, the different energy states are more complex since there are not only electronic energy states, but also rotational and vibrational states associated with the movement of the atoms within the molecule. Quantum theory restricts

the energy states, E , to specific values which, for rotational-vibrational movement in a diatomic molecule, can be written as [Bernath, 2005]:

$$E = BJ(J + 1) + \omega_e(v + \frac{1}{2}) - [DJ^2(J + 1)^2 + \omega_e\chi_e(v + \frac{1}{2})^2], \quad (2.1)$$

where J is the rotational quantum number ($J = 0, 1, 2, \dots$), v is the vibrational quantum number ($v = 0, 1, 2, \dots$), D is the centrifugal distortion constant, and $\omega_e\chi_e$ is the anharmonicity constant. The rotational constant, B , is given by:

$$B = \frac{h^2}{8\pi^2Ic}, \quad (2.2)$$

where h is Planck's constant, I is the moment of inertia of the molecule, and c is the speed of light. And the vibrational energy constant, ω_e , is given by:

$$\omega_e = \frac{1}{2\pi c} \sqrt{\frac{k}{\mu}}, \quad (2.3)$$

where k is the classical spring force constant and μ is the reduced mass of the molecule. The first two terms of Equation 2.1 correspond to a rigid rotor and harmonic oscillator, and the second two terms are the correction for centrifugal distortion and anharmonicity. When a molecule generates an electric dipole moment due to this kind of motion, it can absorb an infrared photon of energy ΔE , where the allowed transitions are $\Delta J = \pm 1$ and $\Delta v = \pm 1, \pm 2, \pm 3, \dots$ [Bernath, 2005]. The energy of a vibrational transition is much greater (photon emitted and absorbed in the infrared) than the energy of a rotational transition (photon emitted and absorbed in the microwave).

Polyatomic molecules also absorb/emit radiation at specific energies, and these too are based on their structure and composition, but the equations governing those energies are more complicated. However, all this means that each kind of molecule has a distinct spectral signature that, when observed, allows us to identify the source. At TAO, we record solar absorption spectra to quantify the abundance of different molecules in the atmosphere by examining their spectral lines at specific wavenumbers.

In reality all spectral *lines* have a certain width and depth, and a specific shape. The depth and shape of the spectral line is dependent on three properties of the absorbing gas:

1. the temperature of the gas,
2. the pressure of the gas, and
3. the concentration of the molecules in the gas.

The pressure, in particular, determines how the line is broadened. The following subsections describe these relationships in more detail.

2.1.1 Line shape

Collisional broadening

When the pressure, P , of a gas is above ~ 1.33 hPa, as in the troposphere, the mechanism of line broadening is dominated by molecular collisions in the gas, and is called *collisional broadening*. The absorption coefficient (related to the shape of the line), centered on wavenumber $\tilde{\nu}_o$, in collision-broadened spectra is Lorentzian [Lorentz, 1906; Liou, 2002]:

$$k(\tilde{\nu}) = \frac{S}{\pi} \frac{\alpha_L}{\alpha_L^2 + (\tilde{\nu} - \tilde{\nu}_o)^2}, \quad (2.4)$$

where $\tilde{\nu}$ is the wavenumber (in cm^{-1}), $k(\tilde{\nu})$ is the absorption coefficient, S is the line strength, and α_L is the half width at half maximum (HWHM) of the collision-broadened line, and is directly proportional to the pressure and temperature of the gas:

$$\alpha_L = \alpha_o \frac{P}{P_o} \sqrt{\frac{T_o}{T}} \quad (2.5)$$

$$= \text{HWHM}, \quad (2.6)$$

where P_o is standard pressure, T_o is standard temperature and α_o occurs when $P = P_o$ and $T = T_o$ and is typically 3×10^9 Hz or 0.1 cm^{-1} .

Doppler broadening

When P is small $\lesssim 1.33$ hPa, as it is in the stratosphere, the shape and width of the spectral lines are dominated by the Doppler effect. The Doppler effect is caused by variations of the speed of the molecule in the direction of the beam. The absorption coefficient of Doppler-broadened lines is Gaussian [Liou, 2002]:

$$k(\tilde{\nu}) = \frac{S}{\alpha_D \sqrt{\pi}} \exp \left[-\frac{(\tilde{\nu} - \tilde{\nu}_0)^2}{\alpha_D^2} \right], \quad (2.7)$$

where α_D is proportional to the HWHM of the band and is given by [Liou, 2002]:

$$\alpha_D = \frac{\tilde{\nu}_0}{c} \sqrt{\frac{2KT}{m}} \quad (2.8)$$

$$= \frac{HWHM}{\sqrt{\ln 2}}, \quad (2.9)$$

where K is the Boltzmann constant, T is the temperature, c is the speed of light, and m is the mass of the molecule. For example, in the H-O-H bending mode of water, the Doppler width, α_D , at room temperature is about 0.0044 cm^{-1} , which is very narrow for an instrument to resolve [Griffiths and Haseth, 2007].

The Voigt Profile

For molecules at pressures between 1.33 hPa and 133.3 hPa, the line width a combination of both Doppler and collisional broadening, and can be modelled using a Voigt profile:

$$k(\tilde{\nu}) = k_L(\tilde{\nu}) * k_D(\tilde{\nu}) \quad (2.10)$$

$$= \frac{S}{\pi^{3/2}} \frac{\alpha_L}{\alpha_D} \int_{-\infty}^{\infty} \frac{1}{(\nu - \nu_0)^2 + \alpha^2 + L} \exp \left[\frac{-(\tilde{\nu} - \tilde{\nu}_0)^2}{\alpha_D^2} \right] d\nu \quad (2.11)$$

where, $k_L(\tilde{\nu})$ and $k_D(\tilde{\nu})$ are the Lorentz and Doppler absorption coefficients from Equations 2.4 and 2.11, respectively. This profile has a HWHM of α_V [Griffiths and Haseth, 2007]:

$$\alpha_V = \frac{\alpha_L}{2} + \sqrt{\left(\frac{\alpha_L}{2}\right)^2 + (\alpha_D \ln 2)^2} \quad (2.12)$$

$$= HWHM. \quad (2.13)$$

Spectra measured with the TAO FTS include absorption from the total column of the atmosphere. That is, the solar spectrum observed from the ground has had absorption along the entire pressure range from 0 (top of atmosphere) to 1000 hPa (at ground level). Therefore the Voigt profile above is appropriate for describing spectral lines measured at TAO.

2.1.2 Line strength

The Beer-Lambert-Bouguer law (also known as *Beer's law*) [Perrin, 1948] states that the attenuation in the intensity of light, $I(\tilde{\nu})$, as the light passes through a thickness, dL , of the atmosphere is related to the density of gas i , ρ_i , with a constant of proportionality equal to the absorption coefficients, $k(\tilde{\nu})$ (e.g., from Equations 2.4 and 2.11 above) [Liou, 2002; Griffiths and Haseth, 2007]:

$$dI(\tilde{\nu}) = -k(\tilde{\nu})\rho_i I(\tilde{\nu})dL. \quad (2.14)$$

When we assume that $k(\tilde{\nu})$ and ρ_i are constant over a layer of atmosphere, L , we can integrate Equation 2.14 to get:

$$I(\tilde{\nu}) = I_o(\tilde{\nu}) \exp(-k(\tilde{\nu})\rho_i L), \quad (2.15)$$

where $I_o(\tilde{\nu})$ is the intensity at the top of the layer. The transmittance, $\tau(\tilde{\nu})$, of a uniform sample of thickness L at wavenumber $\tilde{\nu}$ is given by:

$$\tau(\tilde{\nu}) = \frac{I(\tilde{\nu})}{I_o(\tilde{\nu})} \quad (2.16)$$

$$= \exp(-k(\tilde{\nu})\rho_i L). \quad (2.17)$$

Therefore, with the equations above and knowing the absorption coefficients, and the temperature and pressure profiles of the atmospheric column, one can hypothetically determine the concentration of a gas at various altitudes from its measured spectral line(s).

2.2 Fourier transform spectroscopy: theory

The FTS at TAO is the Bomem DA8, which is coupled to a solar tracker. The light from the Sun gets directed and focused through a series of mirrors and an optical filter into the interferometer (Figure 2.1) and arrives at a beamsplitter. The beamsplitter reflects half of the light to a fixed mirror, and transmits half the light to a moving mirror (or *scan mirror*). Both beams reflect off their respective mirrors and then recombine at the beamsplitter and get sent to a detector. The detector measures the signal over the changing optical path difference, which is called an interferogram. Since the beams travel different paths, it is possible that when they recombine they will be out of phase. In fact, since the scan mirror is constantly moving, the phase of one beam will be continuously changing, causing variation from constructive interference to destructive interference and back again. The interferogram is therefore a pattern of bright and dark fringes dependent on the optical path difference (OPD, the difference between the distances of the two paths).

The interferogram can be converted into a spectrum using a Fourier transform. A Fourier transform is a mathematical transformation that, in this case, changes a function dependent on OPD (the interferogram) into a function dependent on wavenumber (the spectrum). The interferogram, $I(x)$ (where x is the OPD), that the detector records is composed of spectral intensities, $B(\tilde{\nu})$, that depend on all of the wavenumbers, $\tilde{\nu}$, that compose the source. Equation 2.18 shows this relationship:

$$I(x) = 1/2 \int_0^{\infty} B(\tilde{\nu}) \cos(2\pi\tilde{\nu}x) d\tilde{\nu}. \quad (2.18)$$

Now applying a Fourier transform, Equation 2.18 can undergo Fourier decomposition to extract the spectral intensity:

$$B(\tilde{\nu}) = 2 \int_0^{\infty} I(x) \cos(2\pi\tilde{\nu}x) dx. \quad (2.19)$$

Equation 2.19 is the Fourier transform of Equation 2.18, and it is the spectrum derived from the recorded interferogram. The solar absorption spectrum can then be analysed to

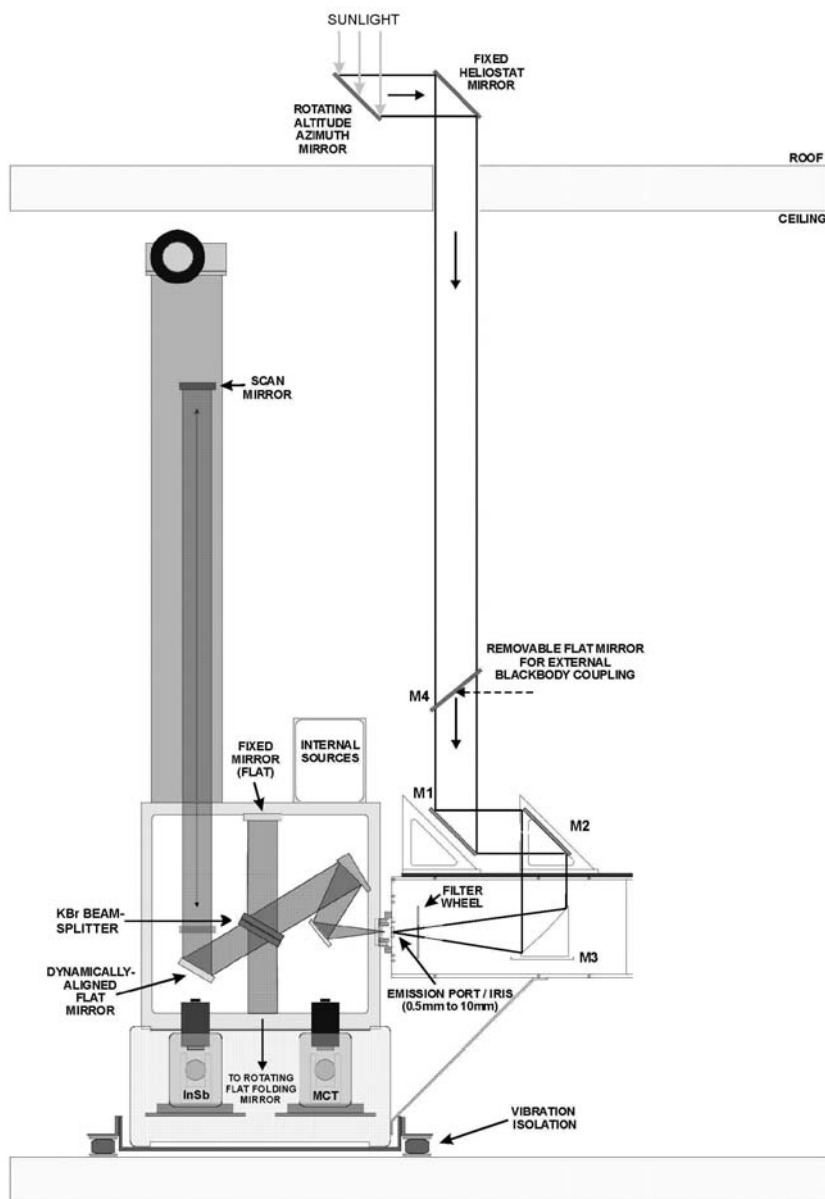


Figure 2.1: The TAO interferometer (adapted from ABB Bomem Inc. facility schematics). Sunlight enters the system at the top and its path is traced by the black lines [Wiacek, 2006].

determine the concentration of the trace gases in our atmosphere as described in Section 2.4.1.

The maximum OPD, x_{max} , of the TAO FTS is 250 cm. Since it is not infinite, one must incorporate an *apodization* function, D , to impose the maximum OPD on the Fourier transform. We use a *boxcar* apodization function, for which the function is 1 from 0 to x_{max} , and zero everywhere else out to infinity. Equation 2.18 gets multiplied by D , and after the Fourier transform, it becomes a sinc function dependent on x_{max} . The sinc function becomes a large factor in determining the instrument broadening of the spectral lines and thus, the spectral resolution of the instrument. Using the full-width at half maximum of the sinc function, the resolution is $0.6/x_{max}$ [Bell, 1972]. However, if a different apodization function is used, then one would achieve a different spectral resolution. Therefore, it is common practice to define the instrument's resolution simply as $1/x_{max}$ [Bell, 1972]. So the OPD of the TAO FTS gives a maximum spectral resolution of 0.004 cm^{-1} .

The advantages of using an FTS as opposed to another kind of spectrometer (e.g., a scanning grating spectrometer) are:

1. the Fellgett advantage [Fellgett, 1951], that is, all wavelengths are measured simultaneously by the interferogram, and,
2. the Jacquinot advantage [Jacquinot and Dufour, 1948], that is, high optical throughput that occurs because a large aperture can be used and the beam is collimated and sent into the instrument without much loss.

2.3 Fourier transform spectroscopy: implementation at TAO

2.3.1 Experimental setup

Externally, the TAO FTS has a filter wheel (Figure 2.1), with six optical filters, which limit the spectral range of the incoming solar radiation in order to reduce photon shot noise. Photon shot noise gives rise to electronic noise caused when the number of discrete photons is small enough to give rise to detectable statistical fluctuations in the measured signal (i.e., the random fluctuations in the rate of the number of photons compared to the average). This noise is proportional to the square root of the number of photons per unit time [*Bell*, 1972].

We use six filters in order to reduce this noise, and Table 2.1 lists the associated spectral ranges and some of the species that can be observed for each one. After the light passes through one of the filters, it must also pass through an external aperture (labelled “Emission Port/Iris” in Figure 2.1) before entering the interferometer. This aperture is usually set to 0.5 mm for filters 1, 3, 4, and 5, and 1.0 mm for filter 2 (which is as small enough to improve spectral resolution, but large enough for adequate signal), which, combined with the 325.12 mm focal length of the external parabolic mirror (M3 in Figure 2.1), gives a half-angle field of view of 1.54×10^{-3} sr [*Taylor*, 2008]. Inside the interferometer, the TAO FTS uses a KBr beamsplitter that has a spectral range of 500 - 4500 cm^{-1} . The TAO FTS has two detectors that record the interferograms in different spectral ranges. The InSb detector covers 1500 - 5000 cm^{-1} and is used for the first five external filters mentioned above. There is also an MCT detector (HgCdTe) that covers 700 - 4500 cm^{-1} and is used for the sixth filter. The filter 6 setup has its 1.3 mm (larger to provide adequate signal, though recently reduced to 1.0 mm because of improved alignment) aperture located internally just before the MCT detector, giving a

half angle field of view of 4.00×10^{-3} sr (now 3.08×10^{-3} sr). It is located inside the instrument to reduce heating of the aperture from direct shining of the solar beam. In this part of the spectral range, that heating would introduced unwanted signal due to emission. The external aperture is usually set to 1.5-2.5 mm during those measurements. All internal components are kept under vacuum at a constant pressure of about 0.093 hPa.

Table 2.1: Spectral coverage of the DA8 FTS filters.

Filter	Wavenumber range (cm^{-1})	Species
1	4000 - 4300	HF
2	2900 - 3500	HCN, C_2H_2
3	2400 - 3100	CH_4 , C_2H_6 , N_2O , HCl, O_3
4	2000 - 2700	CO
5	1500 - 2200	CO, NO
6	750 - 1350	O_3

2.3.2 Semi-automated measurements

The TAO FTS is controlled by a Windows 98 computer that runs Bomem’s PCDA data aquisition software and BGRAMS software. In early 2009, the original Windows 98 computer failed, and a new one was installed. The TAO computer has two special cards: One of the cards communicates with the spectrometer’s computer (an external computer, called the “electronics box”). The second card communicates with the detectors to control the automatic gain switches.

The TAO-FTS scanning mirror moves at 0.5 cm/s (the speed optimized to detector responsivity, though recently changed to 1.0 cm/s to improve measurement frequency). After four scans, the computer records three files: The .IGN file, which is the raw interferogram and boxcar function, the .IGM file, which is the interferogram with phase

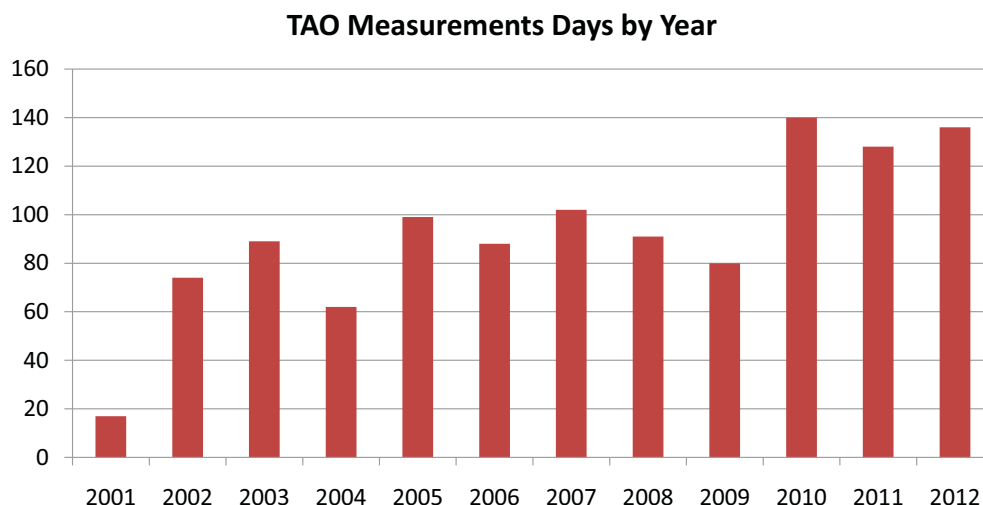


Figure 2.2: Number of measurement days with the TAO-FTS.

corrections made, and the .SPC file, which is the spectrum after a Fourier transform. This whole process takes about 22 minutes for one measurement (13.5 minutes with the new mirror speed). Given that each species is measured in only one of six filters that must be cycled through, we get at most 3-4 measurements of each species per day (~ 6 with the new mirror speed).

Given that the system is not automated, and the technique relies on clear skies, TAO measurement days are historically, from 9am to 5pm on clear sky weekdays (limited by number of personnel, and lack of automation). However, transient clouds, instrument problems and maintenance, and human failure results in even fewer measurements. Figure 2.2 shows a bar chart of the number of measurement days per year, which are typical for some NDACC sites. The sparsity of the TAO measurements is the biggest challenge to overcome when trying to do science with the dataset. Fortunately, the number of measurements started improving in 2010, and has increased again in 2013-2014 (not shown).

2.3.3 Instrument line shape

One way to monitor the performance of the TAO-FTS is to do an instrument lineshape measurement [Hase *et al.*, 1999] using a cell with a known quantity of HBr gas [Coffey *et al.*, 1998]. At TAO, we originally used gas cell #13, which had about half as much gas as the other cells provided by the NDACC-IRWG. About two years ago, we obtained an additional cell, #48. The instrument line shape is a sinc function, which is determined by a Fourier transform of the boxcar apodization function (Section 2.2). Other apodization functions (such as a triangle) reduce the side lobes of the sinc function, but also decrease the resolution of the spectral lines [Bell, 1972]. We run the instrument lineshape analysis using a program called LINEFIT v9 [Hase *et al.*, 1999].

Figure 2.3 shows two typical TAO instrument lineshapes (left), and their modulation efficiencies (top, right), which is a measure of how the signal intensity is maintained as a function of OPD. If the modulation efficiency of the HBr cell measurements varies a lot, then the instrument should be re-aligned [Hase, F., IRWG presentation, 2009]. If the instrument lineshape (and as a result, the spectral lines) is asymmetric, this is seen in the phase error (shown in Figure 2.3, bottom, right). This means that the mirrors are slightly mis-aligned.

The results in Figure 2.3 are typical for the TAO FTS. In the April case, the ILS is slightly asymmetric, and the modulation efficiency drops to <0.6 at maximum OPD. In the October case, which occurred soon after the FTS was aligned, the ILS is more symmetrical, and the modulation efficiency only drops to about 0.96 at maximum OPD. The ILS and drop in modulation efficiency can be accounted for in the retrievals (via the forward model, see next section), and were tested on N_2O and CH_4 retrievals, using a polynomial representation of the drop in modulation efficiency. However, the resulting change in total columns was less than 1%, consistent with what Taylor [2008] found. Also the ILS would be difficult to take into account for all of the retrievals because it changes often (likely because of loose-fitting beamsplitter, and possibly the movement

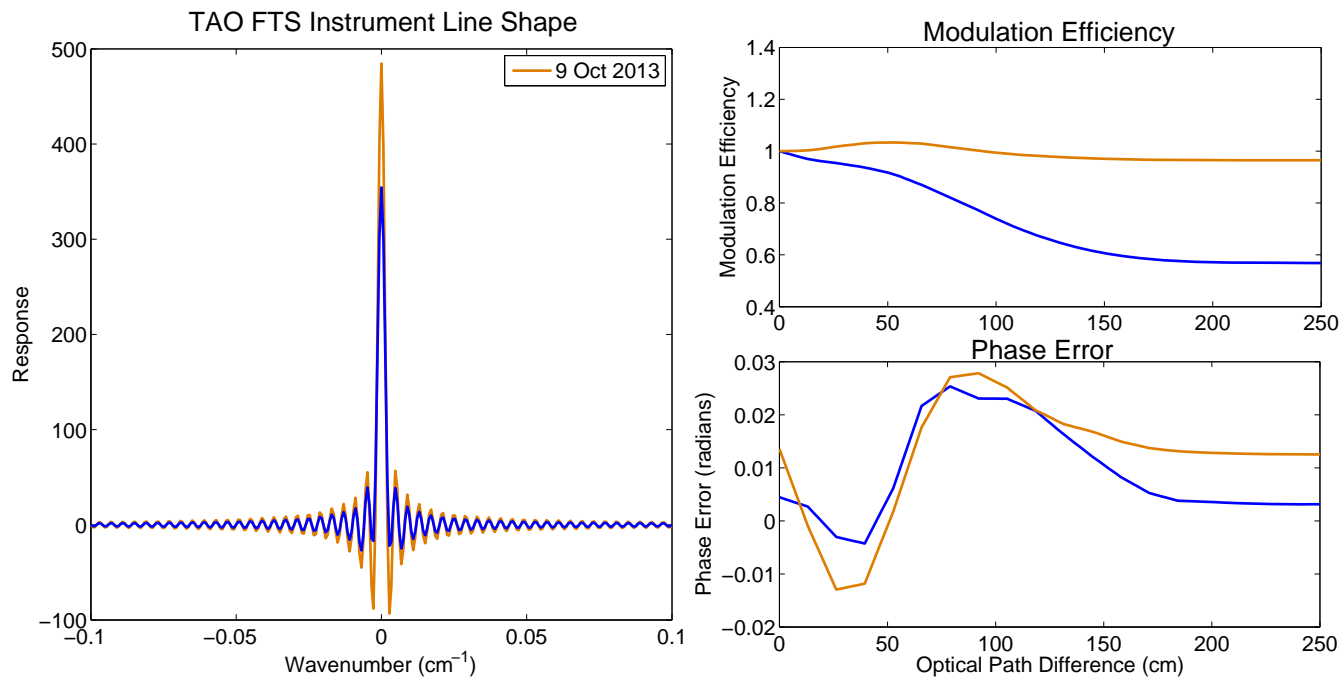


Figure 2.3: Results of two sample TAO FTS instrument line shape tests from 10 April 2013 (blue) and 9 October 2013 (orange): (left) instrument lineshape, (top, right) modulation efficiency, and (bottom, right) phase error.

of the dynamic alignment), and we only test it every few months. Therefore, since the instrument line shape does not have a great effect on the column amounts, we assume a perfect instrument line shape in all TAO retrievals.

2.4 Retrievals

2.4.1 Optimal estimation method

Vertical profiles and total columns of trace gas abundances are *retrieved* from the TAO spectra using the optimal estimation method (OEM) [Rodgers, 1976, 1990, 2000] implemented with a program called SFIT2 v.3.94 [Rinsland *et al.*, 1982, 1998]. These methods are described in detail in Rodgers [2000], Wiacek [2006] and Taylor [2008], but I will briefly outline them here.

First, one selects a small portion of the recorded spectrum, called a *microwindow* (MW), isolating just one or a few spectral lines of interest. Then a forward model, \mathbf{F} , is run with a ray-tracing code called FSCATM. The forward model contains an initial guess of the state of the atmosphere (including an *a priori* vertical profile, \mathbf{x}_a) as well as all of the physics of atmospheric absorption (see Section 2.1). The forward model relates the true atmospheric state, \mathbf{x} (vertical profiles of volume mixing ratios) to an absorption spectrum, \mathbf{y} (measurement space):

$$\mathbf{y} = \mathbf{F}(\mathbf{x}, \mathbf{b}) + \boldsymbol{\varepsilon}, \quad (2.20)$$

where \mathbf{b} is the vector of ancillary model parameters, and $\boldsymbol{\varepsilon}$ is the error. Since we want to determine \mathbf{x} given \mathbf{y} , we assume the forward model function, \mathbf{F} , is invertible. The inverse function, R , is given by:

$$\hat{\mathbf{x}} = R(\mathbf{y}, \mathbf{b}, \mathbf{x}, \mathbf{c}) \quad (2.21)$$

$$= R(\mathbf{F}(\mathbf{x}, \mathbf{b}) + \boldsymbol{\varepsilon}, \mathbf{b}, \mathbf{x}, \mathbf{c}), \quad (2.22)$$

where \mathbf{c} is the vector of ancillary model parameters required for the inverse calculation. R maps the measurement space, \mathbf{y} , into the estimate of atmospheric state space, $\hat{\mathbf{x}}$. Assuming that \mathbf{F} and R are linear over the range of the *a priori* state space and the true state space, and doing a Taylor series expansion about $\mathbf{x} - \mathbf{x}_a$ then:

$$\hat{\mathbf{x}} = R(\mathbf{F}(\mathbf{x}_a, \hat{\mathbf{b}}) + \mathbf{K}(\mathbf{x} - \mathbf{x}_a) + \mathbf{K}_b(\mathbf{b} - \hat{\mathbf{b}}) + \boldsymbol{\varepsilon}, \hat{\mathbf{b}}, \hat{\mathbf{x}}, \mathbf{c}), \quad (2.23)$$

where $\hat{\mathbf{b}}$ is the best estimate of the model parameters, \mathbf{K} is the weighting function matrix, \mathbf{K}_b is the parameter space weighting function matrix and $\hat{\mathbf{x}}$ is the best estimate of the true atmospheric state. Doing another Taylor series expansion about $\mathbf{F}(\mathbf{x}_a, \hat{\mathbf{b}})$ gives:

$$\hat{\mathbf{x}} = \mathbf{x}_a + \mathbf{G}\mathbf{K}(\mathbf{x} - \mathbf{x}_a) + \mathbf{G}\mathbf{K}_b(\mathbf{b} - \hat{\mathbf{b}}) + \mathbf{G}\boldsymbol{\varepsilon} \quad (2.24)$$

$$= \mathbf{x}_a + \mathbf{A}(\mathbf{x} - \mathbf{x}_a) + \boldsymbol{\epsilon}_x, \quad (2.25)$$

where $\boldsymbol{\epsilon}_x$ is the sum of the last two terms in Equation 2.24 combined into one error term, \mathbf{G} is the gain matrix, representing the sensitivity of the retrieved state to the measurements, and \mathbf{A} , the averaging kernel matrix is equal to \mathbf{G} times \mathbf{K} , and represents the sensitivity of the retrieved state to the true atmospheric state.

When the retrieval is run, the optimal solution after several iterations is given by:

$$\hat{\mathbf{x}}_{i+1} = \mathbf{x}_a + (\mathbf{S}_a^{-1} + \mathbf{K}_i^T \mathbf{S}_\varepsilon^{-1} \mathbf{K}_i)^{-1} \mathbf{K}_i^T \mathbf{S}_\varepsilon^{-1} [(\mathbf{y} - \mathbf{F}(\hat{\mathbf{x}}_i)) - \mathbf{K}_i(\mathbf{x}_a - \hat{\mathbf{x}}_i)], \quad (2.26)$$

where i denotes the previous iteration, \mathbf{S}_a is the *a priori* covariance matrix, indicating the error on the *a priori* estimate, and/or the natural variability in the species' profile, and \mathbf{S}_ε is the observation covariance matrix, indicating the observation error:

$$\mathbf{S}_\varepsilon = \sigma_{RMS}^2 \cdot \mathbf{I}, \quad (2.27)$$

where \mathbf{I} is the identity matrix, and σ_{RMS} denotes the noise in the residual of the fit.

Once the retrieval is done fitting in the selected MW(s), a best estimate of the vertical profile of the species of interest is obtained, $\hat{\mathbf{x}}$. For TAO, this is on a 48-layer grid going from the surface to 120 km in altitude. The vertical column amount is then obtained

by integrating the volume mixing ratio (VMR) profile weighted by the air mass density. Note that VMR is formally defined as the amount of gas divided by the total amount of air minus the amount of gas. However, VMR is commonly approximated as the amount of gas divided by the total amount of air [<http://goldbook.iupac.org/M03948.html>], (which is actually the mole fraction) because for trace gases, the difference is negligible. In this thesis, I have used this approximation of VMR.

2.4.2 Implementation with SFIT2

SFIT2 is the algorithm that implements the retrieval. For TAO retrievals, we originally ran SFIT2 v3.82b3 using MATLAB routines as a “wrapper code” to prepare the data, provide all of the necessary inputs, and analyse and plot the results. In 2010, we updated to SFIT2 v3.94 using a Fortran “wrapper code” called zephyr2. The most current version is now SFIT4, which is run with python “wrapper code” called Layer1.

For the spectral line information needed in the forward model, the High-resolution Transmission molecular absorption database (HITRAN) spectral line list is used. Different versions of HITRAN exist. At TAO we originally used HITRAN2004 [*Rothman et al.*, 2005], but when we upgraded to SFIT v.3.94, we also updated to HITRAN 2008 [*Rothman et al.*, 2009]. Other ancillary parameters include the temperature and pressure profiles, which are obtained from the National Centers for Environmental Prediction (NCEP) Climate Prediction Center (CPC) daily meteorological data product [http://hyperion.gsfc.nasa.gov/Data_services/automailer/index.html] for $z = 0-50$ km, and the mean of a 40-year run (1980-2020) of the Whole Atmosphere Chemistry Climate Model (WACCM, version 6, *Eyring et al.* [2007]) for Toronto [*J. Hannigan, NCAR, personal communication*] for $z = 50-120$ km, with an interpolation at the $z=50$ km boundary.

2.4.3 Averaging kernels

As mentioned above, the VMR averaging kernel matrix, \mathbf{A} , is the sensitivity of the retrieved state to the true atmospheric state for each vertical level in the retrieval grid. It can be expressed as follows:

$$\mathbf{A} = (\mathbf{S}_a^{-1} + \mathbf{K}^T \mathbf{S}_\varepsilon^{-1} \mathbf{K})^{-1} \mathbf{K}^T \mathbf{S}_\varepsilon^{-1} \mathbf{K} \quad (2.28)$$

$$= \mathbf{GK} \quad (2.29)$$

The partial column averaging kernels are equal to the VMR averaging kernels weighted by the density, summed over the layers of interest. The sensitivity, S_k , is the fraction of the retrieval at each altitude, k , that comes from the measurement (Equation 2.30, *Vigouroux et al.* [2008]):

$$S_k = \sum_i A_{ki}, \quad (2.30)$$

where \mathbf{A} is the averaging kernel matrix, and the summation is over the i elements of the k^{th} row. When the sensitivity is above 0.5, it means that the measurements are contributing more than 50% to the retrieved profile (with the rest coming from the *a priori* profile).

The degrees of freedom for signal (DOFS) is defined as the trace of the averaging kernel matrix, [*Rodgers, 2000*], and provides the number of independent pieces of information in the retrieval. When $\text{DOFS} \geq 1$ for a partial or total column, then we can trust that the measurement has provided adequate useful information. When $\text{DOFS} \leq 1$ for a partial or total column, then this measurement is partially representing the *a priori* profile.

2.4.4 Errors

There are a number of errors associated with FTIR retrievals. The error budget calculation includes [*Rodgers, 2000; Vanhaelewyn, G., IRWG presentation, 2009; Lindenmaier et al., 2010*]:

- spectroscopic errors (line width and line intensity, which together are the dominant sources of error),
- errors in the temperature profiles,
- interfering molecule errors,
- solar zenith angle (SZA) errors
- measurement errors (spectral measurement noise mapped into state space), and
- smoothing errors (error due to the vertical resolution of the retrieval).

The spectroscopic errors are systematic, and should be disregarded when discussing variability within a time series for one species measured by the same instrument. Also, if comparing two datasets, when one has been smoothed with the averaging kernels of the other (e.g., comparing a dataset to a smoothed model), then the smoothing errors can be disregarded.

We use the method described in *Batchelor et al.* [2009] and *Lindenmaier et al.* [2010] to calculate the errors for each species we retrieve. The spectroscopic, temperature, and SZA errors involve perturbing those parameters (by 5%, 2 K, and 0.1° , respectively), running the retrieval, and seeing how much the result changes. The interfering species, measurement, and smoothing errors are calculated using equations in *Rodgers* [2000]. Because the error calculation takes 10-50 times longer than the retrieval does, I have only performed the calculation on a limited number of spectra with different environmental conditions:

- high SZA, which occurs at midday,
- low SZA, which occurs in the morning and evening, and
- winter, spring, summer, and fall, which occur at different points in the seasonal cycle of the species, and have different SZA ranges.

The final error for each species is the average of the results for different spectra. These are given in Table 3.3, in the next chapter.

2.4.5 Tikhonov regularization

An alternative approach to OEM for retrievals is to use Tikhonov regularization [Tikhonov, 1963]. In this case, \mathbf{x} and \mathbf{y} are related through \mathbf{F} :

$$\mathbf{y} = \mathbf{F}\mathbf{x} \quad (2.31)$$

and to solve the underdetermined problem, we minimize the Euclidean norm of the residual plus a regularization term:

$$\|\mathbf{F}\mathbf{x} - \mathbf{y}\|^2 + \|\Gamma\mathbf{x}\|^2, \quad (2.32)$$

where the first term in Equation 2.32 is the ordinary least squares approach, and the second term is the regularization term. Γ is called the Tikhonov matrix, and this term helps give preference to a particular solution. In fact, it can be scaled with a tuning parameter α in order to give retrievals with a particular mean DOFS. The best estimate is then:

$$\hat{\mathbf{x}} = (\mathbf{K}^T\mathbf{K} + \Gamma^T\Gamma)^{-1}\mathbf{K}^T\mathbf{y} \quad (2.33)$$

where \mathbf{K} is the Jacobian, equal to $\mathbf{F}/\delta\mathbf{x}$. The regularization matrix is determined by [Sussmann *et al.*, 2011]:

$$\Gamma = \alpha\mathbf{L}_1^T\mathbf{L}_1, \quad (2.34)$$

where \mathbf{L}_1 is the discrete first derivative operator, which constrains x such that a constant profile is favoured for the difference $x-x_a$, and α is tuned to get a certain number of DOFS.

This method is easily implemented with SFIT2, however, in this thesis, we only apply the Tikhonov regularization approach on CH_4 retrievals (Section 3.1.1).

2.5 Future work: improvements to TAO

There are a number of improvements that could be implemented at TAO, and some are already underway. In order to increase the number of measurements, efficiency can be increased by the recently implemented remote viewing of the TAO computer and solar beam from the downstairs offices. Sometimes the suntracker can become misaligned, or an error can occur in data acquisition, which causes loss of data. Without remote viewing, the measurements would cease until the operator returned, sometimes hours later. However, with remote viewing, if an error occurs or the signal is lost, the operator can return upstairs to correct the problem immediately.

An increase in automation would also improve efficiency, and thus the number of measurements. For example, valuable time would be saved if the TAO suntracker hatch were automatic (so that the operator does not have to go up onto the roof), and if the detectors were automatically cooled with liquid nitrogen in the mornings before 9am (as this step can take some time, especially if the liquid nitrogen dewar is empty and the operator must go down to the basement to refill it).

The current TAO suntracker stops tracking the sun every day near local noon because of a proprietary software bug. The operator can reset the heliostat, and the suntracker will resume tracking for the afternoon, however measurements have been lost over the years because of this problem. There is new suntracker hardware and software that is poised to replace the original heliostat. Instead of using four photodiodes for active solar tracking, the new tracker records the image of the sun with a camera, and a program fits the curvature of the sun to keep it centered in the field of view [*Gisi et al.*, 2011]. The new tracker uses entirely different software, so it has the potential to improve solar tracking, and thus reduce measurement loss due to poor tracking at TAO.

Chapter 3

Trace gases measured at TAO

The primary measurements used in this thesis were made with a ground-based, high-resolution (0.004 cm^{-1}) Bomem DA8 FTIR spectrometer at the TAO, 43.66°N , 79.4°W , 174 m.a.s.l. [*Wiacek et al.*, 2007]. The TAO FTIR spectrometer was installed in October 2001, and has been operational for weekday measurements, weather permitting, since May 2002. TAO became a site in NDACC in 2004. The previous chapter explained how column concentrations of trace gases can be computed from FTIR solar absorption spectra. This chapter explains how the retrievals at TAO were optimized, and then presents the 11-year total column time series of eight trace gases. The seasonal cycles and long-term trends are discussed in this chapter, as well as the submission of TAO data to the NDACC archive.

3.1 Retrieval optimization and harmonization

Over the course of my PhD, I updated the TAO retrieval algorithm from SFIT2 v3.82 implemented with MATLAB routines to SFIT2 v3.94 implemented with zephyr2. The main differences between these two versions are:

- The new version works with updated spectral line list HITRAN2008 (old version

was HITRAN2004).

- The new version works with a vertical grid up to 120 km, whereas the old version had a 100-km cap.
- The new version has an option to use the Galatry line shape instead of the Voigt line shape, which may improve fits for HF and HCl [*Hannigan, 2012*].

Another new version of SFIT, called SFIT4, was developed during the last couple of years, but was only officially released in January 2014, which was too late for me to re-retrieve all species for this thesis. However, use of SFIT4 is discussed in Section 3.4

As was learned in Chapter 2, Section 2.4, there are a number of retrieval parameters that can be changed, and doing so will affect the outcome of the retrieval. The TAO O₃, HCl, N₂O and CH₄ measurements had been validated during a number of ground-based and satellite intercomparison campaigns [*Wiacek et al., 2007; Wunch et al., 2007; Taylor et al., 2007, 2008*]. However, the previous retrieval parameters were set mostly for stratospheric gases (e.g., tropospheric O₃ was not possible with those settings, and HCN had not been retrieved at TAO before). Also, starting around 2008, the NDACC-IRWG [www.acd.ucar.edu/irwg/] started a harmonization initiative to improve underlying consistency when the data from all IRWG sites are taken together (for example, in global modelling studies). The parameters that are harmonized within the network are the microwindows (MWs), the *a priori* profiles, and the retrieval vertical grid. The parameters that are flexible and station-dependent are the signal-to-noise ratio (SNR) of the measurements, and the *a priori* covariance matrix (\mathbf{S}_a). Hence there is a need to re-evaluate TAO retrieval parameters.

Different MWs for five species (CO, O₃, C₂H₆, CH₄, and N₂O) were tested in my M.Sc. report [*Whaley, 2009*]. Since then, CH₄ microwindows have been re-examined, and several microwindows for HCN have been tested and optimized for TAO (see Section 3.1.1). HF and HCl MWs were left unchanged, as they were already the IRWG recommendation,

and resulted in good retrievals.

The *a priori* profiles and vertical grid were updated to the NDACC-IRWG recommendation at the same time. Initially, at TAO a 63-layer grid was used for the *a priori* profiles, and retrieved on 38 vertical layers. All NDACC-IRWG sites are now encouraged to use *a priori* profiles from the Whole Atmosphere Chemistry Climate Model (WACCM) [Eyring *et al.*, 2007]. Once the WACCM v5 data for each IRWG site were released [J. Hannigan, NCAR, personal communication], we used the WACCM 43-layer grid for the *a priori* profiles. At the same time, the IRWG recommended that all sites retrieve on a specific 49-layer retrieval grid, for consistency across all sites (with the lower layers being different depending on the site’s elevation). Therefore, the effect of the change in grid was not tested separately from the change in *a priori* profiles, however, it was not expected to make much of a difference. Wiacek and Strong [2008] had previously studied different retrieval grids (with layer thickness varying from 0.2 to 2 km in the troposphere) and found less than a 1% change in modelled mid-infrared spectral transmissions, which were below the random noise level. In 2012, when WACCM v6 data were released, we updated the TAO retrievals once again. The effect of changing the *a priori* profiles was tested for the eight primary species, and results are discussed in Section 3.1.2.

The \mathbf{S}_a matrices for most species were left as they had been set in Wiacek [2006], as these were based on the natural variance of these gases over Toronto based on satellite observations. When they were changed, it was to reduce oscillations in the retrieved profiles, or to improve sensitivity to the troposphere, and this will be mentioned in Section 3.1.3.

Retrievals at TAO using SFIT2 are done using the same SNR value for all measured spectra. While the true SNR of the measurements changes (e.g., depending on cloudiness, angle of the Sun, aging of the instrument), only one SNR value is chosen based on a tradeoff curve analysis using spectra from one year. Refer to Section 3.1.3 for this discussion and Table 3.3 for the results.

Retrievals were usually tested on spectra from one representative year, as testing on more than one year would have been time consuming. When each retrieval parameter is tested, determining which one is best is based on the following characteristics of the retrievals:

1. Are individual spectral fits good? Are the residuals of the fits devoid of systematic structure?
2. Which settings achieve the lowest mean root-mean-square (RMS) of the fit residuals?
3. Do individual retrieved profiles look realistic (similar to the *a priori* profile, and without significant oscillations)?
4. Are the mean DOFS greater than one for the total column? Which settings achieve the highest DOFS?
5. Do the averaging kernels look reasonable (vertical sensitivity spread over a large altitude range, and not oscillating)? (Note final averaging kernels are shown in Chapters 4 and 6, except for CH₄, which is shown in this chapter, Section 3.2.5)

3.1.1 Changing microwindows

The choice of spectral microwindow is an important one, as each absorption line has a different strength and different interfering lines from other gases. Furthermore, the size of a microwindow tends to be a balance between minimizing the number of interfering species and lines, and maximizing the information from the wings of the absorption lines. For the results of testing the microwindows of these five species: O₃, CO, CH₄, C₂H₆, and N₂O, I refer the reader to the first appendix (A), where Chapter 3 of my M.Sc. report [Whaley, 2009] is appended. In this section I present the results of my microwindow testing for HCN, and CH₄. The *a priori* profiles, S_a , and S_e values used in all of these

Table 3.1: Microwindows tested for HCN.

Microwindows (cm^{-1})	Test 1	Test 2	Test 3
3267.895 – 3268.300			y
3268.05 – 3268.40	y	y	
3277.775 – 3277.95			y
3286.168 – 3286.482			y
3287.10 – 3287.35	y	y	y
3299.40 – 3299.60	y		y
3301.03 – 3301.30			y
3304.825 – 3305.600			y
3331.40 – 3331.80		y	

MW tests are the “original” ones set by Aldona Wiacek [Wiacek, 2006] and Jeffrey Taylor [Taylor, 2008] in their PhD theses.

HCN

The original IRWG recommendation for HCN is to use the three microwindows listed under ‘Test 1’ in Table 3.1. However, these resulted in less than 1 DOFS in the TAO retrievals because of water vapour absorption interfering at that part of the spectrum. Therefore, we tested the replacement of the third MW with one used in *Paton-Walsh et al.* [2010] and *Vigouroux et al.* [2012] (Test 2), as well as Emmanuel Mahieu’s seven-MW approach (Test 3) [Mahieu et al., 2007]. In all three cases, water vapour (H_2O) is an interfering species, and instead of scaling its *a priori* profile during the retrieval, we have fitted it instead, as this improves the retrievals.

Figures 3.1 to 3.3 show the fits to the MWs for the three test cases. In each figure, the HCN lines are indicated with an arrow. In the seven-MW approach, two of the MWs do not have HCN lines, but are used “to allow precise adjustment of important interfering

species” [Mahieu *et al.*, 2007] – namely, H₂O in the 3286.17–3286.48 MW, and H₂¹⁷O in the 3301.03–3301.30 MW. It becomes clear in these figures why the HCN retrieval is so difficult. In many cases, the lines are barely visible, as they are weakly absorbing compared to the water vapour absorption continuum. The example shown is from 27 October 2010, which is a typical measurement. The *a priori* and retrieved HCN profiles are also shown in Figures 3.1 to 3.3 (bottom right). The retrieved profiles for tests 1 and 3 are very close to the *a priori* profile (Figures 3.1 and 3.3), as is the case when DOFS are low. The retrieved profile in Test 2 is ideal, as it is neither oscillating too much, nor is it too close to the *a priori* profile (Figure 3.2).

Test 1 resulted in mean DOFS of 0.50 over the dataset from 2002 to 2010. Mean DOFS for Test 2 and Test 3 were 1.36 and 0.43, respectively. Figure 3.4 shows the 2002-2010 time series of HCN using the MWs of the three test cases. It shows that the seven-MW approach (Test 3) resulted in fewer data points, especially in the winter, than the two three-MW test cases. The cause of fewer data points is lack of converging retrievals. We can also see in this figure that there is very little variability in the Test 1 and 3 results, reflecting the low DOFS these MWs achieve. Test 2 results in more data points than Test 3, and more variability (associated with higher DOFS) than tests 1 and 3 (Figure 3.4), so it is this MW set that we selected for TAO HCN retrievals. Note that these test results were communicated to the IRWG, and were useful in modifying the recommendation, which is currently to use the three Test 1 MWs, but with the caveat that several alternative MWs are possible depending on H₂O interference.

CH₄

The IRWG originally recommended five microwindows for CH₄, which are listed in Table 3.2, under Test 1. However, CH₄ spectroscopy in HITRAN 2008 (which is the currently-recommended spectroscopy) is known to have issues [Sussmann *et al.*, 2011]. Therefore, some research groups within the IRWG dropped the fifth MW to get better results, and

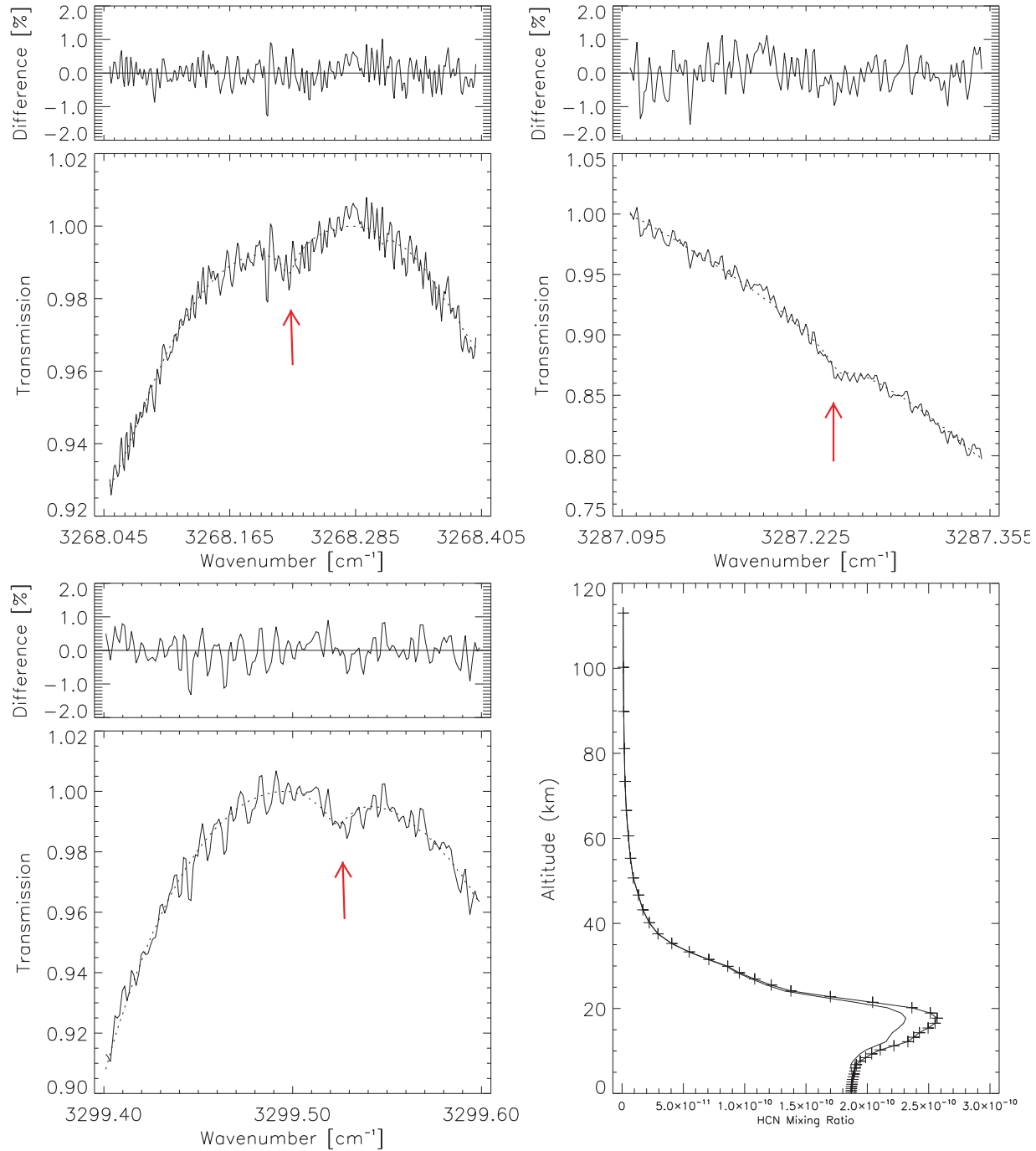


Figure 3.1: Typical spectral fits and residuals (from 27 October 2010) of three MWs of the HCN Test 1 case, and the *a priori* (solid line) and retrieved profiles (crosses) of HCN. Red arrows indicate the location of the HCN absorption lines. Residuals are the measured minus calculated spectra.

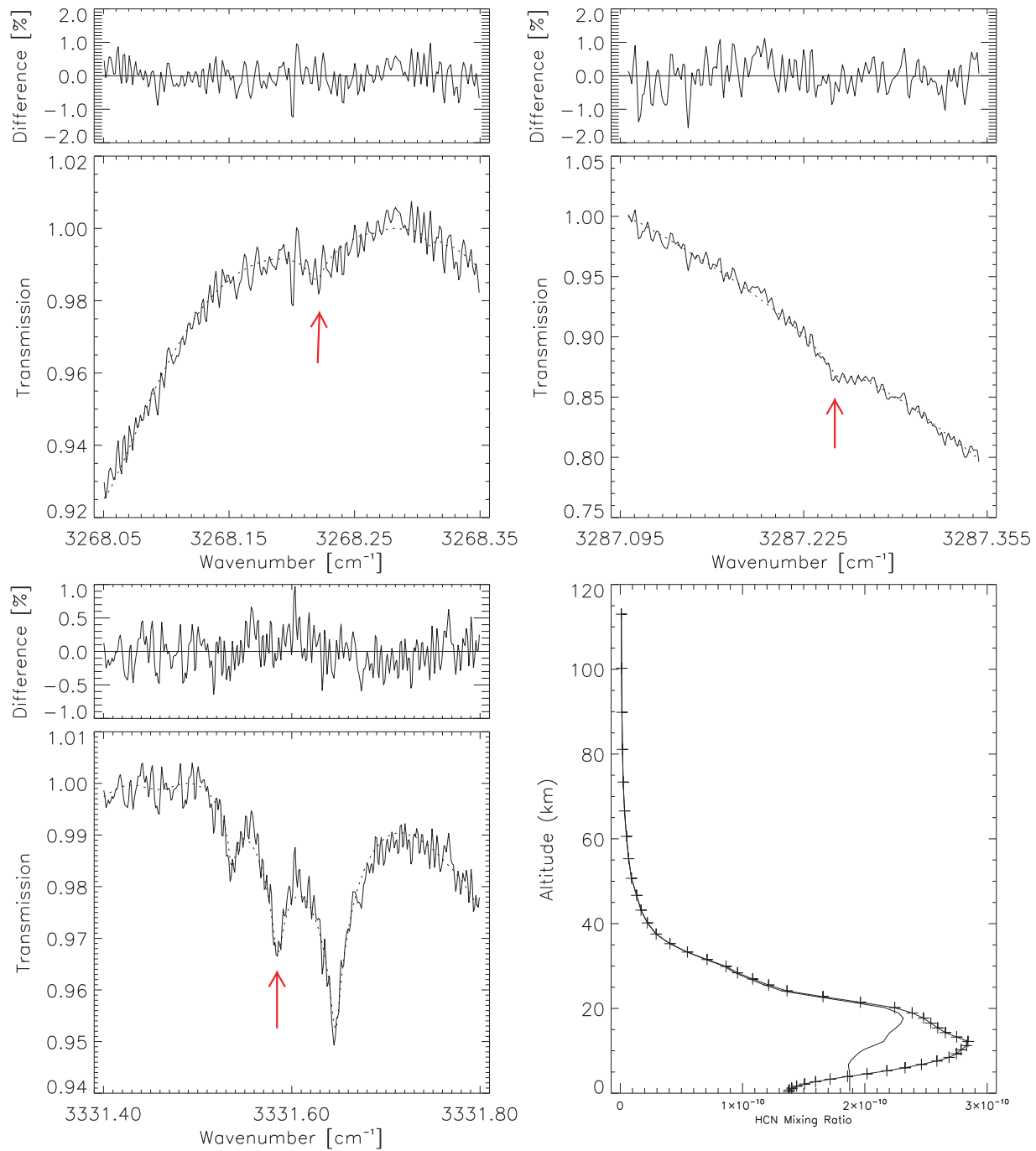


Figure 3.2: Same as Figure 3.1, but for the HCN Test 2 case.

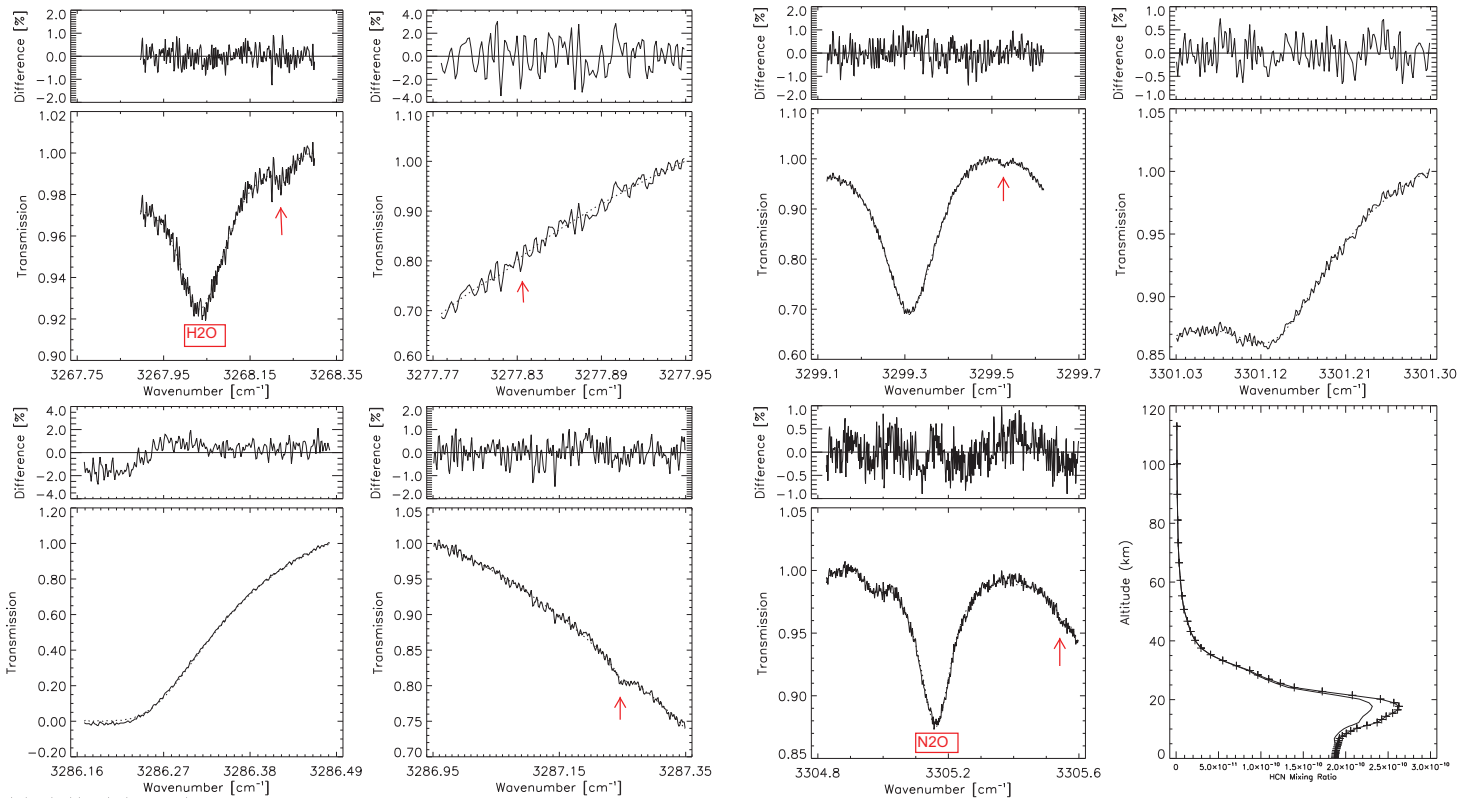


Figure 3.3: Same as Figure 3.1, but for the HCN Test 3 case. Other large absorption features in the MW are labelled with the interfering species. The 3286.17–3286.48 MW (bottom, left), and the 3301.03–3301.30 MW (top, right) only have water vapour absorption.

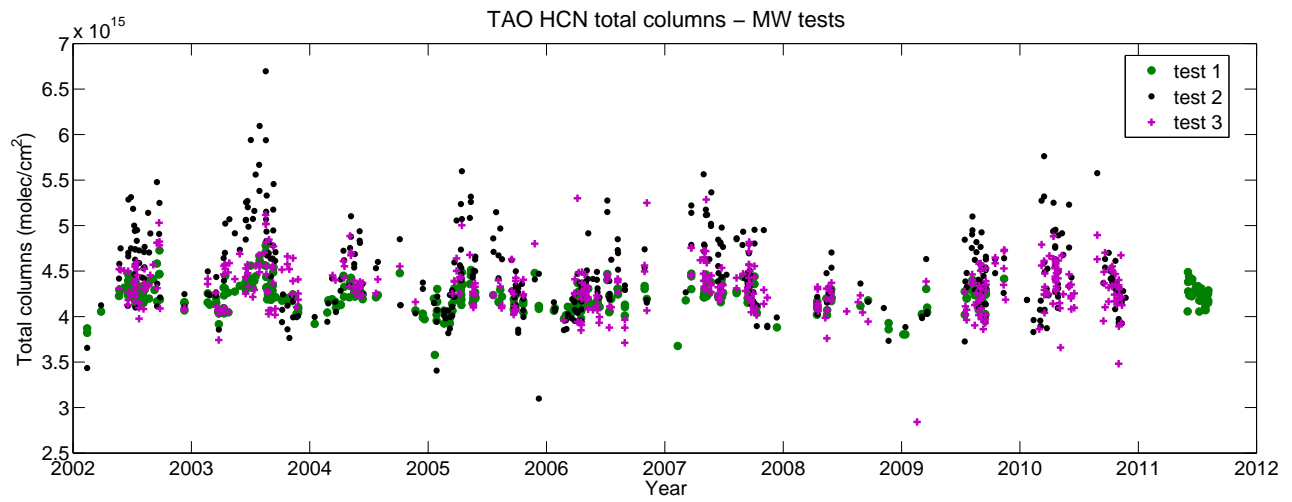


Figure 3.4: TAO HCN total column time series from three sets of MWs: Test 1=green, Test 2=black, and Test 3=purple crosses.

Table 3.2: Microwindows and other settings tested for CH₄.

Microwindows (cm ⁻¹)	Test 1	Test 2	Test 3
2613.70 – 2615.40	y	y	y
2650.60 – 2651.30	y	y	
2835.50 – 2835.80	y	y	y
2903.60 – 2904.03	y	y	
2921.00 – 2129.60	y		y
technique	Tik and OEM	Tik and OEM	Tik
version of HITRAN	2008	2008	2000

another group dropped the second and fourth MW, and switched to HITRAN 2000 for the spectroscopy, which, for CH₄, was based on measurements rather than theoretical calculations [Rothman *et al.*, 2003, 2009; Brown *et al.*, 2003]. This group also uses the Tikhonov (Tik) regularization method [Tikhonov, 1963; Section 2.4.5] for CH₄, rather than the optimal estimation method (OEM), because it can reduce oscillations in the retrieved profiles. These three MW combinations were tested using Tikhonov regularization for TAO for 2005 measurements, and are labelled Test 1, Test 2, and Test 3 (Table 3.2). Test 3 settings are the current IRWG recommendation. We also tested the four- and five-MW options using OEM, and we will show below that Test 2 MWs with OEM gets the best results for TAO.

The Tikhonov test cases resulted in mean DOFS of 2.50 (Test 1), 1.96 (Test 2), and 1.95 (Test 3), and that is because the regularization strength was tuned such that the mean DOFS ≈ 2 for Test 3. While the fifth MW does increase the DOFS, that is not supposed to be relevant for the Tikhonov test cases. It is more important to notice that the residuals are lowest for Test 1 (HITRAN 2008), rather than Test 3 (HITRAN 2000) which was supposed to have better spectroscopy (see Figures 3.5 to 3.7 which show fits and profiles for a typical measurement on 13 December 2005). Also important to note is

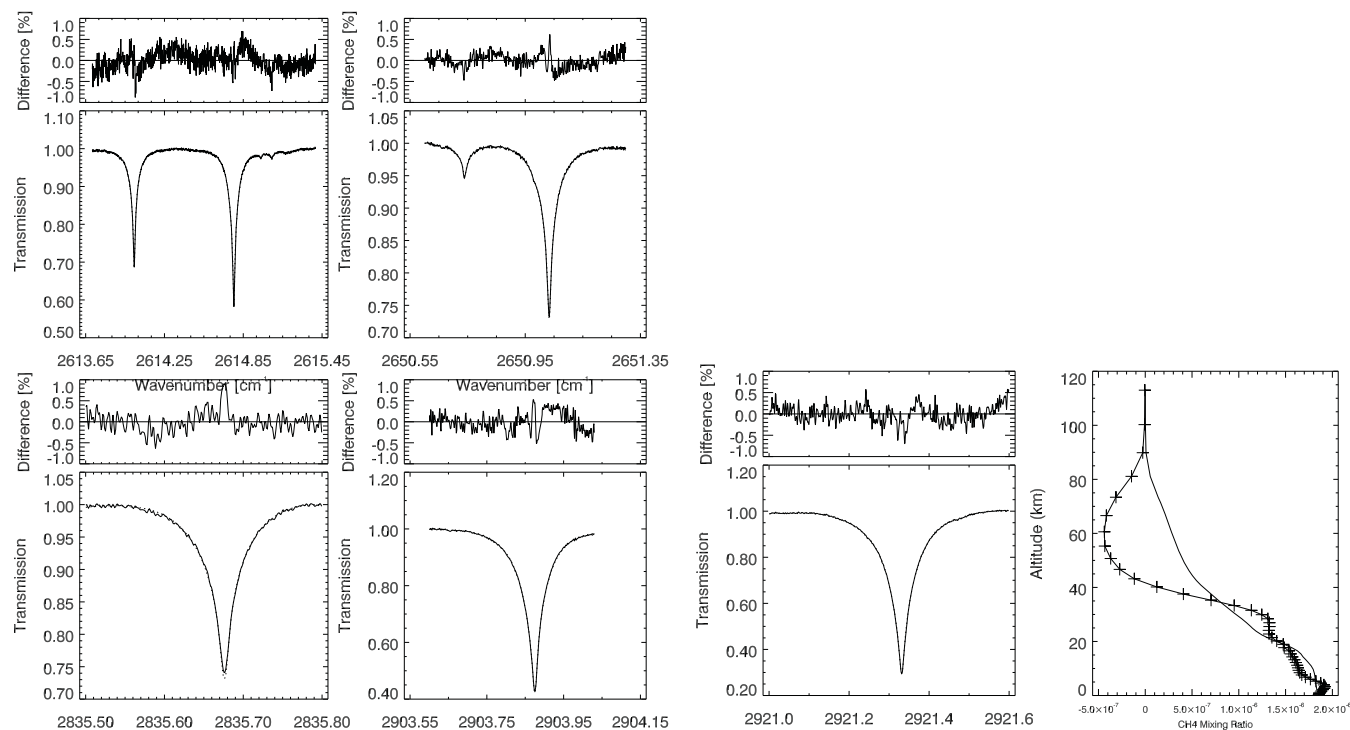


Figure 3.5: Typical spectral fits and residuals (from 13 December 2005) in the five MWs and the *a priori* (solid line) and retrieved profiles (crosses) of CH_4 for Test 1, using Tikhonov regularization. Residuals are the measured minus calculated spectra.

that the total columns are very similar (Figure 3.8). *Sussmann et al.* [2011] argued that the correct seasonal cycle of CH_4 could only be achieved with the Test 3 configuration, however, no real difference is seen in the seasonal cycle at TAO, despite our spectra having similar quality (noise) to those in the publication. Figures 3.5 to 3.7 also show typical retrieved profiles with significant oscillations. Therefore, the claim that Tikhonov regularization would reduce oscillations over OEM is also not true for TAO, unless the SNR (S_e) was adjusted lower. However, it was already set low at 100, and any lower is not realistic. So no reason was found to use Tikhonov regularization for TAO CH_4 retrievals.

In fact, using OEM, reasonable profiles can be achieved, as is shown in Figures 3.9 and 3.10. These two figures also show that the four MW approach (Test 2, Figure 3.10) has

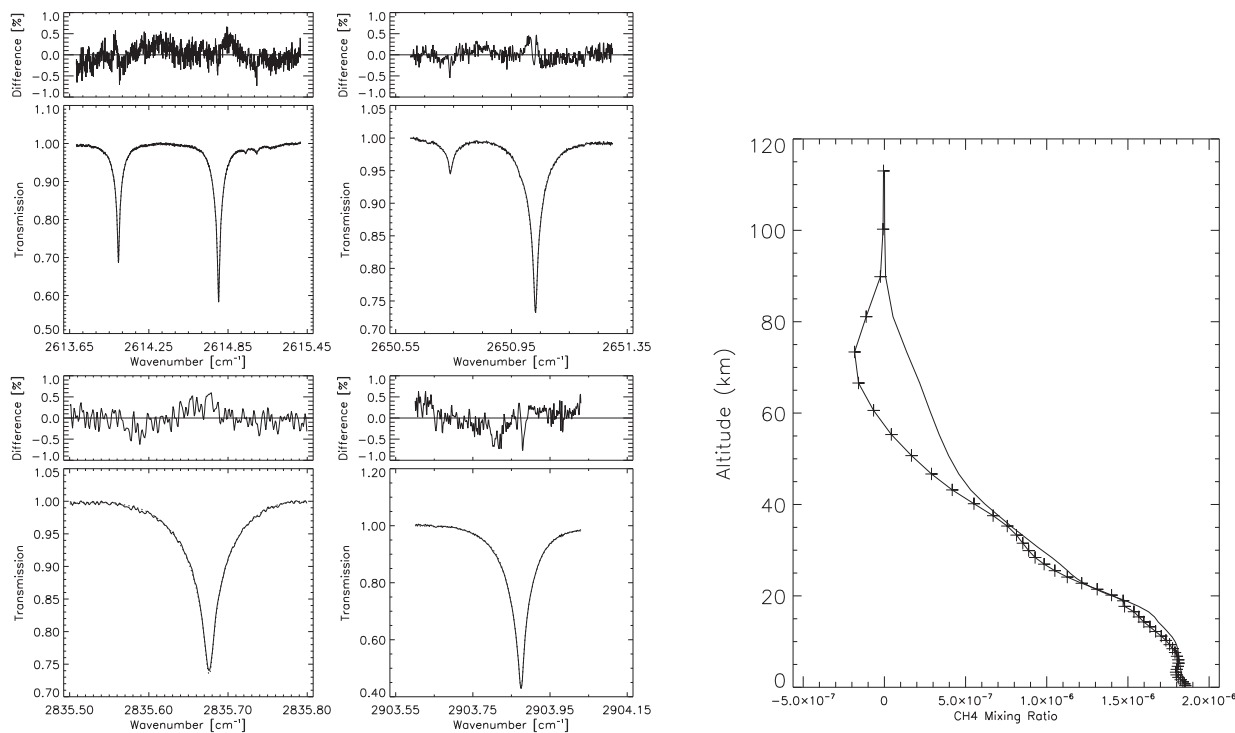
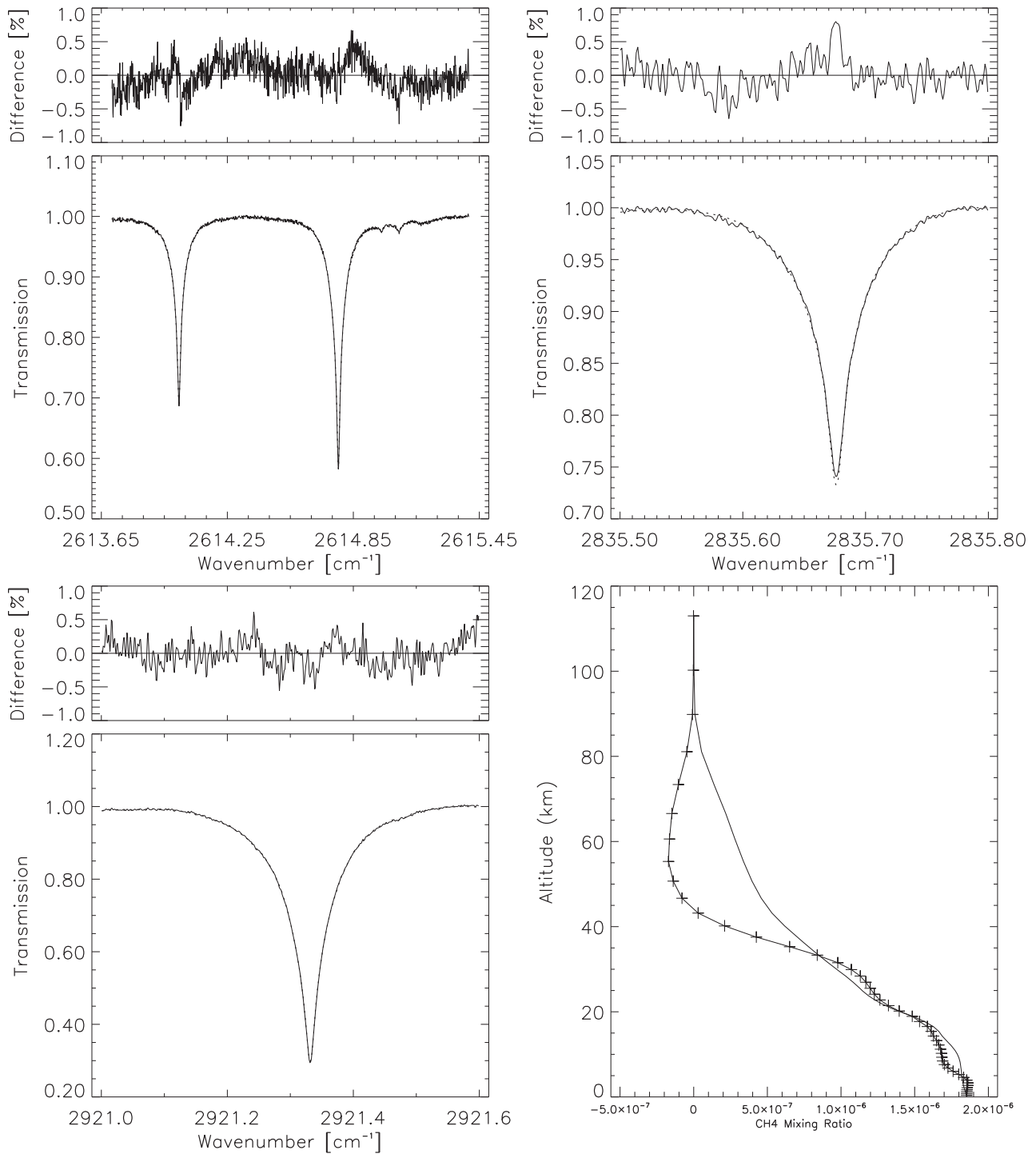


Figure 3.6: Same as Figure 3.5, but for CH₄ Test 2.

better fits (smaller residuals) than the five MW approach (Test 1, Figure 3.9). With four MWs and OEM, not only do we have reasonable fits and profiles, but the mean DOFS are about 3.5, which is much higher than was recommended in the Tikhonov strategy. Of course, the regularization parameter could be tuned to achieve higher DOFS, however, if the profiles were already oscillating significantly at DOFS=2, it would not be wise to increase the DOFS further. Therefore, because of reasonable fits and profiles, we selected OEM with Test 2 MWs and HITRAN2008 for TAO CH₄ retrievals in this study, even though this is not the current IRWG recommendation.

3.1.2 Changing *a priori* profiles and vertical grid

Prior to the IRWG recommendation to use WACCM *a priori* profiles, Wiacek [2006] created 63-layer *a priori* profiles for TAO retrievals based on a number of sources, depending on the species. O₃, HF, and HCl *a priori* profiles were based on the Halogen

Figure 3.7: Same as Figure 3.5, but for CH₄ Test 3.

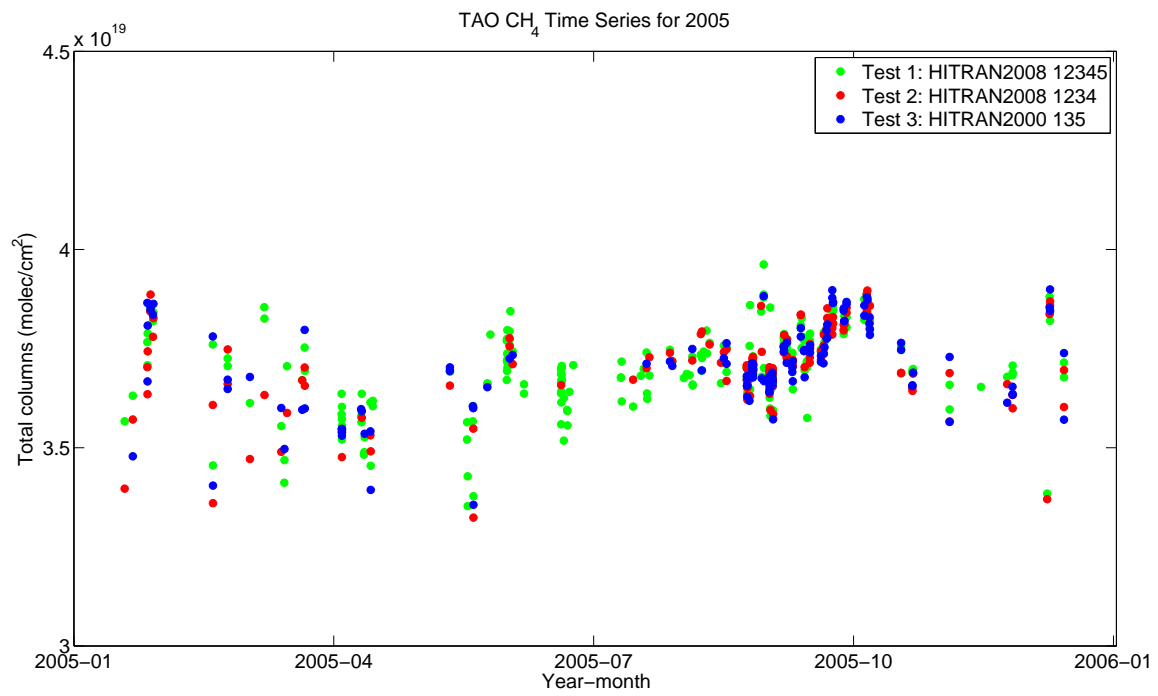


Figure 3.8: TAO CH₄ total column 2005 time series from Tests 1 (green), 2 (red), and 3 (blue), using Tikhonov regularization.

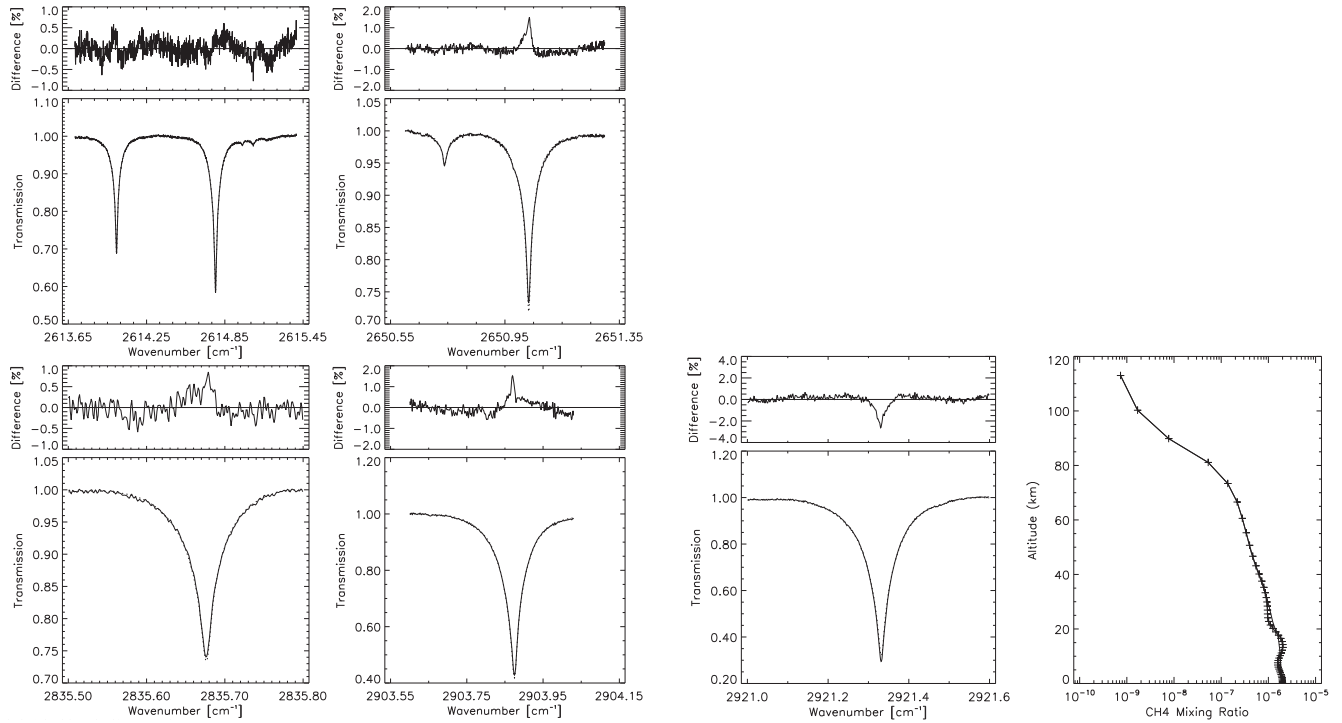


Figure 3.9: Typical spectral fits and residuals (measured minus calculated), from 13 December 2005, in the five MWs and the *a priori* (solid line) and retrieved profiles (crosses) of CH_4 for Test 1, using OEM.

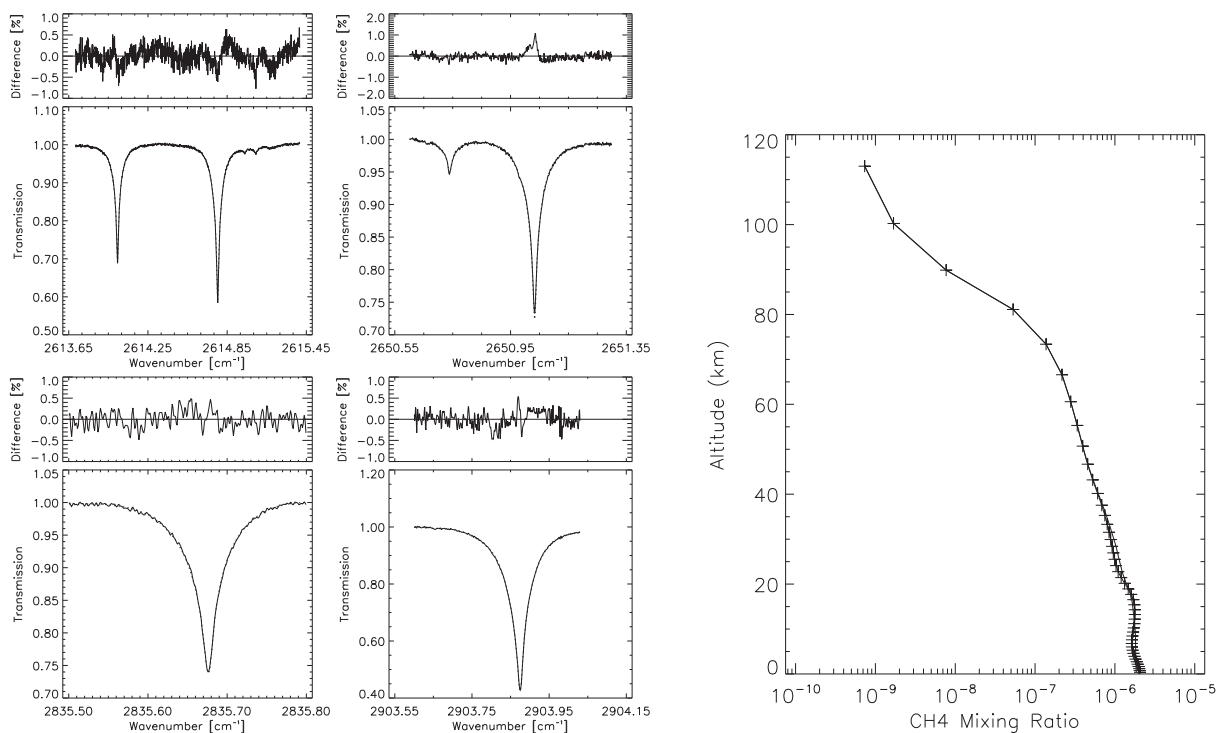


Figure 3.10: Same as Figure 3.9, but for CH₄ Test 2, using OEM.

Occultation Experiment (HALOE) satellite observations, CH₄ and N₂O were based on the Michelson Interferometer for Passive Atmospheric Sounding (MIPAS) satellite observations, and CO and C₂H₆ were based on GEOS-Chem modelled profiles. I evaluated whether switching to WACCM output for *a priori* profiles still resulted in good retrievals, and whether the column amounts changed significantly. The WACCM version 6 *a priori* profiles are average profiles from the monthly mean values of a 40-year (1980 – 2020) run of the WACCM model (see Section 2.4.2). Standard deviations were given, though were not used because they introduced discontinuities in the \mathbf{S}_a matrix.

When we updated the *a priori* profiles to WACCM, we also modified our input vertical grid (for *a priori*, temperature and pressure profiles) from 63 layers (0-100 km) to 43 layers (0-120 km), and we modified our output vertical grid from 38 layers (0-100 km) to 49 layers (0-120 km) in order to harmonize with the NDACC-IRWG for our archived products in the NDACC database. The pressure and temperature profiles up to ~50

km are from the National Centers for Environmental Prediction (NCEP) Goddard Automailer profiles, but above 50 km, we changed from the 1976 U.S. Standard Atmosphere [NOAA, 1976] to the WACCM average atmosphere.

Figure 3.11 shows the original *a priori* profiles from Wiacek [2006] in blue, as well as WACCM v5 (green) and WACCM v6 (red) *a priori* profiles, which were all tested. Note that for O₃, CH₄, and N₂O the WACCM profiles are very similar to the original ones. The retrievals for these three gases did not change significantly with WACCM v6, so that is what is used for the final retrievals, and these species will not be discussed further here.

Compared to the original TAO *a priori* profiles, WACCM is significantly different for CO in the mid-to-upper atmosphere, and for HCN throughout the atmosphere. For C₂H₆, the WACCM v5 *a priori* profile was similar to the original one (which was based on the GEOS-Chem model), but WACCM v6 is greatly reduced in the upper atmosphere. There was no WACCM v5 HF product, but there was from WACCM v6, and it is different from the original *a priori* profile in the upper stratosphere and mesosphere. The WACCM profiles for HCl are also different from the original *a priori* profile in the upper atmosphere. These species are discussed in more detail below.

CO

CO retrievals in 2005 were tested to evaluate the differences resulting from the original GEOS-Chem *a priori* and the WACCM v5 *a priori* profile. The CO columns did not change significantly as a result of the *a priori* change, likely because CO columns are dominated by the troposphere where the difference in *a priori* profiles was small. The total columns were 0-3% lower with WACCM v5, which is on the order of the errors (see Figure 3.12). The DOFS decreased by about 0.2, but this loss is acceptable. The RMS of the residuals of the spectral fits increased, but only slightly. The WACCM v6 *a priori* profile is very similar to WACCM v5 (Figure 3.11(b)), so it is used for the final retrievals.

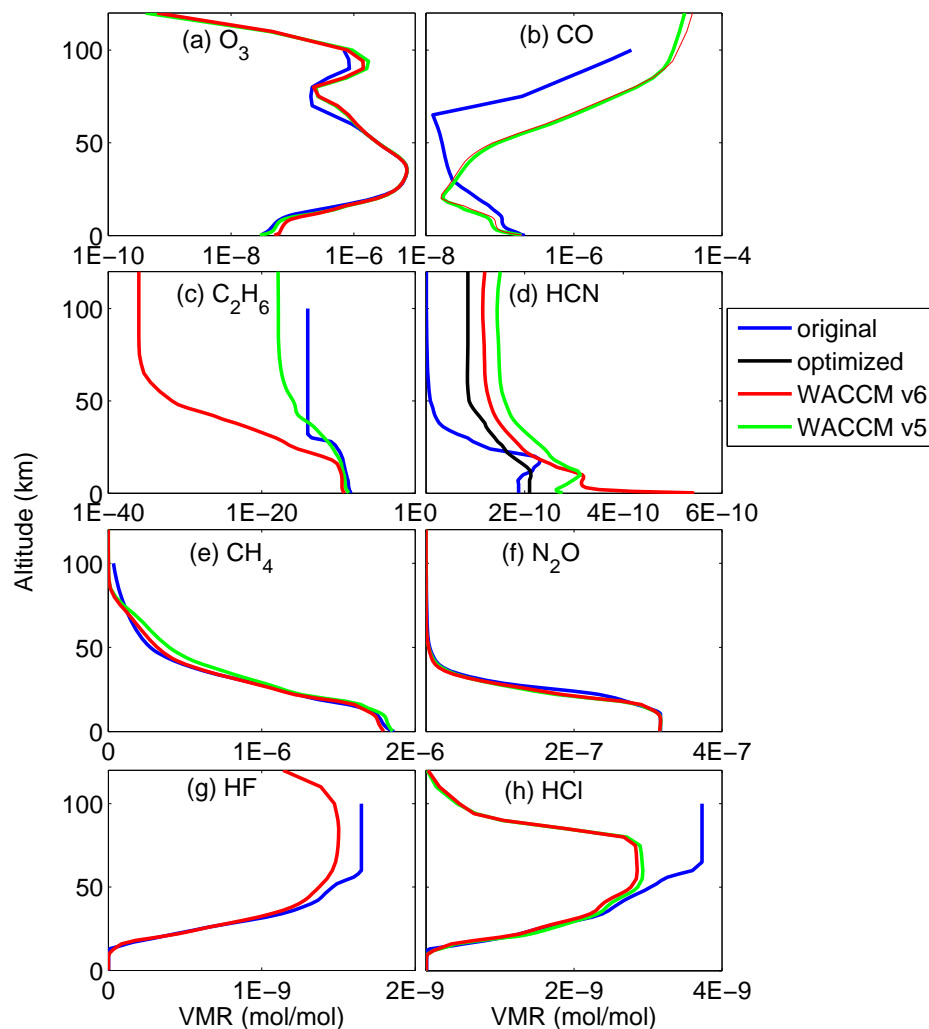


Figure 3.11: Original and WACCM *a priori* profiles (VMR in mol/mol) used for TAO retrievals for (a) O_3 , (b) CO, (c) C_2H_6 , (d) HCN, (e) CH_4 , (f) N_2O , (g) HF, and (h) HCl. For HCN (d), an optimized *a priori* profile is also shown (black line). Note that the x-axis is in log-scale for O_3 , CO, and C_2H_6 to more clearly see the differences.

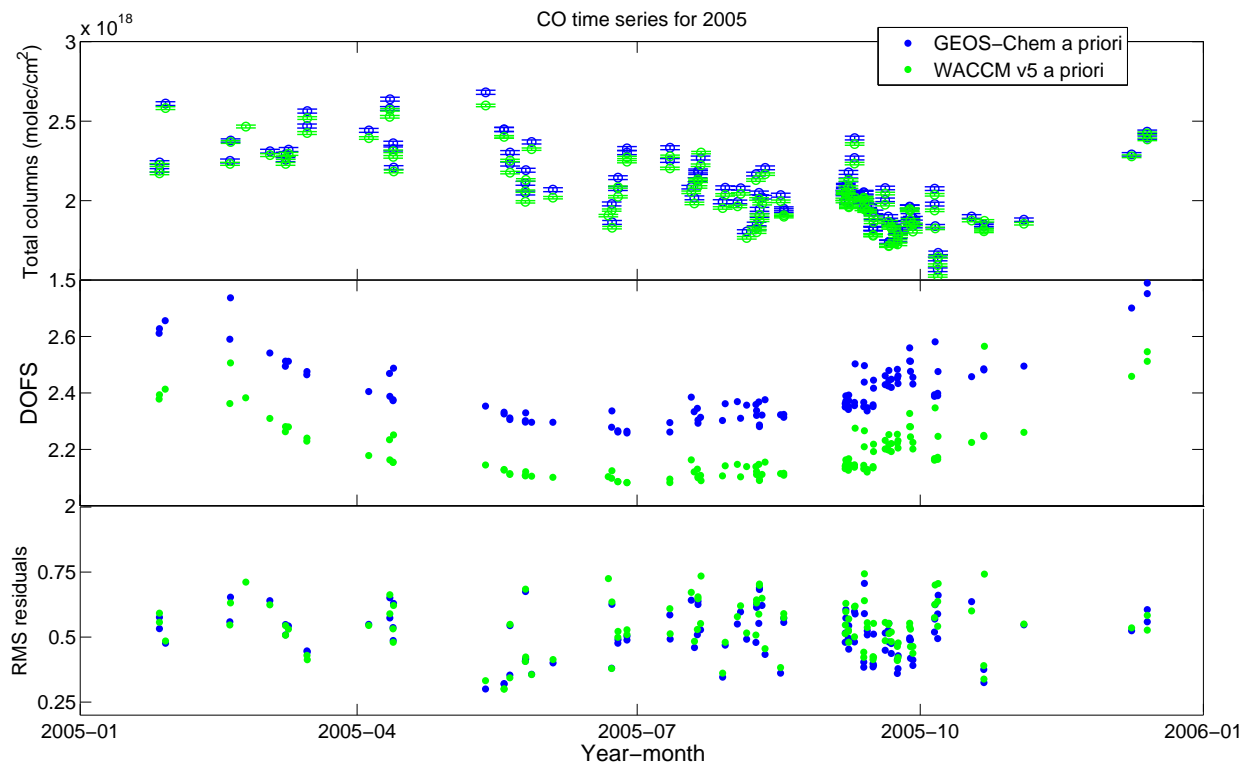


Figure 3.12: TAO CO time series for 2005 of (*top*): total columns (with total error bars), (*middle*): DOFS, and (*bottom*): RMS of the residuals of the spectral fits with different *a priori* profiles.

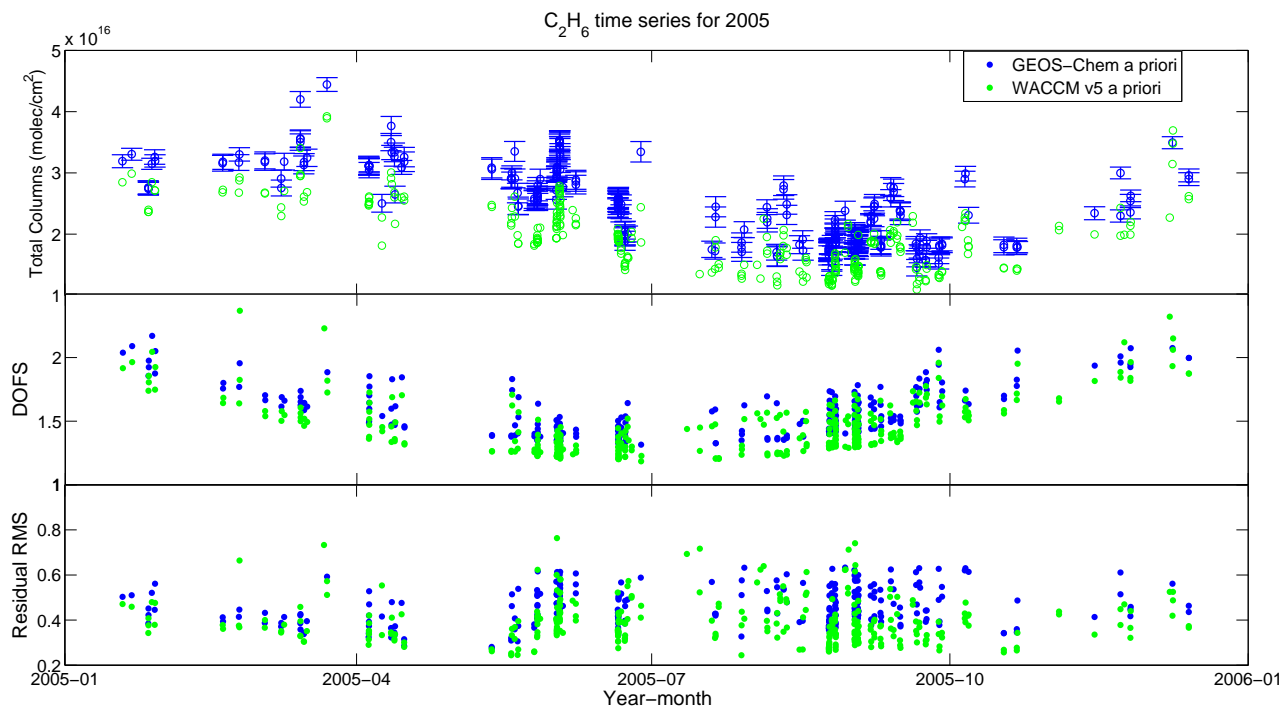


Figure 3.13: TAO C_2H_6 time series for 2005 of (*top*): total columns (with total error bars), (*middle*): DOFS, and (*bottom*): RMS of the residuals of the spectral fits with different *a priori* profiles.

C_2H_6

Like CO, the C_2H_6 columns did not change significantly as a result of the change from the original to the WACCM v5 *a priori* profile because C_2H_6 columns are dominated by the troposphere, where there is little difference between WACCM v5 and GEOS-Chem. The results of this comparison are shown in Figure 3.13. The WACCM v6 profile, however, is quite different and retrievals of C_2H_6 failed with it because the VMRs in the upper atmosphere are so small (order of 10^{-37} ppv) that they cause the SFIT2 v3.94 retrievals to fail. The very small values were rounded to zero in the zephyr2, SFIT2 implementation. Therefore, we use WACCM v5 as the C_2H_6 *a priori* profile for the rest of this thesis.

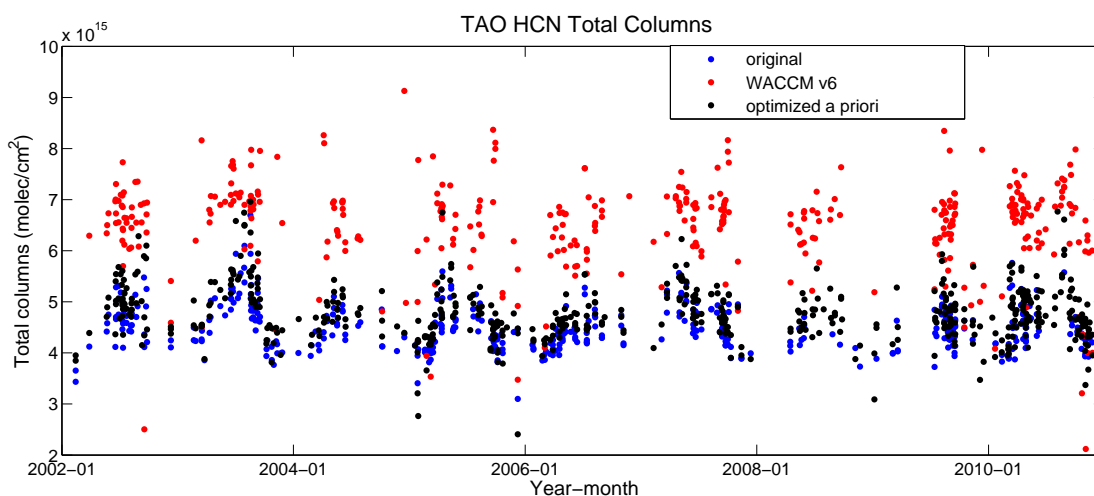


Figure 3.14: HCN total column time series from retrievals with different *a priori* profiles.

HCN

The WACCM profiles of HCN VMRs over Toronto are much greater than the TAO original, which was based on MkIV balloon-borne FTS observations over Kiruna, Sweden (67.85°N , 20.22°E). While we do expect more HCN over Toronto than in a remote location like Kiruna (because of more biomass burning and urban sources), given the large change, the impact of *a priori* profiles on HCN retrievals was investigated.

Both versions of the WACCM *a priori* profile resulted in highly oscillating retrieved profiles, and total columns that were much greater than those retrieved with the original *a priori* profile (Figure 3.14). As can be seen in Figure 3.14, the choice of *a priori* profile for HCN has a large effect on the columns, emphasizing the importance of a good *a priori* selection. HCN columns retrieved using the WACCM v6 *a priori* profile (red) are about 20% greater than those columns retrieved using the original *a priori* profile (blue).

To check the realism of the WACCM HCN profiles, some HCN observations and another model were found. Multiple balloon-borne MkIV FTS observations [Toon *et al.*, 1992] over multiple locations (Sweden, Alaska, and New Mexico) were examined to see how HCN varies over time and location. They are shown in Figure 3.15, along with an

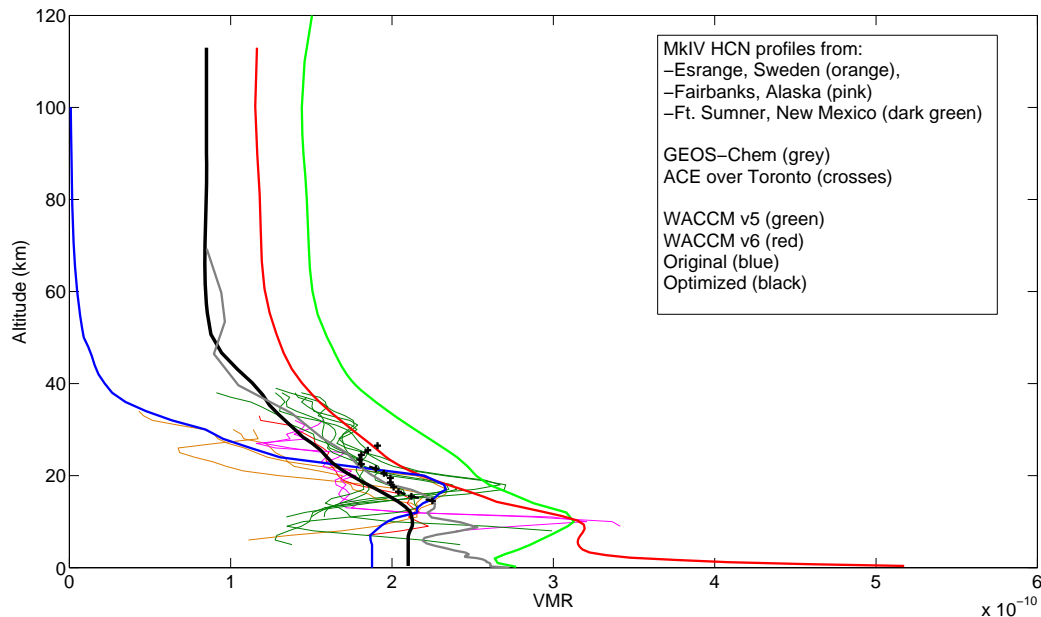


Figure 3.15: HCN profiles. Orange, pink, and dark green thin lines are profiles measured during MkIV balloon campaigns. Grey line is typical GEOS-Chem profile over Toronto. Black crosses indicate a typical ACE-FTS profile over Toronto. Thick blue, green, red, and black lines are *a priori* profiles that were tested.

observation from the Atmospheric Chemistry Experiment (ACE) FTS satellite instrument over the Toronto region. Also shown is the GEOS-Chem (which will be introduced in Chapter 4, Section 4.6) modelled HCN profile over Toronto and the two WACCM profiles. The GEOS-Chem profile is closer to the measured ACE and MkIV profiles than the WACCM modelled profiles or the original *a priori*. Therefore, an ‘optimized’ *a priori* profile was constructed based on the average of the GEOS-Chem and the observed profiles, and it is used for the final HCN retrievals. It is shown in Figure 3.15 (thick black line) and the resulting total columns are shown in Figure 3.14.

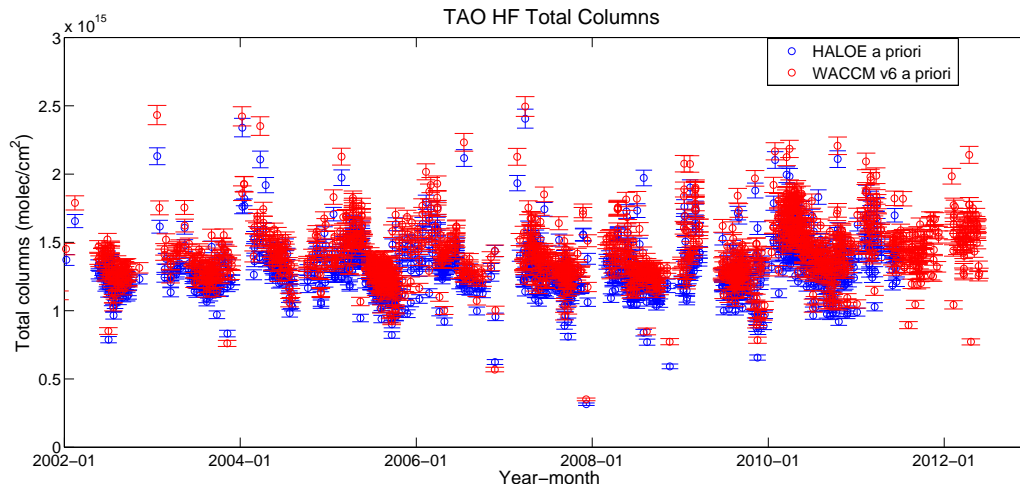


Figure 3.16: HF total column time series from retrievals with different *a priori* profiles.

HF and HCl

Figure 3.16 shows the HF time series from 2002 to 2012, retrieved from the original HALOE-based *a priori* profile (blue), and from WACCM v6 (red). The difference in total columns is about 8.5%, which is well above the total error on the columns (which is 2.9%). While the original *a priori* profile is greater than the WACCM v6 *a priori* profile above ~ 40 km (Figure 3.11), in the lower stratosphere – which contributes more to the column – the WACCM v6 profile is greater. Despite the significant difference in columns, given the IRWG preference to use WACCM v6 for consistency, WACCM v6 will be used.

We also use WACCM v6 for HCl, as the change to WACCM (both versions) from the original HALOE-based *a priori* did not affect the HCl columns in a significant way (not shown because of minimal differences). The difference in the WACCM profiles and the original profile occurs in the upper atmosphere, which does not contribute much to the columns.

Summary of *a priori* profile selection

In summary, we use WACCM v6 retrievals for all species except C₂H₆ and HCN. For C₂H₆ we use WACCM v5 because the values that WACCM v6 gives in the upper atmosphere are so small (order of 10⁻³⁷) that they cause the retrieval to fail. Apparently this is not a problem in SFIT4, but that is beyond the scope of this thesis (see Section 3.4 for future work). For HCN, we use an *a priori* profile based on ACE-FTS satellite and MkIV balloon measurements and the GEOS-Chem model, as WACCM significantly overestimates HCN over Toronto.

3.1.3 Changing SNR and \mathbf{S}_a

The SNR of the measurements (related to the diagonal elements of the error covariance matrix, \mathbf{S}_e , with no off-diagonal elements, *Wiacek et al.* [2007]) were chosen based on RMS fitting residual versus SNR tradeoff curve for each species (e.g., Figure 3.17 for O₃). The *a priori* covariance matrices (\mathbf{S}_a , diagonal elements of corresponding standard deviation listed in Table 3.3) for each species were chosen based on the variance seen in their HALOE observations over Toronto [*Wiacek et al.*, 2007], except for N₂O and CH₄, which were based on the variance in their MIPAS observations. We use a Gaussian correlation length of 4 km for off-diagonal elements of \mathbf{S}_a [*Wiacek*, 2006; *Wiacek et al.*, 2007] for all retrievals except for C₂H₆ and HF retrievals, where doing so did not improve the retrievals.

Determining signal-to-noise ratio

The \mathbf{S}_e matrix is diagonal with elements:

$$\mathbf{S}_e = \frac{1}{(SNR)^2} \cdot \mathbf{I}, \quad (3.1)$$

where \mathbf{I} is the identity matrix. Prior to this PhD, it was standard practice at TAO to calculate the appropriate SNR for each spectrum through an iterative process during the

time of the retrieval. Jeff Taylor's Matlab code would run the retrieval with the given SNR in the binput file, and then take the RMS of the spectral fit residuals, and set the new SNR to $1/\text{RMS} \times 100\%$. With this new SNR, it would run the retrieval again. If the RMS of the residuals of the spectral fits would decrease, then the SNR would be adjusted again in the same way ($1/\text{new RMS}$). Once the new RMS of the retrievals stabilized, the iterative process would stop and the last retrieval would be kept and the SNR would be recorded.

However, I noticed that for some species, the resulting SNR was unrealistically large with this method. For example for C_2H_6 , for which there are few features in the MW due to a large H_2O absorption feature, this method would yield a very large SNR, causing the retrieved profile to be highly oscillating, the time series to be unrealistically scattered (often into negative values), and the DOFS to be overestimated (see Appendix A).

Therefore, I conducted a tradeoff curve Test for each of the eight primary species, in which I manually set the SNR to a range of values from 20 to 500+, and ran retrievals on a subset of spectra (a few spectra from each season). Then I plotted the resulting median RMS residual vs SNR. When the SNR is low, the RMS residual is high because the retrieval puts less weight on the measurements and therefore the modelled spectrum is closer to that of the *a priori*. As the SNR increases, the RMS residual decreases and it puts more and more weight on the measurements, allowing for the modeled spectrum to more closely resemble the measured one. Eventually there comes a point where the RMS residual no longer decreases because any higher SNR just causes the model to try to fit the noise in the spectrum, which is random [Batchelor *et al.*, 2009]. Therefore, we end up with a curve that is a tradeoff between SNR and RMS residual. The ideal SNR is then the one at the elbow of the curve, shown in Figure 3.17 for O_3 . An SNR of 35 was chosen for O_3 retrievals based on this curve.

The \mathbf{S}_a matrices were generally not adjusted by me, as described above, Aldona Wiacek determined appropriate \mathbf{S}_a matrices for TAO for most species [Wiacek, 2006].

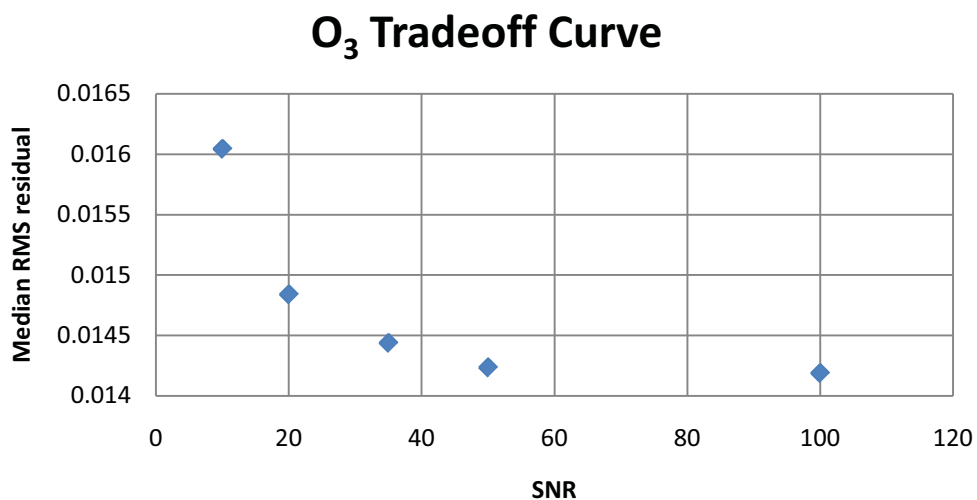


Figure 3.17: TAO O₃ tradeoff curve, showing median RMS residual vs. SNR for a selection of spectra. An SNR of 35 was chosen for O₃ retrievals based on this plot.

The \mathbf{S}_a matrix should reflect how much a species' VMR varies over the course of a day (diurnal variation) or over the course of the year (seasonal variations). However, since I aimed to improve the sensitivity to the troposphere in my O₃ retrievals, I did adjust the O₃ \mathbf{S}_a matrix. Originally it was 20% at all levels. I found slightly improved tropospheric O₃ retrievals when I weighted elements of the \mathbf{S}_a matrix by the layer thickness. The vertical grid is denser at lower levels than it is higher up in the atmosphere. Thus, by dividing by layer thickness, there is an increase in \mathbf{S}_a in the troposphere (giving the retrieval more freedom to fit the measurements) and a decrease in \mathbf{S}_a in the stratosphere and mesosphere.

3.1.4 Quality control

In the attempts to get as many measurements as possible, often we will record spectra at TAO that have had clouds or smoke interfering with the solar beam. As a result, some spectra are noisy and do not produce good spectral fits during the retrieval process. Those data get eliminated by a quality control (or 'filtering') step before plotting the

column time series. The filtering process is to eliminate fits whose RMS residual value falls above a certain threshold. Determining the RMS residual threshold is somewhat an arbitrary process. Three different threshold values were investigated (the third one was taken from *Sussmann et al.* [2011]):

$$Threshold = 1.2 \times RMS_m, \quad (3.2)$$

where the RMS_m is the median RMS residual from all of the spectral fits in the time range;

$$Threshold = RMS_m + 2\sigma, \quad (3.3)$$

where σ is the standard deviation of the RMS; and

$$Threshold : RMS/DOFS = X\% \quad (3.4)$$

where RMS residual and DOFS are those for each spectrum, and those whose ratio is $\leq X\%$ are kept, and $X=0.15\%$ for CH_4 , and $X=0.3\%$ for C_2H_6 (it was only tested for these two species as they were deemed representative, though different measures of quality control are being evaluated in SFIT4 retrievals for all species). Unfortunately, since this third threshold depends on DOFS as well, the cutoff must be species dependent.

I verified whether or not the three threshold values threw away ‘good’ spectra, and/or kept ‘bad’ spectra. The results are shown for C_2H_6 in 2005 in Figure 3.18. Threshold 3.3 is used for final retrievals because the other thresholds appear to have discarded reasonable data. Threshold 3.3 kept the most good data points (Figure 3.18).

3.1.5 Summary of TAO retrievals

Table 3.3 lists the retrieval parameters used for the remainder of this thesis and the resulting median DOFS for the total columns. When appropriate, the DOFS of the 0-5 km and/or 12-50 km partial columns, over the eleven-year dataset are listed as well. The partial columns will be discussed further in Chapters 4, 5, and 6. Table 3.3 also lists the

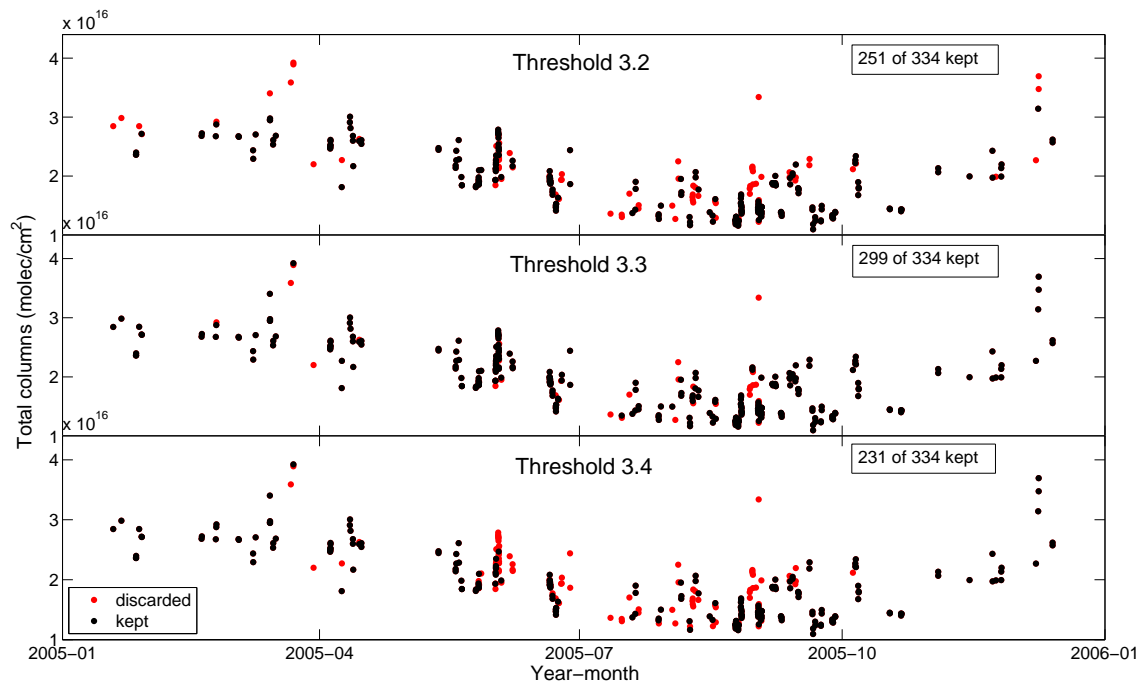


Figure 3.18: C_2H_6 measurements kept (black), and discarded (red) using various thresholds for quality filtering (see text): (top) threshold from Equation 3.2, (middle) threshold from Equation 3.3, and (bottom) threshold from Equation 3.4.

total errors on the total and partial columns, and the random component of the errors (described in Chapter 2, Section 2.4.4).

3.2 Optimized 11-year time series and trends

Using the retrieval parameters from Section 3.1 and Table 3.3, we obtain the total column time series for the eight primary species of this work, and they are shown from May 2002 to June 2013 in Figure 3.19. Each measurement that passed quality filtering is shown in this figure, though the time series is still somewhat sparse. Because FTIR solar absorption measurements can only be made when skies are clear, at TAO we typically have 80 to 100 days of measurements per year, with greater coverage in the summertime, and a greater number of measurement days in recent years due to improvements in efficiency and instrument maintenance. The seasonal cycles of the time series of each species is discussed below. Note that CH_4 is the only species of the eight that will not be discussed in later chapters of the thesis. Therefore, its averaging kernel is shown in Section 3.2.5 below, whereas those of the other seven species are shown in Chapters 4 and 6

3.2.1 Ozone

The total column time series of O_3 is dominated by the stratospheric O_3 layer [Andrews, 2005]. The peak of the seasonal cycle occurs in the spring, and the minimum occurs in the fall. The seasonal cycle is caused by the Brewer-Dobson circulation, which increases the mid-latitude O_3 columns over the course of the winter because it brings O_3 from the tropics (where it is created in the presence of sunlight) to the mid- to high-latitudes, where it descends [Butchart, 2014]. Stratospheric O_3 and the Brewer-Dobson circulation are discussed in more detail in Chapter 6, Section 6.1.

Table 3.3: TAO (and CARE, see Section 4.3) FTIR Retrieval Parameters: species, NDACC filter number, microwindows, interfering species, mean SNR of measurements, diagonal elements of \mathbf{S}_a , partial columns of interest, median DOFS for total/partial columns, total errors for total/partial columns, and random errors on total/partial columns.

Species	NDACC Filter	Microwindow(s) (cm^{-1})	Interfering Species	SNR	\mathbf{S}_a	Partial Columns (km)	DOFS	Total Errors (%)	Random Errors (%)
O_3 (1000)	6	1000.00 – 1000.50	H_2O , CO_2 , CH_4 , O_3 isotopes	35	20%	0-5 and 12-50	4.8/1.0/3.2	5.4 / 19 / 5.4	0.9 / 5.7 / 1.1
O_3 (3051)	3	3051.29 – 3051.90	H_2O , CH_4 , HDO , CH_3D	100	20%	12-50	2.5/2.1	7.4/8.6	1.55/1.51
CO	4	2057.70 – 2058.00	O_3 , CO_2 , OCS	100	20-30%	0-5	2.5/1.1	2.6/4.6	0.9/1.4
		2069.56 – 2069.76	O_3 , CO_2 , OCS						
		2157.50 – 2159.15	O_3 , CO_2 , OCS , N_2O , H_2O , H_2O ,						
C_2H_6	3	2976.66 - 2976.95	H_2O , O_3	120	30%	0-120	1.5	10	5.1
		2983.20 - 2983.55	H_2O , O_3						
		2986.50 - 2986.95	H_2O , O_3						
HCN	2	3268.05 – 3268.35	H_2O , CO_2 , N_2O	75	30%	0-120	1.6	16	4.4
		3287.10 – 3287.35	H_2O						
		3331.40 – 3331.80	H_2O , CO_2 , N_2O						
CH_4	3	2613.70 – 2615.40	HDO , CO_2	300	20%	0-120	3.4	19.2	1.2
		2650.60 – 2651.30	HDO , CO_2						
		2835.50 – 2835.80							
		2903.60 – 2904.03	NO_2						
N_2O	3	2481.30 – 2482.60	CO_2 , CH_4 , O_3 , H_2O , HDO	200	20%	12-50	3.7/1.8	4.3/9.0	0.5/1.8
		2526.40 – 2528.20	CO_2 , CH_4 , O_3 , H_2O , HDO						
		2537.85 – 2538.80	CO_2 , CH_4 , O_3 , H_2O , HDO						
		2540.10 – 2540.70	CO_2 , CH_4 , O_3 , H_2O , HDO						
HF	1	4038.86 – 4039.05	H_2O	250	20%	12-50	1.2/1.2	2.9/3.0	1.10/1.12
HCl	3	2727.73 – 2727.83	O_3 , HDO	300	10-40%	12-50	3.5/3.2	5.5/3.5	4.3/1.8
		2775.70 – 2775.80	N_2O , O_3						
		2925.80 – 2926.00	NO_2 , O_3 , CH_4						

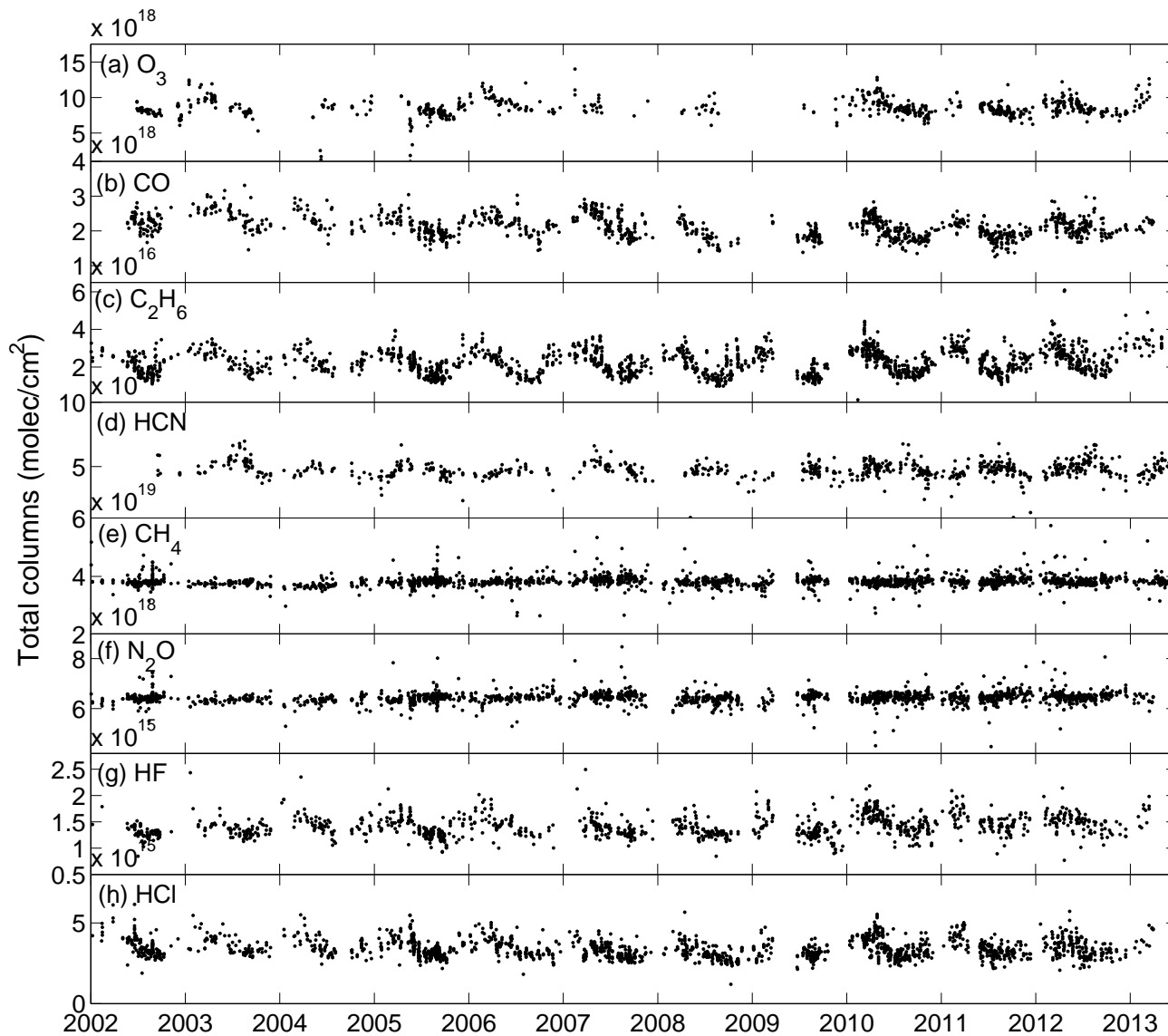


Figure 3.19: TAO total column time series for (a) O₃ (from 1000 cm⁻¹ MW), (b) CO, (c) C₂H₆, (d) HCN, (e) CH₄, (f) N₂O, (g) HF, and (h) HCl.

3.2.2 Carbon monoxide

The total column time series of CO is dominated by the boundary layer, where CO concentrations are highest. The peak of the seasonal cycle occurs in the late winter, and the minima occur in the late-summer (Figure 3.19(b)). The seasonal cycle is caused by the main sink of CO, which is oxidation by OH. OH is present in higher concentrations in the summer because it is created by photolysis. CO, therefore, is lost at a higher rate over the sunnier months. The fossil fuel source of CO may also be higher in the winter, because of increased use of oil and natural gas for heating during the winter. CO is discussed in more detail in Chapter 4, Section 4.1.

3.2.3 Ethane

C₂H₆ is moderately long-lived, with a lifetime of about two months [Jacob, 1999]. The seasonal cycle of C₂H₆ is very similar to that of CO (Figure 3.19(c)), due to the dominance of loss by OH. Maxima and minima occur just a few weeks before those of CO. The CO seasonal cycle lags that of C₂H₆ and other hydrocarbons because CO is a byproduct of hydrocarbon oxidation. The sources of C₂H₆ are natural gas leaks, fossil and bio-fuel combustion, biomass burning, and waste [Jacob, 1999]. TAO measurements of C₂H₆ during the BORTAS campaign of summer 2011 were used by Griffin *et al.* [2013] to identify a biomass burning plume that passed over Toronto on 21 July 2011. The short-term variability in the C₂H₆ time series will be discussed further in Chapters 4 and 5.

3.2.4 Hydrogen cyanide

HCN is emitted mainly from biomass burning, though a smaller amount comes from biofuels [Jacob, 1999]. However, studies show that urban emissions from vehicles are also a significant source of HCN [Baum *et al.*, 2007; Moussa *et al.*, 2013]. It is lost primarily by ocean uptake, and its lifetime is about five months [Jacob, 1999]. Figure 3.19(d) shows

that HCN peaks in the summer, and this peak has a different amplitude from year to year, both features consistent with the biomass burning source. HCN minima occur in the winter. The short-term variability in the HCN time series will be discussed further in Chapters 4 and 5.

3.2.5 Methane

Methane is the most abundant hydrocarbon in the atmosphere, and is the second most important anthropogenic greenhouse gas (GHG) [*IPCC, WorkingGroup1, 2013*]. CH_4 is a long-lived gas with a lifetime of 9-12 years. It is lost at a higher rate in the summer due to oxidation by OH (like CO), however, CH_4 is emitted by natural (e.g., wetlands, termites) and agricultural (rice paddies, livestock) sources over the spring, summer and fall, which compensates for the loss during these seasons [*Jacob, 1999*]. CH_4 is also part of natural gas – a byproduct of extracting fossil fuels, and used extensively for heating homes. Pipe leaks during extraction, in city infrastructure, and in individual homes are a significant source of CH_4 year round [*Wunch et al., 2009*]. CH_4 is also lost, to a lesser extent, by transport to the stratosphere. Because of the complexities of its many sources, and the fact that the tropospheric seasonal cycle is different from the stratospheric seasonal cycle, and the total column mixes them, the amplitude of the seasonal cycle of CH_4 is small and not visible in the TAO total column time series (Figure 3.19(e)), but tends to have a signal that looks like an inverted sine wave starting in January and ending in December in the Northern Hemisphere [*Sussmann et al., 2011*].

The TAO CH_4 total columns were compared with those from the TANSO-FTS SWIR channel on the Greenhouse gas Observing SATellite (GOSAT), and mean difference of the same-day measurements ($\pm 10^\circ$ in latitude and longitude) was always within 3%.

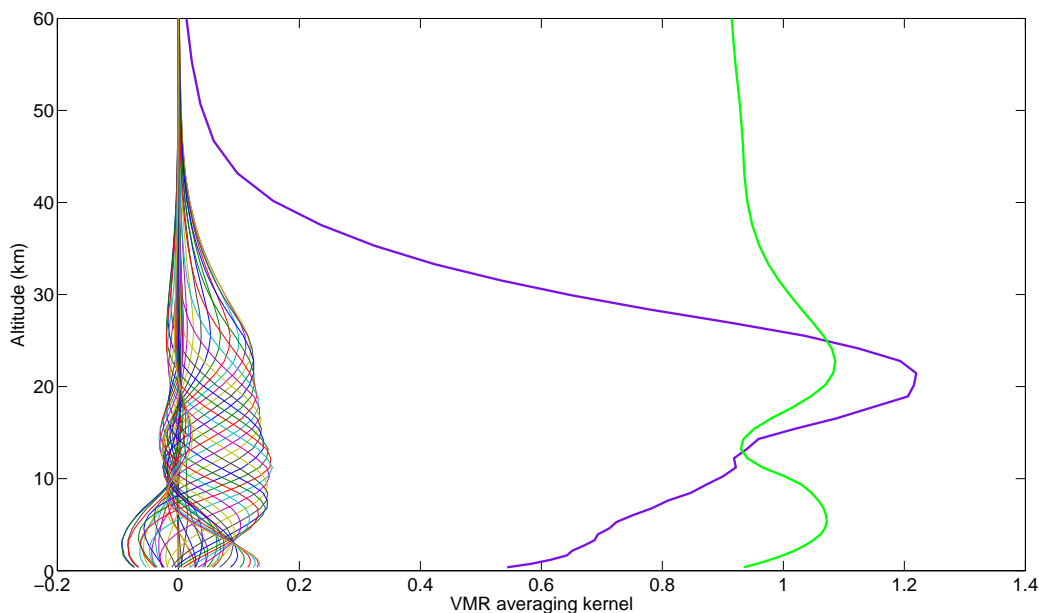


Figure 3.20: Typical CH_4 VMR averaging kernels (coloured lines) from 9 February 2006, total column averaging kernel (thick green line), and sensitivity (thick purple line).

CH_4 averaging kernel

The VMR averaging kernel for CH_4 (using the optimized parameters discussed in Section 3.1.1) is shown in Figure 3.20. Also shown is the total column averaging kernel and the sensitivity (explained in Chapter 2, Section 2.4.3). The median DOFS over the whole time series for the total columns is 3.4, and partial columns with 1 DOFS are roughly 0-6 km, 5-12 km, 12-20 km, and 20-35 km.

3.2.6 Nitrous oxide

N_2O is the fourth most important emitted GHG [IPCC, WorkingGroup1, 2013], and it has also become the most important ozone-depleting substance [Ravishankara et al., 2009]. N_2O is long-lived (~ 114 years), and is only lost to the stratosphere [Jacob, 1999]. Emissions of N_2O are not controlled, thus increasing amounts travel up to the stratosphere

and become a source of NO_x there [Ravishankara *et al.*, 2009]. Its sources are the ocean, soils, biomass burning, chemical fertilizers, and livestock [Jacob, 1999]. The total columns do not show much of a seasonal cycle (Figure 3.19(f)), although the stratospheric partial columns, which are presented and discussed further in Chapter 6, do have a seasonal cycle.

3.2.7 Hydrogen fluoride

HF comes mainly from emissions of chlorofluorocarbons (CFCs). It is a long-lived stable fluorine reservoir, and because of its long lifetime, it is a dynamical tracer for the stratosphere. The total column time series of HF (Figure 3.19(g)) is dominated by the stratosphere, and is discussed in more detail in Chapter 6.

3.2.8 Hydrogen chloride

The total column time series of HCl (Figure 3.19(h)) is also dominated by the stratosphere, and is discussed in more detail in Chapter 6. HCl also comes mainly from emissions of CFCs that get transported up to the stratosphere and then photodissociate. HCl is an unstable chlorine reservoir, so it releases the Cl atom, which takes part in catalytic O_3 destruction chemistry.

3.3 NDACC archiving

During the course of my PhD, the TAO data were archived in the NDACC database twice. The first was in September 2010, when we simply updated the existing submissions to include 2007, 2008 and 2009, keeping the retrieval parameters and data format the same for consistency (even though we had updated to a newer version of SFIT2 at that point, and the retrieval parameters had been updated). Species archived were: O_3 total (0-100 km) and stratospheric (15-50 km) columns, CH_4 total, tropospheric (0-15 km) and

stratospheric columns, N₂O total, tropospheric and stratospheric columns, NO total and stratospheric columns, NO₂ total and stratospheric columns, HF total and stratospheric columns, and HCl total and stratospheric columns.

The second submission was done in October 2013. This time we submitted the complete TAO dataset (May 2002-June 2013), re-analysed with the updated retrieval parameters (the optimized ones, described above in Section 3.1), SFIT4 (beta version), and HITRAN 2008. The total columns of the eight primary species of this thesis, as well as retrieved profiles for C₂H₆, HCN and HF were submitted to the archive in HDF format [www.ndsc.ncep.noaa.gov/data/data_tbl/].

SFIT4 is a newer version of the retrieval algorithm (following SFIT2 v3.94). It was implemented in our group for TAO by postdoc Stephanie Conway. While Stephanie did the SFIT4 retrievals for TAO that were archived, my involvement was in the retrieval parameter optimization described above, and to compare my SFIT2 retrievals to her SFIT4 retrievals to assure that the new algorithm did not give unexpected results.

3.4 Future work

A trend analysis was done using the method described in *De Mazière et al.* [2005] and *Gardiner et al.* [2008], where a fourth order Fourier series plus a linear trend is fit to the data, and a bootstrap resampling method is used to determine the significance of the trend. These fits could be used to study the seasonal cycles in more detail. The resulting trends are included in a table in Appendix B. However, this was just preliminary work on trends and more detailed trend analysis is beyond the scope of this thesis. Therefore, further trend analysis of the TAO dataset would be informative, and as the time series continues to get longer, the trends may become more significant [*Weatherhead et al.*, 1998, 2002].

The TAO solar absorption spectra contain information on many more species that

were beyond the scope of this thesis. New students and postdocs have started working on retrievals of the following species for TAO, and one can expect these to be published in the future: carbonyl sulfide (OCS), formaldehyde (HCHO), formic acid (HCOOH), acetylene (C₂H₂), and ethylene (C₂H₄).

The retrieval algorithm used in the NDACC-IRWG was updated (now SFIT4), and was officially released in January 2014, though a beta version was working in the group prior to that (e.g., Section 3.3). SFIT4 improves over SFIT2 in the following ways:

1. SFIT4 can calculate \mathbf{K}_b matrices (see Chapter 2) for many error components, allowing for errors on each measurement to be calculated automatically,
2. post-fit error calculations given estimates of uncertainties,
3. spectral database building codes (including compatibility with HITRAN2012),
4. batch processing codes,
5. more test cases, and
6. automated SNR calculations for each spectrum.

In the future, we expect to archive the TAO time series on a more regular basis, using retrievals done with SFIT4, and errors calculated on each spectrum (instead of the mean of a handful of spectra).

Finally, the retrievals can be further optimized now that there is more emphasis on retrieved profiles in the IRWG (instead of just columns with DOFS > 1). In order to further reduce oscillations in the retrieved profiles, one may have success using the automated SNR calculation, although the \mathbf{S}_a matrix must be reduced if that approach is used. This is work that postdoc Stephanie Conway is currently doing.

Chapter 4

Toronto tropospheric composition: chemistry, measurements and model

Being able to quantify how much air pollution is coming from local, regional, and long-range sources can help inform policy decisions at the municipal, provincial and federal levels of government. In the following chapter, I aim to answer the question: What are the important sources of Toronto regional air pollution, and can the source contributions be quantified? On their own, TAO measurements over Toronto do not tell us where our air came from and what chemical and dynamical factors have influenced its composition. Therefore to answer the question, we need to use data not only from TAO, but from complementary sources, and a chemical transport model (in this case, GEOS-Chem). This chapter will provide some background about tropospheric chemistry, then describe the different datasets other than TAO that were used. A description of the GEOS-Chem model is also included, and we will see the time series over Toronto from May 2002 to June 2013 of four tropospheric species: O_3 , CO , C_2H_6 , and HCN . Chapter 5 will then show how the short-term variability in the time series can be attributed to different sources.

4.1 Background: tropospheric composition and chemistry

The troposphere contains 85% of the atmosphere's mass [Jacob, 1999] and is a chemically and dynamically complex region of the atmosphere [IGOS, 2004]. All of the surface-atmosphere interactions take place in the troposphere: hundreds of trace gases are emitted by aircraft, industrial smoke stacks, vehicles, soils, farm land, oceans, forest fires and ecological systems. They react chemically, and either are transported up to the stratosphere, get deposited on land or ocean, or get rained out in precipitation. Dynamically, the troposphere is the most active region of the atmosphere as well. It is thermally unstable, with warmer air near the surface, and cooler air above, which causes convection and sometimes violent weather such as hurricanes, tornados, hail, blizzards and thunderstorms. In addition, the wind patterns caused by Earth's rotation are affected by changing topography, which has ramifications for weather, pressure gradients, and transport patterns. For all these reasons, the troposphere is an interesting yet difficult system to fully characterize and there remain many unknowns and uncertainties. The following sub-sections will provide background information on tropospheric O₃ and CO (see Sections 3.2.3 and 3.2.4 for similar information on C₂H₆ and HCN, respectively), which are the two most important gases for air quality that the TAO-FTS can measure well.

4.1.1 Health standards for O₃ and CO

In the middle troposphere, O₃ is a source of OH, which is an oxidant that reacts with other trace gases and cleanses the atmosphere of air pollution. In the upper troposphere, O₃ is a direct GHG, and combined with its indirect effects on GHGs, O₃ is the third most important anthropogenic GHG, after CO₂ and CH₄ [IPCC, WorkingGroup1, 2013].

In the boundary layer, O₃ is the primary component of smog, and it is a volatile

chemical that oxidizes biological tissue causing inflammation of the bronchial tubes when inhaled [EPA, 1999]. For this reason, O₃ air pollution causes about a third of the estimated 3550 hospital admissions and about 15% of the 1300 air-pollution-related deaths each year in Toronto [Toronto Public Health, 2014]. O₃ also causes damage to the stomata of plant leaves, which inhibits their uptake of CO₂ for photosynthesis, reducing crop yields [MOE, 2013]. Through this influence on CO₂ uptake in plants, O₃ also has an indirect climate impact [Sitch et al., 2007].

CO is a poisonous gas at high concentrations, and can enter the bloodstream and reduce oxygen delivery to the organs and tissues. People with heart disease are particularly sensitive to CO pollution [MOE, 2013]. CO is also an indirect GHG because of its role as an OH sink and in creating tropospheric O₃. CO is created when CH₄ and higher order hydrocarbons are oxidized. Other sources of CO include direct emissions from fossil fuel combustion, biomass burning, vegetation and oceans. CO is lost primarily through oxidation by OH, and as such has a lifetime of a few weeks during summers at low latitudes to a few months in the winter at higher latitudes [Jacob, 1999]. The next section will discuss the chemical reactions involved in CO and O₃ production and loss.

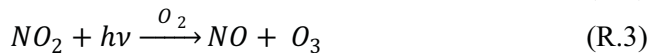
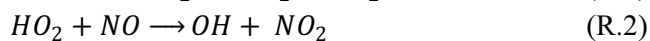
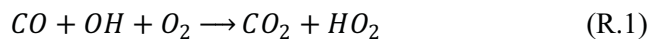
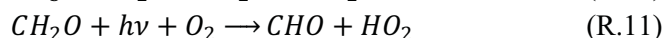
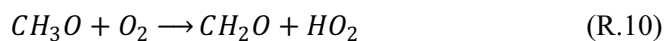
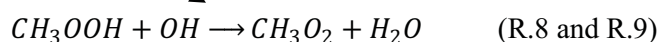
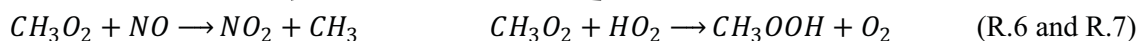
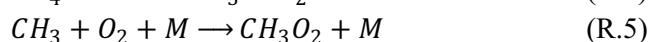
In Ontario, there are two standards for surface pollutant concentrations for human health: the provincial 1-hour criterion, and the Canada-Wide Standard (CWS) 8-hour running average criterion. For O₃, these are 80 ppb and 65 ppb, respectively. The CWS for surface O₃ is still exceeded intermittently in the summer in most parts of Ontario, although more cities are starting to meet the standard than before [MOE, 2013]. From 2002 to 2010, Toronto averaged 8 days per year that exceeded the one-hour criterion for surface O₃, and 18 days per year that exceed the CWS. For CO, the standards are 30 ppm (1-hour) and 13 ppm (8-hour), and these have not been exceeded at any measurement site in Ontario since 1991 [MOE, 2012].

4.1.2 Ozone and carbon monoxide chemistry

Tropospheric O_3 is created through a photochemical process involving NO_x , hydrocarbons, and sunlight [*Jacob, 1999*]. Because of the increase in NO_x and hydrocarbon emissions, tropospheric O_3 has increased by about 80% in the northern hemisphere since pre-industrial times [*Wang and Jacob, 1998*]. Reactions R.1 to R.3 in Figure 4.1 show how O_3 is created as a result of CO oxidation. Starting from hydrocarbons such as CH_4 and volatile organic compounds (VOCs) – of which C_2H_6 and isoprene are examples – the reactions are more complex (shown for CH_4 in Figure 4.1, Reactions R.4 to R.12). The NO_x processing is catalytic, but the chain is terminated by loss of HO_x radicals; either in a self-reaction when NO_x concentrations are very low (Reaction R.15 in Figure 4.1, or in a reaction with NO_2 , making HNO_3 , when NO_x concentrations are very high (Reaction R.14 in Figure 4.1) [*Jacob, 1999*]. The main source of HO_x , which is needed for O_3 production, is photolysis of O_3 , followed by Reaction R.13.

NO_x is the rate-limiter for O_3 production from CO and hydrocarbon oxidation, and in urban environments there is a lot of NO_x , causing rapid O_3 production. The net result of CH_4 oxidation, for the high NO_x case is R.16 in Figure 4.1. And the net result for the low NO_x case is R.17 in Figure 4.1. Therefore, most urban centres around the world have smog problems due to increased NO_x emissions from transport and industry, as well as increased VOC emissions, which react more quickly than natural hydrocarbons to make O_3 during the day. Agriculture is also a source of NO_x , which can increase the background levels of O_3 . However, in urban environments, the greater the NO_x concentrations are, the smaller its O_3 -production efficiency becomes. When NO_x concentrations are very great, O_3 production is hydrocarbon-limited [*Jacob, 1999*].

Reaction R.3 is the only reaction that creates tropospheric O_3 , and it requires HO_x ,

CO oxidation and production of O₃:**CH₄ oxidation and production of O₃:**

followed by 4.1 to 4.3 above.

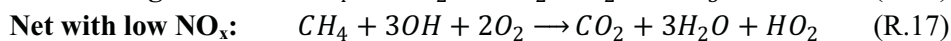
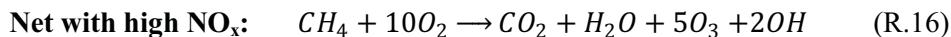
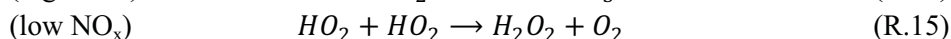
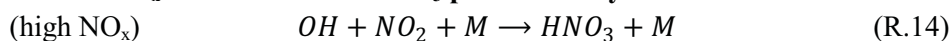
Production of HO_x (needed for O₃ production):**Loss of HO_x and termination of O₃ production cycle:**

Figure 4.1: Schematic of reactions involved in CO and CH₄ oxidation and O₃ production.

and NO_2 . Therefore, Reactions R.2 and R.6 govern production of tropospheric O_3 :

$$\begin{aligned} P_{\text{O}_3} &= \frac{d[\text{O}_3]}{dt} = k_2[\text{HO}_2][\text{NO}] + k_6[\text{CH}_3\text{O}_2][\text{NO}] \\ &\approx 2k_2[\text{HO}_2][\text{NO}] \end{aligned} \quad (4.1)$$

where k_i are the reaction rates (where the number i corresponds to the reactions R.i in Figure 4.1). In a steady state, production of HO_x is equal to the loss of HO_x , so given Reactions R.13 to R.15 in Figure 4.1:

$$\begin{aligned} P_{\text{HO}_x} &= L_{\text{HO}_x} \\ 2k_{13}[\text{O}(^1D)][\text{H}_2\text{O}] &= 2k_{15}[\text{HO}_2]^2 + k_{14}[\text{OH}][\text{NO}_2][\text{M}] \end{aligned} \quad (4.2)$$

In a NO_x -limited regime, the concentration of NO_x is low, and the reaction rate of R.15 is greater than the reaction rate of R.14. So the second term in Equation 4.2 can be ignored, and we can solve for $[\text{HO}_2]$:

$$[\text{HO}_2] = \left[\frac{k_{13}[\text{O}(^1D)][\text{H}_2\text{O}]}{k_{15}} \right]^{1/2} \quad (4.3)$$

Substituting this expression for $[\text{HO}_2]$ into Equation 4.1, we can see that production of O_3 in a NO_x -limited regime is linearly proportional to $[\text{NO}]$:

$$P_{\text{O}_3} = 2k_2[\text{NO}] \left[\frac{k_{13}[\text{O}(^1D)][\text{H}_2\text{O}]}{k_{15}} \right]^{1/2}. \quad (4.4)$$

In a hydrocarbon-limited regime, the concentration of NO_x is high, and Reactions R.1 to R.3 go very quickly. For simplicity, let's consider the CO-only case, where Reactions 4.1 and 4.2 have approximately the same rate:

$$\begin{aligned} R.1 &\approx R.2 \\ k_1[\text{CO}][\text{OH}] &= k_2[\text{HO}_2][\text{NO}] \end{aligned} \quad (4.5)$$

Solving for $[\text{OH}]$, we get:

$$[\text{OH}] = \frac{k_2[\text{HO}_2][\text{NO}]}{k_1[\text{CO}]} \quad (4.6)$$

This gives us an expression for [OH] that we can substitute into Equation 4.2. Since the concentration of NO_x is high, the reaction rate of R.14 is greater than the reaction rate of R.15, the first term on the right hand side of Equation 4.2 can be ignored, and we can solve for $[\text{HO}_2]$:

$$\begin{aligned} 2k_{13}[\text{O}(^1D)][\text{H}_2\text{O}] &= k_{14}[\text{OH}][\text{NO}_2][M] \\ 2k_{13}[\text{O}(^1D)][\text{H}_2\text{O}] &= k_{14}[\text{NO}_2][M] \frac{k_2[\text{HO}_2][\text{NO}]}{k_1[\text{CO}]} \\ [\text{HO}_2] &= \frac{2k_{13}k_1}{k_{14}k_2} \frac{[\text{O}(^1D)][\text{H}_2\text{O}][\text{CO}]}{[\text{NO}][\text{NO}_2][M]} \end{aligned} \quad (4.7)$$

Finally, substituting this expression for $[\text{HO}_2]$ into Equation 4.1, we can see that production of O_3 in a hydrocarbon-limited regime is linearly proportional to $[\text{CO}]$, and *inversely* proportional to $[\text{NO}_x]$:

$$P_{\text{O}_3} = 2k_2 \frac{2k_{13}[\text{O}(^1D)][\text{H}_2\text{O}]k_1[\text{CO}]}{k_{14}k_2[\text{NO}_2][M]} \quad (4.8)$$

Therefore, in a hydrocarbon-limited regime, an increase in $[\text{NO}_2]$ would cause a decrease in $[\text{O}_3]$.

Tropospheric O_3 is lost through chemical processes, usually through reactions with water vapour or HO_x . It is also lost through dry deposition [Jacob, 1999].

North American tropospheric O_3 sources

Figure 4.2(a) shows the total NO_x emissions in North America on a typical summer day (21 July 2005), from all modelled sources (fossil fuels, biofuels, aircraft, lightning, soil, and fertilizer) as given by the emission inventories described below (Section 4.6). NO_x from biomass burning was omitted from this figure as this source is highly variable, although it can contribute a significant fraction to the total (e.g., 6.7% for July 2005). Figure 4.2(b) shows the total North American modelled CO sources, including direct emissions, and the monoterpene sources – again, excluding biomass burning, which contributes an even greater fraction (e.g., 35.2% for July 2005) to the total. The NO_x and CO emissions

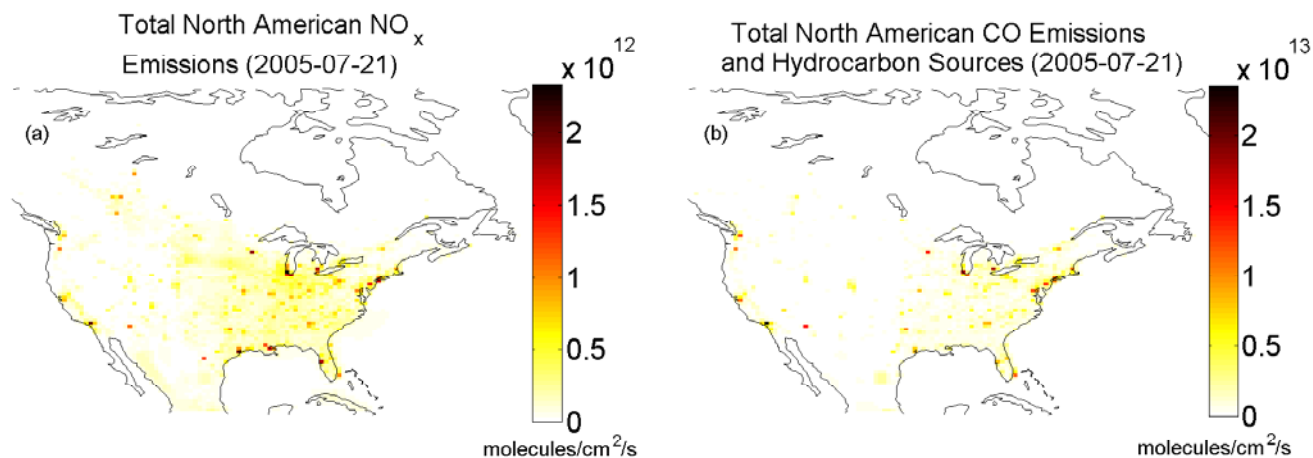


Figure 4.2: Map of total North American (a) NO_x emissions, and (b) CO sources (including direct emissions and the hydrocarbon source) on a typical summertime day (21 July 2005). (a) Total = sum of fossil fuel, biofuel, aircraft, lightning, soil and fertilizer sources. (b) Total = sum of fossil fuel, biofuel, and monoterpene sources. All sources are from the emission inventories used in the GEOS-Chem model (Section 4.6). NO_x and CO from biomass burning are excluded since its location and amount are more variable than the other sources.

in Figure 4.2 tend to be highest in large cities (red points), such as New York City, Los Angeles, Chicago, and Houston (first, second, third, and fourth most populous U.S. cities). There is also a large amount of NO_x emissions from the Ohio Valley, which is an industrial part of the U.S., and from the Great Plains (especially the Minneapolis area) which is an agricultural part of the U.S. (with high soils/fertilizer emissions).

Lifetime of tropospheric O₃

The lifetime of O₃ has a range in the troposphere from a few hours in the boundary layer to a few days in the lower troposphere to a few months in the upper troposphere [*Jacob*

et al., 1996; *Thompson et al.*, 1996; *Wang et al.*, 1998; *Fiore et al.*, 2002]. Therefore, O_3 tends to be strongly influenced by regional sources and sinks. However if O_3 is transported quickly to the free troposphere, it can travel great distances (e.g., from China to the western United States [*Zhang et al.*, 2008, 2009]). Also O_3 precursor gases such as peroxyacyl nitrate (PAN) can be ventilated to the cooler free troposphere, where they are longer lived, and cause background levels of O_3 to increase in more remote locations [e.g., *Hudman et al.*, 2004].

4.1.3 Seasonal cycle of lower-tropospheric O_3

Given the sources and sinks of tropospheric O_3 , the seasonal cycle in the lower troposphere at mid-latitudes tends to peak in the summertime when there is more sunlight, and have a minimum in the winter. This seasonality is quite different a few kilometers higher in the atmosphere, where the Brewer-Dobson circulation effectively brings stratospheric O_3 to the winter mid-latitudes. When the upper troposphere-lower stratosphere is taken into account, the seasonal cycle peaks strongly in the spring and decreases over the course of the summer and fall (see Sections 3.2.1 and 6.1).

4.1.4 O_3 trends

Studies show that tropospheric O_3 may be decreasing in developed countries [e.g., *Gardiner et al.*, 2008] thanks to NO_x emission reductions in both vehicles and industries. However, given the complexity of tropospheric O_3 production, there is not a linear relationship between NO_x reductions and O_3 concentrations. In Ontario, the summer mean surface O_3 decreased at a rate of -0.9%/year from 2002-2011, while the winter mean surface O_3 increased by 2.2%/year [*MOE*, 2013]. The annual mean surface O_3 over Toronto has increased in the last two decades at a rate of 4.1%/year, much higher than the provincial rate [*MOE*, 2013]. The situation is similar in the northeast U.S. for which there are many studies. *Bloom et al.* [2010] found that surface O_3 has decreased up to 6

ppb/decade (looking at 1989-2007) during times of maximum temperature in the most polluted locations. The general findings are that maximum tropospheric O₃ concentrations are decreasing, but the background O₃ is increasing [*Oltmans et al.*, 1998; *Lin et al.*, 2000; *Tarasick et al.*, 2005; *Bloom et al.*, 2010; *MOE*, 2012; *Cooper et al.*, 2012].

4.2 FTIR sensitivity to the troposphere

Prior to my graduate studies, tropospheric O₃ partial columns were not retrieved at TAO. They were made possible by the new microwindow recommended across the NDACC-IRWG and described by *Lindenmaier et al.* [2010]. This section will discuss how well tropospheric O₃ and other species can be retrieved at TAO.

As discussed in Section 2.4.3, the averaging kernels show the sensitivity of the retrieval to the true state of the atmosphere. Those for O₃, CO, C₂H₆, and HCN are shown in Figure 4.3, along with the sensitivity (defined in Equation 2.30, Section 2.4.3), and the partial (0-5 km) and total column averaging kernels. Only CO and O₃ have DOFS ≥ 1 for the 0-5 km partial column. 0-5 km is the minimum partial column for O₃ achieving median DOFS = 1. For CO, 0-3 km is the minimum partial column with median DOFS = 1. C₂H₆ has median DOFS = 1 for 0-8 km, and HCN has median DOFS = 1 for 0-40 km, therefore, only total columns of those two gases are discussed in this thesis.

4.3 Urban versus rural: the CARE FTS dataset

Environment Canada's Centre for Atmospheric Research Experiments (CARE) is located at Egbert, Ontario, about 80 km north northwest of Toronto at 44.23°N, 79.78°W, 251 masl. Measurements with a Bomem DA8 FTIR spectrometer (older model than the TAO FTS) began at CARE in January 1996, although we only examine the dataset from 2002 onwards when we have complementary TAO data. Egbert is relatively close, yet it is located in a rural area. Pollution measured at Egbert likely undergoes the same

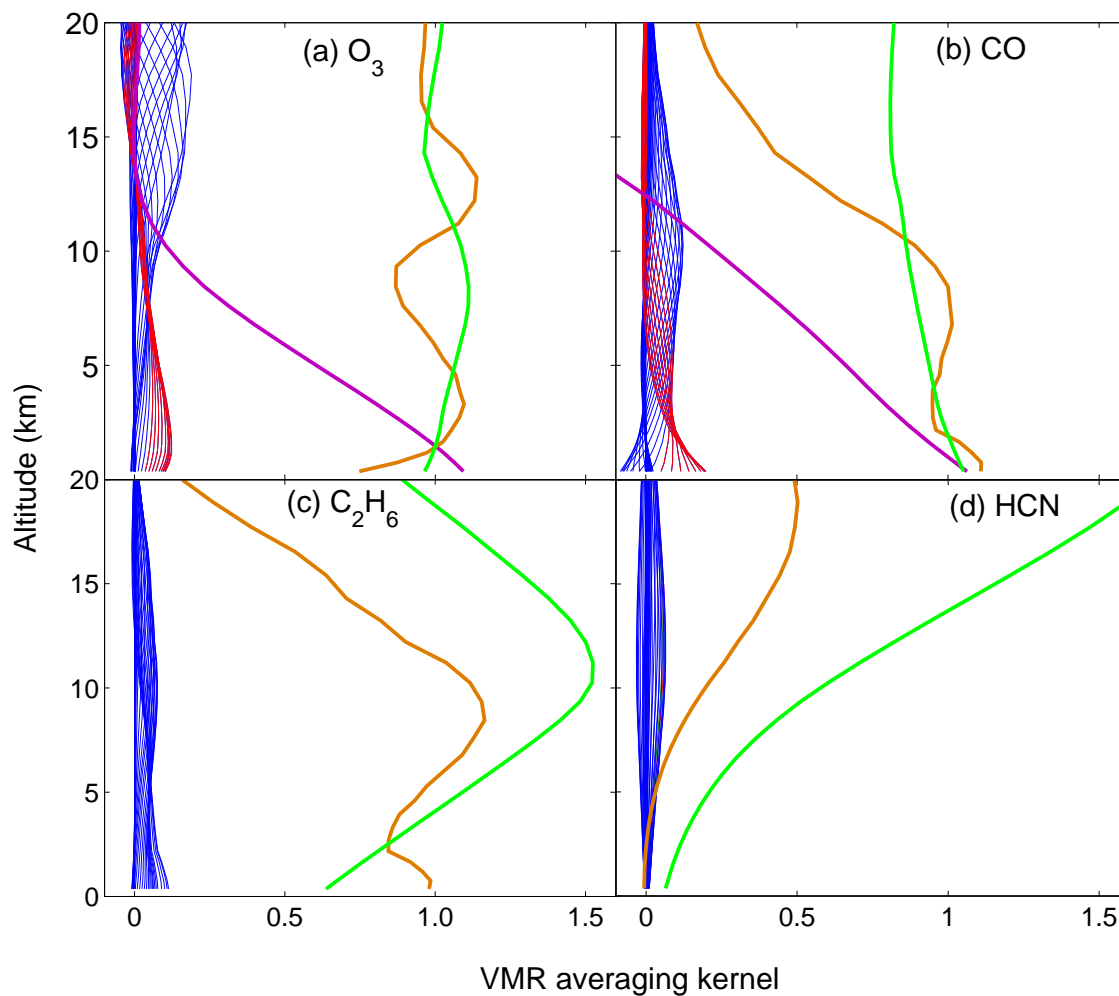


Figure 4.3: TAO VMR averaging kernels (blue lines, with those for the 0-5 km levels in red lines), total column averaging kernels (green lines), partial (0-5 km) column averaging kernels (purple lines), and sensitivity (orange lines) for tropospheric species: (a) O_3 , (b) CO , (c) C_2H_6 , and (d) HCN .

long-range transport as that measured at Toronto, but has fewer local sources, except possibly additional agricultural sources that Toronto wouldn't have.

The frequency of Egbert measurements varies greatly from year to year due to the availability of staff and instrument downtime for maintenance, repair, and upgrades. The greatest number of measurement days (about 30 per year) occurred during 2002–2007, and there were very few in 2008–2010, and none in 2011–2013.

The CARE time series were retrieved using the same parameters as for TAO (Table 3.3), and the averaging kernels are very similar to those in Figure 4.3. The CARE time series are shown as cyan-coloured points in the time series (Figure 4.9) below and in Chapters 5 and 6.

In Figure 4.4, we show the comparison between same-day CARE and TAO tropospheric O_3 (0–5 km), CO (0–3 km and 0–5 km), C_2H_6 , and HCN. Filter 2 measurements at CARE ceased after 2004, which is why the HCN CARE time series is only from 2002 to 2004. The difference between TAO and CARE is smallest for HCN, which is expected as HCN is long-lived, and its dominant source is biomass burning, which would most likely be from long-range transport. There are HCN emissions from vehicles, which would be greater in Toronto, however, the HCN averaging kernel implies that the TAO retrievals are not sensitive to those emissions.

The columns of the other three gases are greater in Toronto than in Egbert (as would be expected given the greater urban emissions), and only the 0–3 km CO partial columns have a marginally significant difference ($19.9 \pm 19.3\%$) given the standard deviation, which is expected given that CO in the boundary layer should dominate the signal in an urban area. The insignificant differences for the other partial columns are likely due to the free tropospheric component, in which both Toronto and Egbert would have similar composition, given their proximity. For example, winds above 3 km are typically 12.6 m/s (taken from the median of the GEOS-5 wind fields over Toronto), so it would only take about 1.8 hours for an air parcel to travel from one place to the other, which is

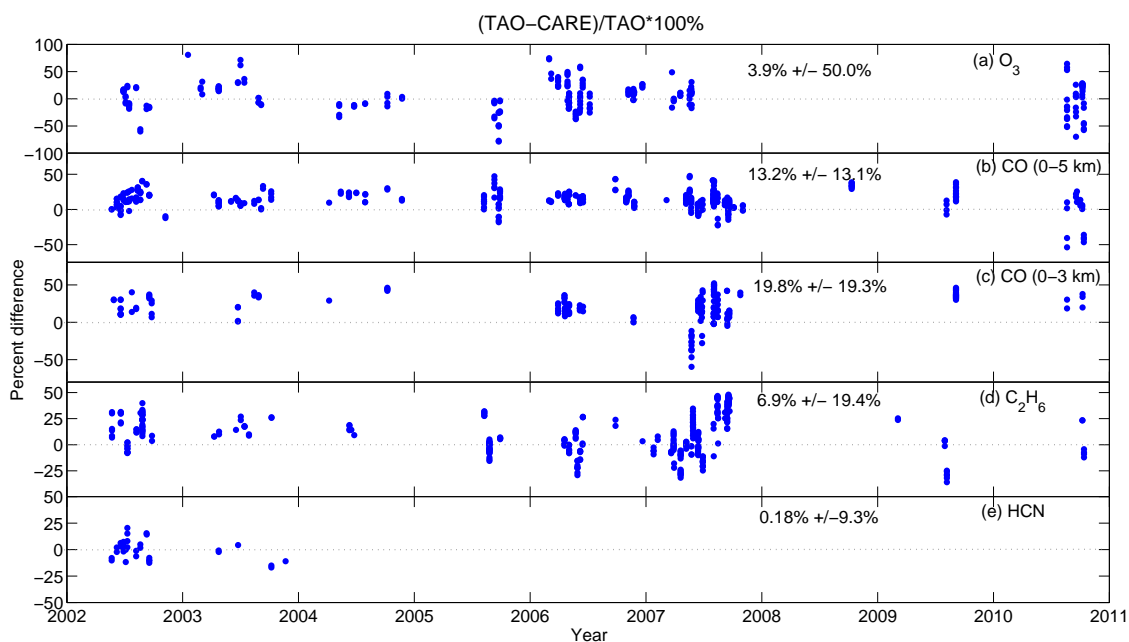


Figure 4.4: Differences between TAO and CARE (a) O_3 (0-5 km), (b) CO (0-5 km), and (c) CO (0-3 km) partial columns, and (d) C_2H_6 and (e) HCN total columns. Also shown are the mean differences $\pm 1\sigma$

shorter than the lifetimes of these gases in the free troposphere. Therefore, for the rest of this thesis, we treat CARE partial columns as a complementary dataset that helps fill in the gaps of the TAO dataset.

4.4 Complementary measurements from space

In order to validate and supplement the TAO FTIR measurements of tropospheric O_3 and CO , we use column measurements from the MOPITT and TES satellite instruments when they pass over Toronto (within 1° latitude and longitude). These instruments and their datasets are described in the sections below.

4.4.1 TES

TES stands for Tropospheric Emissions Spectrometer, and it is one of four instruments flying on NASA’s Earth Observing System Aura satellite (tes.jpl.nasa.gov/). It has measured O_3 in the troposphere, as well as temperature and other trace gases globally since July 2004. The satellite has a highly-inclined, polar, sun-synchronous orbit, with approximately a 5 by 8 km footprint in nadir mode. It arrives at the same geographical location every 16 days [Beer *et al.*, 2001; Beer, 2006].

TES is an infrared (650-3050 cm^{-1}) emission FTS. TES has two methods of observing the atmosphere: nadir and limb viewing, though routine limb-viewing ceased in May 2005 to conserve instrument life [Beer, 2006; Bowman *et al.*, 2007]. Between each measurement, TES calibrates itself by scanning cold space and an on-board blackbody cavity [Beer *et al.*, 2001; Beer, 2006]. Inverse methods are used to compute vertical profiles of trace gases from TES emission spectra [Bowman *et al.*, 2006].

I used the TES version 05 Lite version 007 O_3 product, which comes on 27 pressure levels. As per the User’s Guide, selected only those data with “SpeciesRetrievalQuality”=1 and “O3_CCURVE_QA”=1 [TES Users Guide, 2013]. Data over Toronto were selected, and a median averaging kernel was made and is shown in Figure 4.5 with the 0-5 km levels highlighted in red. These peak at about 700 hPa (~ 2.5 km), which is similar to the TAO averaging kernels (Figure 4.3(a)).

I smoothed TES retrieved profiles with the median TAO averaging kernel [Rodgers and Connor, 2003], although it may be unsound to compare retrievals from instruments with similar vertical resolution but different vertical sensitivity in this way. A better way would be to take a third source (such as GEOS-Chem O_3 columns), and smooth it with the TAO averaging kernels (described in Section 4.6.2), and with the TES averaging kernels, and then see what that difference is. However, since our main goal is to have TES O_3 columns validate the ground-based FTIR O_3 seasonal cycle, we did not pursue other smoothing options. Smoothing the TES time series reduced the bias between TAO

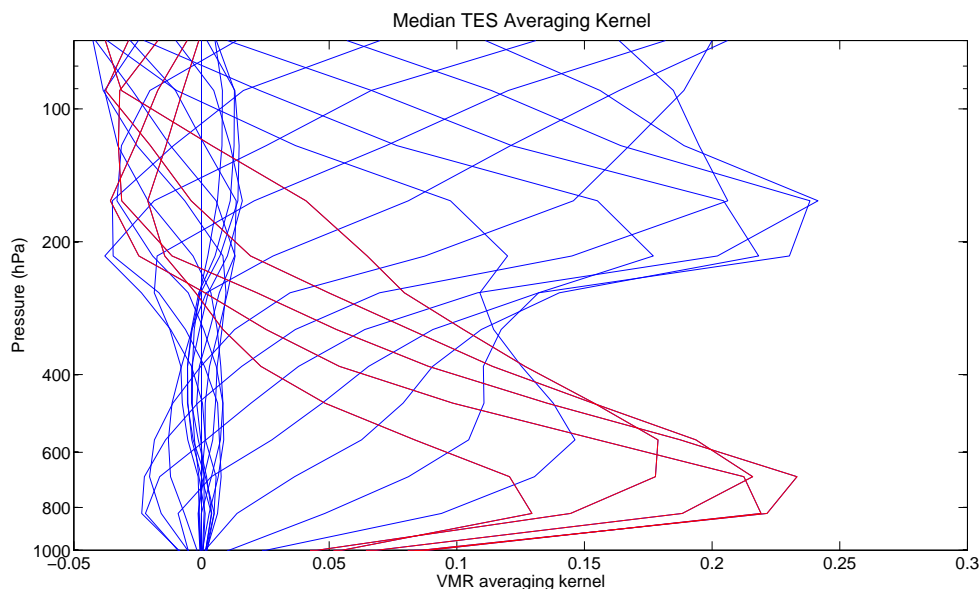


Figure 4.5: TES median VMR averaging kernels (2004–2010, within 1° of Toronto) for O_3 . Red lines indicate the 0-5 km levels.

and TES lower-tropospheric partial columns, so that the agreement was improved.

TES O_3 over Toronto is used to supplement TAO data, although the TES dataset is also sparse and biased slightly high. The 2004 to 2013 smoothed TES O_3 (0-5 km) time series is shown in Section 4.7, and the climatological monthly mean comparison is shown in Figure 4.6. TES O_3 partial columns are about 9.1% greater than TAO O_3 (using $(TAO-TES)/TAO \times 100\%$), and they have good correlation ($R=0.74$, and slope of TES vs. TAO=0.64). The bias with respect to TAO is consistent with the literature [e.g., Nassar *et al.*, 2009]. The O_3 (0-5 km) column seasonal cycle is also similar. The lower-tropospheric columns of O_3 peak in the late spring, early summer (April through June), and have a minimum in the winter, consistent with longer daylight hours during the summer, allowing more photochemical production of tropospheric O_3 . Although the tendency towards a maximum in spring, rather than mid-summer implies that perhaps stratospheric O_3 intruding into the troposphere plays a significant role in the lower-troposphere O_3 concentrations.

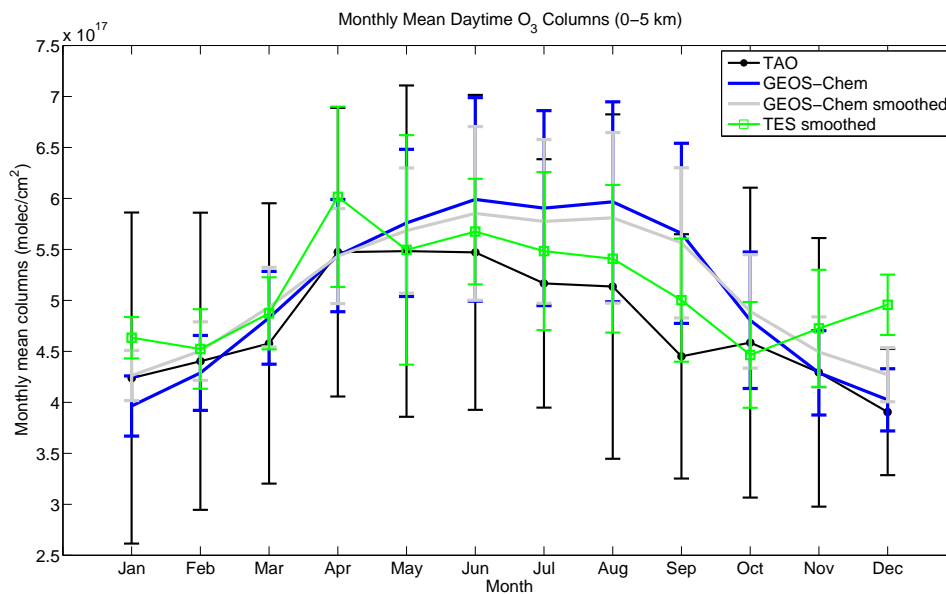


Figure 4.6: Climatological monthly mean O₃ 0-5 km partial columns over Toronto from TAO (2002-2013), GEOS-Chem (2002-2010), and TES (2004-2013). TES and GEOS-Chem profiles were smoothed with a median TAO averaging kernel. Error bars are the standard deviation of the monthly means.

4.4.2 MOPITT

MOPITT stands for Measurements of Pollution In The Troposphere, and it is an instrument flying on NASA’s Earth Observing System Terra spacecraft, measuring CO globally (www2.acd.ucar.edu/mopitt). It has been operational since March 2000, therefore the CO time series for MOPITT can be compared to the entire TAO dataset. Like Aura, the Terra satellite has a highly-inclined, polar, sun-synchronous orbit, which repeats itself every 16 days.

MOPITT is an infrared gas correlation radiometer. It observes in nadir mode with four CO thermal channels (at 2128 cm^{-1}) and two CO solar channels (at 4546 cm^{-1}). The MOPITT version 5 product combines its thermal infrared and near infrared (TIR/NIR) measurements to get more sensitivity to the lower troposphere and the surface [Deeter *et al.*, 2012]. MOPITT retrievals are done on a 10-layer pressure grid, and Figure 4.7 shows the median MOPITT averaging kernels for CO over the Toronto region. The 0-5 km levels peak at about 850 hPa ($\sim 1\text{ km}$), which is higher than where the TAO averaging kernels peak. We select level 2 data that are within 100 km of Toronto, and those with a cloud fraction ≤ 0.01 .

When TAO retrievals (0-5 km partial columns) are smoothed with MOPITT averaging kernels (since MOPITT has lower resolution than TAO for CO), and the two datasets are compared, there is a difference of 5% (using $(\text{TAO}-\text{MOPITT})/\text{TAO}\times 100\%$). Note, however, that, as with TES, two instruments with similar vertical resolution, but different vertical sensitivities are difficult to compare in this way, as both averaging kernels are not taken into account simultaneously. When monthly mean values are compared to those from TAO, we get good correlation ($R=0.88$ and slope of MOPITT vs. TAO=1.5) in the 0-5 km partial columns. Our results are consistent with Deeter *et al.* [2012], who found good agreement ($\sim 2\%$) for the MOPITT v5 lower tropospheric retrievals compared to tall-tower *in situ* measurements in the U.S.

The MOPITT total columns were biased about 14% high compared to smoothed TAO

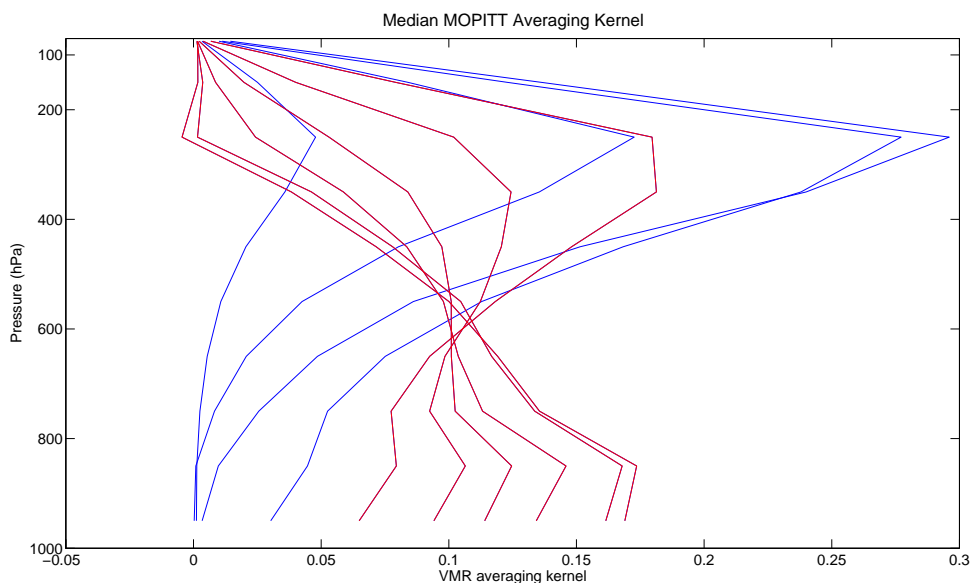


Figure 4.7: MOPITT median VMR averaging kernels for CO (2002–2010, within 1° of Toronto). Red lines indicate the 0-5 km levels.

total columns (Figure 4.8), and this may be due to a problem in the upper-troposphere, lower-stratosphere in the MOPITT v5 retrieval. This is also consistent with *Emmons et al.* [2009], who found a bias of 19% for the MOPITT v3 total columns in 2006 compared to aircraft measurements. Fortunately, for the purposes of our study, only the 0-5 km partial columns are used. The 2002 to 2013 MOPITT time series is discussed in Section 4.7.

4.5 Air quality measurements at the surface

The Environmental Monitoring and Reporting Branch of the Ontario Ministry of the Environment (MOE) operates 40 ambient surface air monitoring sites across Ontario, as part of the NAPS program. Each site measures a number of pollutants hourly. There are four sites in the Toronto region: Toronto West, Toronto North, Toronto East, and Downtown Toronto. The downtown Toronto site (located at Bay St and Wellesley St W.,

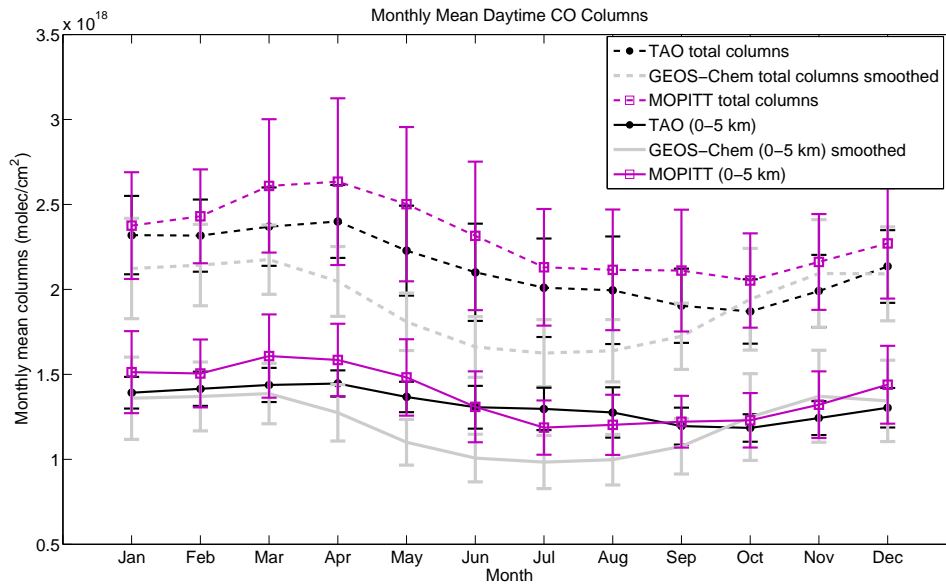


Figure 4.8: Monthly mean total and partial (0-5 km) column CO over Toronto from TAO, GEOS-Chem, and MOPITT. GEOS-Chem profiles were smoothed with a median TAO averaging kernel (TAO and MOPITT are both shown unsmoothed here). Error bars are the standard deviation of the monthly means.

site ID 31103) is nearest to TAO, so its O₃, CO, and NO_x measurements are used in this study.

Instruments used at the air monitoring sites are: Thermo Electron (TE)49C/I UV photometric ozone analyser for O₃, TE48C/I for CO, and TE42C/I for NO_x. For O₃, the instrument employs Beer's law (Equation 2.14) to relate UV absorption of O₃ at 254 nm directly to the concentration of O₃ in the sample air [Bauguitte, 2014]. For CO, the instrument is similar, however, it uses gas filter correlation to relate infrared absorption of CO at 4.6 μm to the concentration of CO in the sample air [Biraud, 2011]. For NO_x, the instrument employs the characteristic chemiluminescence produced by the reaction between NO and O₃, the intensity of which is proportional to the NO concentration. NO₂ measurements are approximated using its thermal reduction to NO by a heated (350°C) molybdenum converter [Bauguitte, 2014].

The errors on the pollutant concentrations are ± 3% [MOE Air Quality Office, personal communication]. Instrument precision is verified by daily automatic internal zero and span checks [MOE, 2013]. All these data were downloaded from the Ministry's air quality information system [www.airqualityontario.com/history/index.php]. The full time series of hourly surface O₃ and CO in downtown Toronto are shown in Figure 4.9(b) and (d), and the surface NO_x time series are shown for selected summers in Chapter 5.

4.6 Model description

GEOS-Chem [www.geos-chem.org] is a global 3D CTM driven by assimilated meteorological fields from the Goddard Earth Observing System (GEOS-4 for 2000-2003, GEOS-5 for 2004-2010) of the NASA Global Modeling and Assimilation Office (GMAO). The full chemistry simulation, first described in *Bey et al.* [2001b], includes NO_x-O_x-hydrocarbon tropospheric chemistry. The model includes more than 300 reactions with over 80 species.

We use version 8-03-02 of the model (as it was the most recent version running in the group that provided realistic global distributions of O_3 , CO, and C_2H_6), and employ the meteorological fields at a horizontal resolution of $2^\circ \times 2.5^\circ$, degraded from their native resolution of $1^\circ \times 1.25^\circ$ for GEOS-4 and $0.5^\circ \times 0.67^\circ$ for GEOS-5. The model has 47 (30) vertical layers in the GEOS-5 (GEOS-4) reduced grid, ranging from the surface to 0.01 hPa. We use the model output for the gridbox containing Toronto and Egbert 43.00° - 45.00° N by 78.75° - 81.25° W). To remove the influence of the initial conditions, we spun up the model for two years (2000–2001).

For selected time periods, we also ran v8-03-02 (with GEOS-5 meteorological fields) of the model at the native resolution ($0.5^\circ \times 0.667^\circ$) over North America, in nested mode, to evaluate pollutant concentrations in North America (more on this in Chapter 5). The nested resolution fields are only available for GEOS-5, which are from 2004 on.

Tracer advection is simulated numerically using the scheme by *Lin and Rood* [1996]. Wet and dry deposition are also simulated. Stratospheric chemistry is simplified in the model, using a linearized (LINOZ) O_3 scheme [*McLinden et al.*, 2000], where the change in stratospheric O_3 over time depends on temperature, O_3 concentrations, and the incident UV radiation field. N_2O oxidation in the stratosphere is parameterized, which provides an upper boundary condition for the transport of stratospheric NO_y down into the troposphere. There is transport of tropospheric chemicals to the stratosphere.

The GEOS-Chem anthropogenic emissions, (the primary source of tropospheric O_3 , CO and C_2H_6) come from the Emissions Database for Global Atmospheric Research (EDGAR), with the following exceptions: emissions in Mexico are based on the Big Bend Regional Aerosol and Visibility Observational (BRAVO) study emissions inventory, emissions in the United States are based on the Environmental Protection Agency (EPA) National Emission Inventory (NEI) 2005. Canadian emissions are based on the Canadian Emissions Inventory of Criteria Air Contaminants (CAC). European emissions are specified according to recommendations from the Co-operative Programme for

Monitoring and Evaluation of the Long-range Transmission of Air Pollutants in Europe (EMEP), and Asian emissions are from *Streets et al.* [2006].

Biomass burning emissions, the primary source of HCN and partial source of CO and C₂H₆, are specified based on monthly mean biomass burning emissions of CO from the Global Fire Emission Database version 3 (GFED3). Monthly mean biofuel emissions are based on *Yevich and Logan* [2003]. Monthly mean biogenic emissions are based on the Model of Emissions of Gases and Aerosols from Nature (MEGAN) inventory. Soil NO_x emissions are based on *Yienger and Levy III* [1995].

CO, C₂H₆ and to a lesser extent, HCN, are lost through reaction with OH in the atmosphere. In the model, we use specified OH fields from a full-chemistry model simulation (v5-07-08 for 2°x2.5° [*Li et al.*, 2009] and v8-02-01 for nested resolution). The full chemistry simulation calculates the OH fields online, however, these archived OH fields are used because they were able to reproduce observed methychloroform lifetimes (a measure of whether modelled OH is accurate), whereas OH from later modelled versions were biased high.

4.6.1 Tagged simulations

There are also offline tagged simulations that can be run in GEOS-Chem for O_x, CO, C₂H₆, HCN, and even CH₄. These simulations use linearized chemistry and allow the pollutant concentrations to be traced back to user-defined geographical source regions and/or emission types. Tagged runs of C₂H₆ and CH₄ are beyond the scope of this thesis, though are suggested for future work (Section 5.8.2). During the course of this research, I have run tagged O_x, CO, and HCN simulations (v8-02-01, v8-03-02, and v9-01-02), however, those results will not be used for the following reasons. The HCN simulation needs improvement, and doing so is beyond the scope of this thesis. However, we have contributed our HCN simulation (v8-02-01, with updates from Q. Li) to a publication by *Vigouroux et al.* [2012]. The tagged CO simulation also needs improvement. In version

8-02-01 and 9-01-02, the seasonal cycles were not simulated properly, and the column concentrations were too low. In version 9-01-02, this was later traced to a compiler issue causing numerical computation problems, and in version 8-02-01, it may have been due to incorrect OH concentrations [Bey *et al.*, 2001a; Fisher *et al.*, 2010]. The tagged O_x simulation results in a good comparison to TAO O₃ because it employs O₃ production and loss rates from the full chemistry simulation, which agrees well with the data (Section 4.7). However, for the purposes of source attribution, we find the model adjoint to be more useful, and this is discussed in Chapter 5, Section 5.3.

4.6.2 Smoothing the model

When GEOS-Chem total or partial columns are compared to FTIR measurements, their profiles are first smoothed with a median averaging kernel from TAO (Equation 4.9) [Rodgers and Connor, 2003]:

$$\hat{\mathbf{x}}_m = \mathbf{x}_a + \mathbf{A}(\mathbf{x}_m - \mathbf{x}_a), \quad (4.9)$$

where \hat{x}_m is the smoothed GEOS-Chem profile, \mathbf{x}_a is the TAO a priori profile, \mathbf{A} is the median TAO averaging kernel (over 2002-2013), and \mathbf{x}_m is the original GEOS-Chem profile. This takes into account the lack of vertical resolution in the measurements, the bias introduced by the a priori profile, and the vertical sensitivity, and results in a version of the model output as though it were measured with the TAO FTS.

4.7 Data and model comparisons

The full tropospheric time series are shown in Figure 4.9: (a) 0-5 km partial columns of O₃ from TAO, CARE, TES, and GEOS-Chem, (b) surface O₃ from MOE and GEOS-Chem, (c) 0-5 km partial columns of CO from TAO, CARE, MOPITT, and GEOS-Chem, (d) surface CO from MOE and GEOS-Chem, (e) total columns of C₂H₆ from TAO, CARE,

and GEOS-Chem, and (f) total columns of HCN from TAO and CARE. All of the datasets and model output generally agree well. Each modelled species is discussed in more detail below.

4.7.1 Ozone

Figures 4.10 and 4.11 plot the O₃ datasets and model output against each other, including surface measurements versus tropospheric column measurements. Figure 4.10(a) shows that the surface measurements are modestly correlated with the TAO tropospheric O₃ columns, with an overall correlation coefficient (R) of 0.39. The correlation between surface concentrations and O₃ columns in the GEOS-Chem model is better, with R=0.78 (shown in Section 5.2.2). The seasons are shown in different colours, and the highest correlation for O₃ surface vs. TAO lower-tropospheric column is in the summer, when O₃ air quality is an issue, followed by fall, then spring, then winter. This seasonal sequence of correlation strength is the same in the model, though the values are higher. We begin to see how FTIR columns can be useful for assessing air quality.

Figure 4.10 also shows how GEOS-Chem (2°x2.5°) captures Toronto surface¹ (b) and lower-tropospheric column (c) O₃ well. The R values are 0.67 for the surface and 0.36 for the columns. The modelled O₃ is about 5% greater than the measured (0-5 km) columns, and the measured columns are more scattered than the model (Figure 4.9(a)), as is often the case in measurement-model comparisons. This scatter is reduced when the monthly means are compared: Figure 4.11 shows the GEOS-Chem vs. TAO monthly means, which have R=0.86, and a slope very close to 1. The seasonal cycle of O₃ (0-5 km) columns is different in the model (Figure 4.6), with the maximum in GEOS-Chem occurring more in the summer than the spring. Note that the monthly mean for GEOS-Chem was calculated using only daytime measurements for a more appropriate comparison to FTIR.

¹Hourly surface data averaged every 3 hours for comparison to GEOS-Chem output, which is 3-hourly.

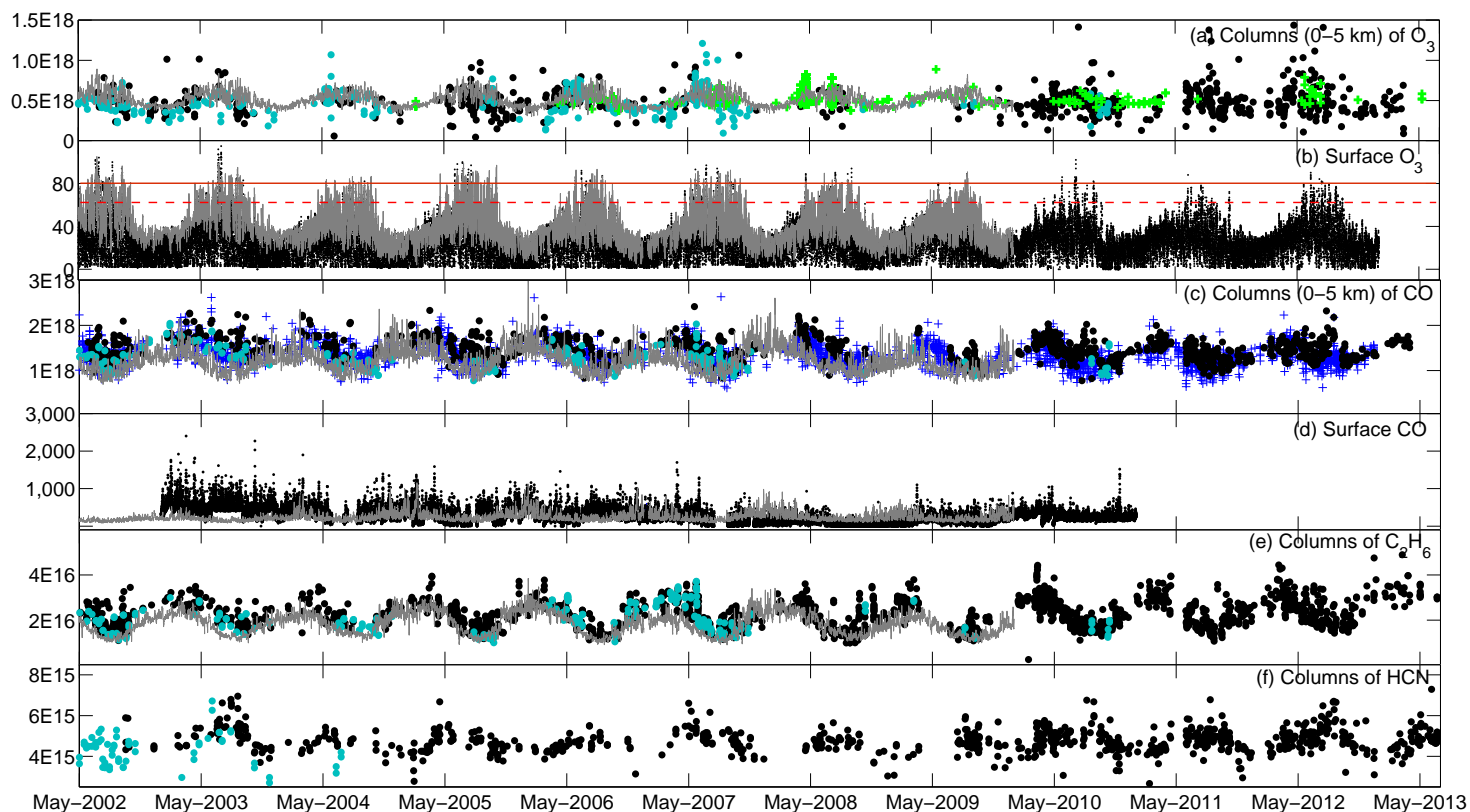


Figure 4.9: Toronto-area tropospheric time series. The smoothed GEOS-Chem model output is shown by the grey lines in panels (a)-(e). (a) Tropospheric columns of O_3 in molecules/ cm^2 (TAO=black, CARE=cyan, TES=green crosses), (b) surface O_3 in ppb (black), and red lines represent the air quality criteria (1-hour is solid, and 8-hour is dashed), (c) Tropospheric columns of CO in molecules/ cm^2 (TAO=black, CARE=cyan, and MOPITT=blue crosses), (d) surface CO in ppb (black), (e) total columns of C_2H_6 in molecules/ cm^2 (TAO=black, CARE=cyan), and (f) total columns of HCN in molecules/ cm^2 (TAO=black, CARE=cyan).

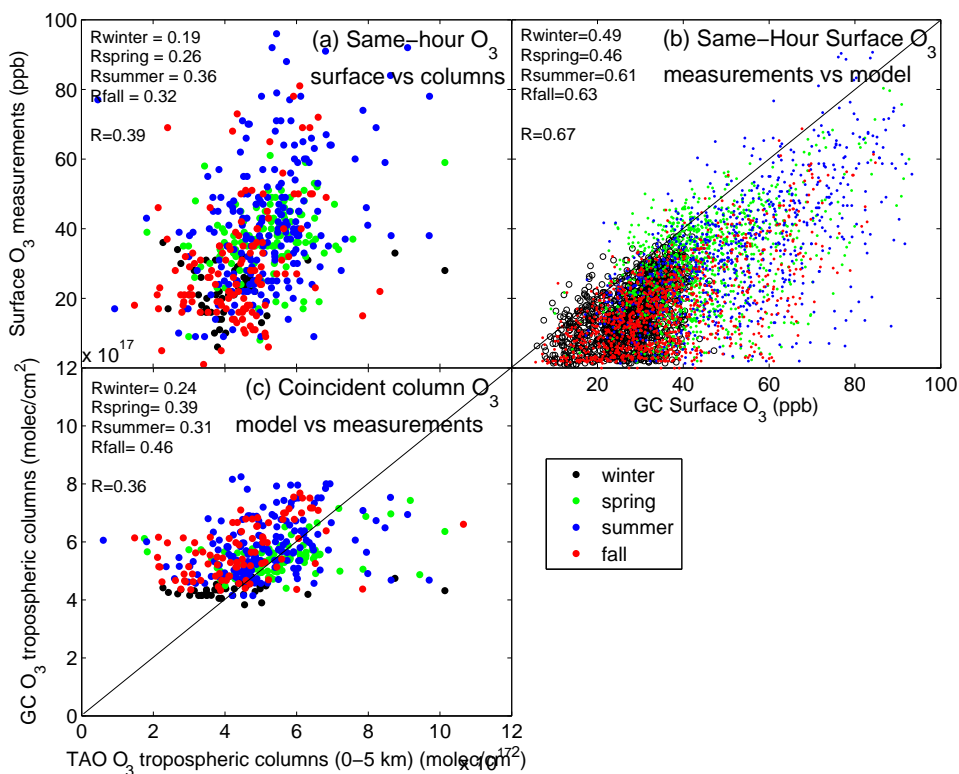


Figure 4.10: (a) Same-hour surface vs. (0–5 km) column O₃ measurements. (b) Same-hour three-hour mean surface O₃ measurements vs. GEOS-Chem (GC) surface O₃ (one-to-one line shown). (c) Coincident (closest-in-time) tropospheric O₃ columns: GEOS-Chem smoothed vs. TAO measurements (one-to-one line shown). Different colours are for the different seasons, and correlation coefficients (R) are listed for each case.

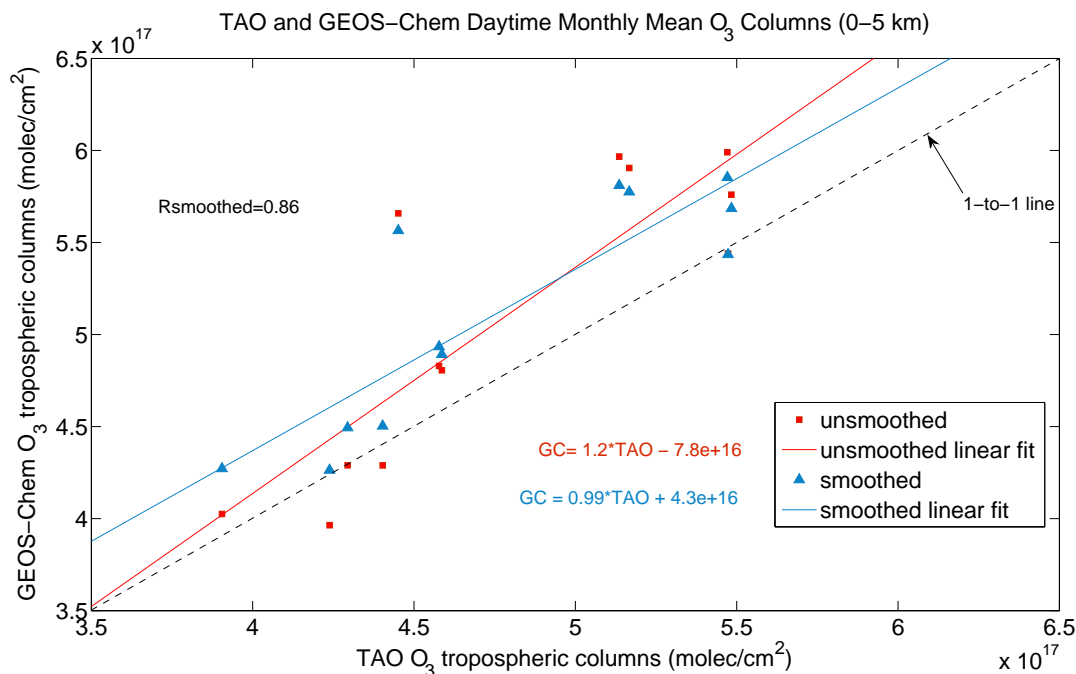


Figure 4.11: Monthly mean Toronto O₃ partial columns from GEOS-Chem (GC, smoothed and unsmoothed) versus those from TAO.

4.7.2 Carbon monoxide

The measured surface-column correlation (Figure 4.12(a)) is poorer for CO, with $R=0.26$ overall, and the best correlation occurring in the fall ($R=0.50$). GEOS-Chem does a poorer job of simulating surface (b) and column (c) CO. The correlation coefficients are 0.11 for surface and 0.31 for columns. The poor correlation with surface measurements is likely because of the $2^\circ \times 2.5^\circ$ resolution of the model not representing a point-measurement at the surface in downtown Toronto. GEOS-Chem tropospheric columns of CO are biased low relative to FTIR measurements by a mean of 27%, and the seasonal minima and maxima come a month or two earlier than those of the FTIR measurements. The monthly means of the model are shown in Figure 4.8, and the model monthly means are correlated to the TAO monthly means with $R=0.47$ (Figure 4.13).

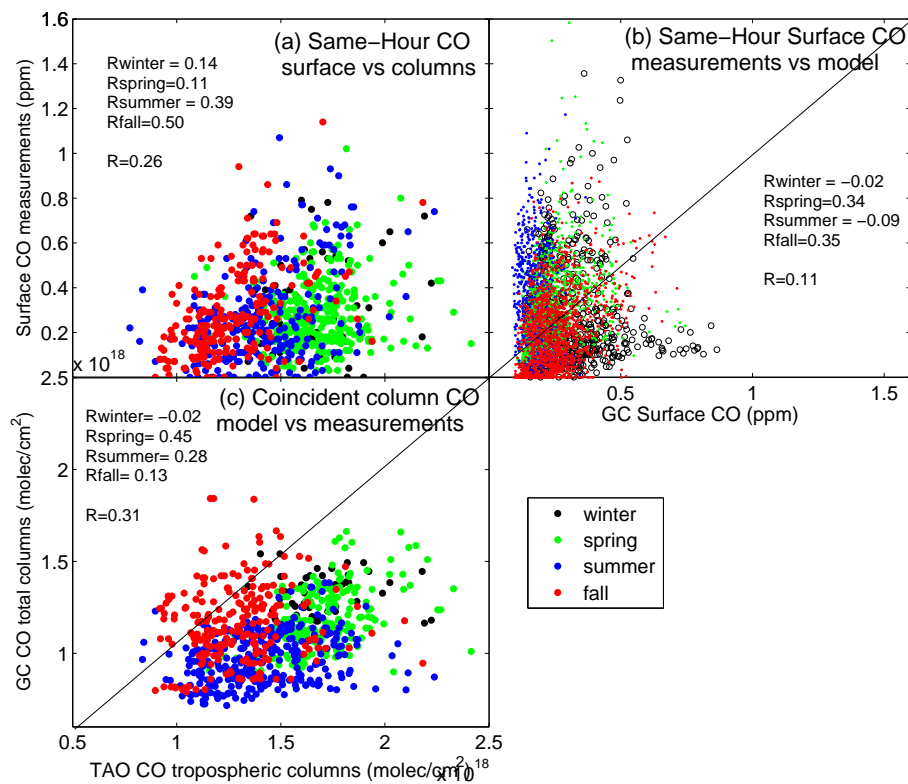


Figure 4.12: (a) Same-hour surface vs. column CO measurements. (b) Same-hour three-hour mean surface CO measurements vs. GEOS-Chem (GC) surface CO (one-to-one line shown). (c) Coincident (closest-in-time) tropospheric CO columns: GEOS-Chem smoothed vs. TAO measurements (one-to-one line shown). Different colours are for the different seasons, and correlation coefficients (R) are listed for each case.

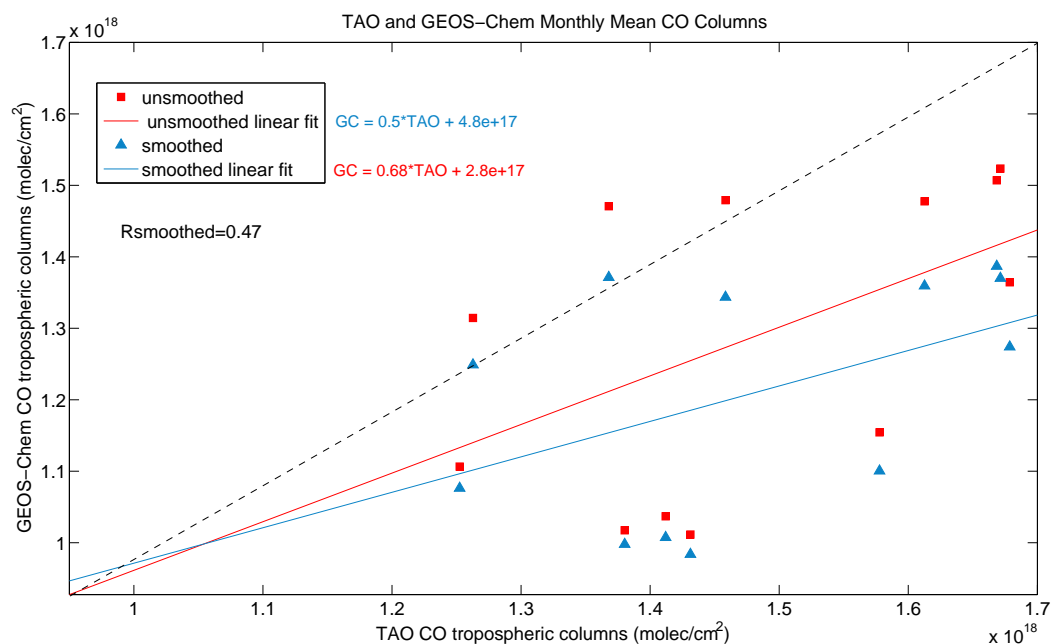


Figure 4.13: Monthly mean Toronto CO partial columns from GEOS-Chem (GC, smoothed and unsmoothed) versus those from TAO.

4.7.3 Ethane

Figure 4.9(e) shows that the agreement between GEOS-Chem and FTIR C₂H₆ total columns is good, though GEOS-Chem is lower on average by 19.2%. The total errors on the C₂H₆ FTIR measurements is about 10%. GEOS-Chem simulates the seasonality well. The correlation coefficient is 0.65 overall, and the best seasonal correlation is in the summer (R=0.52, Figure 4.14), which is good for this study which focusses on summertime pollution (see Chapter 5). The slope of GEOS-Chem vs. TAO C₂H₆ is 0.65 (Figure 4.14). The C₂H₆ total columns from model and measurements will provide additional information on pollution events in the next chapter.

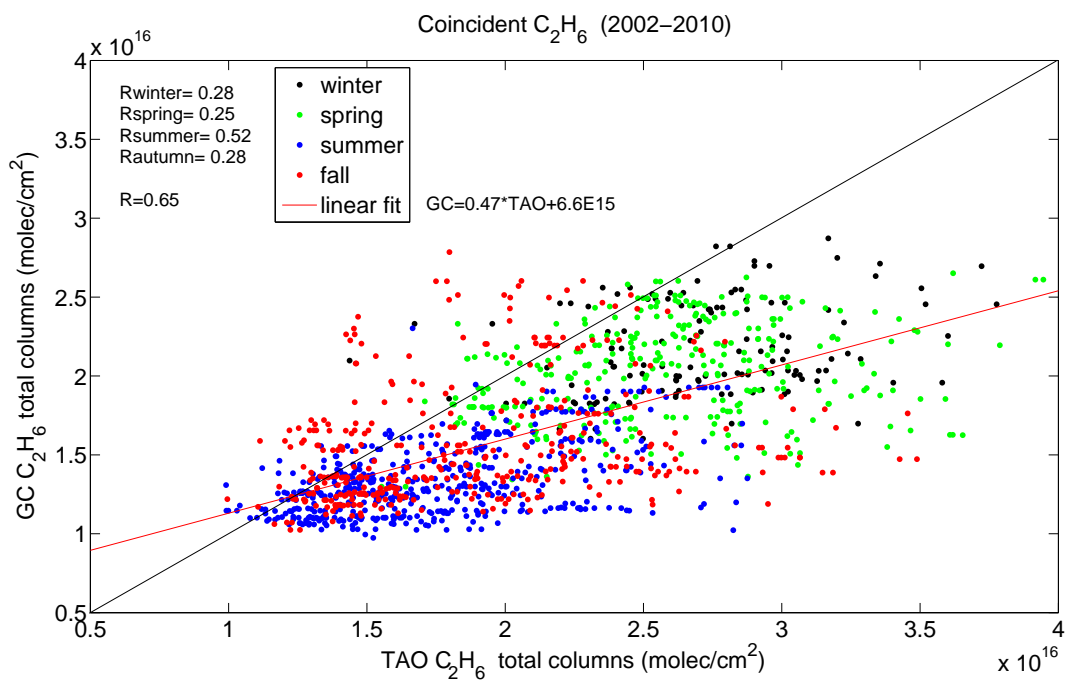


Figure 4.14: Toronto C_2H_6 total columns from GEOS-Chem (GC, smoothed) versus those from TAO.

Chapter 5

Interpretation of TAO tropospheric variability: identifying and quantifying Toronto pollution sources

The previous chapter presented the eleven-year time series of tropospheric species over Toronto, and showed how GEOS-Chem compares with the measurements of O_3 , CO, and C_2H_6 . In this chapter we use meteorology, the GEOS-Chem adjoint, and back-trajectory calculations to determine the sources of pollution episodes found in both the lower-tropospheric columns and the surface data. In this way, we show how FTIR column measurements are useful for air quality studies, and the important sources of Toronto O_3 pollution for selected case studies are identified. First we start with some background on regional air quality.

5.1 Background: O₃ air pollution in eastern North America

Surface O₃ pollution is highly correlated with high temperatures. Not only do higher temperatures increase the rates of the reactions that create O₃, but high temperatures are often associated with high-pressure systems. *Vukovich et al.* [1977], *Logan* [1989] and *Vukovich* [1995] have shown that the descending air in high-pressure systems traps the pollutants that make O₃ in the boundary layer, thus high surface-O₃ values are correlated with high-pressure systems. High-pressure systems also usually have clear skies, enhancing the photolysis of NO₂ (Reaction 4.3 in Chapter 4).

O₃ pollution events in southern Ontario and the northeast U.S. are typically associated with the development of a high-pressure, anticyclone system in central Canada that moves eastward, either south into the midwest U.S. or across the Great Lakes and then eastward where it passes over Toronto [*Zishka and Smith*, 1980; *Yap et al.*, 2005]. Along the way, pollutants accumulate (circulating clockwise) and create O₃. The pollution episode dissipates when a low-pressure system follows and ventilates the pollution out of the boundary layer, and/or causes precipitation to remove a lot of the pollutants. Additionally, *Zhu and Liang* [2012] have shown that the westward extent of the Bermuda High (a semi-permanent system over the Atlantic Ocean) has a large effect on air quality in the northeastern U.S. (and by extension, southern Ontario as well). When the system is very large or positioned to the west, the air circulating clockwise on its west side brings clean ocean air to the southeast U.S., but by the time it reaches the northeast U.S. it has accumulated a large amount of isoprene (a VOC) and anthropogenic pollutants, which create O₃.

A study of Toronto's surface O₃ in the summer of 1998, on O₃-exceedance days, attributed only 9% to Ontario emissions, and the rest to transboundary transport of pollutants [*Yap et al.*, 2005]. Fortunately, in the U.S. the air quality policies such as the

Clean Air Act, the EPA's State Implementation Plan (known as the "NO_x SIP Call" program, which was a NO_x emissions trading program among 22 eastern states from 2003 to 2008), the Clean Air Interstate Rule (CAIR), and the Tier 2 Light Duty Vehicle Emission Standards [EPA, 2012] have caused NO_x emissions to be reduced by industries and transportation at a rate of about 2-3%/year [Gilliland *et al.*, 2008; Godowitch *et al.*, 2010; EPA, 2012; Zhou *et al.*, 2013]. In Canada, air quality policies, such as the Industry Emission Reduction Program (ERP, also a cap and trade NO_x program), the phase-out of coal power plants in Ontario, and Ontario's Drive Clean Program [Yap *et al.*, 2005] have also caused NO_x emission reductions in Ontario at a rate of 3.6%/year [MOE, 2013]. There was also the Canada-U.S. Air Quality Agreement in 1991 that was initially intended to address acid rain, but was amended to include an Ozone Annex in 2000 [Yap *et al.*, 2005]. The result is that the number of high-O₃ days has been dramatically reduced in both the eastern U.S. and Canada.

That said, air quality is an issue that remains. Mean surface O₃ in Toronto increased at 4.2%/year from 1991-2011 [MOE, 2013], and air quality is expected get worse with climate change [Leibensperger *et al.*, 2008; Jacob and Winner, 2009; Millstein and Harley, 2009]. Not only will global warming increase surface temperatures, it is expected to reduce the number of cyclones (low-pressure systems) that remove O₃ air pollution, and shift the cyclones poleward [Leibensperger *et al.*, 2008]. Also background O₃ caused by hemispheric anthropogenic emissions of NO_x and VOCs is increasing [Fiore *et al.*, 2002; Zhang *et al.*, 2011], thus resulting in larger O₃ tropospheric columns and surface concentrations. Therefore, NO_x emissions will have to be further reduced to maintain good air quality. In fact, the best air quality policy would be one that is tied to a strong climate change policy.

5.2 How does Toronto pollution vary with wind direction?

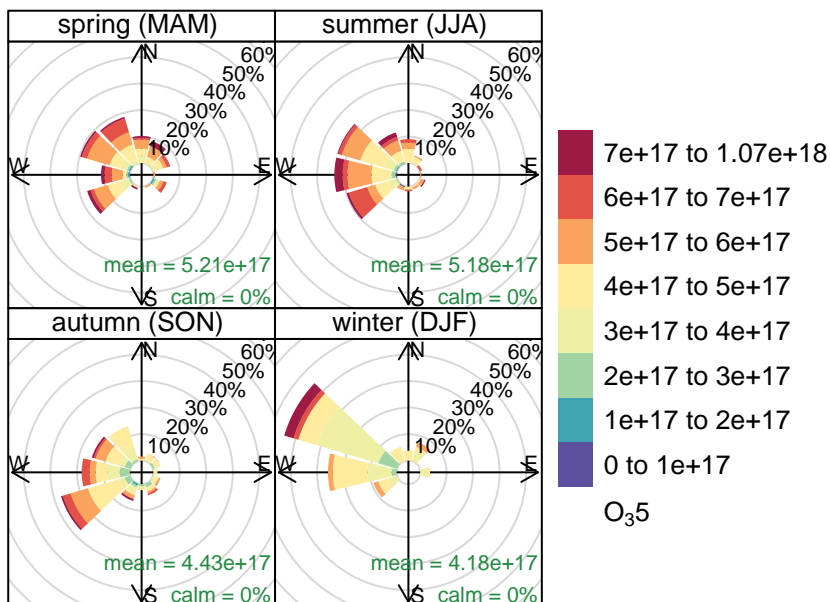
We will begin to explore the causes of short-term variability in the TAO tropospheric time series by showing how tropospheric O_3 and CO vary with wind direction. To determine wind direction, the GEOS-4 and GEOS-5 wind fields were used. The winds in the $2^\circ \times 2.5^\circ$ Toronto grid box were averaged from 0.2 to 2 km in height, every 3 hours, and the ones that were closest in time to the TAO or surface observation were taken.

5.2.1 Pollution roses

Pollution roses show the concentrations of CO and O_3 as a circular histogram, where the direction of each bar corresponds to the wind direction. Figures 5.1 to 5.4 show the pollution roses for tropospheric and surface O_3 and CO, separated out by season to remove the effects of the seasonal cycles.

Figure 5.1 shows the tropospheric (0-5 km) O_3 columns by wind direction. We see the highest values in the summer, and the lowest values in the winter. We see that overall, the bars are greatest in the westerly direction, and smallest in the south-easterly quadrant, implying that most of the time, Toronto's air is transported from the northwest (across the Great Lakes), west (across northern Michigan), and southwest (across industrial areas such as Ohio, south Michigan (including Detroit), and southern Ontario (including the Nanticoke power plant, and Hamilton). While high values of O_3 ($>$ the mean) come from all directions, unsurprisingly, in the summer, tropospheric O_3 has higher values more often coming from the southwest (that is, a larger fraction of high values to low values) and lower values more often coming from the northwest. This is consistent with a study of Toronto surface O_3 by *Geddes et al.* [2009], and the same is true in the winter¹

¹Although there are still high values coming from the northwest in the winter, but the *fraction* of low- O_3 columns from that direction is much greater than from

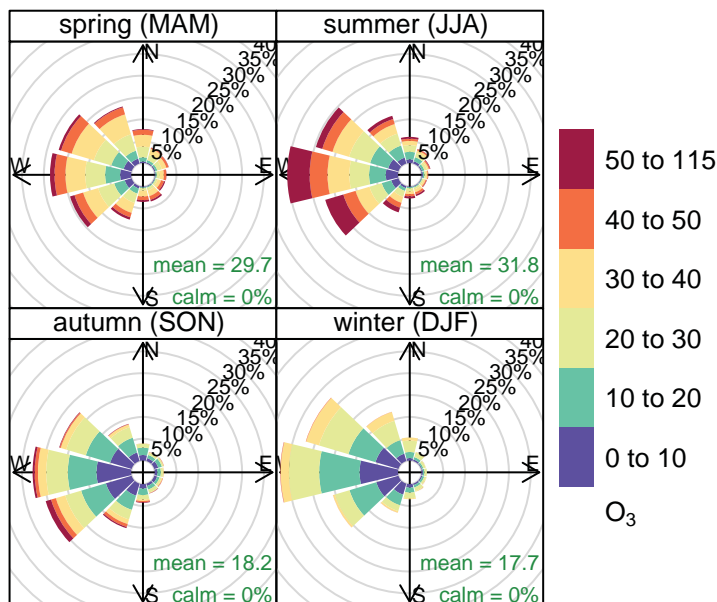


Frequency of counts by wind direction (%)

Figure 5.1: Pollution rose for 2002-2013 TAO tropospheric O₃ (0-5 km) in molecules/cm², using GEOS-4 and GEOS-5 wind fields. Means of the O₃ columns for each season are given.

the southwest direction and the fall, however not so for the spring. The source of high O₃ values coming from the northwest in the spring may be related to stratospheric O₃ intrusions, as spring is when downward transport of stratospheric O₃ is at a maximum. Tagged O₃ simulations that were run (results not shown) confirm a stratospheric source in the 0-5 km partial columns of $0.5-1.5 \times 10^{17}$ molecules/cm² during March and April.

Figure 5.2 shows the surface O₃ concentrations by wind direction. Similar to the O₃ tropospheric columns, we see the highest values in the summer, and lowest in the winter. The surface measurements have much greater density than the FTIR measurements, so it is good to confirm that overall, the size of the bars in each direction is similar – meaning that with the TAO FTS we sample a representative fraction of the true wind direction frequencies. This is especially true for the summer, but not really in the winter because in the winter, we have fewer O₃ measurements and thus, do not have enough measurements



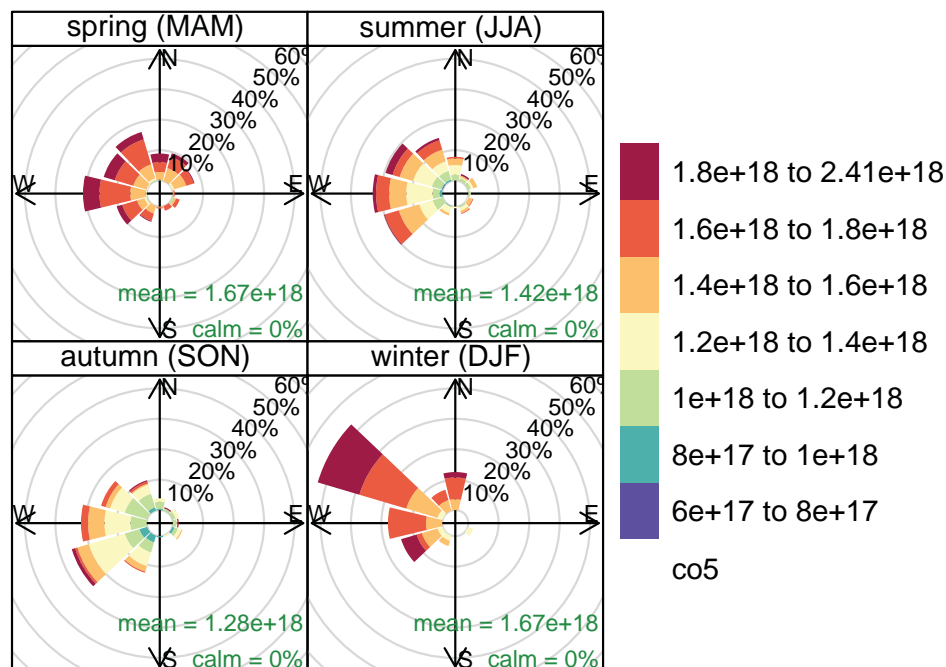
Frequency of counts by wind direction (%)

Figure 5.2: Pollution rose for 2002-2011 surface O₃ in ppb, using GEOS-4 and GEOS-5 wind fields. Means of the O₃ VMRs for each season are given.

to sample the wind direction distribution properly.

Like the lower-tropospheric columns, the surface O₃ also has high values coming from most wind directions, but the fraction of high O₃ values is greater for the southwest direction (again, consistent with *Geddes et al.* [2009]) compared to the northwest direction in the summer and fall. In the winter and spring, it is difficult to see any difference in the O₃ distribution by direction (Figure 5.2).

Figures 5.3 and 5.4 show the tropospheric CO columns and surface CO concentrations by wind direction, respectively. By comparing the two figures, again, we see that in all seasons, except for winter, that TAO measurements sample the true wind direction distribution. The highest values of column CO are in the winter, and lowest values are in the fall, whereas for surface CO, winter values are only slightly greater than the VMRs in the other seasons. For surface CO, there is a slightly larger fraction of high CO concentrations from the west and southwest directions, though the difference is

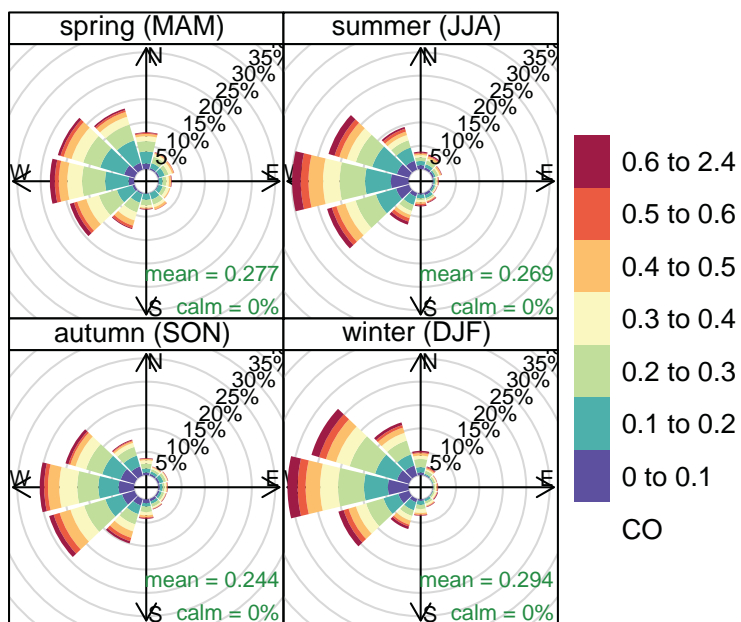


Frequency of counts by wind direction (%)

Figure 5.3: Pollution rose for 2002-2013 TAO tropospheric CO (0-5 km) in molecules/cm², using GEOS-4 and GEOS-5 wind fields. Means of the CO columns for each season are given.

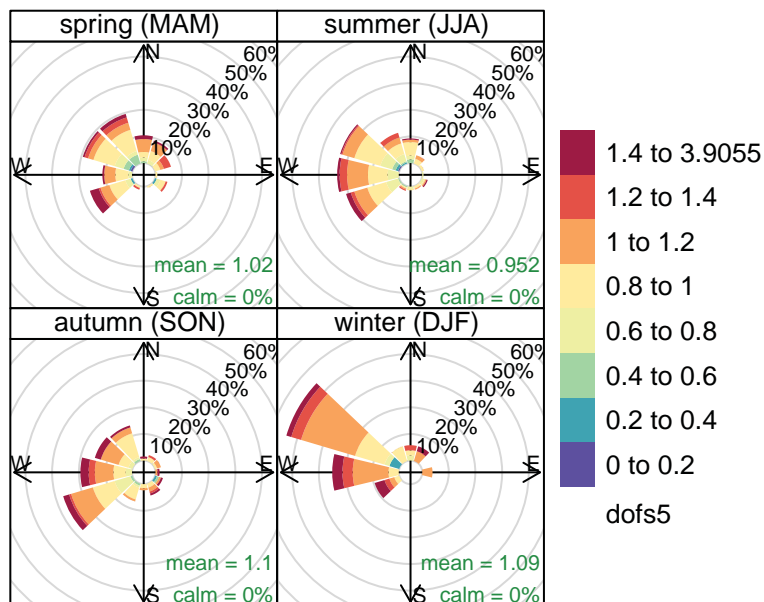
small, implying that surface CO concentrations are probably dominated by local sources, whereas the CO columns (in all seasons) are more frequently greater when the air is coming from the north and northwest directions. This directionality is consistent with the latitudinal gradient in CO, and also has two likely explanations: 1. Northern air is more likely to have biomass burning as a source of high CO concentrations, and 2. CO is lost through oxidation by OH, and there is more OH at lower latitudes than higher latitudes [Spivakovsky *et al.*, 2000].

What is also interesting to note, is that the FTIR sensitivity, given by the DOFS, increases for some wind directions. This is especially true for O₃, possibly because there is more tropospheric O₃ coming from those directions. Figure 5.5, summer panel, shows



Frequency of counts by wind direction (%)

Figure 5.4: Pollution rose for 2002-2011 surface CO in ppm, using GEOS-4 and GEOS-5 wind fields. Means of the CO VMRs for each season are given.



Frequency of counts by wind direction (%)

Figure 5.5: DOFS rose for 2002-2013 TAO tropospheric O₃ columns (unitless), using GEOS-4 and GEOS-5 wind fields. Means of the DOFS for each season are given.

that the DOFS of the TAO retrievals are higher when air comes from the southwest and west, rather than from the northwest. Presumably this is because there is more O₃ coming from the U.S., and when there is more O₃, the solar absorption lines are stronger and contain more information.

5.2.2 Wind direction bins

After considering the pollution roses, and the location of Toronto, it becomes clear that the winds can be grouped into three regions, transporting very different kinds of air (see Figure 5.6. Map from www.geographicguide.com): (1) *From Canada*, where we would expect the air to be relatively clean because it would be passing over the Great Lakes, or from northern Ontario. It may, however, be more polluted if it carries a biomass burning plume, or if it comes from southern Ontario or Quebec. (2) *From the west*, where we



Figure 5.6: North American map showing the three wind bins used to sort the O_3 and CO data.

would expect the air to be more polluted as it would be passing over Chicago, Detroit, and/or Hamilton, which are major industrial cities. (3) *From the southeast*, from where we would expect the most polluted air, as it encompasses the most densely populated part the U.S. (the northeast), the industry of the Ohio Valley, and the VOC emissions from the southeast U.S., which, while natural, still contribute to O_3 production.

If we bin the FTIR measurements into these three wind directions, 46% come from Canada, 33% come from the west, and 21% come from the southeast. These percentages will be compared later in the chapter for FTIR measurements that are considered “pollution events” (Section 5.5.2).

O₃-CO correlations

The O₃-CO correlation can reflect the strength of O₃ photochemical production. We expect that Toronto CO and O₃ tropospheric columns would have the best correlation in the most polluted wind bin (from southeast), because these two species have similar anthropogenic sources (fossil fuel combustion), but different natural sources (biomass burning for CO, stratosphere and lightning for O₃). Positive CO-O₃ correlations have been reported for polluted regions in the summertime by *Chin et al.* [1994]; *Hudman et al.* [2009]; *Voulgarakis et al.* [2011] and *Mao et al.* [2013] for example. However, the lifetimes of O₃ and CO are different, and O₃ is not directly emitted like CO is. Therefore, O₃-CO correlations are usually interpreted in the context of the age of the plume. We have not isolated aged air for our study, however, we have plotted same-day TAO CO vs O₃ tropospheric columns, which have been “deseasonalized” (by subtracting the monthly medians) to remove the effect of the seasonal cycles of these two species (Figure 5.7). The resulting correlation coefficients are R=0.47 for the from southeast bin (Figure 5.7(b)), R=0.31 for the from west bin (d), and R=0.05 for the from Canada bin (c), which are ordered as predicted.

O₃-CO correlations in the literature are mixed. At the high end, *Chin et al.* [1994] found correlation coefficient of R=0.4-0.9 in the northeast U.S. using summertime surface measurements. At the low end, a global TES study found correlation coefficients of R=0-0.2 for the southern Ontario region in the summer [*Voulgarakis et al.*, 2011], and this is consistent with the overall summertime correlation of R=0.01. In the winter, the correlations are often negative, as the higher NO_x concentrations can titrate O₃, but leave high CO [e.g., *Parrish et al.*, 1998; *Voulgarakis et al.*, 2011]. The correlations in the winter are positive, except in the from Canada bin, for which we don’t expect very high NO_x conditions. Therefore, our values are inconsistent with the literature for winter. However, the number of FTIR measurements in the winter is very low, so the FTIR dataset probably does not have enough measurements for good statistics. In the spring,

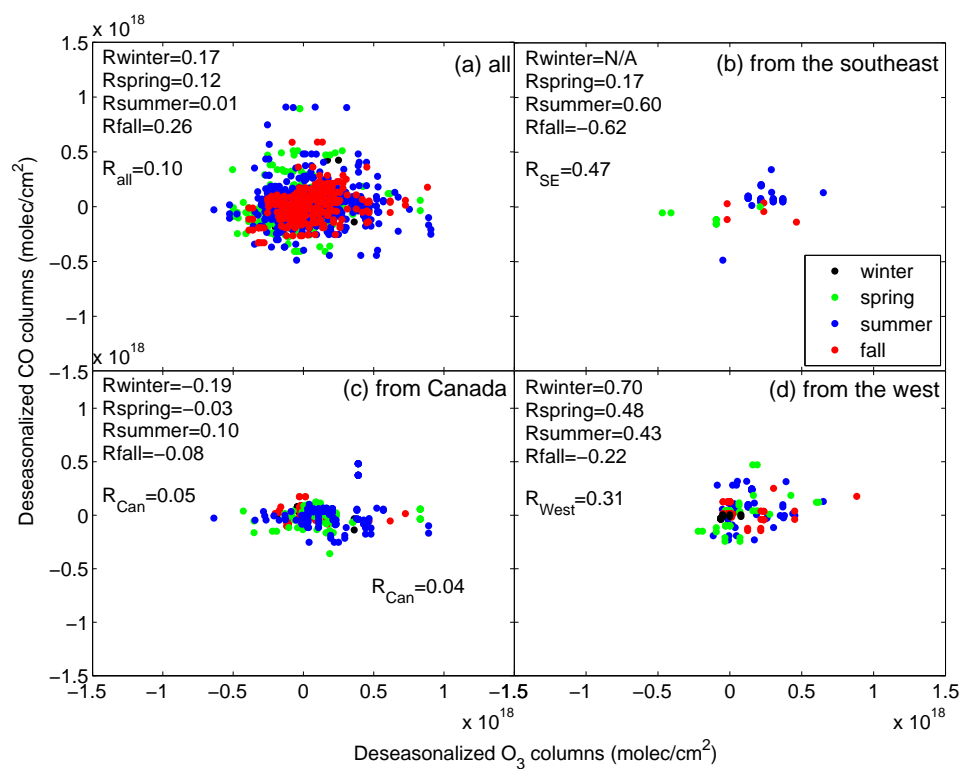


Figure 5.7: Deseasonalized TAO tropospheric columns of CO vs. O₃: (a) all data, and separated into three wind bins: (b) from the southeast, (c) from Canada, and (d) from the west.

the correlations can be negative because of stratospheric intrusions bringing O₃-rich, and CO-poor air into the troposphere [Parrish *et al.*, 1998; Voulgarakis *et al.*, 2011]. Again, only the from Canada bin has a negative correlation for the springtime measurements (Figure 5.7).

Surface-column correlations revisited

In Chapter 4, Figure 4.10(a) showed the correlation between surface and tropospheric column measurements of O₃. In Viatte *et al.* [2011], ground-based FTIR O₃ measurements were qualitatively compared to surface *in situ* measurements, and the results were promising for using FTIR for air quality studies, as two pollution events over Paris, France were found in both datasets in the summer of 2009. We now take a closer look at the column-surface correlations by separating the data by wind direction bins. The result is that the best correlation between surface and column O₃ comes from the west bin (R=0.45, Figure 5.8), followed by the southeast bin (R=0.38). Given that air transported from remote northern regions is less influenced by surface anthropogenic emissions, and more influenced by high-altitude sources such as the stratosphere, lightning, and biomass burning, it makes sense that the surface and column concentrations are not as well-correlated in the from Canada bin (R=0.27). However, air transported from industrial or populated regions would have been exposed to more surface anthropogenic emissions, so it makes sense that the surface and column concentrations would be better correlated in these bins.

Overall (using data from 2002-2010), the correlation between surface and column O₃ is greatest in the summer (R=0.36, Figure 5.8(a)), however, the southeast (b), and west (d) bins have higher correlations in the spring and fall than they do in the summer. It is not clear why that is the case. Nor is it clear why the summer correlation is the best for the from Canada bin. The answer may simply be that the number of data points is too small when the measurements are separated both by three wind bins *and* seasons.

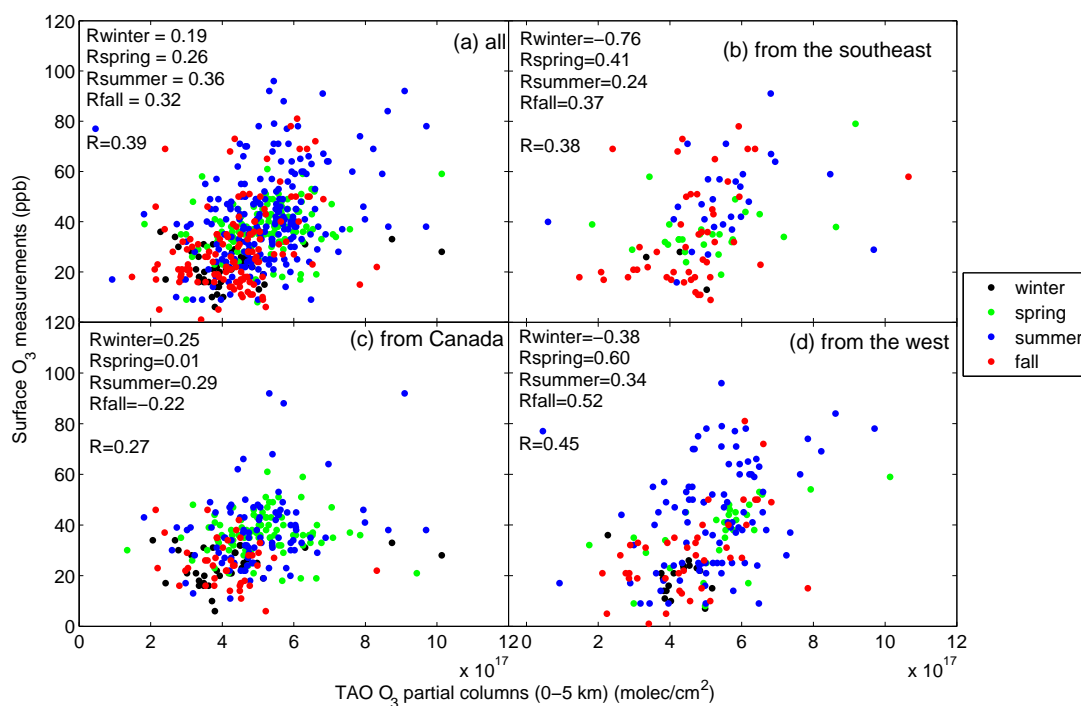


Figure 5.8: Toronto surface O₃ vs. TAO lower-tropospheric O₃ (a) overall (2002-2010), and separated into three wind bins: (b) from the southeast, (c) from Canada, and (d) from the west. Different colours are shown for the four seasons.

Therefore, I tested the surface-column correlations using all of the GEOS-Chem model output, and found some similarities and differences in the seasonal and directional correlations (Figure 5.9). The sequence of correlation strength by wind direction is same in the model as in the measurements (from west has the highest R value, followed by from the southeast, and from Canada). However, in the model, the correlation coefficient is highest in the summertime in the from southeast and from west bins (unlike for the measurements). The correlation coefficient is also highest in the summer from Canada, and this is consistent with the measurements (Figure 5.9).

The GEOS-Chem model adjoint, described in the next section, is now used, as it is the most efficient means to determine the sources of the high values of O₃ and CO measurements.

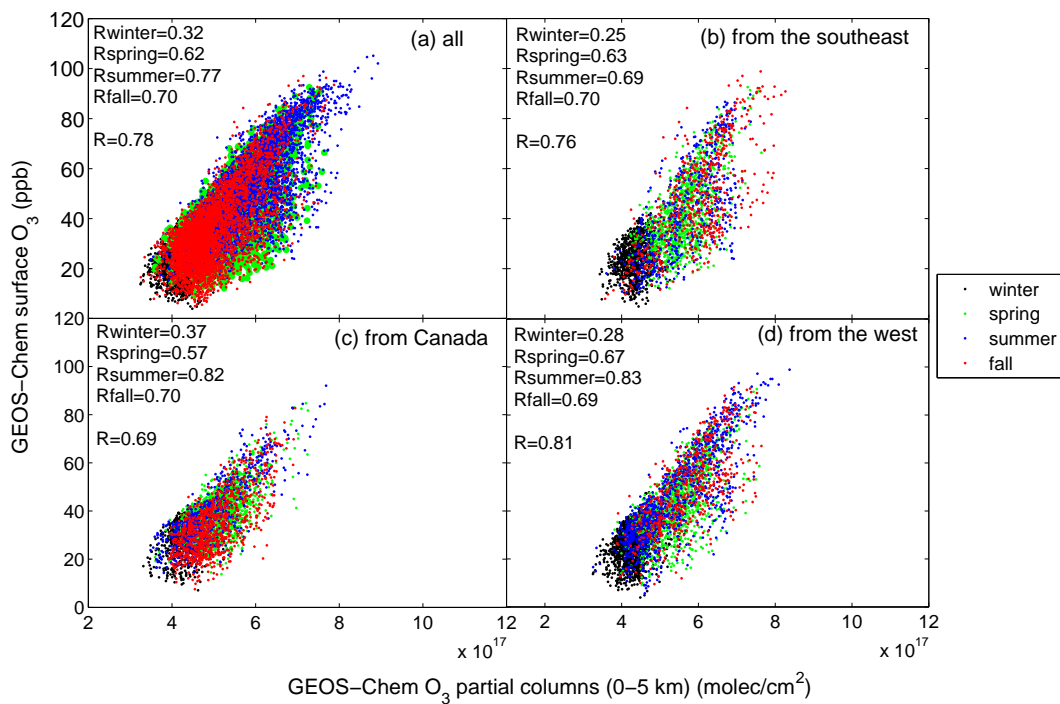


Figure 5.9: Same as Figure 5.8, but from GEOS-Chem model output.

5.3 Model adjoint description

The GEOS-Chem adjoint model was initially described in *Henze et al.* [2007]. The current adjoint version, v35, which we run at the North American nested resolution ($0.5^\circ \times 0.67^\circ$, available for 2004 on), is based on the GEOS-Chem forward model, version v8-02-01, but is updated in parallel with the forward model. The adjoint allows efficient calculation of the gradients of the model outputs (e.g., concentrations) to the model inputs (e.g., emissions, p_a), which is a measure of the sensitivity of the outputs to the inputs.

For example, we define the cost function (J), as the modelled O_3 (or CO) from 0 to 5 km in the Toronto grid box, on the day and hour that the pollution event was observed in the column. Note that this is not the traditional definition of a cost function, which typically minimizes the difference between a model and measurement. However, the term “cost function” stems from the GEOS-Chem adjoint’s use in data assimilation, and it is common in the literature to also use “cost function” to represent model predictions in sensitivity studies [e.g., *Henze et al.*, 2007; *Paulot et al.*, 2012; *Parrington et al.*, 2012; *Walker et al.*, 2012; *Lee et al.*, 2014]. The adjoint then computes the change in the cost function with respect to a change in the unitless emissions scale factor ($s=p/p_a$) in each North American grid box. We then use the semi-normalized sensitivities (λ), which are the gradients, divided by the cost function:

$$\lambda = \frac{1}{J} \frac{\delta J}{\delta s}. \quad (5.1)$$

Thus, λ represents the fractional change in the Toronto O_3 (or CO) partial columns due to an incremental change in the emissions in each model grid box.

For O_3 sensitivity simulations, the adjoint calculates the sensitivity of the Toronto O_3 partial column to emissions of: NO_x and CO from anthropogenic sources (mainly from fossil fuel combustion) and biomass burning, NO_x from aircraft, biofuels, soil, and lightning, and isoprene.

For CO sensitivity simulations, the adjoint calculates the sensitivity of the Toronto

CO partial column to emissions of CO from fossil fuels, biomass burning, and biofuels, and emissions of isoprene (which is the dominant non-methane VOC source of CO).

5.4 HYSPLIT back-trajectories

HYSPLIT stands for Hybrid Single Particle Lagrangian Integrated Trajectory Model. It can compute simple air parcel trajectories - both forward and backward - as well as complex dispersion and deposition scenarios. It was initially developed by the National Oceanic and Atmospheric Administration (NOAA) and Australia's Bureau of Meteorology. It runs with a variety of meteorological reanalyses, depending on the time period [www.arl.noaa.gov/HYSPLIT_info.php]. For this work, we run the simple back-trajectories using the interactive model online [ready.arl.noaa.gov/HYSPLIT_traj.php]. We select three altitudes over Toronto's latitude and longitude coordinates (which are usually 0.5 km, 1 km, and 3 km, unless otherwise noted), and run the back-trajectory for those three air parcels backwards in time for three days (unless otherwise noted). This provides information about the transport history of Toronto's air, which could influence the composition of the 0-5 km partial columns. It is also useful to corroborate the transport in the GEOS-Chem adjoint results.

5.5 Enhanced O₃ and CO columns: Toronto pollution events

For the rest of this chapter, we define a *pollution event* as a day or series of days when the FTIR (TAO or CARE) tropospheric column(s) of O₃ or CO was \geq one standard deviation above the monthly mean (which we call an *enhanced FTIR measurement*), and surface O₃ measurements exceed the 1-hour provincial standard (80 ppb) or the 8-hour CWS (65 ppb) within 1.5 days of the enhanced FTIR measurement. Both O₃ and CO FTIR

columns were used in order to obtain more pollution events, as the tropospheric O_3 time series is sparse, and CO is a precursor to O_3 . We have used both FTIR lower-tropospheric columns and surface O_3 measurements in our pollution event definition because we want to examine cases in which the columns may provide additional information on long-range sources of pollution that impact health standards in Toronto.

A total of 37 days (from 2002 to 2010) met the criteria above. When a subset of these days is sequential, they are treated as one pollution event. This results in a total of 28 pollution events, which will be discussed below.

5.5.1 Pollution events in the annual time series

Figure 5.10 shows the number of pollution events per year (bottom panel), and the average maximum Toronto temperatures in the summers (average of June, July, and August mean maximum temperatures) of each year (top panel). Temperature data are from Environment Canada, [climate.weather.gc.ca/climateData/]. Overall, Figure 5.10 shows that the number of pollution events each year is correlated with the maximum summertime temperatures ($R=0.64$), with an overlying decreasing trend, which may be due to NO_x emission reductions. The correlation of O_3 pollution with temperature is unsurprising, and reported in previous publications [e.g., *Yap et al.*, 2005; *Geddes et al.*, 2009].

Below, Figures 5.11 to 5.16 show the late-spring to early-fall time series for each year of all of the measurements and the model output for the Toronto region for 2002 to 2007. These figures are similar to Figure 4.9 in Chapter 4, but we have also included surface NO_x measurements and GEOS-Chem results. The *pollution events* are circled for all measurements that were enhanced. While we have data and model output for 2008 through 2010, those annual time series are not shown because 2008 and 2010 only had one pollution event (with the 2010 event not modelled well), and 2009 had none (2009 had a relatively cool summer, Figure 5.10), and given the length of time to run the full

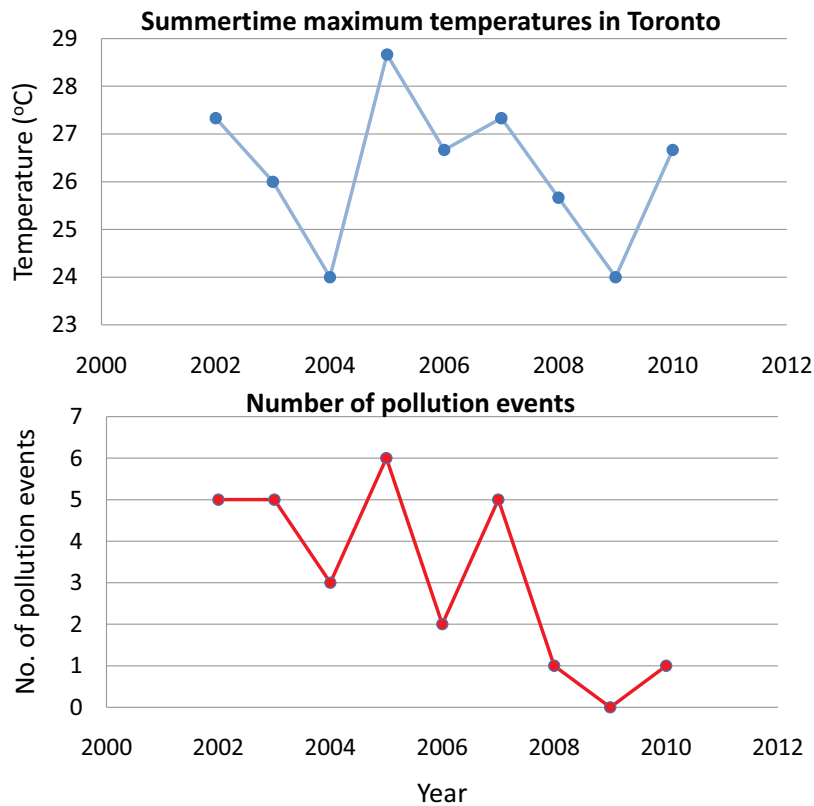


Figure 5.10: (top) Average Toronto summertime maximum temperatures, based on monthly mean temperature data from Environment Canada, which were averaged for June, July, and August of each year. (bottom) Number of pollution events (defined in text, Section 5.5) in each year.

chemistry nested adjoint and the time constraints of the project, only 2004 through 2007 pollution events were studied further.

There were five pollution events detected in 2002 between June and September (Figure 5.11), and five pollution events in 2003 between April and August (Figure 5.12). However, they cannot be analysed with GEOS-Chem adjoint at high resolution ($0.5^\circ \times 0.67^\circ$). There were no surface CO or NO_x measurements in 2002, which is why only the model results (at $2^\circ \times 2.5^\circ$) are shown in panels (d) and (e) of Figure 5.11.

There were three pollution events in 2004: 13 May, 30 June, and 21 July (Figure 5.13). The summer of 2004 was relatively cool in the Toronto region (Figure 5.10), making O₃ air quality rather good overall. In fact, the 1-hour provincial criterion was only exceeded twice that year (on days that did not qualify as pollution events). For the three events above, the 8-hour average O₃ was 66 ppb, 66 ppb, and 75 ppb, respectively. The May event also had enhanced surface CO, and NO_x. The July event had enhanced surface NO_x as well. The nested adjoint results for these three events will be shown in Sections 5.5.4 and 5.5.5 below.

There were six pollution events in 2005 (which also had the hottest summer, Figure 5.10): 27 June, 20-21 July, 3-4 August, 7 September, 12-13 September, and 5 October. They are highlighted in Figure 5.14 where we see that 1-hour surface O₃ was up to 94 ppb during the June event. The 8-hour average was up to 80 ppb for this event as well, and the C₂H₆ column was also enhanced. For the July event, 1-hour surface O₃ was up to 97 ppb, and 8-hour O₃ was up to 86 ppb. For the August event; only the 8-hour criterion was exceeded at 72 ppb, but the surface CO and NO_x and the C₂H₆ column were also enhanced. For the 7 September event, only the 8-hour criterion was exceeded at 68 ppb. For the 12-13 September event, surface O₃ was 80 ppb (1-hour) and 76 ppb (8-hour). And for the 5 October event, only the 8-hour criterion was exceeded at 71 ppb, although the surface NO_x was very high (>10 ppb), as was the C₂H₆ column. The nested adjoint results for all of these events will be shown in Sections 5.5.4 and 5.5.5 below, and the

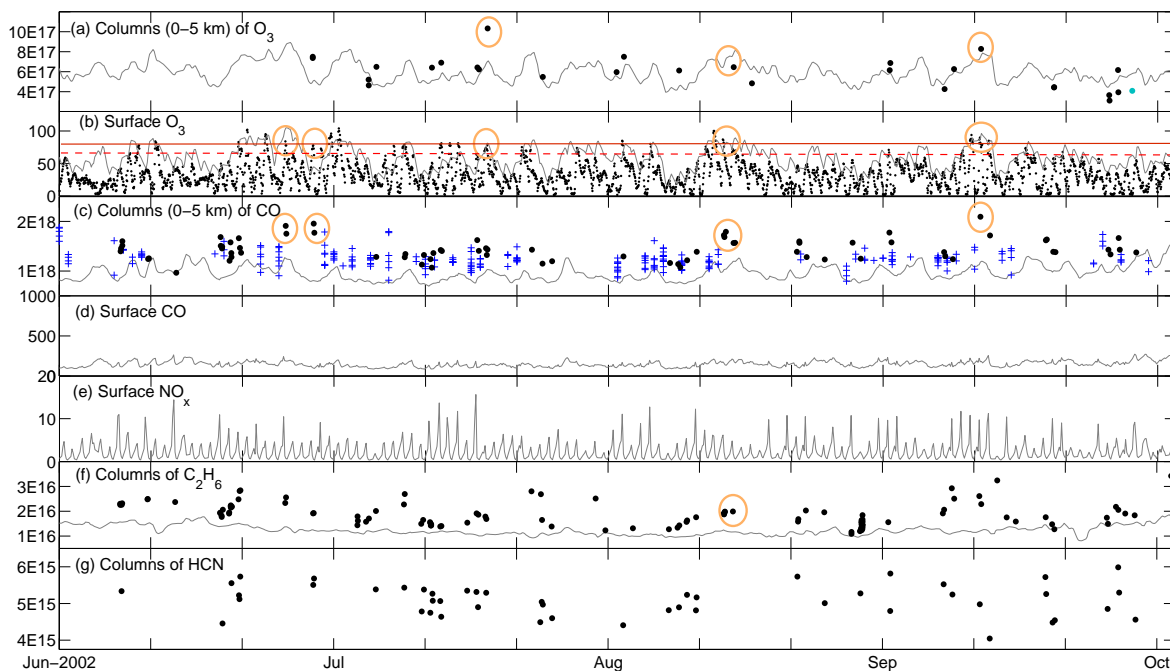


Figure 5.11: Toronto-area tropospheric time series for summer to fall 2002. The smoothed GEOS-Chem model output is shown by the grey lines. (a) Tropospheric columns of O_3 in molecules/cm² (TAO=black, CARE=cyan, TES=green crosses starting in 2006), (b) surface O_3 in ppb, with red lines representing the air quality criteria (solid for the 1-hour criterion, and dashed for the 8-hour criterion), (c) tropospheric columns of CO in molecules/cm² (TAO=black, CARE=cyan, and MO-PITT=blue crosses), (d) surface CO in ppb, (e) surface NO_x in ppb, (f) total columns of C_2H_6 in molecules/cm² (TAO=black, CARE=cyan), and (g) total columns of HCN in molecules/cm² (TAO=black, CARE=cyan). Pollution events are defined in the text, and highlighted by orange circles.

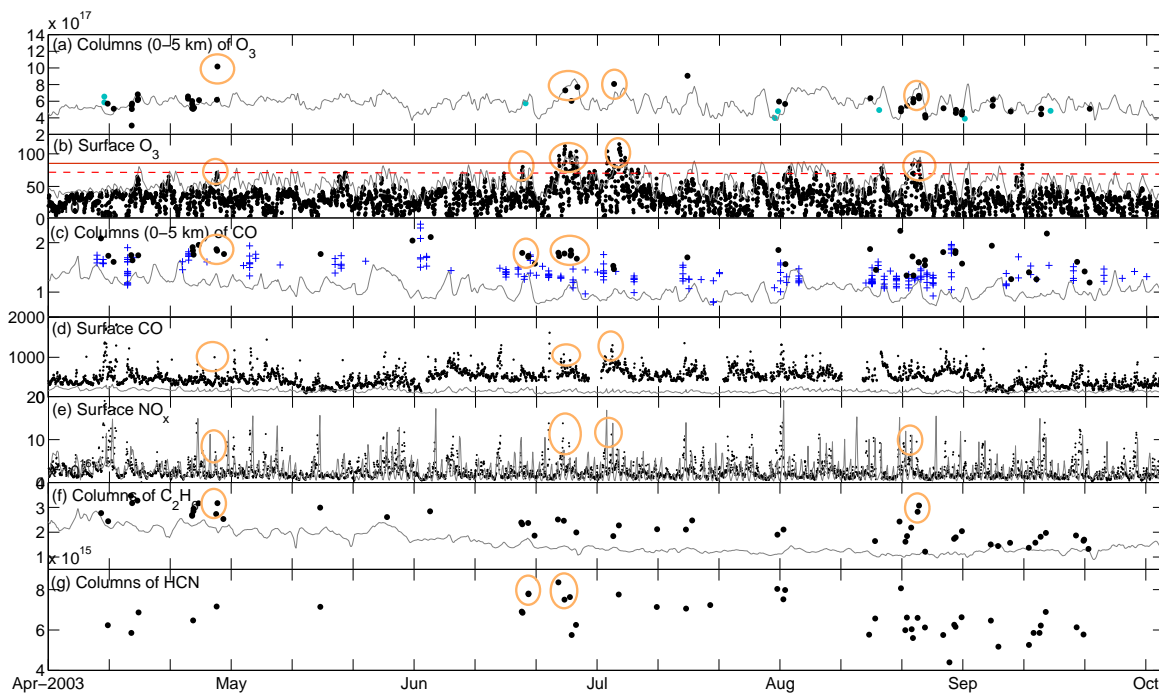


Figure 5.12: Same as Figure 5.11, but for 2003.

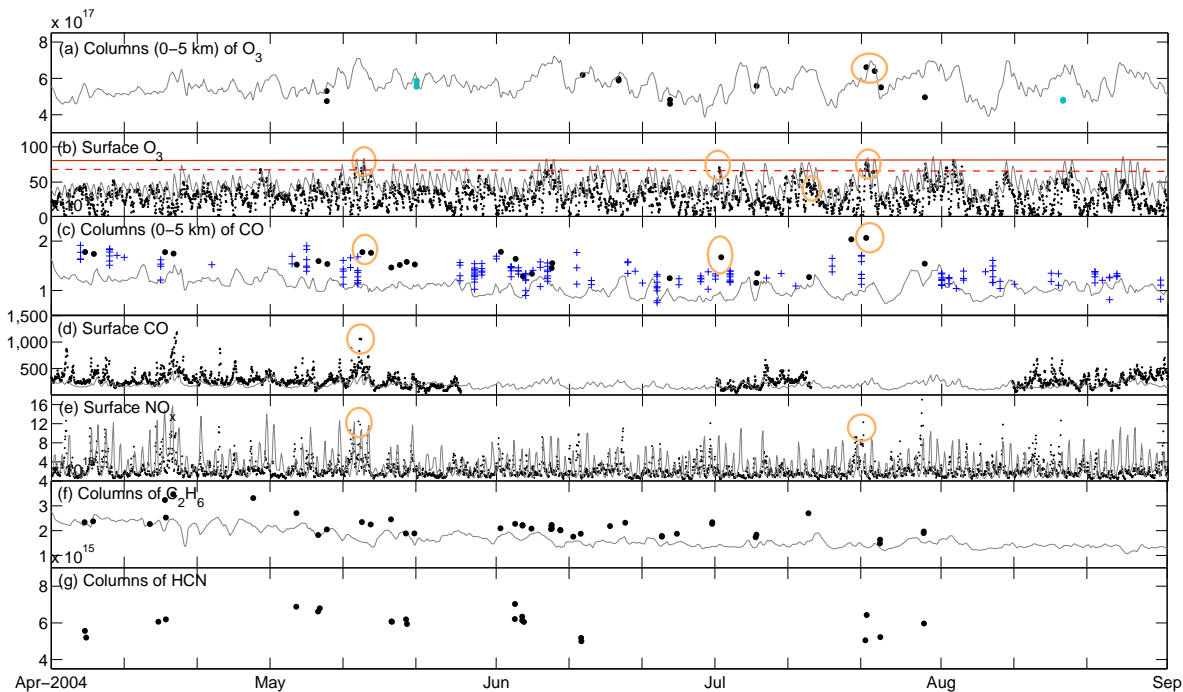


Figure 5.13: Same as Figure 5.11, but for 2004.

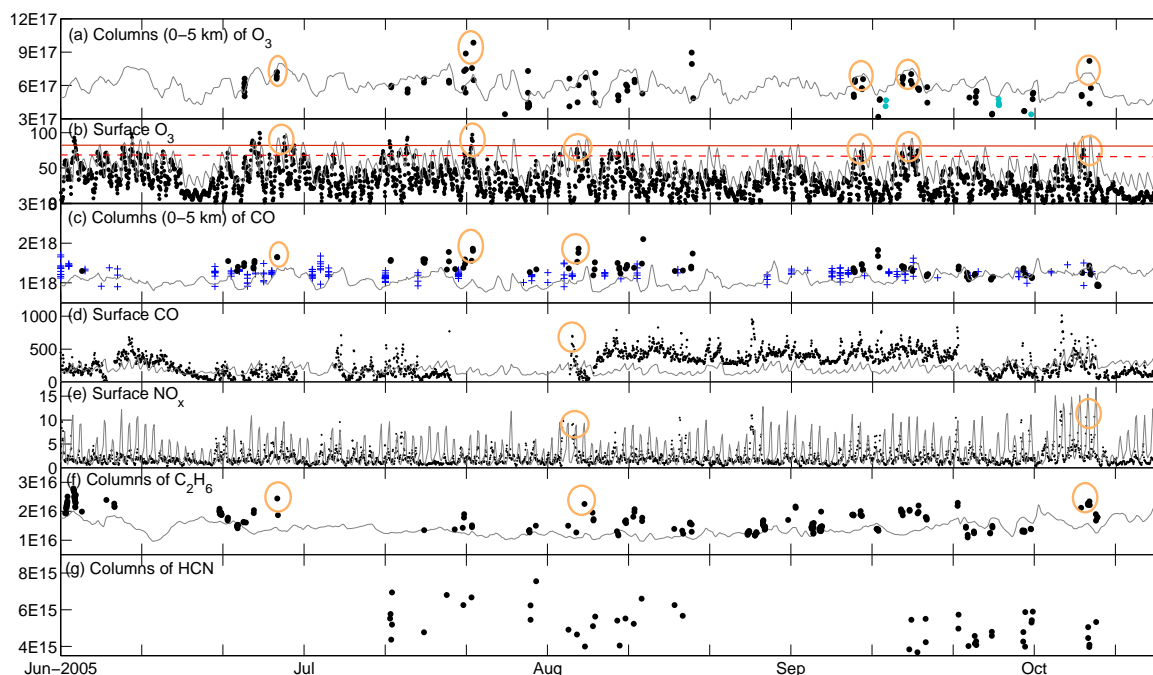


Figure 5.14: Same as Figure 5.11, but for 2005.

October and July pollution events were chosen as case studies for further analysis (see Section 5.6).

There were only two pollution events in 2006: 30 May and 28 June. They are highlighted in Figure 5.15. The May event had 8-hour O_3 up to 77 ppb, and 1-hour O_3 up to 86 ppb. The June event only exceeded the 8-hour criterion, at 68 ppb. Another feature we see in the time series, is on 7 July 2006, when column CO (including total columns, not shown), C_2H_6 , and HCN were significantly enhanced (red circles in Figure 5.15). This feature does not qualify as a pollution event because O_3 was not enhanced at the time, however, we selected this as a case study, and will show that biomass burning played a role in the CO enhancement (see Section 5.6.5).

2007 had five pollution events: 24 April, 24–25 May, 27 June, 1–3 August (3-day event), and 7 September, which are highlighted in Figure 5.16. The 8-hour average O_3 was slightly above the CWS at 68 ppb for the April event. The 8-hour O_3 was up to 82 ppb, and the 1-hour O_3 was up to 93 ppb for the May event. The 8-hour O_3 was up to 88

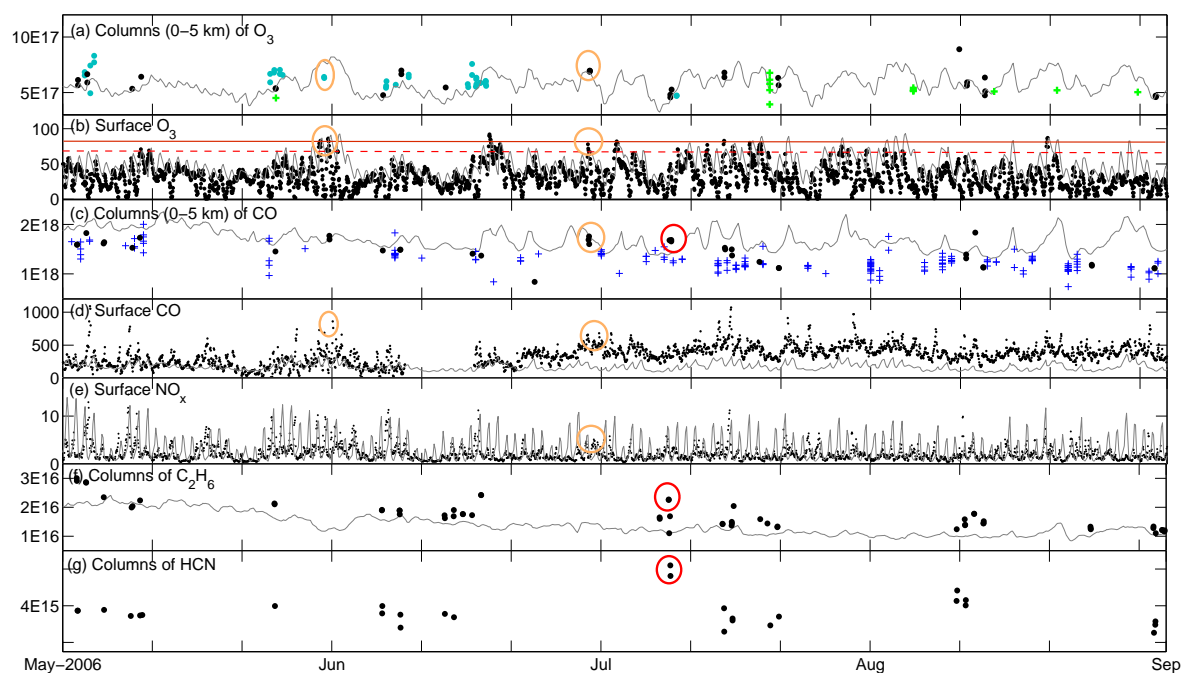


Figure 5.15: Same as Figure 5.11, but for 2006. Red circles highlight a biomass burning event.

ppb, and the 1-hour O_3 was up to 97 ppb for the June event, which had an enhancement in all panels of Figure 5.16, except HCN. The August event had 1-hour O_3 up to 91 ppb, but the CWS was not exceeded. The August event is selected as a case study for which long-range transport played a significant role in Toronto’s air quality (see Sections 5.5.5, and 5.6.2). Finally, the September event had 8-hour O_3 up to 77 ppb, and 1-hour O_3 up to 81 ppb. This last event is selected as another case study for which transport from the southeast and northeast U.S. played a significant role in Toronto’s air quality.

As mentioned above, 2008 to the present are not analysed further, but are discussed as “future work” (see Section 5.8).

5.5.2 Pollution events and wind direction

When the 28 pollution events we found in the 2002-2010 time series (the 26 mentioned above, plus one in 2008 and one in 2010) are binned by wind direction, 16% come from

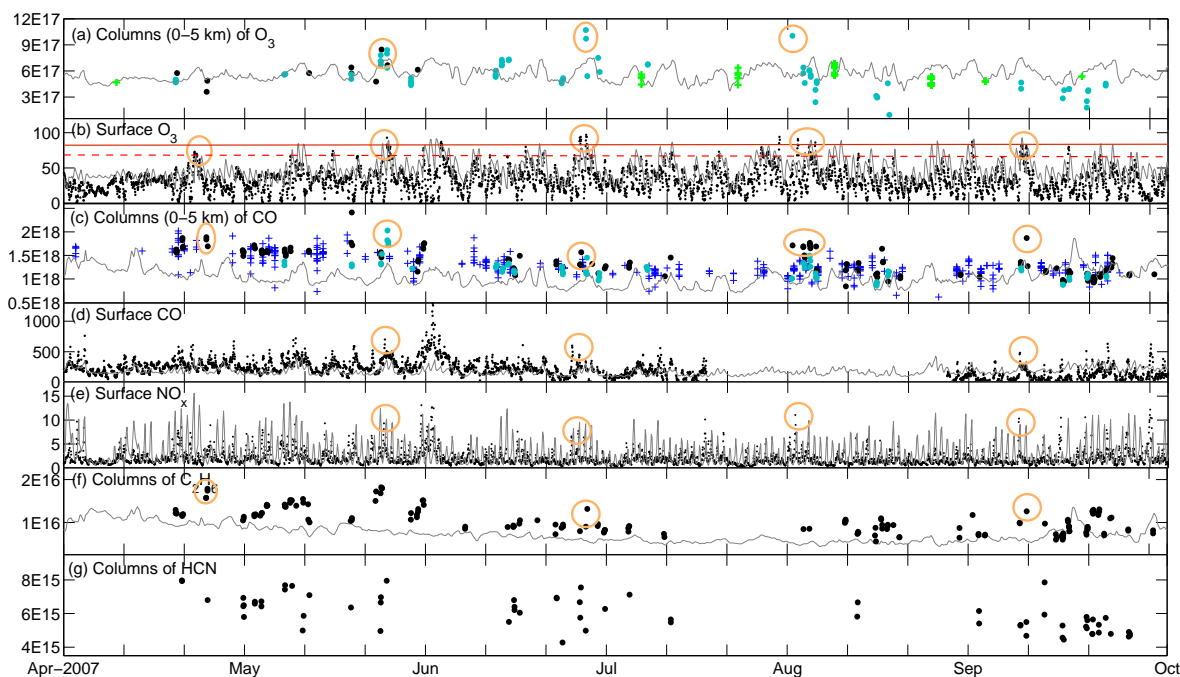


Figure 5.16: Same as Figure 5.11, but for 2007.

Canada, 53% come from the west, and 31% come from the southeast. Comparing these percentages to those for all of the FTIR measurements (see Section 5.2.2, or Table 5.1) we see greater representation from the west and southeast bins for pollution events. These pollution events were constrained by exceedances in surface O_3 criteria. If we consider all enhancements in the FTIR columns ($>$ monthly mean $+1\sigma$), then the distribution is: 39% from Canada, 44% from the west, and 17% from the southeast. The percentage in the western bin is slightly greater, and those in the Canada and southeast bins are slightly less than when all FTIR measurements are used. This is consistent with the FTIR pollution roses (Figures 5.1 and 5.3), indicating that high CO and O_3 columns can come from any direction. These results are summarized in Table 5.1.

5.5.3 Do FTIR tropospheric columns capture poor air quality?

About half (48%) of the surface O_3 exceedances (on days in which there is an FTIR measurement) had an enhanced tropospheric column of O_3 and/or CO. This means that

Table 5.1: Percentage of measurements coming from the three wind-direction bins defined in Figure 5.6. Shown for all FTIR measurements, only enhanced FTIR measurements, and only FTIR measurements that were associated with pollution events, as defined at the beginning of Section 5.5.

	all FTIR measurements	enhanced FTIR measurements	pollution events
from Canada	46%	39%	16%
from the west	33%	44%	53%
from the southeast	21%	17%	31%

the FTIR measurements are useful for diagnosing poor air quality only about half of the time (using our definition of enhancement). That said, the fraction may improve if more stringent surface O_3 standards were used (e.g., setting the 1-hour and 8-hour thresholds less than 80 ppb, and 65 ppv, respectively), because the surface O_3 could actually be enhanced relative to the background when the columns are, yet still not exceed the O_3 standards.

Only a quarter (24.8%) of the enhanced FTIR columns (between April and October²) coincided with a surface O_3 exceedance. This means that 3/4 of the time, the FTIR tropospheric columns are enhanced due to other factors, such as a pollution plume that passes through the free troposphere, but does not reach the surface. The fraction of enhanced FTIR columns associated with a surface O_3 exceedance is about 10% higher if only the summer months are considered (between June and August), however, still 2/3 of the column-enhancements occur when the surface O_3 is not exceeded.

²So as not to include the wintertime, when surface O_3 never exceeds the air quality criteria.

5.5.4 Sensitivity of Toronto pollution: North American emissions

For the 26 pollution events highlighted in Figures 5.13 to 5.16, the GEOS-Chem full chemistry nested adjoint was run for the subset of 15 events between 2004 and 2007 to determine the sensitivity of Toronto O_3 and CO to their precursor emissions (Equation 5.1). The sensitivities to the total North American emissions are shown in Figures 5.17 to 5.21.

Figure 5.17 shows the sensitivity of Toronto tropospheric (0-5 km) O_3 columns to total North American fossil fuel NO_x (top) and CO (bottom) emissions for each pollution event. We see that the Toronto O_3 columns increase by 10% to 25% per NO_x emission increase. For CO emissions, the sensitivity is an order of magnitude smaller, implying that NO_x is more important for creating Toronto-area O_3 . Also the event with the highest NO_x sensitivity (7 September 2007), does not have the highest CO sensitivity (in fact, it is one of the smallest for CO), even though NO_x and CO both come from fossil fuel emissions. And the reverse is also true: the 28 June 2006 event has the highest sensitivity to CO emissions, but relatively low sensitivity to NO_x . This is because some of the sensitivities to NO_x are negative – meaning that if NO_x emissions were increased further, they would act to decrease Toronto’s O_3 (recall Equation 4.8 in Section 4.1.2). However, we do not see a case where increasing CO reduces O_3 , so the sensitivity to CO is always positive. Therefore, when summing over all of North America, there are competing positive and negative influences from NO_x , but the influence from CO is always positive. Figure 5.17 also shows how variable the sensitivity can be between pollution events. Anthropogenic emissions tend to be relatively stable, so the differences between each event are largely due to differences in transport.

Figure 5.18 shows the sensitivity of each O_3 pollution event to isoprene emissions. These are typically 4% to 8%, with one large outlier on 5 October 2005, which is up

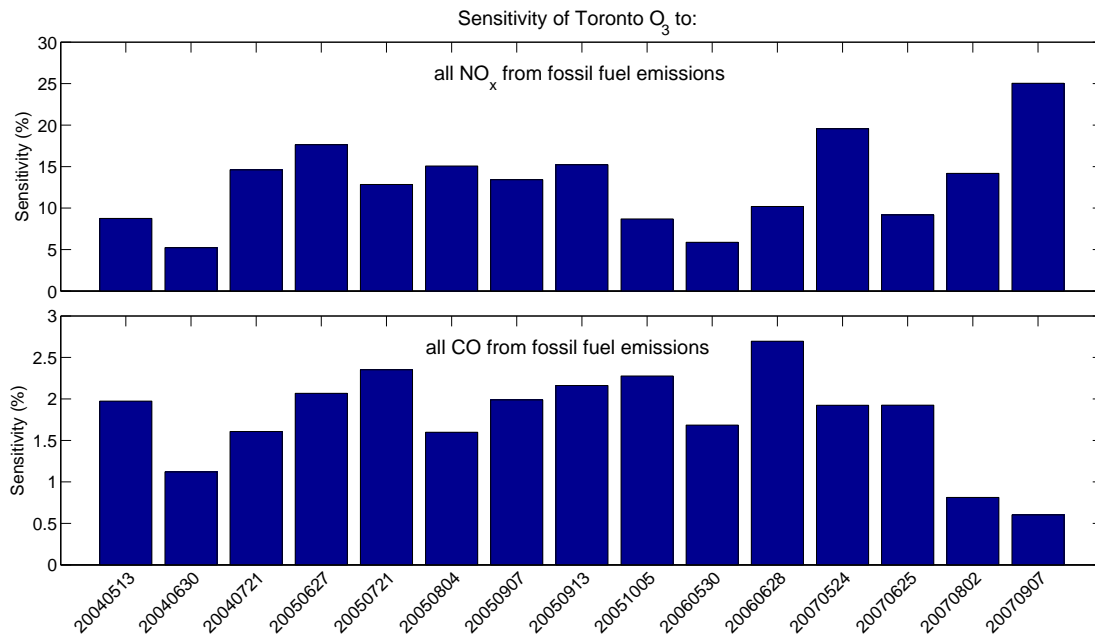


Figure 5.17: Sensitivity of Toronto tropospheric O_3 columns (0-5 km), on the dates shown, to total North American (top) fossil fuel NO_x emissions, and (bottom) fossil fuel CO emissions.

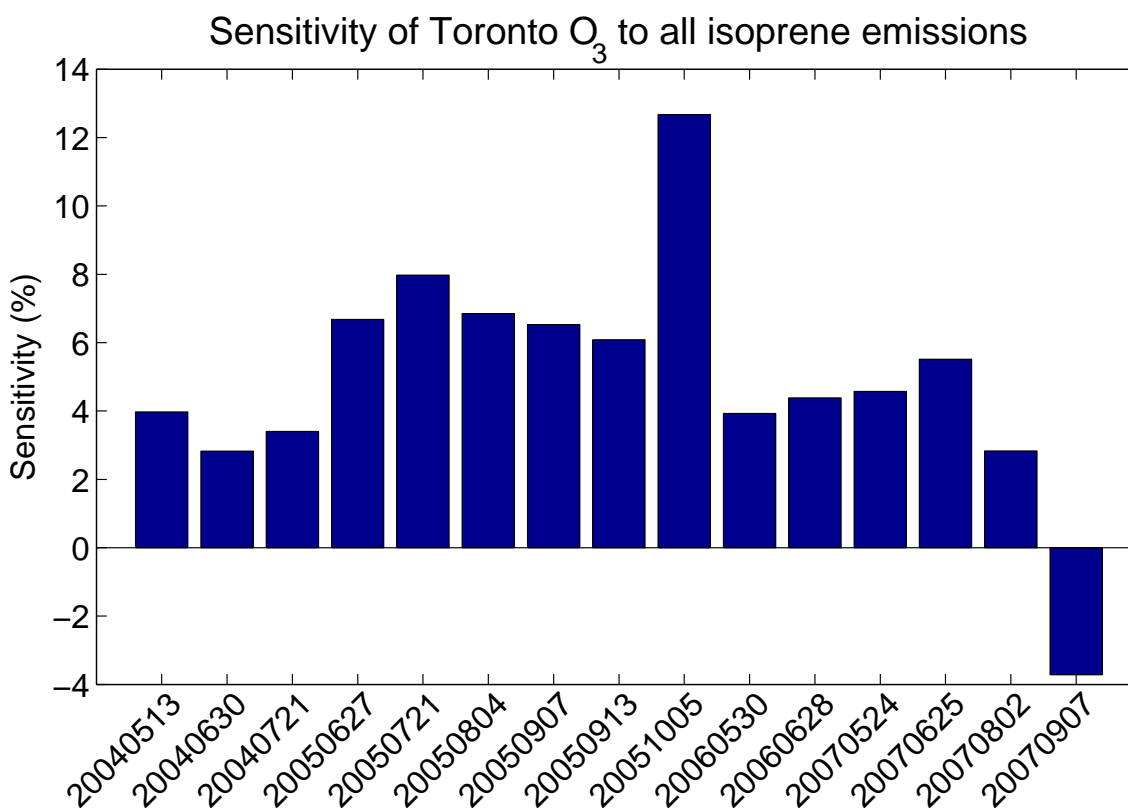


Figure 5.18: Sensitivity of Toronto tropospheric O₃ columns (0-5 km), on the dates shown, to isoprene emissions.

to almost 13% (more than the combined anthropogenic sources for this event, shown in Figure 5.17). Isoprene is emitted from plants when they are growing, and tends to increase when the temperature is high [Monson *et al.*, 1992; Guenther *et al.*, 1993]. Therefore, it is surprising to see such a high sensitivity in October. However, the sensitivity to VOC emissions would increase if O₃ production were in a hydrocarbon-limited regime (Section 4.1.2). The October 2005 pollution event is a case study that will be discussed further below (Section 5.6.1). Another outlier in Figure 5.18 is 7 September 2007, which is significantly negative. This means that if isoprene emissions were increased, they would act to reduce Toronto's O₃. This will be discussed further when this case study is explored in Section 5.6.2.

Figure 5.19 shows the sensitivity of each O₃ pollution event to (top) lightning and

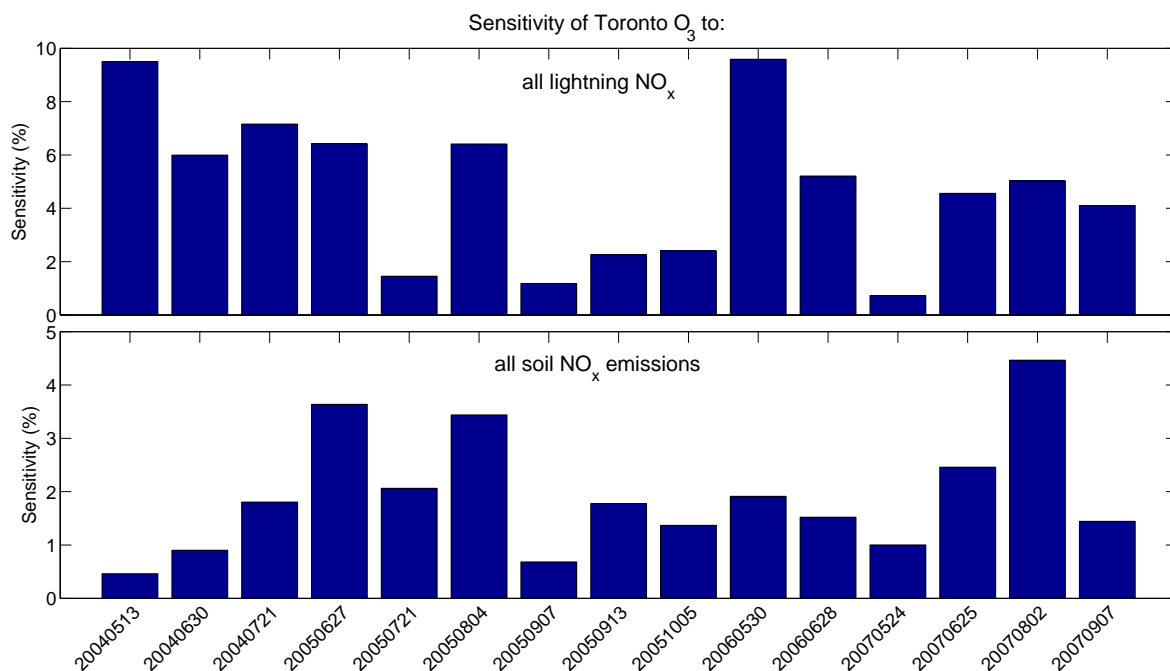


Figure 5.19: Sensitivity of Toronto tropospheric O₃ columns (0-5 km), on the dates shown, to (top) lightning NO_x emissions, and (bottom) soil NO_x emissions.

(bottom) soil NO_x emissions. NO_x is created by lightning, as the heat breaks apart the N₂ molecules, which then react with molecular oxygen. NO_x is emitted by microbes in soils during nitrogen fixation [Yienger and Levy III, 1995]. Soil NO_x emission is enhanced by recent burning, use of nitrogen fertilizers, and recent precipitation [Shepard et al., 1991; Yienger and Levy III, 1995; Jaeglé et al., 2004]. The highest sensitivity to soil NO_x is on 2 August 2007, where it is about 4.5%. This event is our fourth case study, described in Section 5.6.4.

Figure 5.20 shows the sensitivity of each O₃ pollution event to biomass burning emissions of (top) NO_x, and (bottom) CO. These show the pollution events that may have been influenced by biomass burning plumes, which are sporadic events. Toronto O₃ is sensitive to biomass burning up to 3% for the 21 July 2004 event (from NO_x and CO

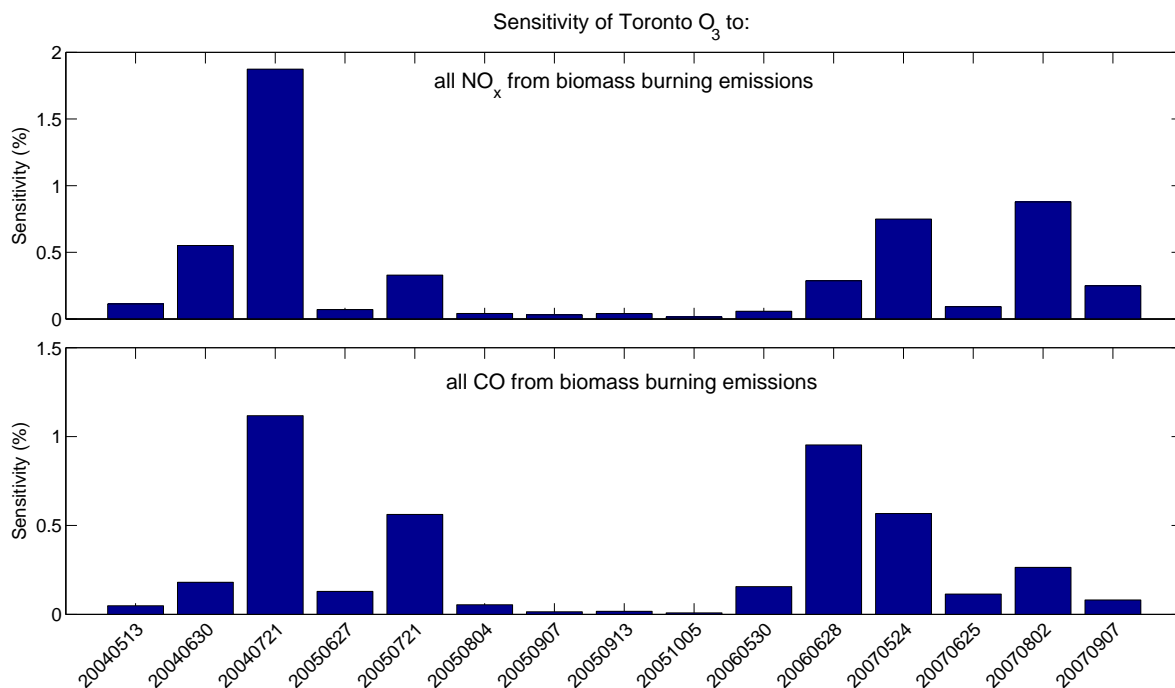


Figure 5.20: Sensitivity of Toronto tropospheric O₃ columns (0-5 km), on the dates shown, to biomass burning NO_x emissions (top) and CO emissions (bottom).

combined), but only 1% or less for the other events. Whether or not biomass burning emissions actually increase tropospheric O₃ remains a subject of debate, which will be discussed further in Section 5.7. The TAO HCN columns are too sparse during this time period to confirm an enhancement due to biomass burning (Figure 5.13).

Finally, Figure 5.21 shows the sensitivity of each O₃ pollution event to (top) aircraft NO_x emissions, and (bottom) biofuel emissions. These sensitivities are of the order of 1% for aircraft, and extremely small for biofuels. That is because – although growing – emissions from the aviation industry are still relatively small, and modern aircraft are more and more fuel-efficient. However, modern aircraft engines generate more NO_x due to high temperatures, and industry growth is outpacing other industries [Brasseur *et al.*, 1998; Lee *et al.*, 2010]. Also, a large fraction aircraft emissions occur above the 0-5 km

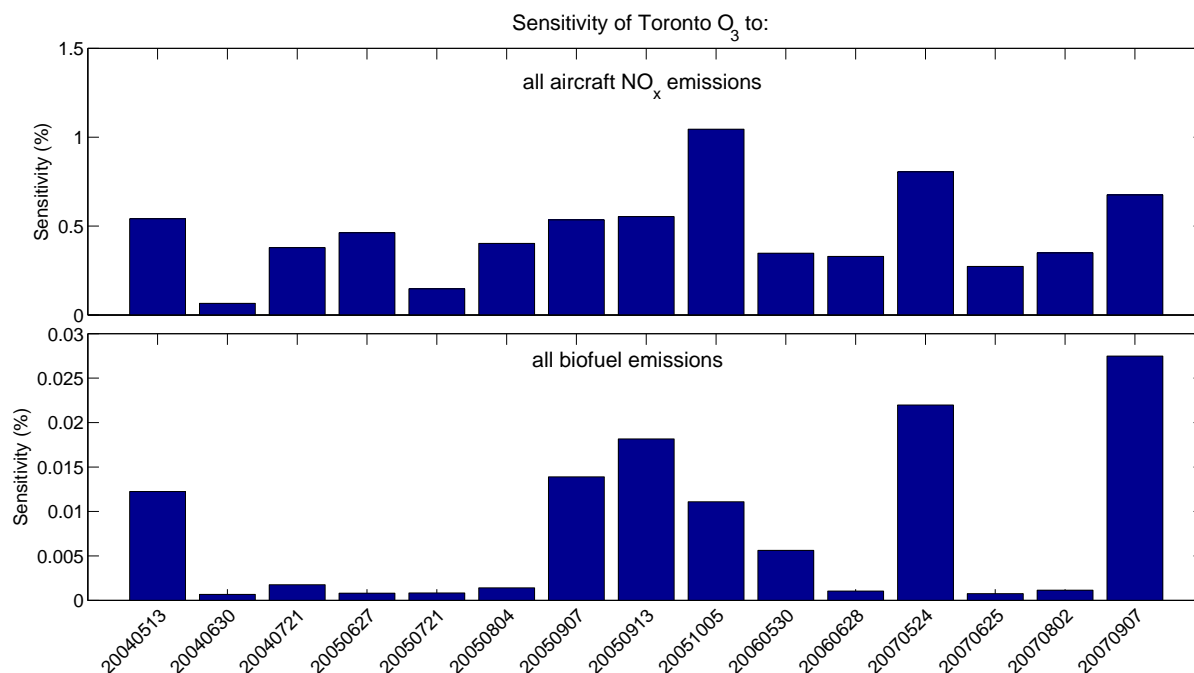


Figure 5.21: Sensitivity of Toronto tropospheric O₃ columns (0-5 km), on the dates shown, to aircraft NO_x emissions (top) and biofuel emissions (bottom).

partial column we are considering. Biofuel use, such as wood burning for heating and cooking, is very low in North America, however, their use may increase as biofuels are adopted as a replacement for fossil fuels in the future. The variability in sensitivity to biofuels is influenced not only by transport, but likely the time of year as well. The cases that are greater are in the spring and fall, when biofuels may be used for heating.

The GEOS-Chem adjoint was run for Toronto CO tropospheric columns as well, and these results are presented in Figure 5.22. There are four main emission sources of CO that the model adjoint can calculate: fossil fuels, isoprene, biomass burning, and biofuels. Fossil fuels dominate CO sensitivity at 20%-50% (Figure 5.22(a)). Sensitivity of Toronto CO to isoprene emissions (Figure 5.22(b)) is around 10%-25%, and it is interesting to note that the 5 October 2005 event is not particularly high compared to the other events,

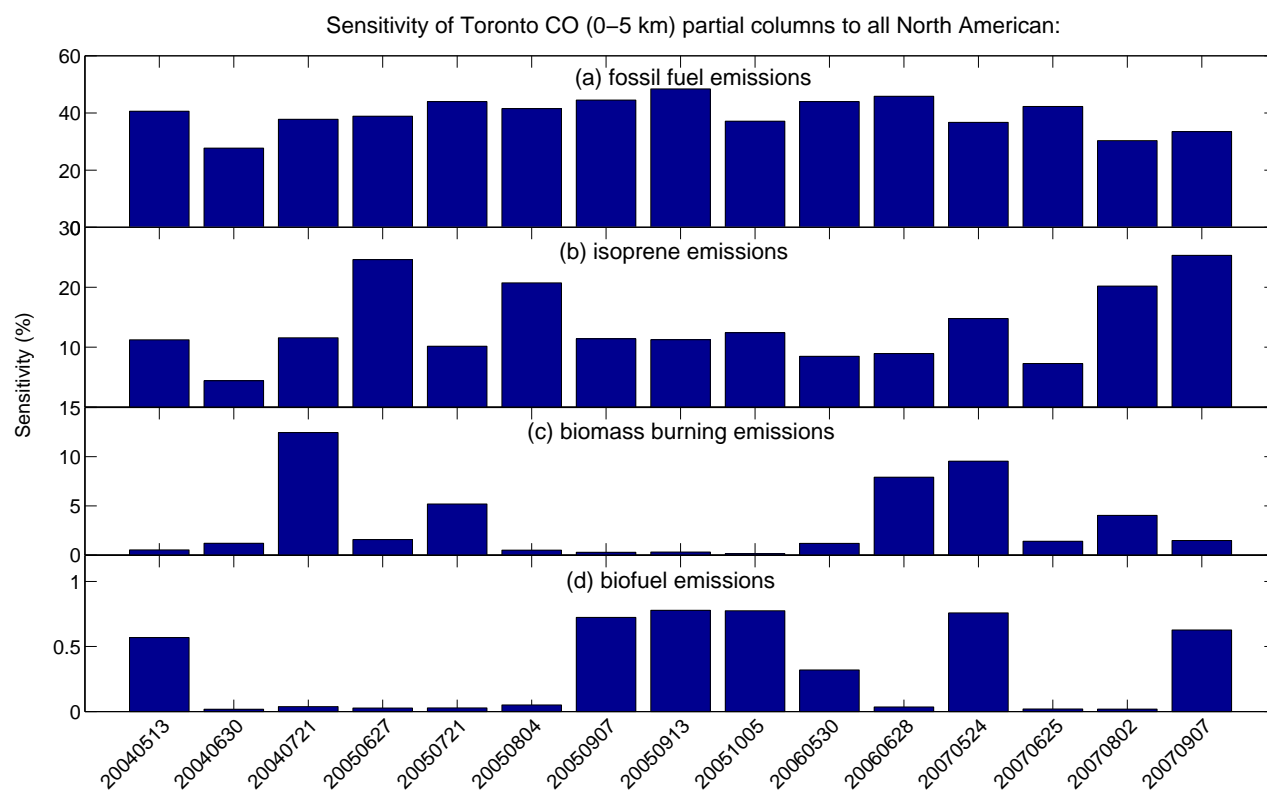


Figure 5.22: Sensitivity of Toronto tropospheric CO columns (0–5 km), on the dates shown, to (a) fossil fuels, (b) isoprene oxidation, (c) biomass burning, and (d) biofuels.

unlike the case for Toronto O_3 (Figure 5.18). This implies that emissions of isoprene were not particularly high for that event, but that the O_3 production regime was hydrocarbon-limited (more on the 5 October 2005 event is provided in Section 5.6.1). Sensitivity of Toronto CO to biomass burning is sporadic, and can be large when a biomass burning plume is present, as in the 21 July 2004 pollution event, when it is up to 13% (Figure 5.22(c)). Sensitivity of Toronto CO to biofuels is very low ($<1\%$) (Figure 5.22(d)) for the same reasons as for O_3 described in the previous paragraph.

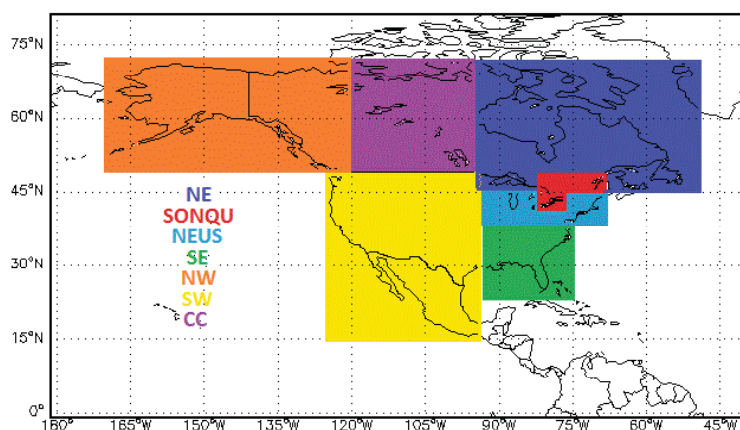


Figure 5.23: Regions selected for further analysis of GEOS-Chem sensitivity results.

5.5.5 Sensitivity of Toronto pollution: regional analysis

Figure 5.23 shows the regions selected to further explore the sensitivity of Toronto O_3 and CO. These regions were chosen such that the U.S. and Canada are separated, and boxes are smaller closer to Toronto to distinguish between nearby sources. They are: southern Ontario and Quebec (SONQU), northeast U.S. (NEUS), southeast U.S. (SE), southwest North America (SW), northwest North America (NW), central Canada (CC), and northeast Canada (NE).

Figures 5.24–5.25 and 5.27–5.29 are similar to Figures 5.17 to 5.22, however, they show the sensitivities summed over the regions defined in Figure 5.23, rather than summed over all of North America. These help us to see the dominant regions for each event, and also to see how they differ from event to event.

Certainly anthropogenic emissions from southern Ontario and Quebec and the northeast U.S. have a large influence on Toronto O_3 during many of the events (Figure 5.24). However, anthropogenic emissions from the southeast U.S. are dominant in the 13 May 2004, 24 May 2007, and 7 September 2007 events. For the 13 May 2004 event, sensitivity to southern Ontario/Quebec is negative, implying that the NO_x emissions there were high enough such that additional increases in NO_x emissions would have resulted in a

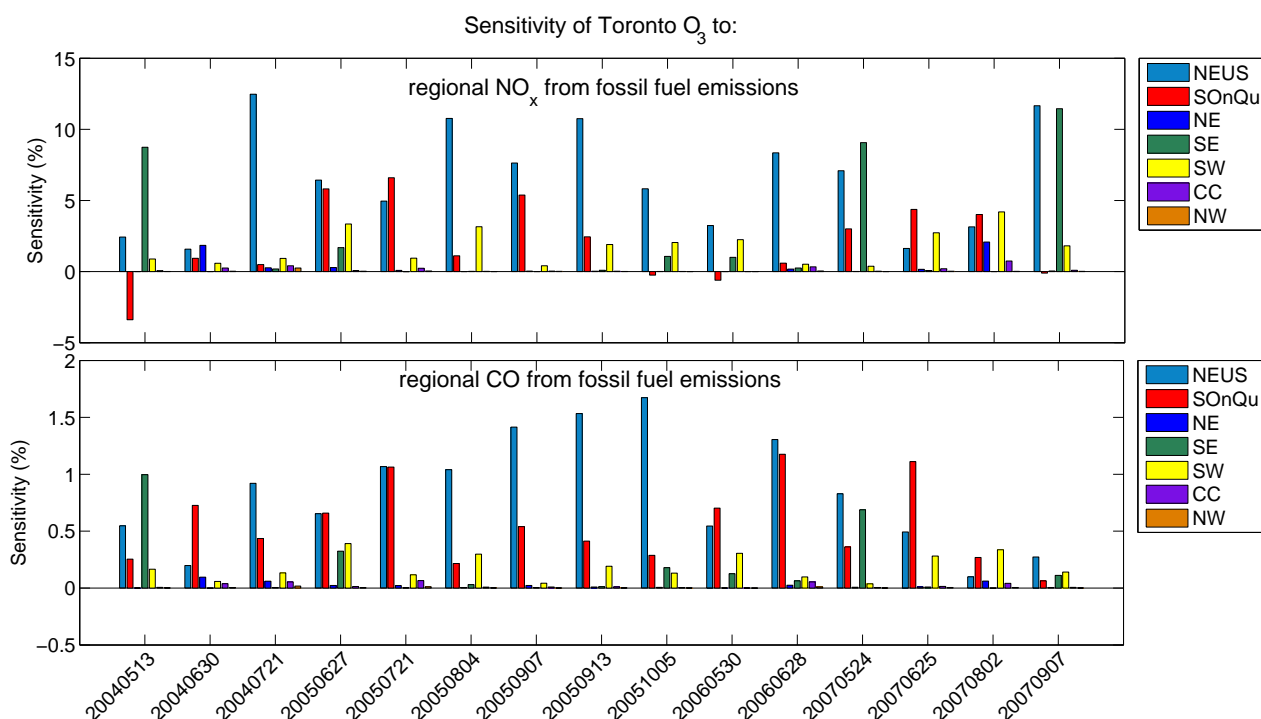


Figure 5.24: Sensitivity of Toronto tropospheric O₃ columns (0-5 km), on the dates shown, to regional fossil fuel emissions of (top) NO_x and (bottom) CO emissions. The colours here correspond to the colours in Figure 5.23.

reduction of O₃ in Toronto (Equation 4.8). Although this would increase O₃ downwind.

Surprising is that isoprene from the southeast U.S. is not a greater factor for our pollution events (Figure 5.25), as emissions of isoprene there are quite high, as seen in Figure 5.26, which shows North American isoprene emissions in the model (from the MEGAN inventory). For the most part, the greatest sensitivity to isoprene emissions is from the northeast U.S. and southern Ontario/Quebec dominate most pollution events. The 7 September 2007 case is interesting as the sensitivity of Toronto O₃ to isoprene in the eastern U.S. is significantly negative. This can be the case when isoprene concentrations are particularly high. We discuss this case more in Section 5.6.2.

Figure 5.27 shows the sensitivity of Toronto O₃ to lightning (top) and soil (bottom)

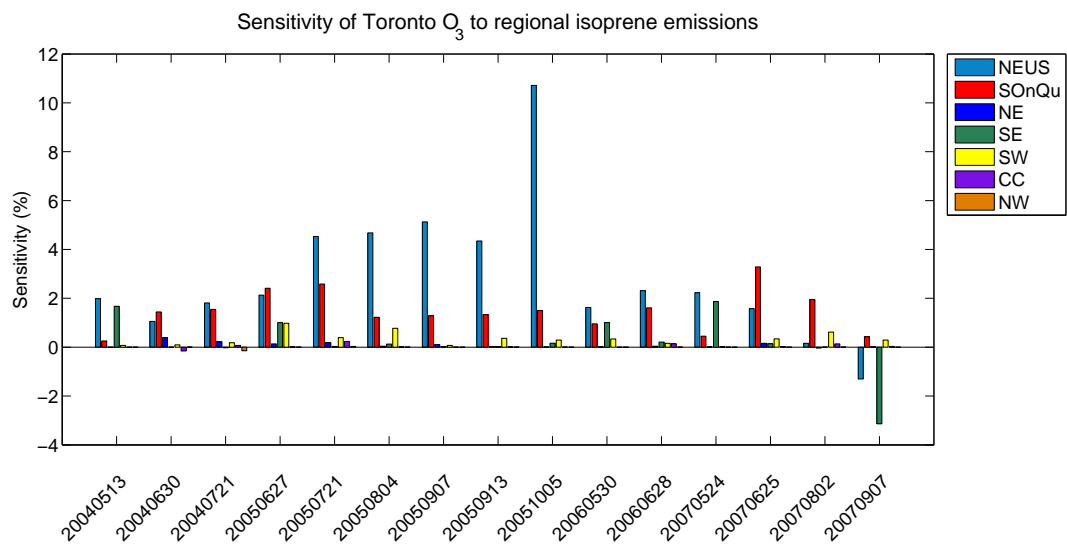


Figure 5.25: Sensitivity of Toronto tropospheric O_3 columns (0-5 km), on the dates shown, to regional isoprene emissions.

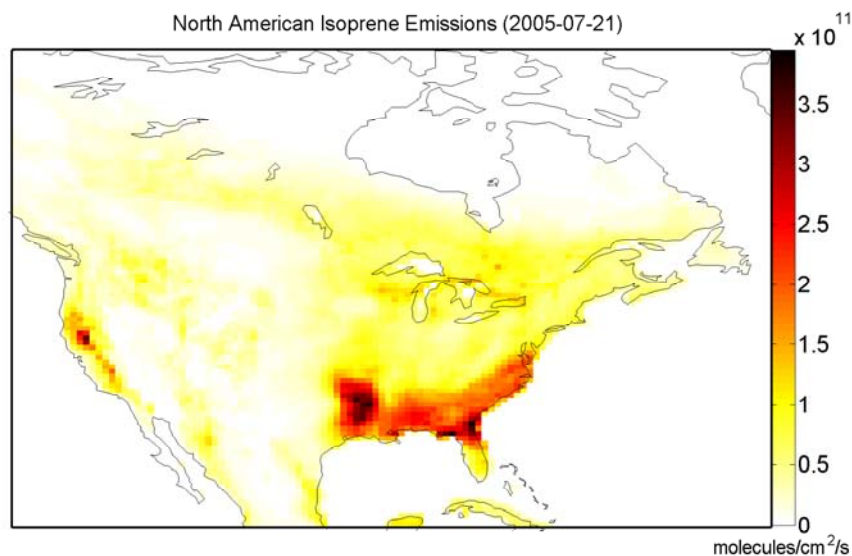


Figure 5.26: Map of total North American isoprene emissions on a typical summertime day (21 July 2005) in the model (from the MEGAN inventory).

NO_x . We see here that the emissions from the southwest box start to play a more significant role (especially for soils) than they have for other kinds of emissions. There are more soil emissions from this box because there is a large amount of agriculture, with nitrogen fertilizers causing increased soil NO_x emissions [Shepard *et al.*, 1991].

Figure 5.28 shows the sensitivity of Toronto O_3 to biomass burning from NO_x (top) and CO (bottom). We see here the origin of the biomass burning plumes: it was northwest Canada or Alaska (NW) for the 30 June 2004 event; it was central Canada (CC) for the 21 July 2004 and 28 June 2006 events; it was the southeast U.S. (SE) for the 24 May 2007 event, and it was the western U.S. or Mexico (SW) for the 2 August 2007 event.

Since the sensitivities to aircraft and biofuel emissions were $<1\%$, we do not show them separated regionally. However, both come from the northeast U.S. box most often, although the southeast U.S. plays a larger role on 13 May 2004 and 7 September 2007.

Finally, Figure 5.29 shows the sensitivity of Toronto CO (0-5 km) partial columns

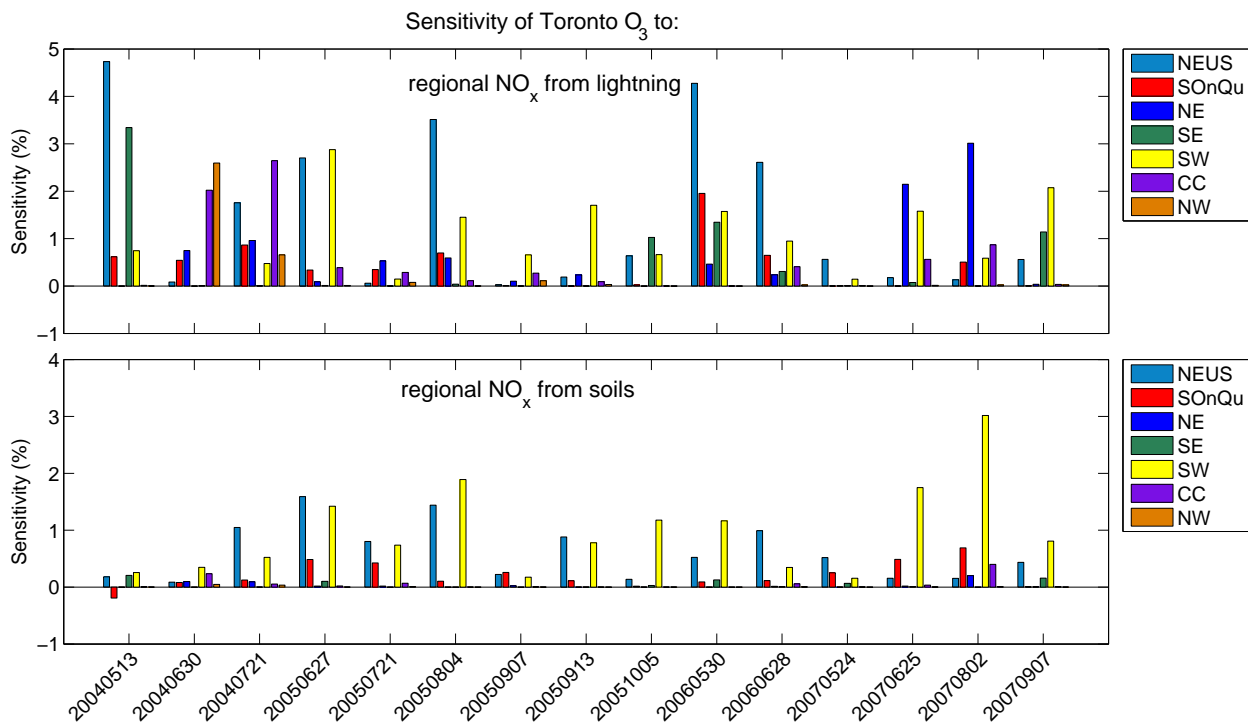


Figure 5.27: Sensitivity of Toronto tropospheric O₃ columns (0-5 km), on the dates shown, to regional lightning (top) and soil (bottom) NO_x emissions.

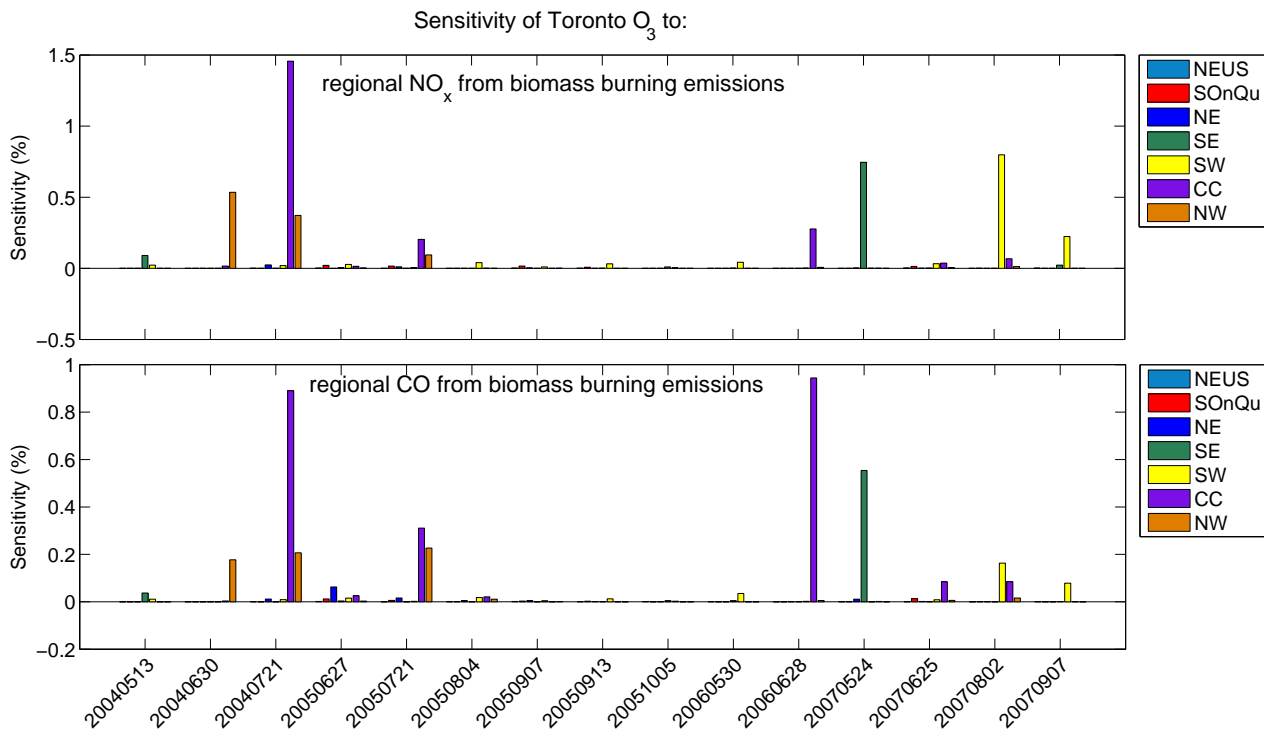


Figure 5.28: Sensitivity of Toronto tropospheric O₃ columns (0-5 km), on the dates shown, to regional biomass burning emissions of (top) NO_x, and (bottom) CO.

to different emissions, separated by region. In panel (a) we see that sensitivity to fossil fuel emissions from the local box (SONQu), and the nearby northeast U.S. box (NEUS) is dominant during each pollution event, except for the 13 May 2004, 24 May 2007, and 7 September 2007 events, which also have a significant southeast contribution due to transport. For isoprene emissions (Figure 5.29(b)), the sensitivity is largely from the northeast U.S., and very little is from the local box. Given that isoprene emissions in southern Ontario, and the northeast U.S. are similar (Figure 5.26), this is likely because the northeast box is larger, so we are summing over a larger region. There are four events where the large southeast isoprene emissions (Figure 5.26) play a significant role: 13 May 2004, 27 June 2005, 24 May 2007, and 7 September 2007 (Figure 5.29(b)). Figure 5.29(c) shows sensitivity of Toronto CO to biomass burning by region, which agrees with the regional sensitivity of O₃ (Figure 5.28) for the five events with significant biomass burning. Sensitivity to biofuels is mainly from the northeast U.S. (Figure 5.29(d)).

5.6 Case studies

We now select five interesting case studies to examine further: (1) short-range transport of pollution from the northeast U.S., (2) mid-range transport from the southeast U.S., (3) a local pollution event under stagnant weather conditions, (4) a long-range transport event, and (5) a biomass burning event. Each case study includes back-trajectories from HYSPLIT, sensitivity maps from the GEOS-Chem full chemistry nested adjoint, meteorological maps from the NCEP reanalysis, as well as other data gathered (e.g., temperatures from Environment Canada, winds from GEOS fields, etc.) to provide more information for each pollution event to determine the causes.

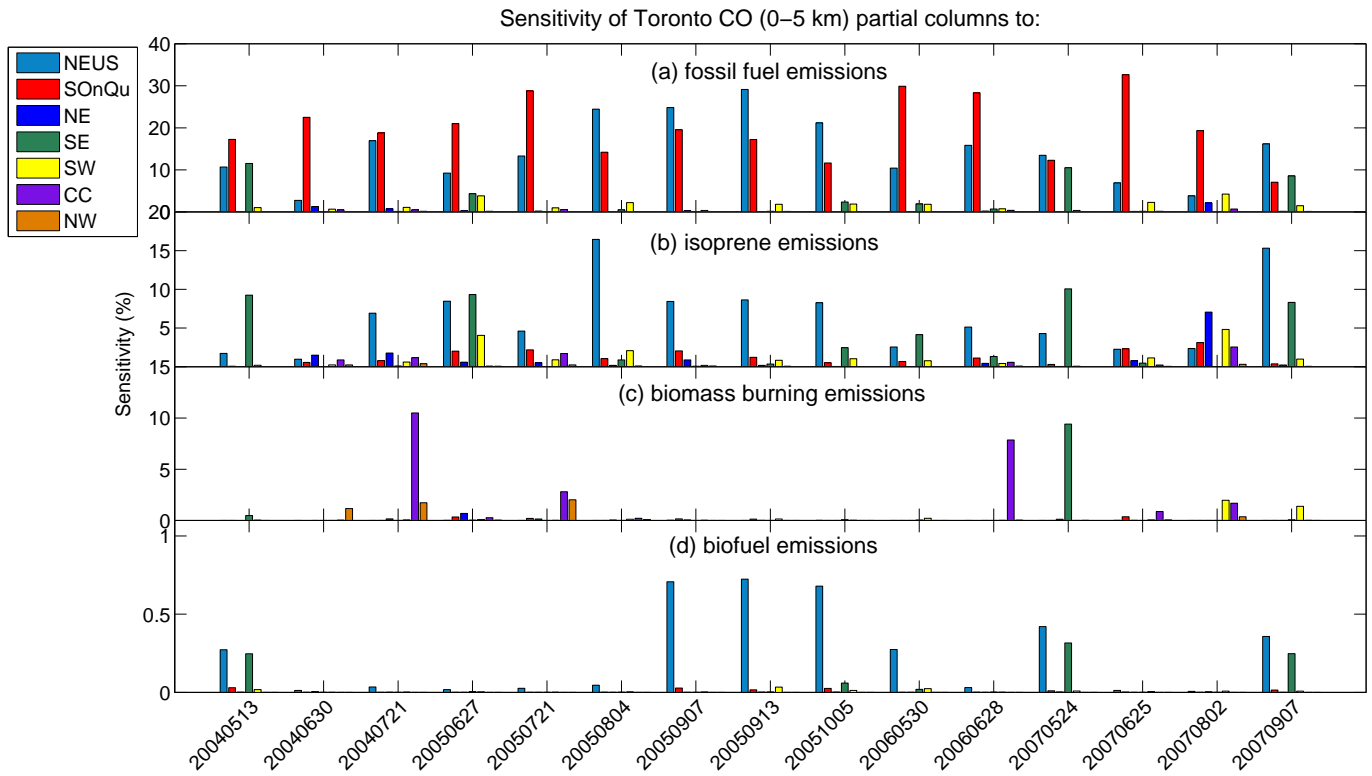


Figure 5.29: Sensitivity of Toronto tropospheric CO columns (0–5 km), on the dates shown, to each kind of emission, separated by region.

5.6.1 Case 1: a high-pressure system brings pollution from the northeast U.S. during abnormally high temperatures

On 5 October 2005, the surface O₃ 8-hour average in Toronto was 71 ppb (6 ppb above the CWS). The maximum temperature was abnormally high at 25°C. The temperature anomaly over the region is shown in Figure 5.30 (left), using daily mean composites of NCEP reanalysis data [www.esrl.noaa.gov/psd/data/composites/day/]. The anomaly is defined as the difference between the average surface temperature for the day and the 30-year climatological mean. The TAO O₃ column on 5 October 2005 was 37% (1.5σ) greater than the monthly mean, and the CO columns (both from TAO and MOPITT) were not particularly enhanced, although still 11% ($<1\sigma$) greater than the monthly mean. The average wind over Toronto (from 0.2-2 km) was 7.3 m/s (relatively slow), and was coming from the southwest. The HYSPLIT back-trajectories in Figure 5.31 show the transport going backwards in time for three days starting at three vertical levels over Toronto: 0.5 km, 1.0 km, and 3.0 km. It shows that the wind was circulating around from the highly-populated northeast coast of the U.S at all three vertical levels. This odd transport pattern was likely caused by the high-pressure system, which can be seen in the geopotential height anomaly at 500 hPa in Figure 5.30 (right).

The full-chemistry, nested forward model of GEOS-Chem shows that enhanced O₃ originated around Maryland, Pennsylvania, and New Jersey, and then travelled along the path indicated by HYSPLIT³, expanding with time. Maps of O₃ VMR at about 1.3 km in altitude are shown for 2, 3, and 5 October 2005 in Figure 5.32.

The full chemistry, nested adjoint shows that the dominant O₃ sensitivities for this pollution event were to both isoprene emissions (Figures 5.25 and 5.33, right) and anthropogenic NO_x emissions (Figure 5.24 and 5.33, left). Figure 5.33 shows that Toronto O₃ columns were sensitive to emissions along the transport path. On the left, the sensi-

³The HYSPLIT back trajectories were verified for consistency with the transport in the GEOS-Chem adjoint maps for all 15 pollution events between 2004 and 2007, and in case, they agree.

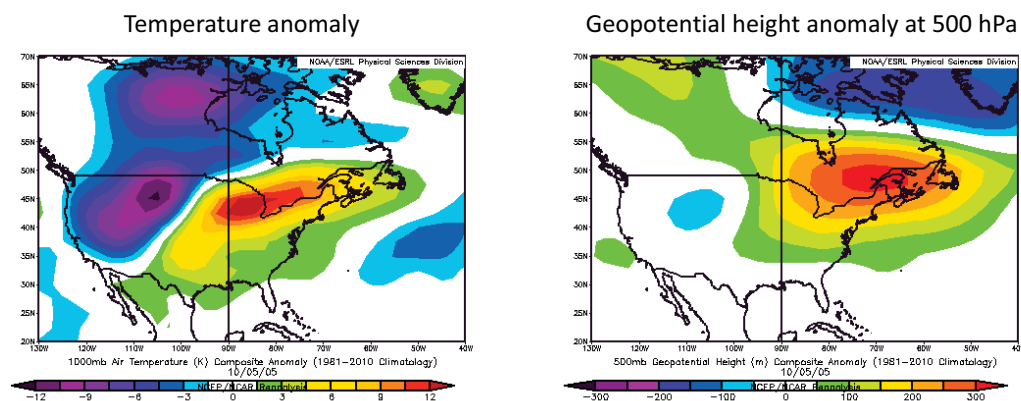


Figure 5.30: NCEP maps (daily mean composites) on 5 October 2005 of: (left) surface temperature anomaly, and (right) geopotential height anomaly compared to the 30-year climatological means.

tivity is strongest to NO_x fossil fuel emissions from Washington, D.C., however, there is a strong negative sensitivity to the Toronto grid box (down to -1%), and to the Pittsburgh area. This implies that the NO_x concentrations from those regions are high enough that any further increase would reduce Toronto O_3 . On the right, the sensitivity to isoprene is strongly positive. The sensitivity is so high that it is likely that O_3 production was hydrocarbon-limited at the time (Section 4.1.2).

We investigate the O_3 production regime using a “species indicator ratio” [Sillman, 1995; Cohan *et al.*, 2007]. Figure 5.34 plots the surface VMR ratio of $\text{H}_2\text{O}_2/\text{HNO}_3$ in North America (VMRs taken from the GEOS-Chem model) on 5 October 2005. The ratio is expected to be higher in NO_x -limited regimes and lower in hydrocarbon-limited regimes because H_2O_2 is the major sink for HO_x in NO_x -limited regimes, and HNO_3 is the main sink for HO_x in hydrocarbon-limited regimes. O_3 tends to be hydrocarbon-limited when the ratio is below 0.3 [Cohan *et al.*, 2007]. It appears in Figure 5.34 that Toronto, and most of southern Ontario, is in a hydrocarbon-limited regime on this date. Thus, it is consistent with the negative NO_x sensitivity in the adjoint.

Thus, we conclude that the combination of being in a hydrocarbon-limited regime

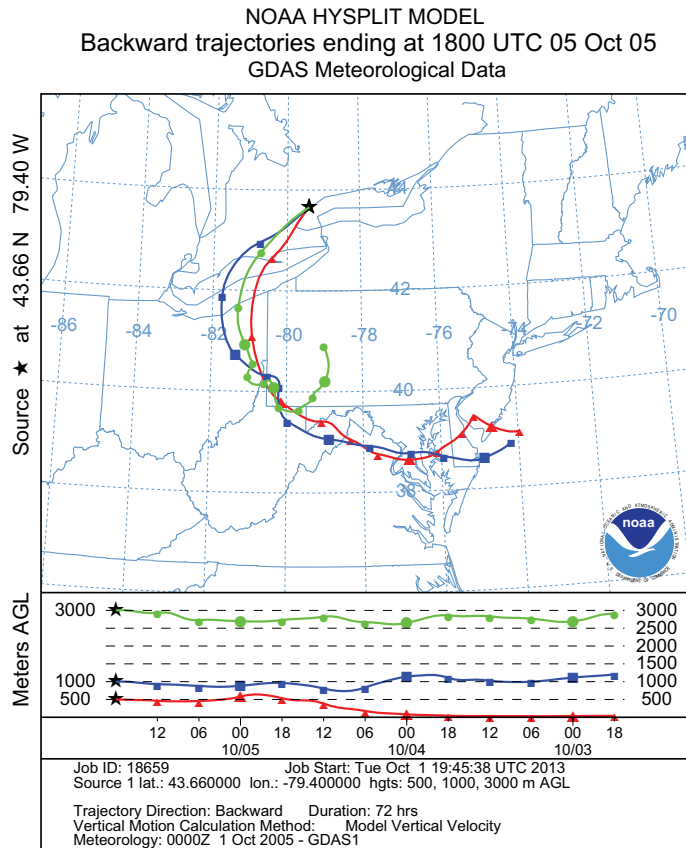


Figure 5.31: HYSPLIT back-trajectories for Toronto, starting on 5 October 2005, 18:00 UT, going back three days with points every 6 hours. Three altitudes are shown, starting at 0.5, 1.0 and 3.0 km over Toronto.

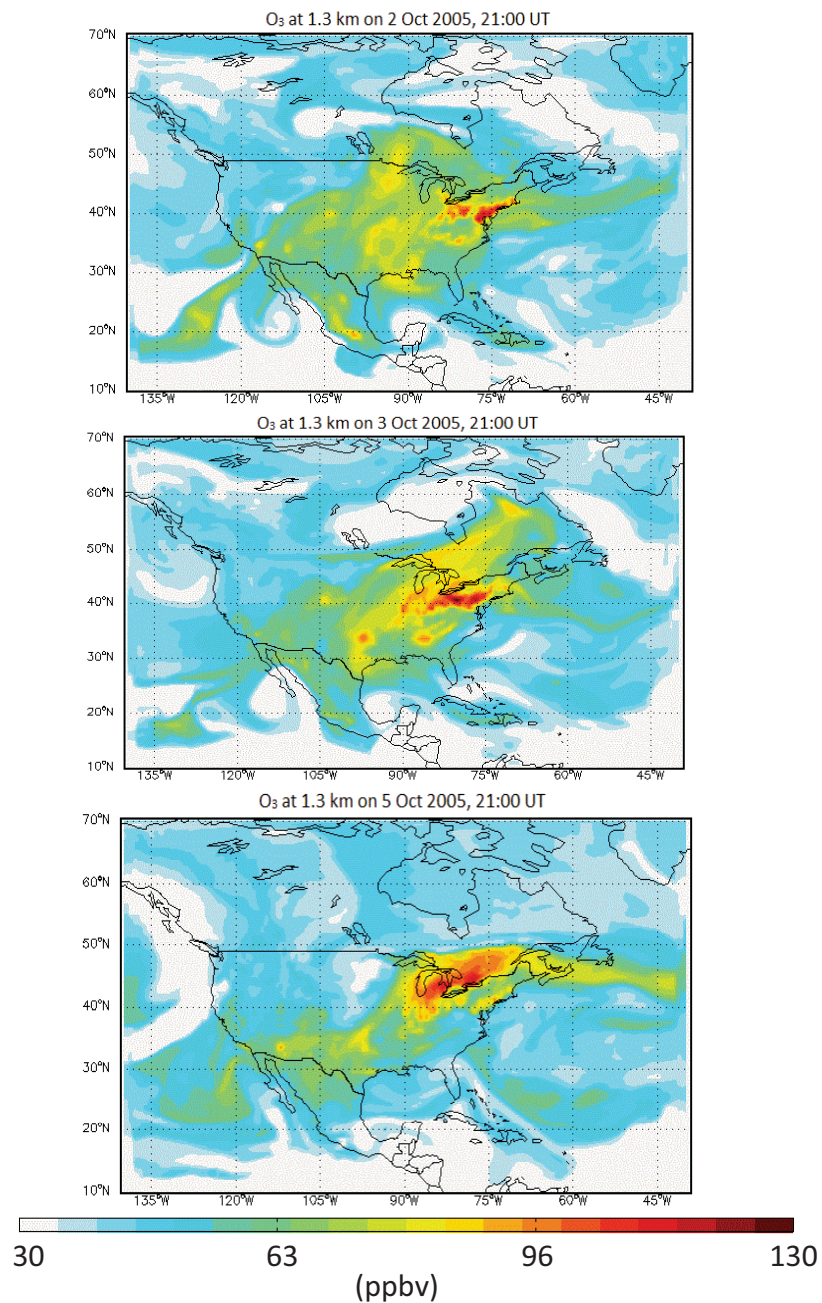


Figure 5.32: GEOS-Chem modelled O_3 at 1.3 km altitude on 2, 3, and 5 October (top, middle, and bottom, respectively) at 21:00 UT. We see the transport and evolution of enhanced O_3 concentrations.

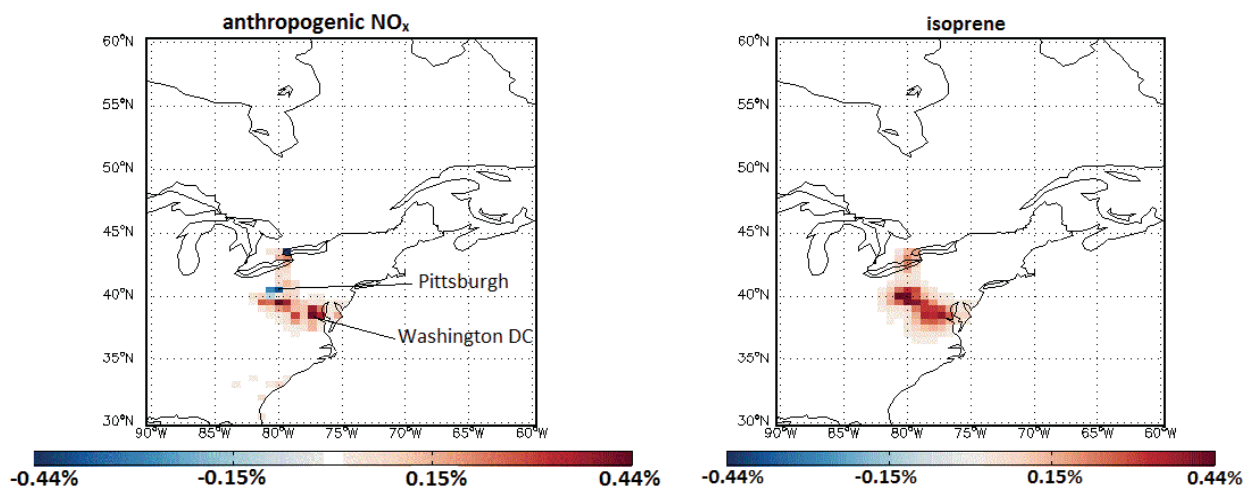


Figure 5.33: GEOS-Chem adjoint results for 5 October 2005, showing sensitivity of Toronto O₃ tropospheric columns to (left) anthropogenic NO_x emissions, and (right) isoprene emissions.

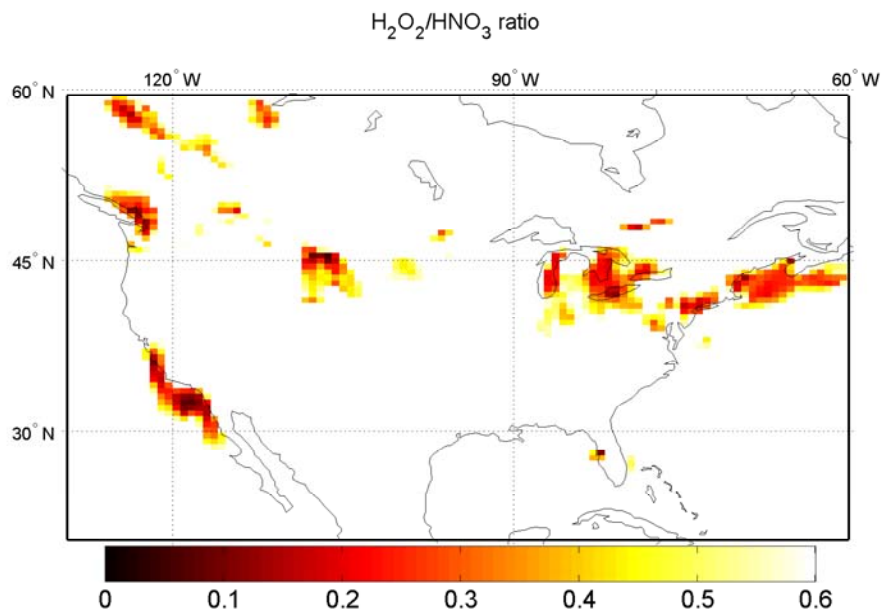


Figure 5.34: GEOS-Chem surface H₂O₂/HNO₃ ratios across North America on 5 October 2005. Ratios less than 0.3 may be hydrocarbon-limited for O₃ production.

(due to urban, NO_x -rich air) during a period of high temperatures (more hydrocarbon emissions) caused the pollution event on 5 October 2005. While, the high urban NO_x actually lowered O_3 , it was responsible for causing the high sensitivity to VOCs.

5.6.2 Case 2: high local temperatures and transport from the southeast U.S.

On 7 September 2007, the 1-hour surface O_3 in Toronto was 81 ppb (1 ppb above the provincial criterion). The maximum temperature was abnormally high at 33°C , and the NCEP temperature anomaly shows high temperatures over all of Ontario and southern Quebec (Figure 5.35). We did not measure O_3 at TAO this day, and there are no TES or CARE measurements either, however the TAO CO column was 53% (3σ) greater than the monthly mean. The average wind over Toronto was 20.6 m/s, and was coming from the southwest. The HYSPLIT back-trajectories show that the wind was circulating around from the southeast U.S. (Figure 5.36), a region known for high VOC emissions (Figure 5.26). The transport pattern was likely caused by the high-pressure system, which can be seen in the geopotential height anomaly at 500 hPa in Figure 5.35 (right).

The full chemistry nested adjoint of GEOS-Chem shows that the dominant sensitivity of O_3 was NO_x fossil fuel emissions from the northeast and southeast U.S. (Figures 5.24 and 5.37, left). Recall that this event had the highest sensitivity to total North American fossil fuel emissions, which was 25% (Figure 5.17). The sensitivity to isoprene emissions is strongly negative in the southeast U.S. region (Figures 5.18 and 5.37, right). Figure 5.37 shows the sensitivity of Toronto O_3 tropospheric columns to emissions along the transport path. On the left, the sensitivity is strongest to Nashville and Atlanta, and there is a small negative sensitivity to the Toronto grid box (less than -0.25%). This implies that if the NO_x concentrations from Toronto would increase, they would reduce Toronto O_3 by a small amount. On the right, the sensitivity to isoprene is positive nearby, but quite negative in the southeast U.S. where isoprene emissions are high. When isoprene is

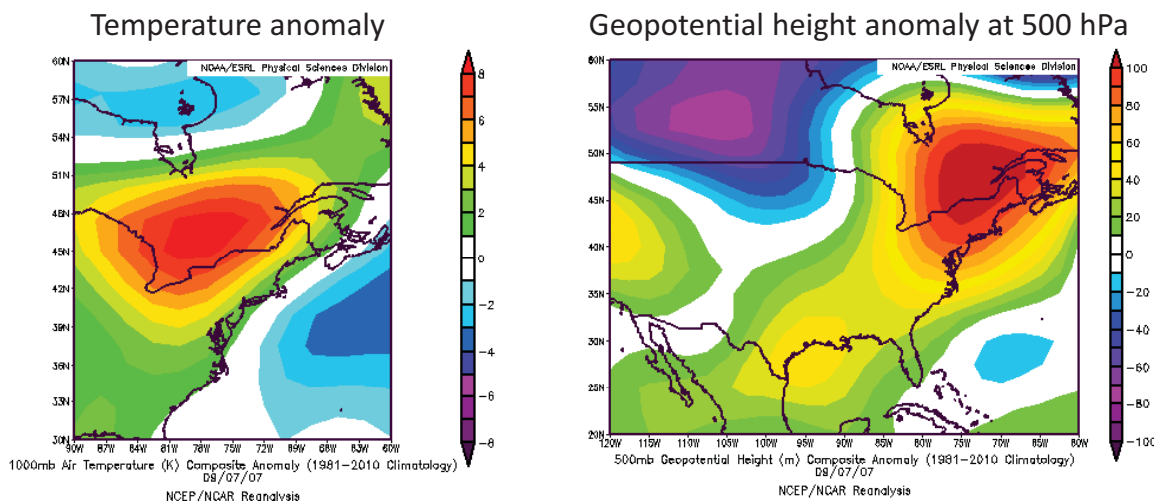


Figure 5.35: NCEP maps on 7 September 2007 of: (left) surface temperature anomaly, and (right) geopotential height anomaly compared to the 30-year climatological means.

oxidized, it goes through many reactions involving OH and NO [Mao *et al.*, 2013]. In this version of the model, the OH and NO are consumed in the isoprene chemistry scheme [Mao *et al.*, 2010, 2013; Zhang *et al.*, 2011], leaving little-to-no OH or NO_x to create O₃ (OH titration). Thus, an increase to isoprene would act to reduce Toronto O₃. However, if the chemistry scheme in the GEOS-Chem adjoint were updated to that in Mao *et al.* [2013] (it is now an option in the forward model, v9-01-03), the sensitivity would be positive, as their version of isoprene oxidation recycles NO_x back into the system, rather than removing it. Thus, modelled Toronto O₃ would be even greater (and it already over-predicts both surface and column O₃, Figure 5.16(a) and (b)). We expect O₃ production in this case to be NO_x-limited, and the species indicator ratio (not shown) supports that scenario.

If the isoprene oxidation scheme in the model adjoint is correct, it appears that fossil fuel emissions from the eastern U.S. (including Nashville and Atlanta) during a period of high temperatures played a role in the pollution event on 7 September 2007. However, if the newer isoprene oxidation scheme [Mao *et al.*, 2013] is correct, the VOC emissions

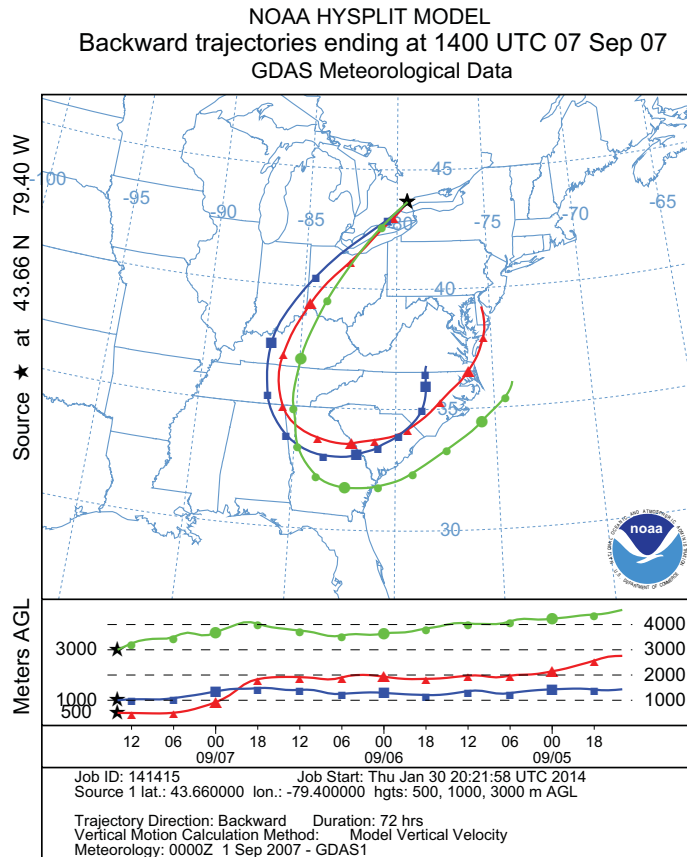


Figure 5.36: HYSPLIT back-trajectories for Toronto, starting on 7 July 2006, 14:00 UT, going back three days with points every 6 hours. Three altitudes are shown, starting at 0.5, 1.0 and 3.0 km over Toronto.

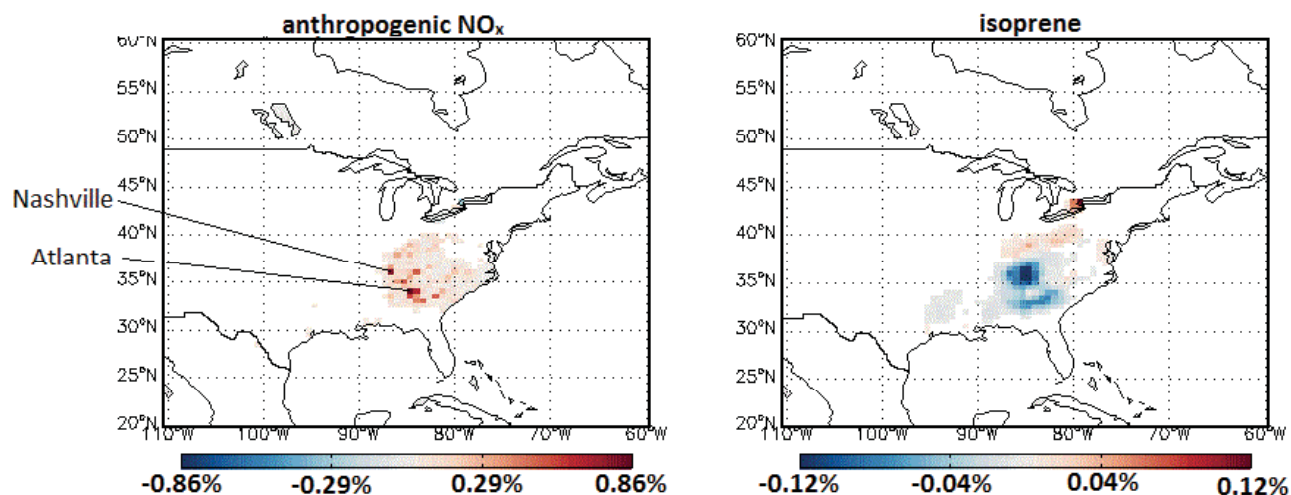


Figure 5.37: GEOS-Chem adjoint results for 7 September 2007, showing sensitivity of Toronto O_3 tropospheric columns to: (left) anthropogenic NO_x emissions, and (right) isoprene emissions.

from the southeast U.S. could have played a more significant role (although how large a role is uncertain).

5.6.3 Case 3: westerly transport and stagnant conditions cause almost 100 ppb surface O_3 in Toronto

On 21 July 2005, the 1-hour surface O_3 in Toronto was 97 ppb (17 ppb above the provincial criterion). The maximum temperature was high at almost 34°C . The TAO O_3 column was 73% (almost 2σ) greater than the monthly mean, and the TAO CO column was 33% (2σ) greater than the monthly mean. The average wind over Toronto was 6.6 m/s (slowest of the four pollution events in the case studies), and was coming from the west. The HYSPLIT back-trajectories (Figure 5.38) confirm that the wind was coming from the west, along a more typical transport pattern than those seen in the first two case studies.

The temperature and geopotential height anomalies from NCEP (Figure 5.39) show

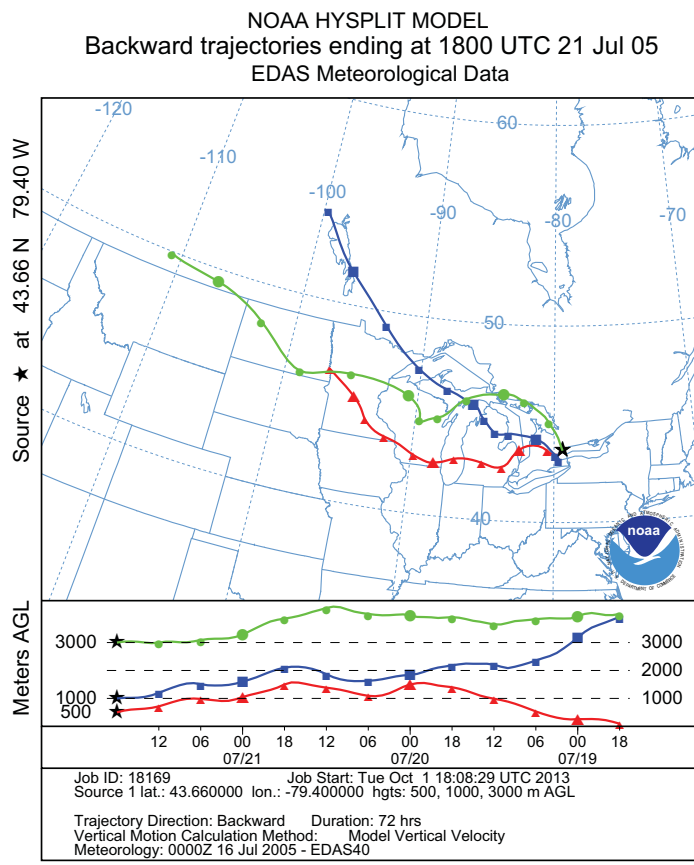


Figure 5.38: HYSPLIT back-trajectories for Toronto, starting on 21 July 2005, 18:00 UT, going back three days with points every 6 hours. Three altitudes are shown, starting at 0.5, 1.0 and 3.0 km over Toronto.

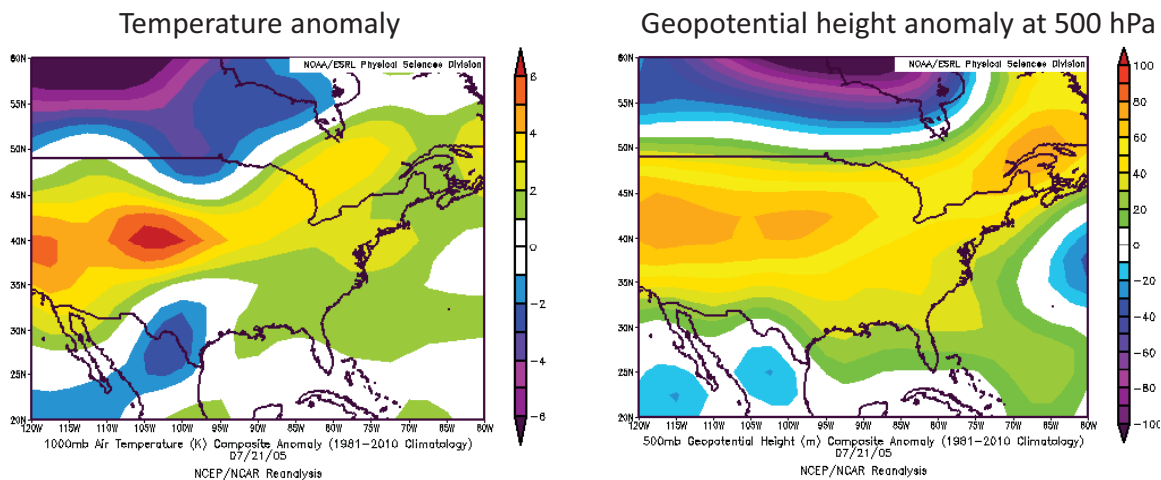


Figure 5.39: NCEP maps on 21 July 2005 of: (left) surface temperature anomaly, and (right) geopotential height anomaly compared to the 30-year climatological means.

that most of the U.S., southern Ontario, and Quebec had appropriate conditions for high O_3 (abnormally high temperatures and pressures).

The full chemistry, nested model adjoint shows that Toronto O_3 was most sensitive to anthropogenic NO_x emissions from Toronto and Hamilton (Figure 5.40, left). Recall that this was the case with the highest local sensitivity (see SOnQu in Figure 5.24, top). The sensitivity to isoprene emissions is about half as large (Figure 5.40, right). Figure 5.40 shows that the sensitivity of Toronto O_3 columns to emissions along the transport path is always positive for both NO_x and isoprene.

Given the stagnant conditions, and the high NO_x emissions in Toronto, Hamilton, and nearby U.S. cities (e.g., Detroit, Chicago), it is a little surprising that O_3 production is not hydrocarbon-limited. However, both the positive adjoint sensitivity (including in the Toronto gridbox), and the species indicator ratio ($H_2O_2/HNO_3 \sim 0.5-0.6$, map not shown) show that our region is NO_x -limited for this pollution event.

The 21 July 2005 pollution event over Toronto was thus caused during hot, stagnant conditions by local NO_x and isoprene emissions, which both have a positive influence on O_3 production, resulting in very high concentrations.

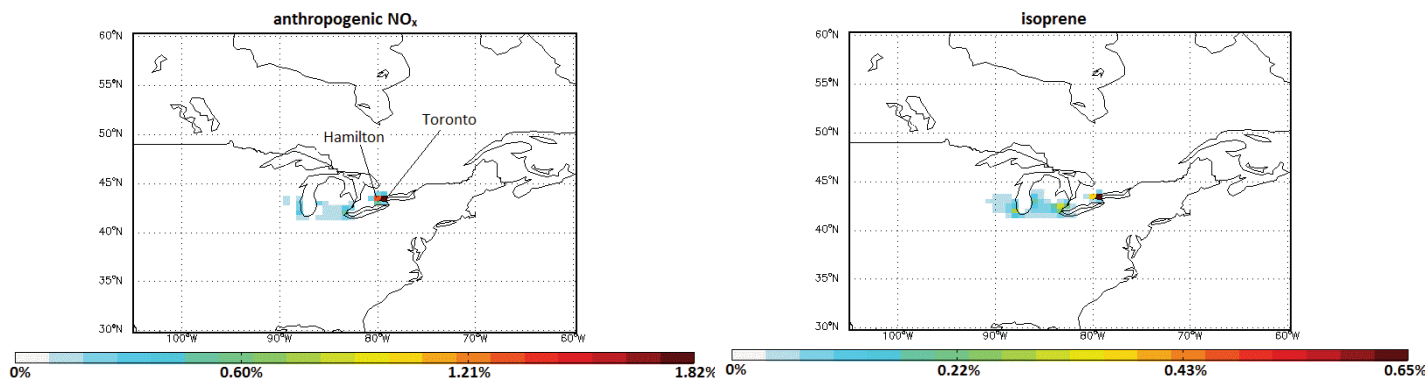


Figure 5.40: GEOS-Chem adjoint results for 21 July 2005, showing sensitivity of Toronto O_3 tropospheric columns to: (left) anthropogenic NO_x emissions, and (right) isoprene emissions.

5.6.4 Case 4: long-range transport from the west coast

We present this case study on 2 August 2007 (the pollution event actually lasted from 1 to 3 August 2007 – Figure 5.16). This was the pollution event with the highest sensitivity to the southwest region (see 20070802 in Figure 5.24, top), where the sensitivity to anthropogenic NO_x was greater 4% – slightly larger than the southern Ontario-Quebec regional sensitivity for this event (see Figure 5.41). The 1-hour surface O_3 in Toronto was 86 ppb (6 ppb above the provincial criterion), and the 8-hour average was 71 ppb (6 ppb above the CWS). The maximum temperature was high, at almost 35°C . The CARE O_3 column was 107% (almost 3.5σ) greater than the FTIR monthly mean, and the FTIR CO columns were up to 33% (1.6σ) greater than the FTIR monthly mean. The average wind over Toronto was 7.5 m/s, and was coming from the southwest. The HYSPLIT back-trajectories (Figure 5.42) confirm that the wind was coming from the west, and going back seven days prior to the pollution event, we see that the air originated from the west coast of the U.S.

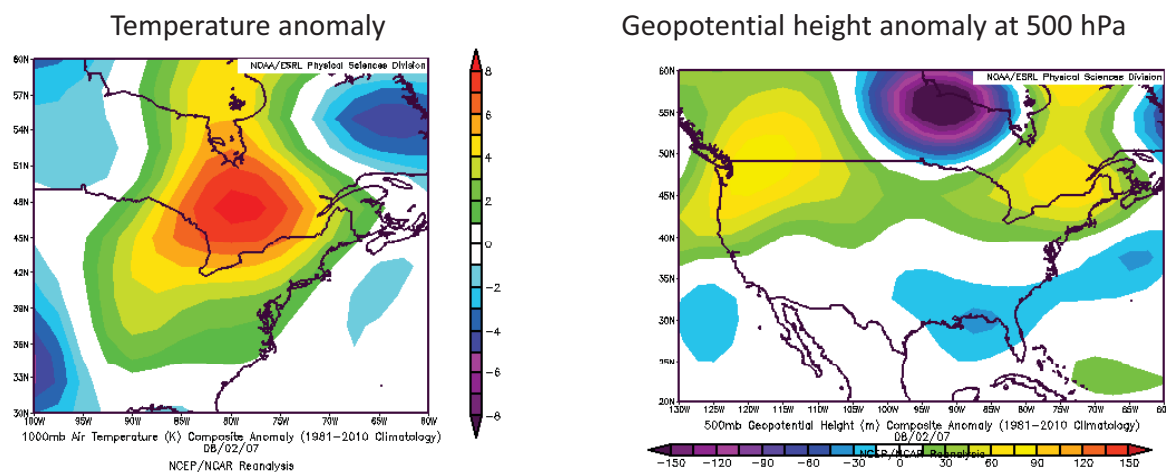


Figure 5.43: NCEP maps on 2 August 2007 of: (left) surface temperature anomaly, and (right) geopotential height anomaly compared to the 30-year climatological mean.

The temperature and geopotential height anomalies from NCEP confirm above-average temperatures over southern Ontario and western Quebec. The long-range transport from the west was likely due to the shape and location of the geopotential height anomaly (Figure 5.43), which had high-pressure systems in the west and in the east.

The full chemistry, nested model adjoint shows that Toronto O_3 was most sensitive to anthropogenic NO_x emissions from southern Ontario and Michigan (Figure 5.44, top). The darkest grid box is in Michigan and contains two coal-burning power plants: Dan E. Karn and J. C. Weadock. The sensitivity to soil NO_x emissions is the greatest for this pollution event ($>4\%$ total, Figure 5.19, and about 3% from the southwest region, Figure 5.41), and Figure 5.44, middle, shows positive sensitivity over a large swath of the Great Plains. Figure 5.44, bottom, shows that the sensitivity of Toronto O_3 columns to isoprene emissions was mostly local, and slightly negative in northern Michigan.

Since the sensitivity to fossil fuel NO_x is negative in the Toronto grid box (Figure 5.44, top), again the H_2O_2/HNO_3 ratio (not shown) was verified for the O_3 production regime, and we found that it is NO_x -limited.

We thus conclude that the August 2007 pollution event was strongly influenced by

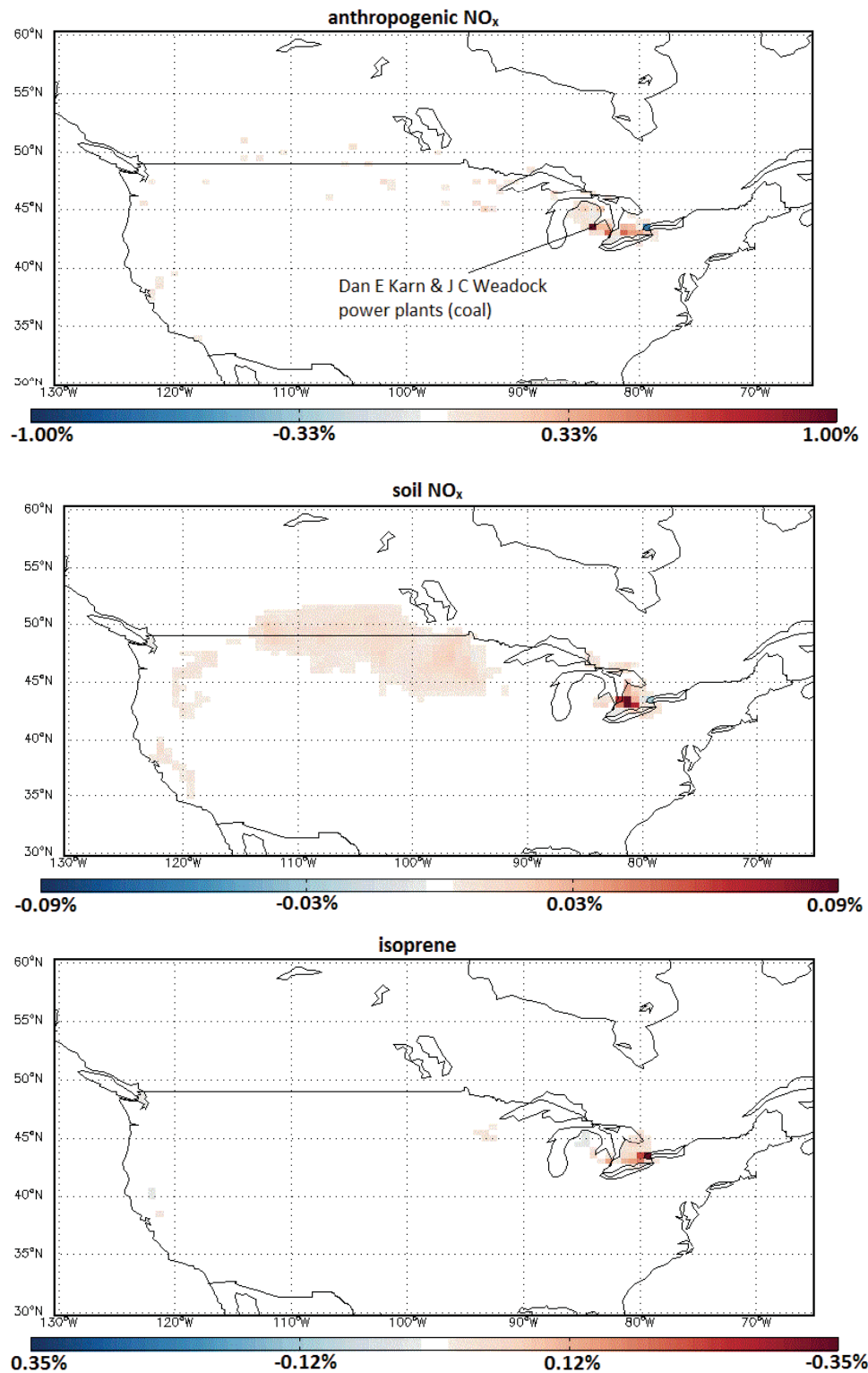


Figure 5.44: GEOS-Chem adjoint results for 2 August 2007, showing sensitivity of Toronto O₃ tropospheric columns to (top) anthropogenic NO_x emissions, (middle) soil NO_x emissions, and (bottom) isoprene emissions.

nearby fossil fuel emissions (including coal power plants in the U.S.), isoprene emissions, and long-range transport of soil emissions from the western-U.S. and the Canadian prairies.

5.6.5 Case 5: biomass burning causes large CO column increase, but has little effect on Toronto O₃

On 7 July 2006, surface concentrations of O₃ and CO were not enhanced, nor was the O₃ column. However, the TAO CO column was 21% (1.2σ) greater than the monthly mean. The average wind over Toronto was coming from the northwest, and the HYSPLIT back-trajectories indicated that transport was from northern Ontario. However, since the surface concentrations were not elevated, we checked the back-trajectory slightly higher at 4 km, which indicated transport from central Canada (Figure 5.45, left). A MODIS fire map (Figure 5.45, right) reveals a large number of fires in northern Saskatchewan. The GEOS-Chem adjoint shows that the sensitivity of the CO partial column to biomass burning is almost as great as the sensitivity to fossil fuels (almost 15% and almost 20%, respectively, when sensitivities in all regions are added. Figures 5.46 and 5.47).

We consider this event to be a biomass burning case study, and it is representative of the handful of biomass burning events found in the FTIR dataset (using CO column enhancements). Common to these events was: (a) biomass burning events tend not to elevate O₃ columns or concentrations over Toronto, and (b) biomass burning events tend not to elevate surface O₃ and CO concentrations over Toronto, although column CO (and C₂H₆ and HCN) do increase.

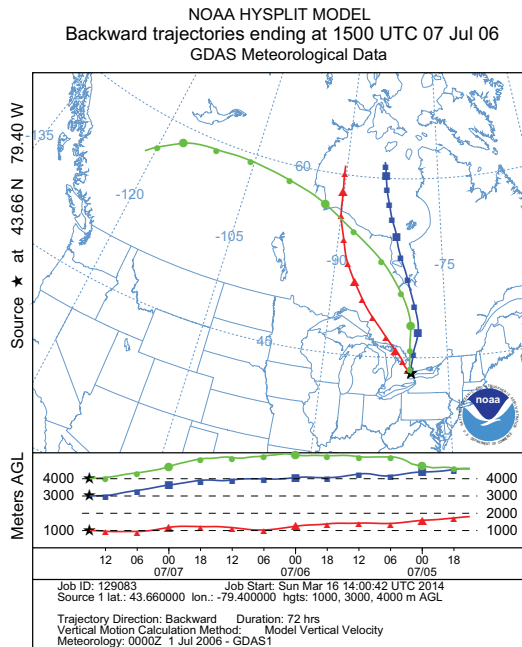


Figure 5.45: (left) HYSPLIT back-trajectories for Toronto, starting on 21 July 2005, 18:00 UT, going back three days with points every 6 hours. Three altitudes are shown, starting at 1.0, 3.0 and 4.0 km over Toronto. (right) A MODIS fire map for a period from 30 June 2006 to 9 July 2006, showing a cluster of fires in northern Saskatchewan.

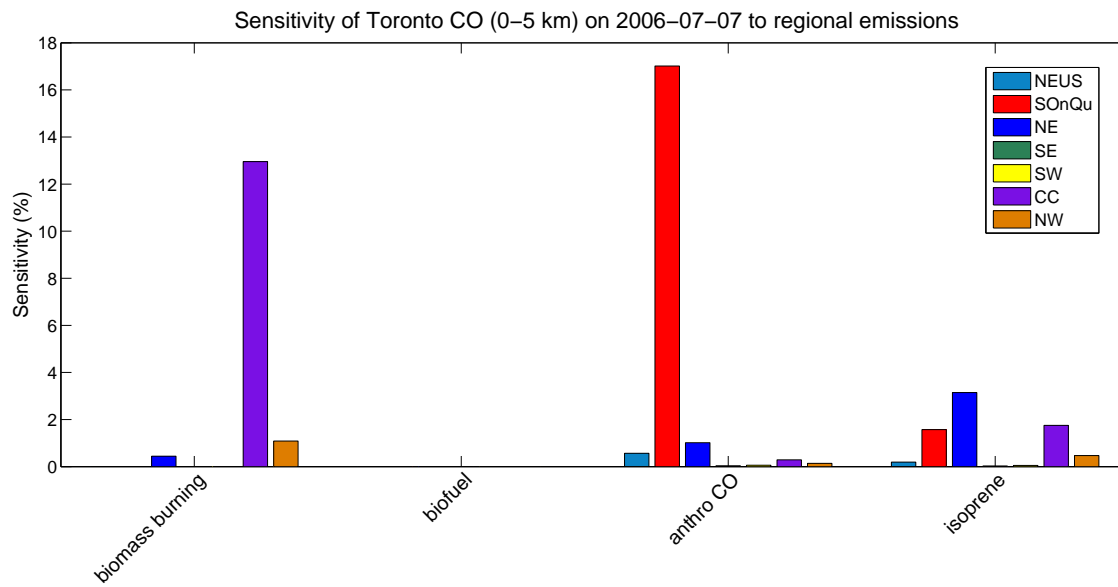


Figure 5.46: GEOS-Chem adjoint results for 7 July 2006, showing sensitivity of Toronto CO tropospheric columns to North American emissions separated by regions.

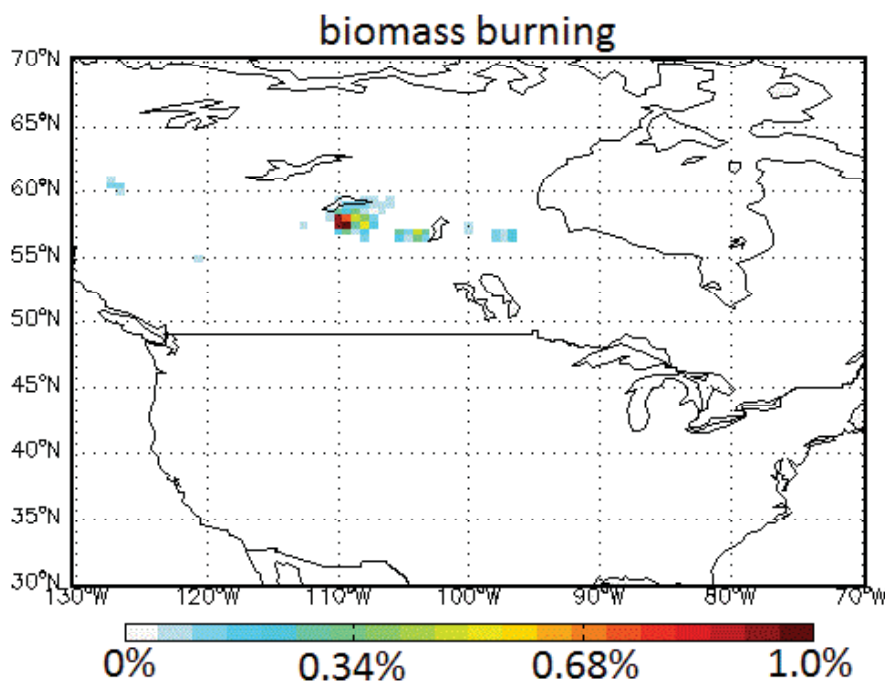


Figure 5.47: GEOS-Chem adjoint results for 7 July 2006, showing sensitivity of Toronto CO tropospheric columns to biomass burning emissions.

5.6.6 What do FTIR columns tell us that the surface measurements can't?

In this section, we also explore the difference between the amount of information the tropospheric columns and the surface measurements provide for Toronto-area tropospheric O_3 by running the GEOS-Chem adjoint for both measurement scenarios (the tropospheric O_3 column measurement, described in Section 5.3, and the surface O_3 measurement). By doing so, I hope to motivate the use of FTIR measurements in addition to traditional surface measurements for air quality studies. The tropospheric columns of O_3 are more sensitive to the background contributions to O_3 than are the surface measurements, and background O_3 is increasingly becoming important for air quality [Fiore *et al.*, 2002; Zhang *et al.*, 2008, 2011]. Thus, adjoint runs were performed for case studies 1, 2, and 4, as they represent short-, mid-, and long-range transport scenarios. Figure 5.48 shows

the sensitivity of Toronto (left) tropospheric column O_3 and (right) surface O_3 to anthropogenic NO_x emissions. The left and right panels are shown on the same colour scale, and there is a small amount (<1%) of sensitivity to emissions that have contributed to tropospheric O_3 over Toronto that are not captured by the surface measurements.

Case 4 (bottom panel of Figure 5.48) illustrates how valuable the FTIR column measurements can be. For this pollution event, the CWS for surface O_3 was exceeded in Toronto, and the O_3 and CO columns were enhanced as well. Although small in each contributing grid box, the columns were sensitive to pollution transported from the west coast of North America, whereas the surface measurements were only sensitive to pollution transported from as far away as $115^\circ W$ (Calgary, AB). Case 2 (middle panel of Figure 5.48) also illustrates the value of the FTIR columns, though to a lesser extent. While the surface O_3 was sensitive to emissions coming from the southeast U.S., only the tropospheric columns were sensitive to emissions from along the Gulf Coast (e.g., from Houston, TX; Gulfport, MS; and Mobile, AL). That said, the shorter the distance of the transport pattern, the less important the tropospheric columns become for air quality studies. For example, for case study 1 (top panel of Figure 5.48), which had transport from the relatively nearby northeast U.S., the sensitivity of Toronto's surface O_3 was very similar to that of Toronto's column O_3 . The lower-tropospheric columns were sensitive to a little information between 30° - $35^\circ N$ that the surface measurements were not, but the surface measurements were sensitive to a little information at $35^\circ N$ that the columns were not.

5.7 Summary of case studies and conclusions

Cases 1, 2, and 3 show interesting results. One might expect the case with transport from the northeast U.S. (case study 1) Toronto O_3 would be most sensitive to anthropogenic emissions, but the model suggests that the sensitivity to isoprene, emitted from natural

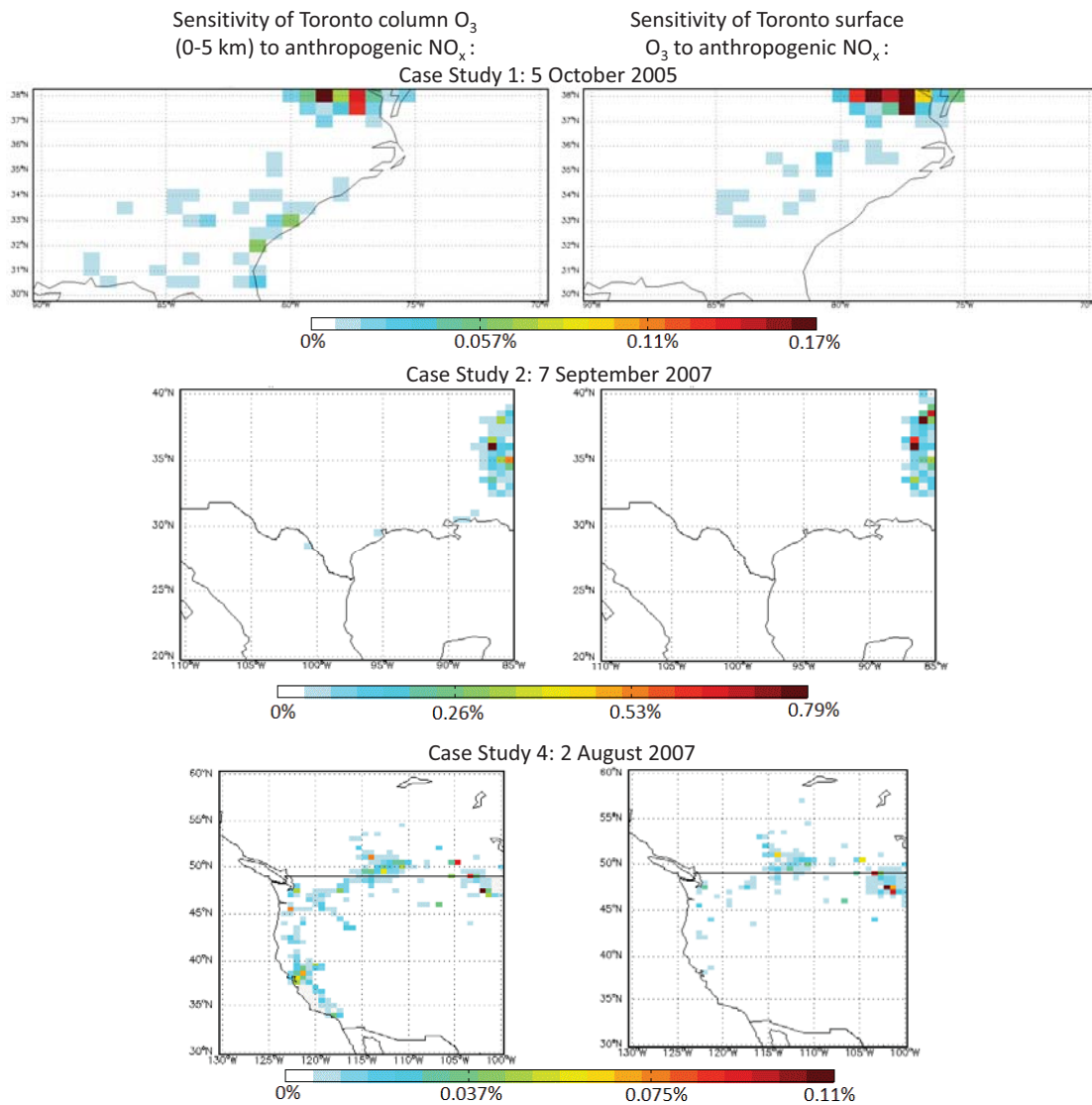


Figure 5.48: (left) Sensitivity of Toronto tropospheric column O_3 and (right) surface O_3 to anthropogenic NO_x emissions, for three case studies demonstrating (top) short-range, (middle) mid-range, and (bottom) long-range transport.

sources, was greater. One might also expect the case with transport from the southeast U.S. (case study 2) to have dominant sensitivity to the isoprene source [e.g. *Kang et al.*, 2003, Figure 5.26]. However, GEOS-Chem showed that Toronto's tropospheric O₃ column had a negative sensitivity to isoprene, and the greatest positive sensitivity was to the anthropogenic source of NO_x. Finally, one might expect that the case with transport coming from the midwest U.S. (case study 3) would bring pollution from the industrial Ohio Valley to Toronto, however, this case had the largest local influence, with sensitivity to Toronto and Hamilton area emissions dominating.

While the results are surprising, they have each been explained. In case 1, isoprene emissions were high because of the high temperatures in the region [*Monson et al.*, 1992; *Guenther et al.*, 1993], (Figure 5.30, left), and NO_x concentrations were so great that O₃ was likely VOC-limited. In case 2, isoprene concentrations were high enough to remove other O₃ precursors, although they would have had a positive effect on Toronto O₃ had the isoprene oxidation chemistry been updated in the adjoint model [*Mao et al.*, 2013]. In case 3, the conditions were rather stagnant, thus trapping local emissions.

Case 4 provided an example of long-range transport, demonstrating the usefulness of tropospheric O₃ measurements from ground-based FTIR for air quality studies. In this case, sensitivity to long-range sources was equal in magnitude to sensitivity to nearby sources, though only for the tropospheric column. The surface O₃ was only sensitive to nearer sources.

Case 5 provided an example of a biomass burning plume over Toronto, which did not show an enhancement in O₃. Whether or not tropospheric O₃ is enhanced by biomass burning emissions remains an area of study. *Crutzen and Andea* [1990], *Thompson et al.* [2001], and *Jaffe et al.* [2004] (for example) indicate that O₃ is enhanced due to biomass burning, but e.g., *Mauzerall et al.* [1998] and *Parrington et al.* [2013] indicate that it is not. In the fifteen pollution events studied here, only three (21 July 2004, 24 May 2007, and 2 August 2007) had any significant sensitivity to biomass burning emissions (up to

at most $\sim 3\%$, Figure 5.20). The sparse nature of the TAO O_3 measurements presents a challenge for meaningful conclusions about biomass burning and O_3 to be drawn.

Table 5.2 summarizes the findings for the five case studies discussed in this chapter.

5.8 Future work

5.8.1 Source attribution over the whole time series

This chapter described pollution events mainly between 2004 and 2007, inclusive, identified using both FTIR tropospheric columns of O_3 and CO, and surface O_3 exceedances. There were ten pollution events in 2002 and 2003 that were presented but did not discussed because the high-resolution inputs for the GEOS-Chem adjoint and forward model were not available. However, those pollution events could be studied using GEOS-Chem at coarser resolution ($2^\circ \times 2.5^\circ$), or with a different regional air quality model at high resolution.

Similarly, pollution events from 2008 to the present were not shown or discussed in this chapter. There was only one pollution event (as we have defined them) in 2008 (7 July), none in 2009, and one in 2010 (30 August). Events in 2011 through to the present were not modelled because, at the time, the biomass burning emission inventories were not available for input into the model. However, GEOS-Chem could be run for those years in the near future, and more recent pollution events could be studied. It would be interesting to see how the sensitivities change with time, as NO_x emission reductions over the last decade were significant, especially in the Ohio River Valley (which is upwind of Toronto), where the NO_x SIP Call Program had a large effect [Gilliland *et al.*, 2008]. We expect that air quality will improve with those reductions, however, it is also expected that air quality will worsen with climate change. Therefore, continuing to monitor pollution events in Toronto remains important.

The data density at TAO increased in 2010, as a service visit to the instrument and an

Table 5.2: Summary of findings for the five pollution event case studies presented in this chapter: date and time of the events, surface O_3 VMR (if the surface O_3 criteria were exceeded, \sim if they were not) from MOE, the FTIR column enhancement (factor of sigma above the monthly mean if greater than 1σ , \sim if not, and x if no measurement), the maximum temperature in Toronto on the day of the event from Environment Canada, the average GEOS wind direction and speed over the $2^\circ \times 2.5^\circ$

Toronto grid box at the given date/time, and the cause/sources of the pollution event.

case study	date/time (UT)	surface O_3 1-hour/8-hour (ppb)	O_3/CO tropospheric column enhancement (σ)	maximum temperature ($^\circ C$)	wind direction ($^\circ$)/speed (m/s)	cause/sources
1	2005-10-05/21	$\sim/71$	1.5/ \sim	25	231/7.3	High NO_x and O_3 transport from northeast U.S. (e.g., Washington, D.C.).
2	2007-09-07/14	81/ \sim	x/3	33	225/20.6	NO_x transport from southeast U.S. (e.g., Nashville, Atlanta) and maybe high isoprene emissions.
3	2005-07-21/18	97/ \sim	2/2	34	306/6.6	Local NO_x and isoprene (e.g., Toronto, Hamilton).
4	2007-08-02/13	86/71	3.5/1.6	35	234/8.0	Nearby and long-range fossil fuel NO_x (e.g., Michigan power plants, southern Ontario), long-range transport of soil NO_x .
5	2006-07-07/14	\sim/\sim	$\sim/1.2$	29	315/3.9	Local CO from fossil fuels (Toronto), and biomass burning from northern Saskatchewan.

upgrade to the computer that runs the TAO-FTS improved the quality and quantity of the measurements. In March 2014, measurement frequency was further improved by an increase in the scan mirror speed (from 0.5 cm/s to 1.0 cm/s). With this improvement, it may become possible to analyse variations on the diurnal scale at TAO.

If enhancements over a longer time series (e.g., 2004 to 2014 at high resolution) were analysed in a similar way to this work, some statistics on the sources and causes of Toronto O₃ pollution could be determined, with possible implications for policy. For example, one could determine the percentage of pollution events that were dominated by the northeast U.S. box (Figure 5.23) in the 2004-2007 time period, and compare that with the percentage of pollution events that were dominated by the northeast U.S. box in the 2011-2014 time period, and see if it has changed. If it has, this could be a result of the NO_x emission reduction policies in that region of the U.S., as well as the downturn in industry that began in the 2008 recession. If it hasn't, it could be a result of climate change offsetting the emission reductions. This kind of calculation could be repeated for all of the other North American regions, with investigations into what changed in each region during the last decade.

I did not discuss the low-lying outliers in the TAO tropospheric species. These “clean episodes” may be due to low-pressure systems passing over Toronto, ventilating pollution and perhaps washing out pollution in precipitation. This could be a topic for future investigation.

5.8.2 Source attribution for other species

GEOS-Chem is a powerful model for many species, with many applications. To start, it would be interesting to run the tagged CH₄ and C₂H₆ simulations to see how well they compare to the TAO time series, and if the comparison is good, to see how much of the Toronto columns come from each emission source and geographical region. *Paton-Walsh et al.* [May 2011] did a tagged C₂H₆ simulation of global emission sources using

GEOS-Chem, and looked at the output for Wollongong, Australia and Toronto (and compared to TAO data that we provided). They found that the natural gas source was responsible for over 90% of the Toronto C_2H_6 columns, with biomass burning contributing sporadically, and biofuels contributing only a very small amount. We could run the simulations ourselves, defining source regions (e.g., those in Figure 5.23) for the natural gas source to further pinpoint the dominant sources for Toronto. We could then do the same for CH_4 . For CH_4 , *Wunch et al.* [2009] found that urban emissions (e.g., from natural gas leaks and from waste) were a significant source of CH_4 , but that these were not accounted for well in emission inventories. If the TAO CH_4 columns differ greatly from the tagged GEOS-Chem model, this could point to errors in emissions inventories.

Once a formaldehyde (HCHO or CH_2O) retrieval from TAO is available, it would be useful to compare it to GEOS-Chem HCHO, which is included in the full chemistry simulation. If the TAO product is uncertain, the model could help validate the TAO HCHO measurements, as GEOS-Chem HCHO has been validated in other studies [e.g. *Palmer et al.*, 2003; *Abbot et al.*, 2003; and *Millet et al.*, 2008]. Once confidence in the retrieval is achieved, HCHO could be useful in investigating the chemical processes that create O_3 , since it is an intermediate chemical produced by the oxidation of CH_4 and VOCs (4.10). It is lost through oxidation by OH and through photolysis (4.11), and only has a lifetime of a few hours [*Jones et al.*, 2009; *Vigouroux et al.*, 2009]. The seasonal cycle of HCHO is strong and peaks in the summertime because it is closely tied to the OH concentrations. Because of its short lifetime, its spatial distribution closely matches that of its sources, and therefore can be used as a tracer to constrain VOC emissions over land [*Vigouroux et al.*, 2009]. The long-term trends are not clear, but HCHO is likely increasing globally because of increasing CH_4 and VOCs in developing countries [*Jones et al.*, 2009].

5.8.3 FTIR data assimilation

Finally, given the dense distribution of North American anthropogenic emissions around Toronto (Figure 4.2), and the uncertainty in the emission inventories, TAO and CARE FTIR measurements of O_3 and CO could be assimilated into the model to see how anthropogenic NO_x and CO emissions change. A preliminary observing system simulation experiment (OSSE) was done to show this promise. Those results are shown in Figure 5.49, where a scale factor close to one indicates regions where the Toronto column measurements can constrain anthropogenic NO_x emissions well. Similarly, one could use O_3 and CO data from all of the NDACC-IRWG stations in a global inversion analysis to constrain anthropogenic emissions.

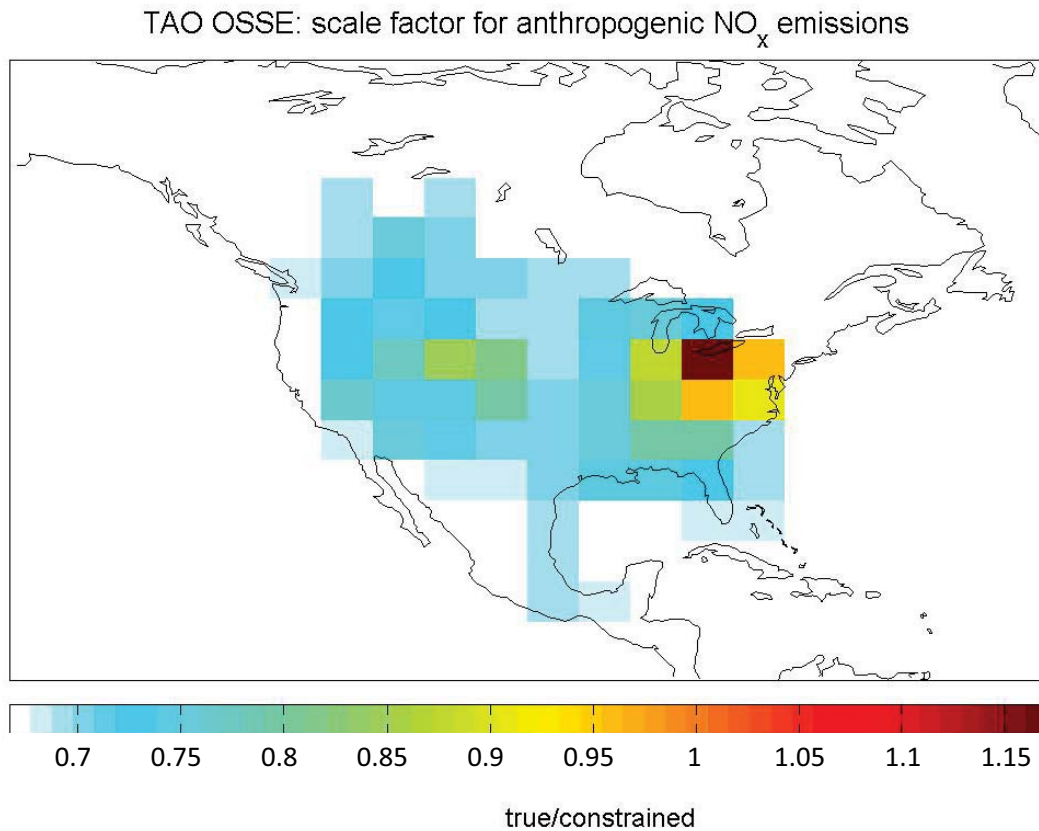


Figure 5.49: TAO OSSE using real TAO observation frequency in July 2010. The scale factors are true emissions divided by constrained emissions for an a priori “bad guess” of 50% more anthropogenic NO_x emissions ($1.5\times$). Here scales of 0.5 = no constraint, 1 = get back the true emissions, and >1 = over-constrained.

Chapter 6

Interpretation of TAO stratospheric variability: effect of polar vortex dynamics

In this chapter, I aim to answer the question: Are polar vortex dynamics responsible for variability of stratospheric trace gases measured over Toronto? In addition to the TAO and CARE datasets described in previous chapters, complementary O₃ data from the Optical Spectrograph and InfraRed Imaging System (OSIRIS) satellite instrument were used. Also the Modern-Era Retrospective Analysis for Research and Applications (MERRA) reanalysis, derived meteorological products (DMPs), the Global Modelling Initiative (GMI) and the Modèle Isentrope du transport Mésos-échelle de l'Ozone Stratosphérique par Advection (MIMOSA) were used to study polar vortex intrusions over our site in the mid-latitudes.

The goals of this chapter are to use long-term measurements to estimate how often polar intrusion events occur over the Toronto region, and to determine whether these polar intrusion events can explain some of the variability in the FTIR time series of trace gases observed at TAO and CARE. This study is the first to report polar intrusion events

over southern Canada, using long-term ground-based measurements of stratospheric partial columns (12-50 km) of HF and N₂O obtained by FTIR spectroscopy to identify their occurrence. It was published as a paper in the Journal of Geophysical Research - Atmospheres [Whaley *et al.*, 2013].

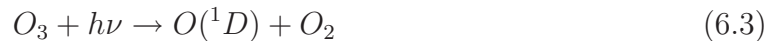
This chapter is organized as follows. The next section (6.1) provides background information about the stratospheric polar vortex. Section 6.2 shows how FTIR measurements at TAO are sensitive to the stratosphere. Section 6.3 briefly describes the complementary measurements. Section 6.4 describes the MIMOSA model and the MERRA data assimilation system from which potential vorticity (PV) has been used to confirm the occurrence of polar intrusion events. The GMI CTM, and DMPs are also described in this section. This is followed by a discussion of our results (Section 6.5), and conclusions (Section 6.6).

6.1 Background: the stratosphere and the polar vortex

The stratosphere contains less than 15% of the atmosphere's mass, although it contains the bulk of the O₃ in the atmosphere [Andrews, 2005]. Stratospheric O₃ protects life on Earth from the Sun's harmful ultraviolet (UV) radiation. While east-west motion in the stratosphere is faster, the most important flow in the stratosphere is the Brewer-Dobson circulation, which involves tropospheric air entering the stratosphere in the tropics, then slowly moving poleward through the lower stratosphere to the winter pole. Air then descends at mid- to high-latitudes, slowly returning to the troposphere there [Butchart, 2014]. The Brewer-Dobson circulation is driven by Rossby wave breaking which decelerates the polar jet, resulting in mid-latitude air intruding into the polar region, where it cools and descends. The descending air at the winter pole requires, by mass conservation, that tropical air move in to replace it, which requires tropospheric air at the tropics to

ascend to replace that [Brewer, 1949; Dobson, 1956].

The reason the bulk of the atmosphere's O_3 is in the stratosphere is because it is there that there is enough of the Sun's high energy (short wavelength, $\lambda < 240$ nm) radiation to break apart O_2 molecules into ground-level triplet state (3P) oxygen atoms, which then react with atomic oxygen to create O_3 :



where M is a third body. These reactions are called the Chapman mechanism [Chapman, 1929]. Stratospheric O_3 is lost through photodissociation, and catalytic loss cycles with hydrogen oxides (HO_x), which originate from tropospheric H_2O , and nitrogen oxides (NO_x), which originate from tropospheric N_2O . These production and loss reactions create the natural steady state of the ozone layer [Jacob, 1999]. Additional O_3 loss can occur due to catalytic loss cycles with chlorine radicals (ClO_x), which originate from industrial chemicals called chlorofluorocarbons (CFCs).

The stratospheric polar vortex is a large low-pressure system that persists over the winter pole for many months, characterized by low temperatures, high PV, and high winds near its boundary. PV is defined as:

$$PV = \frac{\omega_I \cdot \nabla\theta}{\rho} \quad (6.5)$$

where ω_I is the vorticity vector in the inertial frame, θ is the potential temperature (the temperature a parcel of air would have if it were adiabatically brought to surface pressure), and ρ is the fluid density [Andrews, 2005]. $\nabla\theta$ is the stratification term, so PV is proportional to the dot product of vorticity and stratification. PV increases with altitude, so it is often more useful to use *scaled potential vorticity* (sPV, Equation 6.6).

sPV is calculated such that it is similar at all vertical levels in the stratosphere [*Dunkerton and Delisi*, 1986; *Manney et al.*, 1994].

$$sPV = \frac{PV}{\delta\theta/\delta p} \quad (6.6)$$

The descent of air within the polar vortex and its relative isolation result in a distinctive chemical composition; hydrogen chloride (HCl), hydrogen fluoride (HF) and O₃ total and stratospheric columns tend to be enhanced because when these stratospheric gases descend in altitude they maintain their mixing ratio but their number densities increase. O₃ columns in particular are increased (in the absence of chemical O₃ loss) during winter because of poleward transport from the tropics and then descent via the Brewer-Dobson circulation described above. Similarly, the descent of long-lived tropospheric gases like N₂O (which is destroyed in the stratosphere) results in diminished columns of N₂O in the polar vortex [*Schoeberl et al.*, 1992, 1995; *Brasseur et al.*, 1999].

The northern polar vortex typically extends down to about 65°-68°N in latitude when centered near the North Pole, and its edge has been defined in a number of ways: using PV gradients and wind speeds [e.g., *Nash et al.*, 1996], the Q-diagnostic method [e.g., *Harvey et al.*, 2002], and sPV [e.g., *Manney et al.*, 2007 and this study]. In the spring, when the vortex breaks up, parts or fragments of a highly distorted vortex can extend to much lower latitudes [*Waugh et al.*, 1994; *Orsolini*, 1995; *Hauchecorne et al.*, 2002]. Excursions of the polar vortex to mid-latitudes have been observed and modelled [*Godin et al.*, 2002; *Marchand et al.*, 2003; *Konopka et al.*, 2003; *Durry and Hauchecorne*, 2005; *Duchatelet et al.*, 2009], as have filaments breaking off the polar vortex and extending to the mid-latitudes [*Leovy et al.*, 1985; *Andrews et al.*, 1987; *Pierce and Fairlie*, 1993; *Manney et al.*, 1998, 2000; *Newman et al.*, 1996; *Orsolini et al.*, 1998; *Godin et al.*, 2002; *Hauchecorne et al.*, 2002; *Marchand et al.*, 2003; *Millard et al.*, 2003; *Tripathi et al.*, 2006]. Filaments are formed when the vortex edge is deformed by meridional winds induced by planetary Rossby waves breaking [*McIntyre and Palmer*, 1984; *Waugh et al.*, 1994] and subtropical anticyclones [*Pierce and Fairlie*, 1993]. The filaments are stretched out by the

meridional gradient of the zonal wind over the course of a few days [*Pierce and Fairlie, 1993; Marchand et al., 2003*].

The previous studies of polar intrusion events mentioned above used measurements of O_3 , CH_4 , N_2O , HCl , H_2O , CO_2 , COF_2 , and CFCs from lidars, ozonesondes, aircraft-borne photometry and spectroscopy, ground-based spectroscopy, and balloon-borne *in situ* instruments, as well as reverse domain-filling trajectory calculations [e.g., *Sutton et al., 1994; Schoeberl et al., 1995; , 1998, 2000*], and 3-D CTMs such as the Single Layer Isentropic Model of Chemistry And Transport (SLIMCAT), the Chemical Lagrangian Model of the Stratosphere (CLaMS), and MIMOSA to detect and model polar intrusion events. There have been several studies of polar intrusion events observed over Europe [*Orsolini et al., 1997, 1998; Godin et al., 2002; Durray and Hauchecorne, 2005*], but only a few over North America (and Hawaii) [*Newman et al., 1996; Manney et al., 1998; Tripathi et al., 2006*].

Polar intrusion events can have varying, but significant, effects on mid-latitude O_3 columns. When the vortex is cold and stable, conditions are favourable for chemical O_3 depletion, but are unfavourable for filamentation, and thus to transport to mid-latitudes [*Hauchecorne et al., 2002; Millard et al., 2003*]. Conversely, when a stratospheric warming occurs, the polar vortex is more likely to break up and extend to mid-latitudes [*Waugh et al., 1994; Hauchecorne et al., 2002*]. It has been reported that up to 50% of mid-latitude O_3 VMR decreases at 475 K can be accounted for by polar intrusions of O_3 -poor polar air to mid-latitudes [*Marchand et al., 2003; Millard et al., 2003*]. However, increases in mid-latitude O_3 due to polar vortex intrusions have also been reported [e.g., *Godin et al., 2002; Tripathi et al., 2006*].

HF is an excellent dynamical tracer for the polar vortex because it has a long lifetime, and, as mentioned previously, it has a greater density inside the polar vortex [*Chipperfield et al., 1997; Toon et al., 1999; Mellqvist et al., 2002; Coffey et al., 2008*]. Therefore, we examine eleven years of Toronto FTIR data (January 2002 to March 2013), looking for

outliers of HF as an indicator of polar air. Polar intrusions are then either confirmed or discounted as the source of the outliers using sPV, models and satellite observations, which provide more spatial coverage, showing the polar vortex structure at the time of the HF outlier.

6.2 FTIR sensitivity to the stratosphere

Detecting polar vortex intrusions using ground-based FTIR spectroscopy has a few advantages over the other measurement techniques mentioned in Section 6.1: It can be used to measure multiple trace gases simultaneously, or nearly so, including HF; it has sensitivity extending to the upper stratosphere; and it can provide datasets that cover long time periods (e.g., there have been semi-regular measurements at TAO since 2002). That said, the TAO dataset is somewhat sparse, and there are many other instruments that measure stratospheric O_3 .

As discussed in Section 2.4.3, the TAO averaging kernels characterize the vertical information contained in the FTIR retrievals [*Rodgers, 2000*]. Figure 6.1 shows typical TAO VMR averaging kernels for total column HF, HCl, O_3 , and N_2O retrievals along with the stratospheric partial column (12-50 km) averaging kernels. The weighting by density, along with some smearing of information to higher altitudes, is what causes the partial column averaging kernel to increase at higher altitudes for HF, HCl, and O_3 . Also plotted is the sensitivity (Equation 2.30), which was explained in Section 2.4.3. The HF, HCl, and O_3 retrievals all have excellent sensitivity ($S_k \sim 1$) in the stratosphere. While the N_2O retrievals have more sensitivity to the troposphere, S_k is > 0.5 throughout most of the stratosphere, and the DOFS is 1.8 for the 12-50 km partial columns (see Table 3.3). Thus, the N_2O retrievals have good sensitivity in the stratosphere as well.

About 80% of the stratospheric columns (12-50 km) come from 12-35 km (360-1000 K), 12-32 km (360-850 K), 12-20 km (360-500 K), and 12-32 km (360-850 K), for HF,

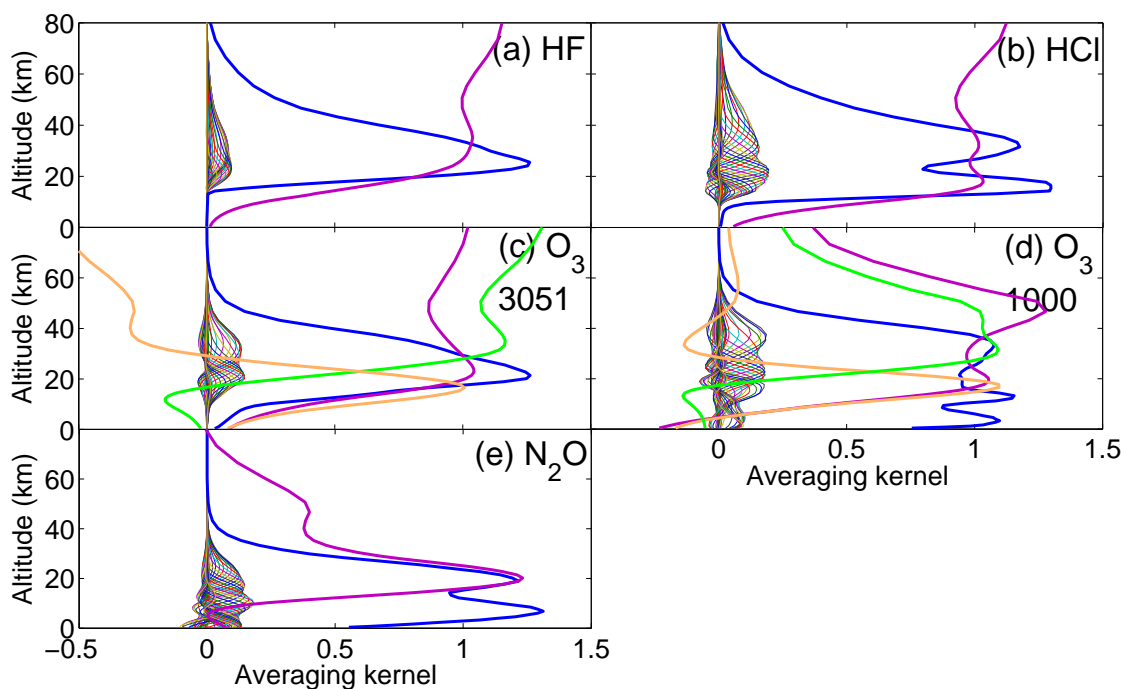


Figure 6.1: VMR averaging kernels (thin coloured lines), sensitivity (thick blue lines), and stratospheric partial column (12-50 km) averaging kernels (thick purple lines) for TAO retrievals of (a) HF, (b) HCl, (c) O₃ (from 3051 cm⁻¹ microwindow), (d) O₃ (from 1000 cm⁻¹ microwindow), and (e) N₂O. In panels (c) and (d), the O₃ partial column averaging kernels for 12-23 km and 23-50 km are shown in orange and green, respectively.

HCl, N₂O and O₃, respectively.

6.3 Complementary measurements

6.3.1 CARE FTIR spectrometer

Refer to Chapter 4, Section 4.3 for a description of the CARE FTS. The CARE DA8 has the same characteristics as the DA8 spectrometer at TAO, and HF, HCl, O₃, and N₂O stratospheric columns were retrieved in the same way as described in Chapter 3 and using the parameters in Table 3.3. The errors of the Egbert stratospheric columns are also the same as those for TAO, which are 3%, 3.5%, 8.6%, and 9.0% for HF, HCl, O₃, and N₂O, respectively. The Egbert results complement those from TAO, as the two sites are generally close enough to be looking at the same stratospheric air. That is, the two sites are less than 1° apart, which is the resolution of the MIMOSA and MERRA maps. Theoretically though, a small filament could be over one site and not the other.

6.3.2 OSIRIS

We use O₃ partial columns (12-50 km) from OSIRIS on the Odin satellite [Murtagh *et al.*, 2002; Llewellyn *et al.*, 2004], over the Toronto region (within 600 km, or approximately 5°, of Toronto, 43.66°N, 79.40°W) to complement our TAO and CARE O₃ time series. These data are available from November 2001 to the present, and have previously compared favourably to TAO O₃ [Taylor *et al.*, 2007]. We also use OSIRIS O₃ maps centered over the North Pole, to examine O₃ distributions at the time of the observed polar intrusion events. To produce polar maps at fixed potential temperature levels, we use the method in Adams *et al.* [2013b], where OSIRIS data were passed through a Gaussian filter with a 12° full width at half maximum onto a 5°x5° latitude/longitude grid. For each grid-point, the angular distance between the grid-point and the OSIRIS measurements was calculated. Weights based on the angular distance between the measurements and the grid-point were

calculated using the Gaussian function. The weighted mean of OSIRIS measurements at the given grid-point was then calculated. If the sum of weights at a given grid-point was < 1 , the grid-point was left empty. The Gaussian filter and the interpolation grid were tested for various cases to ensure that smoothing and interpolation did not introduce any spurious features in the maps. The 5° filter provided the best balance between showing the details in the OSIRIS measurements and not leading to large gaps in the figure. The choice of interpolation grid did not have a significant impact on the maps for the measurement dates considered.

OSIRIS observes limb-radiance profiles of scattered sunlight from 280 to 800 nm at 1-nm spectral resolution, with a 1-km vertical field-of-view over tangent altitudes ranging from approximately 10 to 100 km. Vertical profiles are obtained every 5° along the Sun-synchronous satellite track inclined at 98° , and are nominally measured in the orbit plane, limiting the maximum latitude coverage to 82° . Approximately 15 orbits are performed each day, providing measurements every 24° of longitude at the equator and much denser coverage at high latitudes. OSIRIS measures within 600 km of Toronto several times per day and measures O_3 , aerosol, and NO_2 during the Northern Hemisphere spring and summer (starting in mid- to late-February for Toronto).

The SaskMART (Multiplicative Algebraic Reconstruction Technique) [*Degenstein et al.*, 2009] v5.01 O_3 product was used in this study. O_3 absorption information in both the UV and visible parts of the spectrum is used to retrieve number density profiles from 60 km to the cloud tops (down to a minimum of 10 km in the absence of clouds). The 12-50 km partial columns were derived from these number density profiles. OSIRIS O_3 mixing ratios, calculated from number density and neutral density profiles, are also available. SaskMART v5.0x O_3 has been well validated, with less than 2% bias compared to other satellite measurements [*Degenstein et al.*, 2009; *Adams et al.*, 2013a, 2014].

6.4 Models and meteorological analyses

GMI, MIMOSA, MERRA and DMPs derived from MERRA can be used to trace the location and extent of the polar vortex. We use all of these to confirm the passage of polar vortex air over Toronto in this study.

6.4.1 Potential vorticity from MIMOSA and MERRA

We use PV maps centered over the North Pole to determine the location and extent of the polar vortex. PV is an excellent polar vortex tracer because the polar vortex is defined by the polar night jet, and as the vortex spins up in the autumn, PV increases and strong PV gradients form along the vortex edge [e.g., *Nash et al.*, 1996]. PV is conserved on potential temperature surfaces and behaves similarly to a chemical tracer in the absence of diabatic and frictional effects [*Hoskins et al.*, 1985].

We have obtained PV maps from the MIMOSA model, and the MERRA data reanalysis for this study. We have also extracted the MIMOSA and MERRA PV time series over TAO's coordinates to look for enhancements in potential vorticity that coincide with the enhancements in our stratospheric partial column measurements.

MIMOSA is a high-resolution (1° by 1°) advection model of PV developed at the Service d'Aéronomie (for a full description, see *Hauchecorne et al.* [2002]). MIMOSA is driven by the European Centre for Medium-Range Weather Forecasts (ECMWF) wind fields, which are advected along potential temperature surfaces [ether.ipsl.jussieu.fr/ether/pubipsl/mimosa_uk.jsp]. PV is given in potential vorticity units ($1 \text{ pvu} = 10^{-6} \text{K m}^2 \text{ kg}^{-1} \text{ s}^{-1}$). MIMOSA was developed to quantify the effect of transport of polar air on lower stratospheric O_3 at mid-latitudes [*Marchand et al.*, 2003], and has been shown to be capable of predicting filament locations to within 100 km [*Hauchecorne et al.*, 2002], making it well suited for this study.

MERRA is a long-term meteorological data reanalysis using NASA's GMAO GEOS-5

data assimilation system (see Section 4.6 for acronyms). It was developed at the NASA Goddard Earth Sciences Data and Information Services Center [*Rienecker et al.*, 2011]. The GEOS-5 system is run at a resolution of 0.5° latitude by 0.67° longitude, but PV for MERRA is output on a reduced resolution grid (1° by 1.25°), and on pressure levels, over which PV is not conserved. We interpolated MERRA PV onto potential temperature levels, and compared PV at four vertical levels (435 K, 475 K, 675 K, and 950 K) to that from MIMOSA. MERRA and MIMOSA maps agree well despite being based on different meteorological analyses, so the two independently confirm the location of the polar vortex and its filaments. MERRA output goes as far back as 1979 and has output every three hours for each day (in Section 6.5 I present MERRA output at 15 UT on each day, which coincides closely with morning measurements at TAO), whereas MIMOSA output is only available beginning in 2005 and only output at 12 UT on each day. Therefore, the MERRA fields alone allow us to check for polar intrusion events in our dataset between 2002 and 2004.

6.4.2 N_2O and O_3 from GMI

Since the chemical lifetime of N_2O in the stratosphere is much longer than dynamical timescales, we use modelled N_2O from the GMI 3D CTM [*Strahan et al.*, 2007] as another polar vortex tracer. Because N_2O is a passive tracer of air motions, it has been used in previous dynamical studies [e.g., *Orsolini et al.*, 1998; *Orsolini and Grant*, 2000; *Manney et al.*, 2000]. GMI O_3 is also used in this study as its chemical lifetime is long in the lower stratosphere in the absence of heterogeneous chemical O_3 depletion. In Section 6.5, I present GMI O_3 maps in order to both track the location of the polar vortex and assess whether polar O_3 is reduced or enhanced at the time of our events.

GMI includes both tropospheric and stratospheric chemistry, and is driven by assimilated meteorological fields from MERRA [*Rienecker, M. M. et al.*, 2011]. Combined stratosphere-troposphere runs [*Duncan et al.*, 2007] were used in this study, and natu-

ral and anthropogenic emissions were both considered. The horizontal resolution of the model is $2^\circ \times 2.5^\circ$, output on 72 pressure levels, with a lid at 0.015 hPa (~ 75 km). We present polar maps interpolated onto four potential temperature surfaces (435 K, 475 K, 675 K, and 950 K) that were produced from the output at 12-12:30 UT.

6.4.3 Derived meteorological products

Schoeberl and Newman [1995] have shown that the vertical extent of polar vortex filaments varies greatly. Typically, filaments are shallow (a few kilometers thick), but sometimes they can extend through much of the depth of the stratosphere. In order to determine the vertical extent of our observed polar vortex intrusions, we use DMPs [*Manney et al.*, 2007] based on MERRA meteorological fields, which include temperature, potential temperature, pressure, equivalent latitude (EqL), PV, sPV (given in vorticity units (10^{-4} s^{-1}), tropopause height, horizontal winds, and vortex edge location, all interpolated to the measurement locations. EqL is the latitude that would enclose the same area between it and the pole as a given PV contour [*Butchart and Remsberg*, 1986; *Manney et al.*, 2007]. The vortex edge is defined as in *Manney et al.* [2007], by the EqL of the maximum of the wind speed times the horizontal PV gradient.

We use the time series of sPV over Toronto at four stratospheric levels (see previous section), and we also examine the vertical profiles of sPV over Toronto during the polar intrusion events to determine the vertical extent over which the polar intrusions occurred. sPV is used to determine when Toronto is inside the polar vortex; the outer edge of the vortex is defined to be at an sPV of $1.2 \times 10^{-4} \text{ s}^{-1}$, and the inner vortex edge is defined to be at an sPV of $1.6 \times 10^{-4} \text{ s}^{-1}$ [*Manney et al.*, 2007]. Note that, except during vortex breakup, the EqL and sPV methods of determining the vortex edge location agree quite well in the lower stratosphere (which comprises the bulk of the O_3 column), but that no automated vortex edge identification works especially well in the springtime [*Manney et al.*, 2007].

6.5 Results and discussion

6.5.1 Identification and frequency of polar intrusion events

The complete TAO and CARE time series, from January 2002 until March 2013, of individual measurements of stratospheric HF, HCl, O₃, and N₂O partial columns are shown in Figure 6.2. These gases have seasonal cycles, with HF, HCl, and O₃ stratospheric columns having maxima in the spring and N₂O stratospheric columns anti-correlated, having maxima in the late-summer/early-fall. There are also many outliers in the time series (Figure 6.2) that are associated with good spectral fits and realistic retrieved profiles, and so we would like to determine the causes of some of this atmospheric variability. OSIRIS O₃ partial columns (12-50 km) over Toronto (within 600 km) are included to help fill in the gaps in the FTIR time series, and they agree well with the TAO DA8 O₃ measurements, with only a 5% systematic bias (OSIRIS greater than TAO). Therefore, there is a good connection between the ground-based measurements and the OSIRIS maps that appear in Section 6.5.3. Figure 6.2 also includes the sPV time series at four vertical levels in the stratosphere; 435 K (~16 km), 475 K (~18 km), 675 K (~25 km), and 950 K (~32 km), and the two horizontal lines indicate the boundary of the outer vortex edge (at sPV= $1.2 \times 10^{-4} \text{ s}^{-1}$), and the inner vortex edge (at sPV= $1.6 \times 10^{-4} \text{ s}^{-1}$). Note that there are more polar intrusions over Toronto in the upper stratosphere (650 K and 950 K) because the polar vortex is typically larger, and filaments tend to tilt away from the pole at higher altitudes [*Schoeberl and Newman, 1995*].

To identify polar intrusion events, we started with the sPV definition of inner and outer vortex edge, and the sPV time series over Toronto from the DMPs. Scaled PV on the four levels suggests that between January 2002 and March 2013, there were 675 days (16% of days) when the polar vortex (sPV > $1.6 \times 10^{-4} \text{ s}^{-1}$) passed over Toronto, and 1492 days (36% of days) when the edge of the polar vortex ($1.2 \times 10^{-4} \text{ s}^{-1} < \text{sPV} < 1.6 \times 10^{-4} \text{ s}^{-1}$) was over Toronto. Figure 6.3(a and b) shows these days distributed by

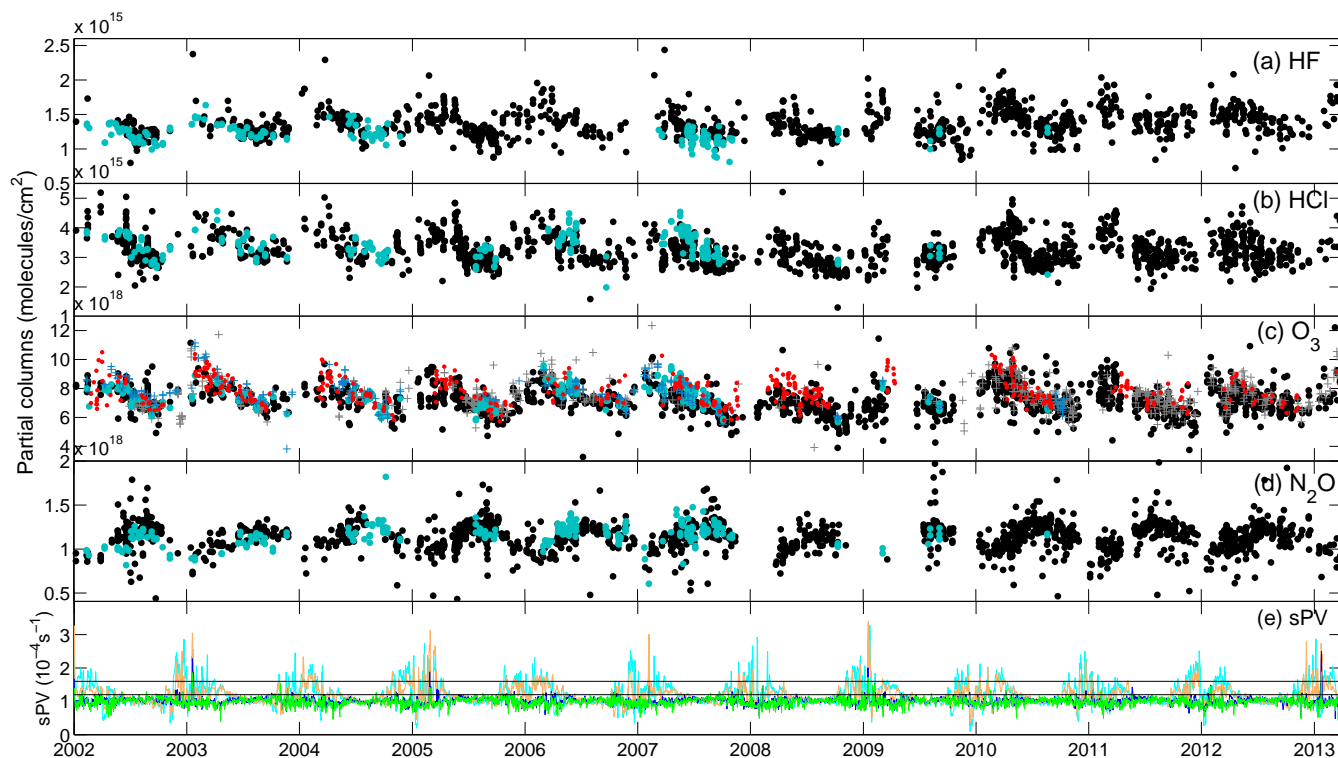


Figure 6.2: TAO (black), CARE (cyan), and OSIRIS (red) stratospheric partial columns (12-50 km) of (a) HF, (b) HCl, (c) O_3 (from the 3051 cm^{-1} microwindow) and (d) N_2O . In the O_3 panel (c), the grey and blue crosses are retrievals from the 1000 cm^{-1} microwindow for TAO and CARE, respectively. Panel (e) is sPV over Toronto at 435 K (green), 475 K (blue), 675 K (orange), and 950 K (cyan), and the inner ($\text{sPV}=1.6 \times 10^{-4} \text{ s}^{-1}$) and outer ($\text{sPV}=1.2 \times 10^{-4} \text{ s}^{-1}$) vortex edges are indicated by the upper and lower horizontal lines, respectively.

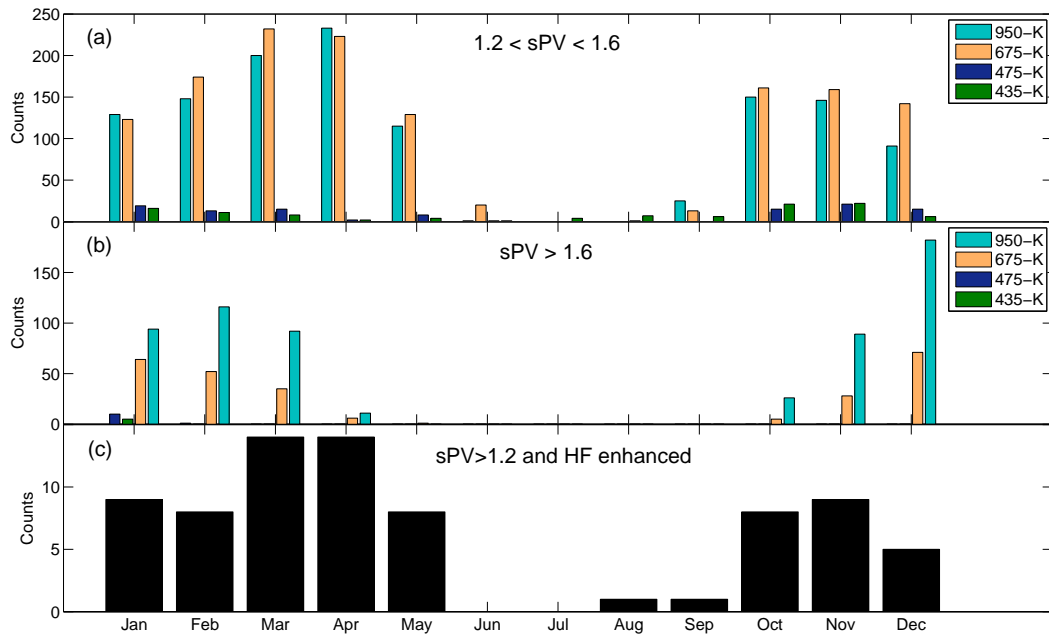


Figure 6.3: Number of polar intrusion days at four vertical levels (950 K, 675 K, 475 K, and 435 K) over Toronto from January 2002 to March 2013, from the MERRA DMPs, separated by month. sPV given in 10^{-4} s^{-1} . Panel (a) shows the number of intrusions that are within the vortex edge region, and (b) shows the number of intrusions that are within the vortex. Panel (c) shows the number of intrusion days that met the four criteria described in Section 6.5.1.

month, and Figure 6.4(a and b) shows these days distributed by year. Since the FTIR spectrometer cannot measure on cloudy days and has sporadic downtime for maintenance and repairs, the gaps in the dataset make it certain that we are not detecting all of these polar intrusion events over southern Ontario. In fact, there are FTIR measurements at TAO on only $\sim 14\%$ of those “enhanced sPV ” ($> 1.2 \times 10^{-4} \text{ s}^{-1}$) days. However, while the FTIR dataset is missing 86% of the polar intrusions (in enhanced sPV), its subset of measurement days gets a similar percentage with polar intrusions to that found with the sPV time series.

Since HF is a good dynamical tracer, we expect polar vortex intrusions to cause

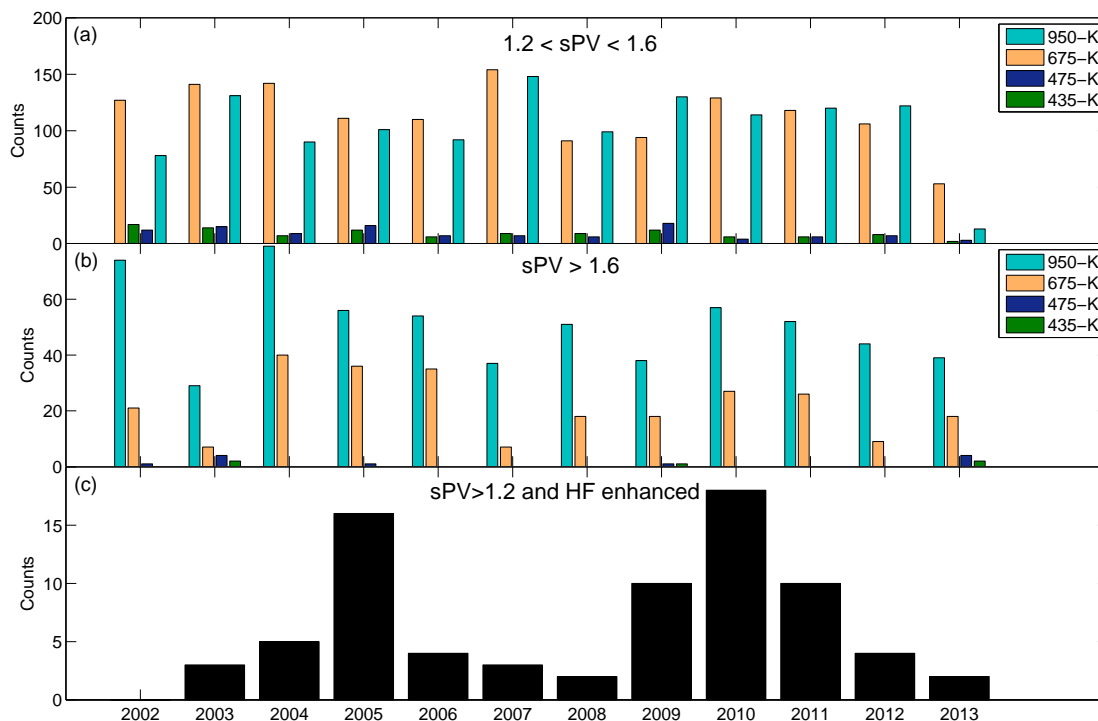


Figure 6.4: Same as Figure 6.3, but separated by year.

variability in the FTIR time series (although to a lesser extent if the polar intrusion is shallow and/or much higher than 35 km where it is not contributing a large amount to the column). Therefore, we looked at (1) the HF stratospheric columns that were *enhanced*, defined as when the HF stratospheric column was more than 1σ greater than the monthly mean (in either the singular monthly mean, or the climatological (2002-2013) monthly mean). We flagged those days as “enhanced HF” days. Then we determined whether these flagged days also had (2) reduced N_2O stratospheric columns (compared to a few days before and after the event), and (3) $\text{sPV} > 1.2 \times 10^{-4} \text{ s}^{-1}$. Finally, (4) we checked the MIMOSA and MERRA PV maps at the four vertical levels in the stratosphere mentioned above to see if there was a vortex excursion or filament over Toronto on those dates. Using these four criteria, we found 47 polar vortex intrusions. Six additional polar intrusions were found that did not quite satisfy all of the criteria. Either there were not enough HF measurements to make the 1σ statistic meaningful

(but the HF column was increased and sPV was $> 1.2 \times 10^{-4} \text{ s}^{-1}$), or the sPV value was just below $1.2 \times 10^{-4} \text{ s}^{-1}$ (but the HF column was enhanced and the polar map confirms a filament). Nevertheless, we include those six in this study for a total of 53 “polar intrusion events”, on which we focus the rest of the discussion. There were an average of four events detected in the FTIR time series per year. Between November and April inclusive (“winter/spring”), the polar intrusion events consist of 16% of our measurements.

The monthly and yearly distribution of these 53 polar intrusion events are shown in Figures 6.3(c), and 6.4(c), respectively. Note the monthly distribution is similar to the enhanced sPV distribution, with the differences being due to the measurement sampling bias. It turned out that all of the HF enhancements in December through March were during polar vortex intrusions. The HF enhancements in April, May, October, and November were rarely coinciding with a polar vortex intrusion, and only one enhancement in the summer (August 2005) was during a polar intrusion event. This suggests that the December to March variability in the HF time series is due to polar vortex air passing over Toronto. The late-spring, summer, and fall variability in HF must be due to other causes, and this variability (in May through September) is about half that during the winter (see Section 6.5.2 for more discussion on HF variability).

Note that no one criterion for *HF enhancements* (e.g., 1σ , median absolute deviation, absolute cutoff, etc.) captured all of the polar intrusion events so there could be more intrusions in the FTIR dataset that were missed. Also the DMPs (and hence, sPV), are interpolated values; therefore, a slight mis-match in the location of the filament between MERRA and the “truth” could make the difference between considering something inside or outside the vortex [Fairlie et al., 1997; Manney et al., 1998] – hence the six additional days.

6.5.2 Effect on trace gases: variability

All of the polar intrusion events we found in the measurements are highlighted by the grey (met all four criteria) and yellow (met three out of four criteria) boxes in Figures 6.5 and 6.6. These figures show the time series expanded for each year.

The variability introduced in the FTIR time series by the polar intrusion events (Var) for each trace gas in the complete time series is calculated for each year and for the complete time series, with the latter given in Table 6.1. This table shows the percent differences between the standard deviations calculated from our FTIR measurements with (σ_{with}) and without (σ_{wout}) the polar intrusion events:

$$Var = \frac{\sigma_{with} - \sigma_{wout}}{\sigma_{with}} \times 100\%. \quad (6.7)$$

The upper-stratospheric O_3 value in Table 6.1 is negative; this means that the polar intrusion events *decreased* the variability in the time series. The magnitude of the negative value is small ($< -0.5\%$), which may just be interpreted as a negligible effect on the time series variability. However, O_3 variability can be reduced by the following scenarios: (i) the polar vortex filament may have a similar amount of O_3 to that in unperturbed mid-latitude air, or (ii) a springtime polar vortex filament may have O_3 -poor air, making the column more like the summertime O_3 columns (when there is a seasonal minimum and more FTIR measurements).

From 2003 to 2012, polar intrusion events cause a mean increase in variability of 15.1%, 7.1%, and 5.7% for stratospheric HF, HCl, and O_3 , respectively. We left out 2002 and 2013 from our calculations because early 2002 was before regular daily measurements commenced at TAO and therefore there were very few measurements during January to April 2002, and the 2013 dataset was not complete at the time of this study.

The variability introduced by the polar vortex intrusions is greatest for HF, consistent with it being a good dynamical tracer. For example, in January 2003, we have one of the highest outliers in the HF (and N_2O) columns (Figure 6.5), which occurred when the

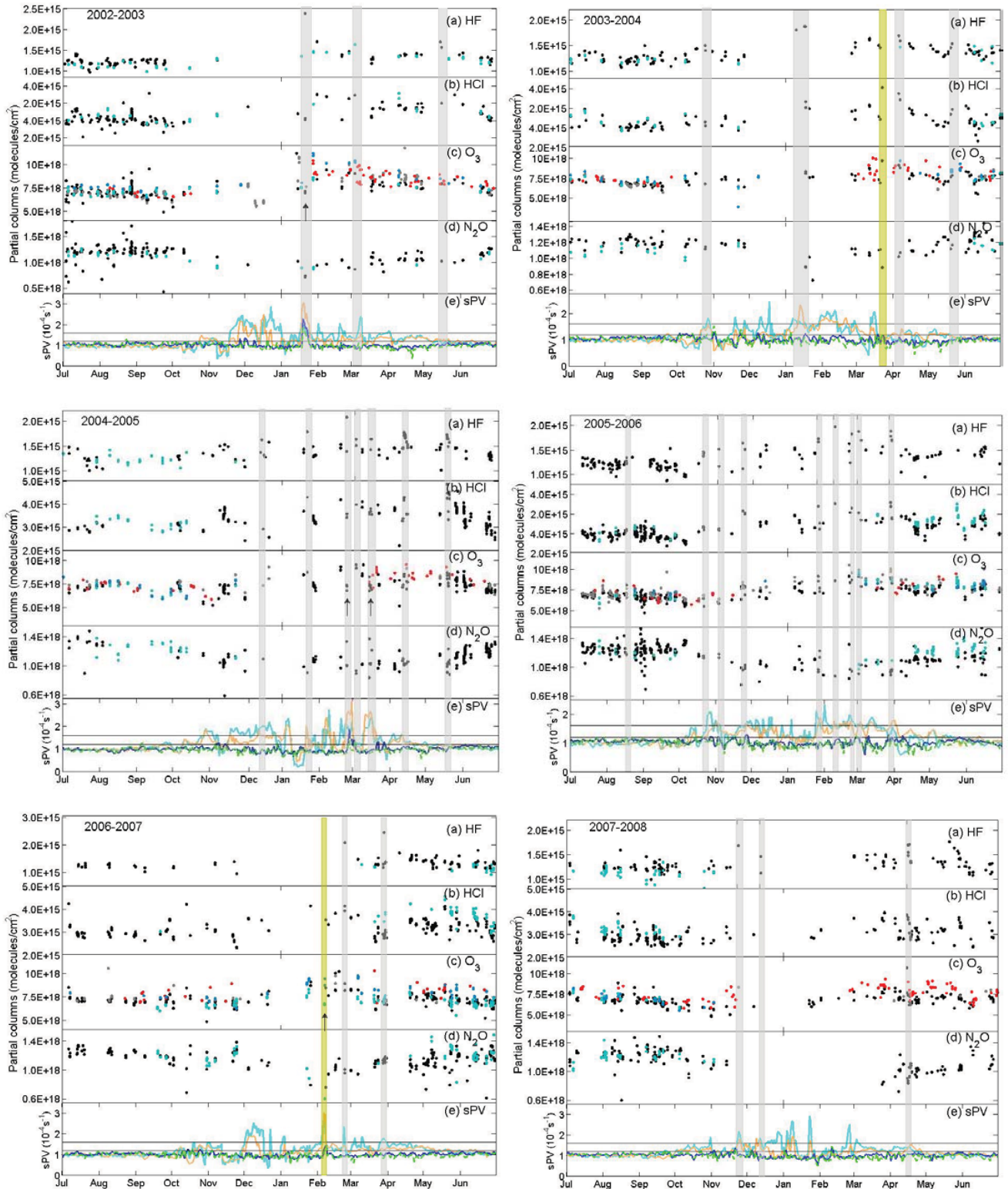


Figure 6.5: Same as Figure 6.2, but an expanded view of each year, and 3051 and 1000 O₃ products are combined into black (TAO) and cyan (CARE) points. Grey and yellow boxes highlight the polar intrusion events (grey showing events that met the four criteria, and yellow showing events that met only three of the four criteria).

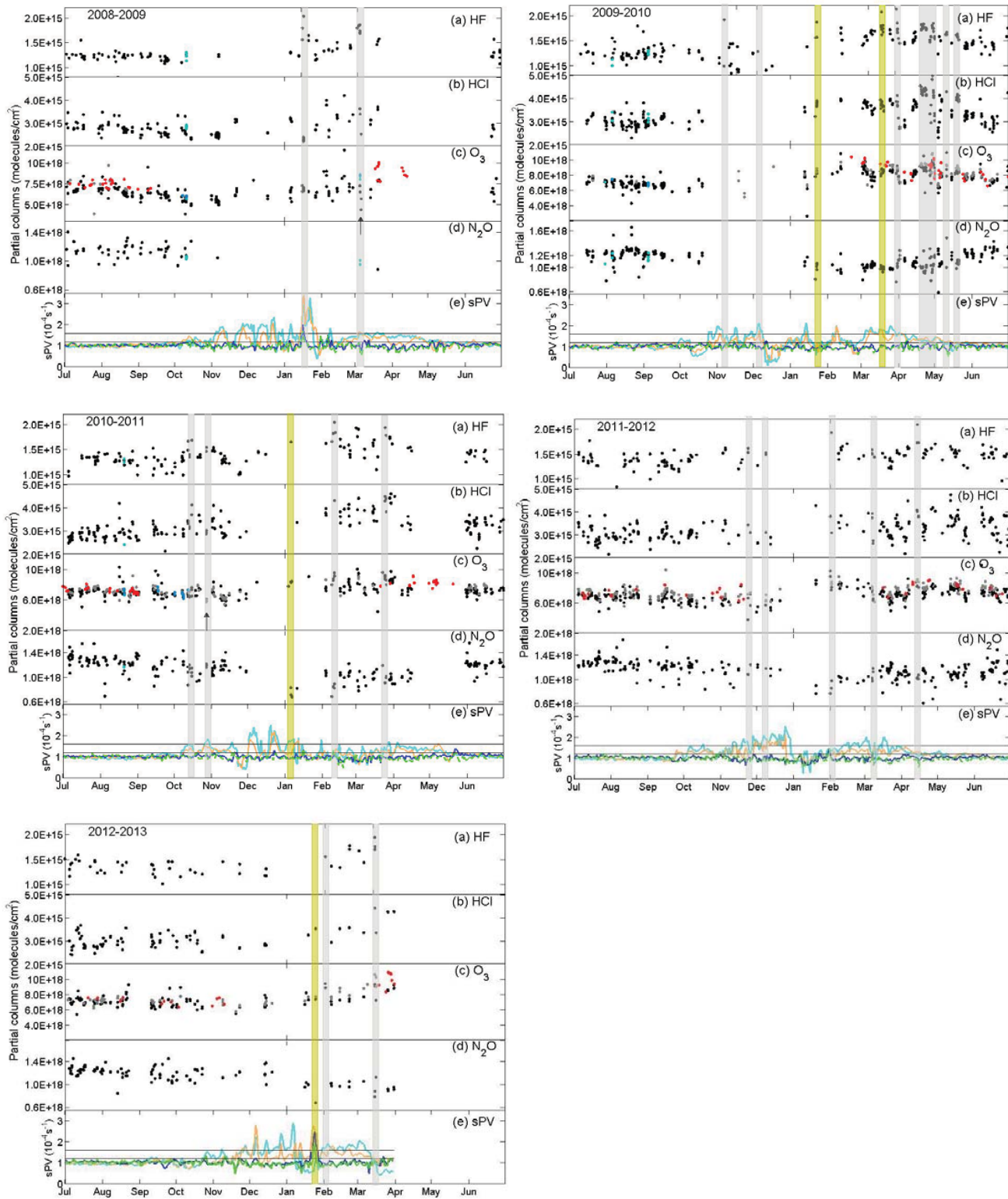


Figure 6.6: Same as Figure 6.5, but later years.

Table 6.1: Percent increase in 2003–2012 stratospheric column variability and sPV variability over Toronto due to polar intrusion events. O_3 products are from the 1000 cm^{-1} and 3051 cm^{-1} microwindows combined. The first set of sPV variability is due to the 53 polar intrusion events during the FTIR measurement days. The second set of sPV variability is due to all polar intrusion days in the sPV time series, not constrained by FTIR measurement days.

Species	Mean Increase in Variability (2003-2012)
HF (12-50 km)	15.1%
HCl (12-50 km)	7.1%
N_2O (12-50 km)	1.7%
O_3 (12-50 km)	5.7%
O_3 (12-23 km)	3.8%
O_3 (23-50 km)	-0.5%
sPV 435 K	4.4%
sPV 475 K	11.2%
sPV 675 K	14.5%
sPV 950 K	5.2%
sPV 435 K	9.3%
sPV 475 K	14.4%
sPV 675 K	58.8%
sPV 950 K	62.0%

polar vortex was over Toronto for the largest altitude range (see mauve line in Figure 6.12). In this year, the polar intrusions caused a 35% increase in HF variability. The variability of HCl is less sensitive to the polar vortex intrusions in most years, likely because dynamical enhancements of HCl can be offset by chemical processing. However, HCl is still significantly affected by polar vortex air, consistent with *Coffey et al.* [2008]. The polar vortex intrusions have a smaller effect on the variability of O₃ because the amount of O₃ in the filaments is not consistently greater than (like HF and HCl), or less than (like N₂O) than in mid-latitude air. The amount of O₃ in a filament is influenced by the altitude range at which it occurs, the dynamics of the polar vortex system, and chemical processing. Finally, the small effect on N₂O variability is likely due to the smaller altitude range that contributes to the N₂O stratospheric column (see end of Section 6.2). Therefore, only lower-stratospheric polar intrusions would have a significant effect on the N₂O time series.

Figure 6.7 shows the variability (given by the standard deviation from the climatological monthly mean) of each species for the complete time series (black circles), and the time series without the polar intrusion events (red crosses). In addition to Table 6.1, this figure shows that the largest effect on variability occurs for HF, during the winter and early-spring months. Figure 6.7 illustrates that there is about twice as much variability in the HF time series in the winter as there is in the summer, and that about half of the increase of the winter variability compared to summer is due to the polar intrusion events.

The variability in sPV at four different levels (435 K, 475 K, 675 K, and 950 K) was also calculated, and included in Table 6.1 and Figure 6.7. The first set of sPV values in Table 6.1 is the result when we only consider the 53 events and their effect on sPV during the FTIR measurement days. The second set of sPV values is the result if we are not constrained to FTIR measurement days, and consider the full sPV time series, during which there are a total of 2167 polar intrusion days from January 2002 to March 2013.

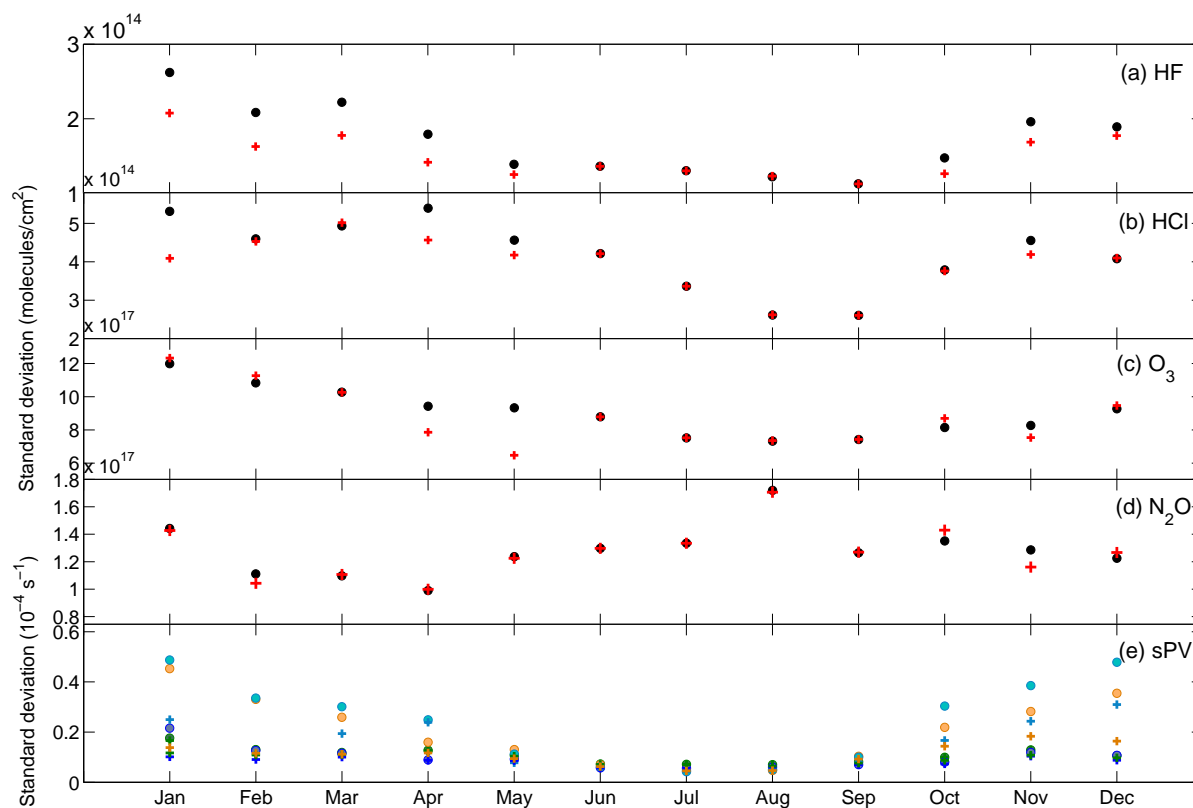


Figure 6.7: Variance in TAO stratospheric partial columns of (a) HF, (b) HCl, (c) O₃, and (d) N₂O, and in (e) sPV, as given by the standard deviation from the climatological monthly mean for each month. Circles are for the full time series, and crosses are for the time series without the polar intrusion events. In panel (e), 435 K is green, 475 K is blue, 675 K is orange, and 950 K is cyan, and the crosses are for the time series without the enhanced sPV days.

When all of these days are taken into account, their effect on sPV variability is 9.3%, 14.4%, 58.8%, and 62.0%, at 435 K, 475 K, 675 K, and 950 K, respectively, and Figure 6.7 shows this effect by month (with circles showing the variability of the full sPV time series, and crosses showing the variability of the sPV time series without the enhanced sPV days). Note that the monthly HF variability with and without polar intrusion events follows a very similar shape to the sPV variability (Figure 6.7(a) and (e)), which supports the use of FTIR HF columns to detect polar vortex intrusions.

Effect on O₃ columns

Generally speaking, stratospheric O₃ columns above Toronto are slightly greater during the polar intrusion events, consistently agreeing with the GMI model, the Microwave Limb Sounder (MLS) on the Earth Observing System Aura satellite, the Earth Probe/Total Ozone Mapping Spectrometer (EP/TOMS), the Ozone Monitoring Instrument (OMI), and OSIRIS O₃ measurements. The O₃ stratospheric columns can be split into 12-23 km, and 23-50 km, as these partial columns have at least 1 DOFS each. Though not shown in Figures 6.5 and 6.6, these lower and upper stratospheric partial columns provide more insight into which region of the stratosphere any changes to the O₃ column are occurring. The total errors on these partial columns are: 7.5% (12-23 km) and 11.6% (23-50 km) for the 3051 cm⁻¹ microwindow, and 9.0% (12-23 km), and 5.7% (23-50 km), for the 1000 cm⁻¹ microwindow. When only random errors are considered, they are: 2.6% (12-23 km), and 2.3% (23-50 km), for the 3051 cm⁻¹ microwindow, and 2.0% (12-23 km), and 2.1% (23-50 km), for the 1000 cm⁻¹ microwindow.

In 2005, 2010, and the total time series, there were significant (greater than the standard error in the O₃ partial columns) changes in the average of the FTIR stratospheric O₃ columns due to the polar intrusion events. The only significant *decreases* in annual stratospheric O₃ columns due to the polar intrusion events were in the 23-50 km partial columns, in 2003, 2005, and 2009. These changes in O₃ are summarized in Table 6.2,

Table 6.2: Percent change in stratospheric columns of O₃ over Toronto due to polar intrusion events for the given year, and for the total time series (2002 to 2013). Bold values highlight changes that are greater than the standard error of the mean difference.

Partial Column	2003	2004	2005	2006	2007	2008	2009	2010	2011	2012	Total (2003-2012) mean
12-50 km	-1.3%	2.3%	2.1%	4.2%	0.3%	1.4%	0.3%	15.3%	-3.3%	5.1%	4.5%
12-23 km	1.0%	2.9%	7.3%	5.7%	0.0%	1.5%	5.8%	14.9%	-1.2%	3.3%	4.8%
23-50 km	-4.2%	-0.5%	-7.0%	-1.4%	0.4%	-0.1%	-6.5%	-2.9%	-2.1%	1.3%	-0.9%

and were calculated using:

$$Change = \frac{\overline{O_{3with}} - \overline{O_{3wout}}}{\overline{O_{3with}}} \times 100\%, \quad (6.8)$$

where $\overline{O_{3with}}$ and $\overline{O_{3wout}}$ are the means of the stratospheric O₃ partial columns for a given year, with and without the polar intrusion events, respectively. The bold values in Table 6.2 indicate that the changes in O₃ are greater than the standard error on $\overline{O_{3with}}$. However, since our FTIR measurements are neither frequent or uniform in time, these statistics apply only to our dataset, and should not be interpreted as representing the increase/decrease in O₃ over the Toronto region that would be observed in a continuous dataset.

6.5.3 Effect on trace gases: case studies

As mentioned in Section 6.5.1, polar PV maps from MERRA and MIMOSA (when available) were used to verify structures extending from the polar vortex southward over the Toronto region. Figures 6.8 to 6.11 present these maps for four sample polar intrusion events, at the vertical levels at which the intrusion occurred. In these maps, Toronto's location is marked by a white circle, and two white contours indicate the inner and outer vortex edges (equivalent to the horizontal black lines in Figures 6.2(e), 6.5, and 6.6). In Figures 6.9 to 6.11, the shape of the polar vortex and its filaments given by MERRA PV

were confirmed with the MIMOSA PV maps (for which the magnitudes of PV are also similar), and modelled N₂O from GMI. Also from GMI, is modelled O₃, which will be discussed below.

For all 53 polar intrusion events, the VMR of N₂O given by GMI is much lower inside the polar vortex and filaments compared to mid-latitudes as discussed in Section 6.1 (see Figures 6.9 to 6.11 for four examples). Recall that GMI is driven by MERRA meteorological fields, therefore, we would expect the GMI maps to agree well with MERRA PV maps, which is why we also include MIMOSA PV in this study as a more independent check on the location of the polar vortex and its filaments.

The next section discusses the impact of polar intrusions on Toronto-area O₃ using three case studies. The first two (January 2003 and February 2007) are examples of when polar O₃ depletion caused a reduction in stratospheric O₃ over Toronto, and the third (March 2011) is an example of when polar O₃ depletion did not have an effect on Toronto stratospheric O₃. This is followed by a section that discusses an example of stratospheric warming causing the polar vortex to split apart.

Impact on O₃

Unlike some previous studies that focus on reduced O₃ at mid-latitudes [*Marchand et al.*, 2003; *Millard et al.*, 2003; *Konopka et al.*, 2003; *Keckhut et al.*, 2007], we find that the majority of the polar intrusion events identified over Toronto resulted in either a small increase or a negligible change in the O₃ stratospheric columns (consistent with *Newman et al.* [1996]; *Orsolini et al.* [2001]; *Godin et al.* [2002], and *Hauchecorne et al.* [2002]). *Marchand et al.* [2003] modelled the effect of chemically depleted polar vortex air on northern mid-latitudes with MIMOSA-CHIM (MIMOSA with chemistry), and reported that mid-latitude O₃ VMRs became increasingly affected by the polar vortex starting from around March (when it was responsible for 15% of diminished O₃ at 475 K from 45°-55°N), reaching a maximum in April (when it was responsible for 50% of the

diminished O_3 at 475 K from 45° - 55° N). Since the Toronto region is located just south of their reported latitude band and most of our polar intrusion events occurred in March or before, we would expect polar intrusions to have less of an effect on our O_3 columns. *Marchand et al.* [2003] also reported negligible O_3 reductions in the filament structures (rather than vortex excursions). Since most of the events were filaments, our findings are consistent with the *Marchand et al.* [2003] study, as reduced O_3 columns were rarely measured as a result of a filament over Toronto.

We only found reduced O_3 columns during six of the 53 polar intrusion events; on 20 January 2003, 23 February 2005, 15-16 March 2005 (both 2005 events supported by *Rösevall et al.* [2008]), 6 February 2007, 3-4 March 2009, and 27 October 2010 (see small arrows in panel (c) of Figures 6.5, 2004-2005 and 6.6, 2010-2011). The lower (12-23 km) and upper (23-50 km) stratospheric columns were affected differently during these six events, with three having a decrease in the lower-stratospheric partial column, and little change in the upper-stratospheric partial column, and the other three having a decrease in the upper-stratospheric partial column, and little change in the lower-stratospheric partial column. Two of these events are discussed in more detail below.

On 20 January 2003, we have FTIR observations of reduced O_3 in the 12-50 km (Figure 6.5) and 23-50 km partial column, and MERRA PV maps showing a large filament over Toronto at all four levels (Figure 6.8) due to a vortex split during a major stratospheric warming [*Jayanarayanan et al.*, 2011], but there are no O_3 observations by OSIRIS on this date, nor is there GMI output. O_3 total column observations from EP/TOMS exist (from <http://ozoneaq.gsfc.nasa.gov>), and are shown in Figure 6.8 (note the different orientation of the map). In this figure, there is a large amount of O_3 to the west of the polar vortex structure (over western Canada and over the Pacific ocean) which represents regular mid-latitude O_3 , but where the intrusion occurs (over Ontario and Quebec), the O_3 total columns are reduced, in agreement with the ground-based measurements. The winter of 2002/2003 had appropriate conditions for chemical O_3 loss inside the vortex

through late January, as it was cold [WMO, 2007], and Arctic O₃ depletion was reported [e.g., Christensen *et al.*, 2005; Singleton *et al.*, 2005; Jayanarayanan *et al.*, 2011]. The HCl stratospheric column is also decreased (Figure 6.5), which is consistent with chemical O₃ loss, as it implies that Cl is activated.

On 6 February 2007, the CARE O₃ 12-50 km partial column is reduced (Figure 6.5). The MIMOSA and MERRA PV maps and the GMI N₂O and O₃ maps at 475 K (Figure 6.9) all show a large filament over the Toronto region, but the GMI 475-K map on 6 February 2007 has *enhanced* O₃ compared to the surrounding mid-latitudes. However, the GMI 575-K (~23 km) O₃ map does show reduced O₃ in both the vortex and filament. There is no OSIRIS coverage over the Northern Hemisphere during early February to compare with GMI, but Rösevall *et al.* [2007], Sonkaew *et al.* [2011], and Søvde *et al.* [2011] report significant Arctic O₃ depletion that winter, including on the date of our observation at the 575-K level. Observations of O₃ from MLS at 490 K (not shown) show vortex O₃ that is comparable to mid-latitude O₃ [http://mls.jpl.nasa.gov/plots/mls/mls_plot_locator.php] consistent with the GMI 475-K map. The O₃ total column map from OMI (from <http://ozoneaq.gsfc.nasa.gov>) is shown in Figure 6.9, and supports the ground-based measurements, as the O₃ columns in the polar vortex region (including the filament over Ontario and Quebec) are smaller than the O₃ columns at other mid-latitudes (e.g., over the rest of Canada).

In contrast to the events on 20 January 2003 and 6 February 2007 discussed above, polar intrusions on 23 February 2007 and 23-25 March 2011, do not show reduced O₃ columns (Figures 6.5 and 6.6), which might have been expected given chemical O₃ depletion observed in the polar vortex by Rösevall *et al.* [2007] in 2007, and Manney *et al.* [2011] in 2011. In these cases, O₃ was not reduced in the vortex filaments, which extended over Toronto (e.g., the 25 March 2011 case shown in Figure 6.10, first and last rows). It would seem that the filaments were not O₃-poor because O₃ depletion was not uniform throughout the vortex. For example, at the end of March 2011, the vortex was O₃-poor

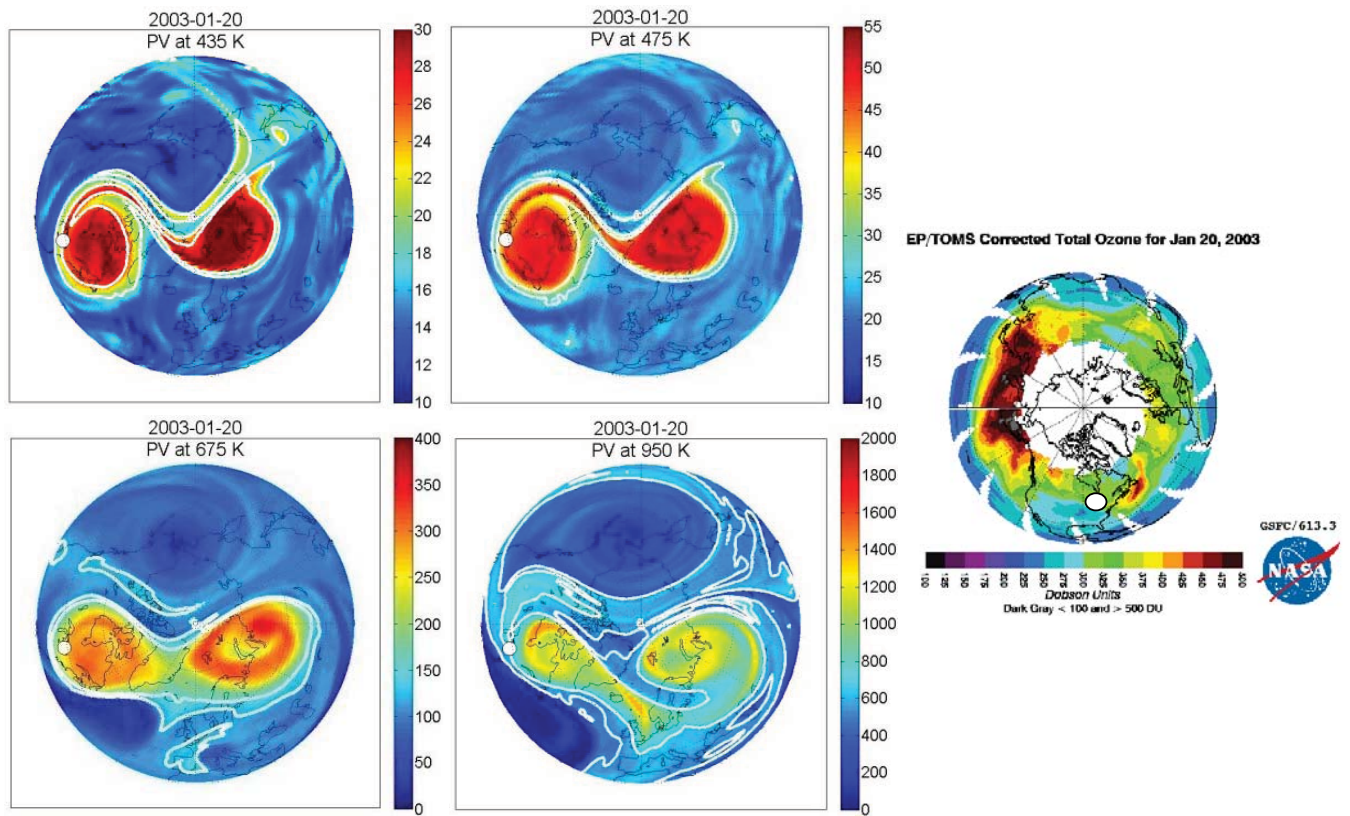


Figure 6.8: Polar intrusion event on 20 January 2003. Left panels: MERRA PV (in pvu) at 435 K, 475 K, 675 K, and 950 K. White contours denote the inner and outer vortex edge limits. Right panel: EP TOMS total O_3 column (note this map is oriented 90° counter-clockwise compared to the MERRA maps). White circles on each map represents the location of Toronto/Egbert.

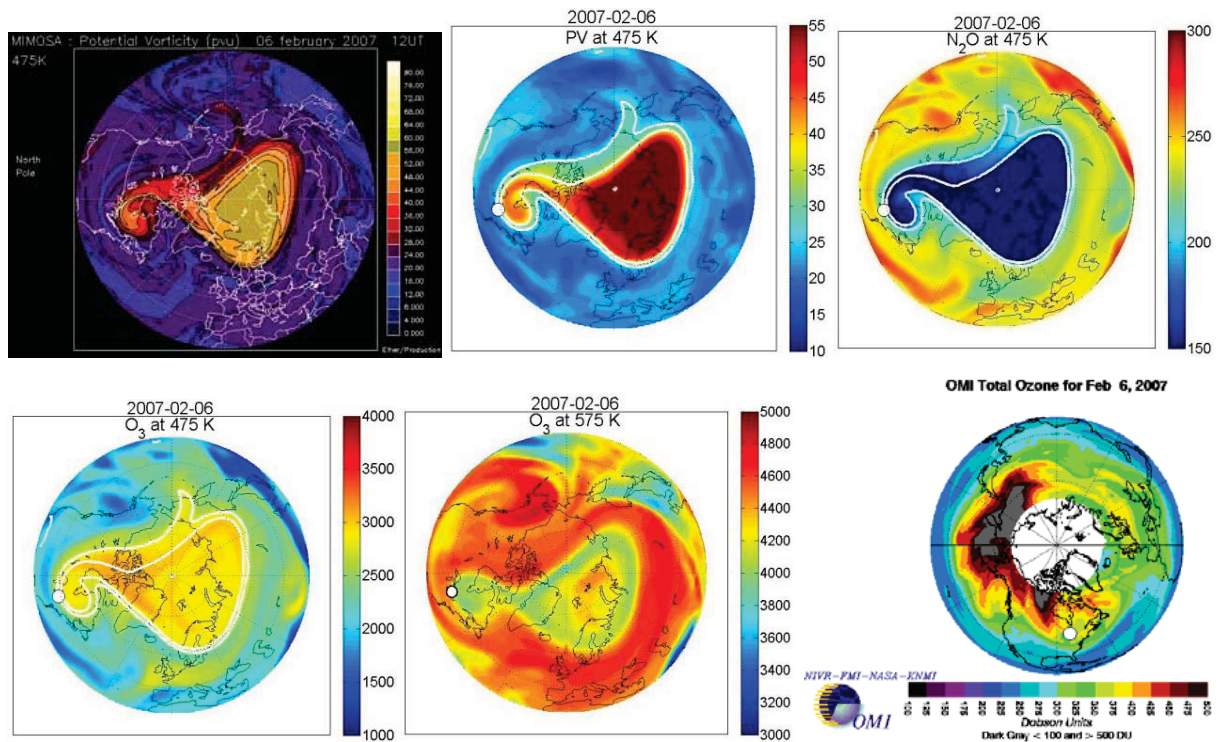


Figure 6.9: Polar intrusion event on 6 February 2007. *Top row*: MIMOSA PV, MERRA PV (both in pvu), and GMI N_2O (in ppbv). *Bottom row*: GMI O_3 at 475 K, and 575 K (both in ppbv), and OMI total column O_3 (note the OMI map is oriented 90° counter-clockwise compared to the other maps). White circles denote the location of Toronto/Egbert. White contours denote the inner and outer vortex edge limits.

near the centre, but not around its edge (see O_3 in top row of Figure 6.10). The filament originated from the edge region, therefore the filament has enhanced O_3 compared to mid-latitude air. In contrast, on 6 February 2007 (discussed above), the O_3 -poor air is located near the edge of the polar vortex at 575 K, hence its filament is also O_3 -poor (Figure 6.9).

The polar intrusion event on 23-25 March 2011 is shown for one day in Figure 6.10 at 675 K and 950 K, which are the levels where the polar intrusion occurred, and 475 K, which is approximately where the peak contribution to the O_3 stratospheric column occurred. The OSIRIS O_3 maps are also shown for this day, confirming the GMI results, and the OMI total column O_3 is shown, confirming reduced O_3 inside the polar vortex, but not in the filament that passed over Toronto.

Impact of a stratospheric warming

Similarly to January 2003 (Figure 6.8), January and February of 2009 had interesting polar vortex activity, when a major mid-winter warming occurred [*Manney et al.*, 2009; *Labitzke and Kunze*, 2009], and the vortex split in two, one half passing over southern Ontario in early February. The maps in Figure 6.11 show the beginning of this breakup, and the polar vortex is already over Toronto as early as 16 January 2009. Figure 6.6 shows the effect on the FTIR columns. The HCl stratospheric column is decreased. The upper-stratospheric O_3 columns (23-50 km) were reduced, while the lower-stratospheric O_3 columns (12-23 km) were enhanced (not shown), resulting in the stratospheric O_3 columns (12-50 km) being unchanged (shown in Figure 6.6). These results are consistent with the GMI modelled O_3 , though the OMI total column O_3 appears to be slightly reduced in the polar vortex region (Figure 6.11).

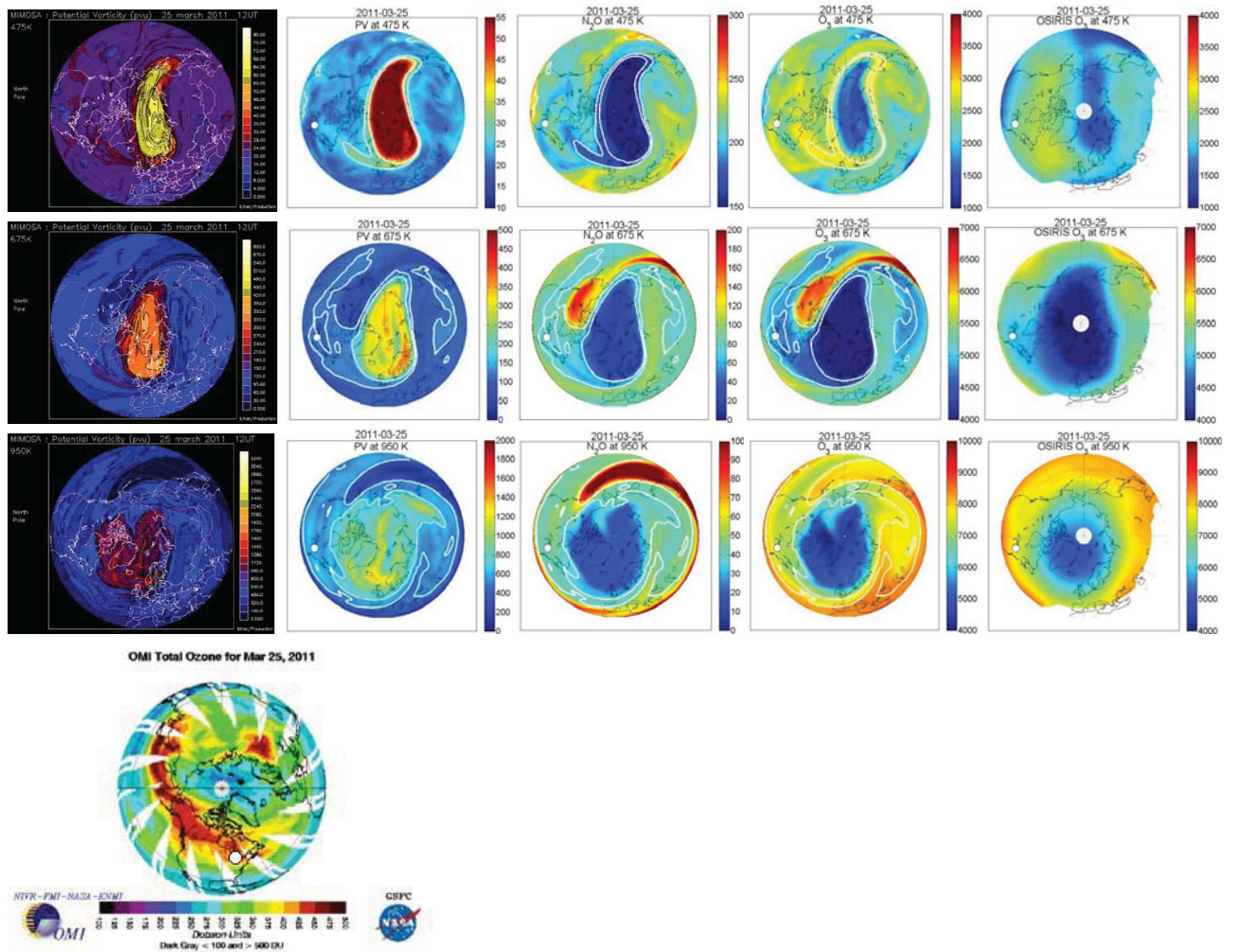


Figure 6.10: Polar intrusion event on 25 March 2011. *From left to right:* MIMOSA and MERRA PV (both in p.u.), GMI N_2O and O_3 (both in ppbv), and OSIRIS O_3 (also in ppbv). At the bottom is OMI O_3 total column (note the different orientation). *From top to bottom:* 475 K, 675 K, and 950 K. White circles denote the location of Toronto/Egbert. White contours denote the inner and outer vortex edge limits.

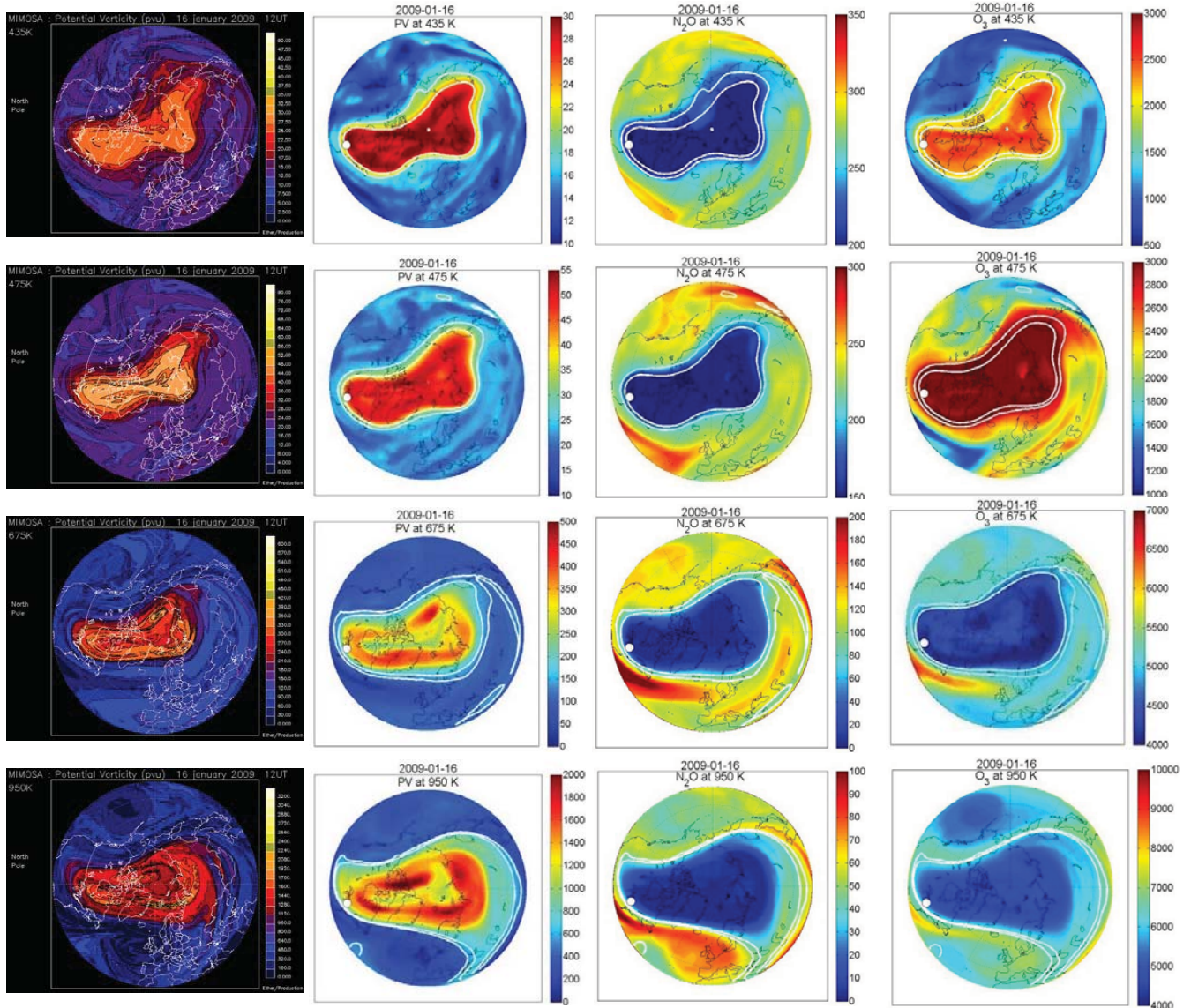


Figure 6.11: Polar intrusion event on 16 January 2009. *From left to right:* MIMOSA and MERRA PV (both in pvu), GMI N_2O and O_3 (both in ppbv), and the OMI total O_3 column map is also shown (note the different orientation). From top to bottom, the intrusion is shown at 435 K, 475 K, 675 K, and 950 K. White circles denote the location of Toronto/Egbert. White contours denote the inner and outer vortex edge limits.

6.5.4 Vertical structure of polar intrusion events

Figure 6.12 shows the vertical extent of the 53 polar intrusion events in sPV. The vertical grey lines in Figure 6.12 indicate the outer and inner polar vortex edges, as given by the sPV criterion described in Section 6.4.3. The mean sPV profile from non-intrusion ($\text{sPV} < 1.2 \times 10^{-4} \text{ s}^{-1}$) days and its standard deviation are the thick black lines, shown for comparison. Most of the polar intrusion events have sPV values that are within the edge region, but at least half of our 53 events have even higher sPV values, putting them well inside the polar vortex at some part of the profile. In most cases, sPV tends to be large compared to the non-event mean from about 370 to 1500 K (or 12 to 45 km), which coincides with the vertical range over which the FTIR retrievals are sensitive (see Figure 6.1 and Section 6.2).

These results indicate that FTIR partial column measurements provide useful information for polar intrusion detection. Previous publications describing mid-latitude polar intrusion events have presented trace gas vertical profiles from aircraft, lidar, and balloon-borne *in situ* measurements [Newman *et al.*, 1996; Orsolini *et al.*, 2001; Godin *et al.*, 2002; Durrý and Hauchecorne, 2005; Tripathi *et al.*, 2006]. However, these aircraft, lidar and balloon measurements were limited to the lower stratosphere (about 10-30 km, or 350-800 K), which may miss events that occur between 30 and 50 km (~ 800 -2200 K) (e.g., the 14 May 2003 and 14 December 2004 events detected in this study – red and dark green lines in Figure 6.12, respectively). For HF, HCl, N₂O, and O₃, the 30-50 km partial columns contain about 45%, 27%, 2%, and 30% of the stratospheric (12-50 km) columns, respectively.

The vertical thickness of the intrusions ranges from about 5 km (e.g., 3 March 2005 – orange line in Figure 6.12) to about 30 km (e.g., 16 January 2009 – pink line in Figure 6.12), and there is often more than one peak in the vertical profiles of sPV (e.g., 27 October 2010 – light green line in Figure 6.12), indicating vortex-filament structures occurring at more than one level. These results for vertical extent are consistent with Newman

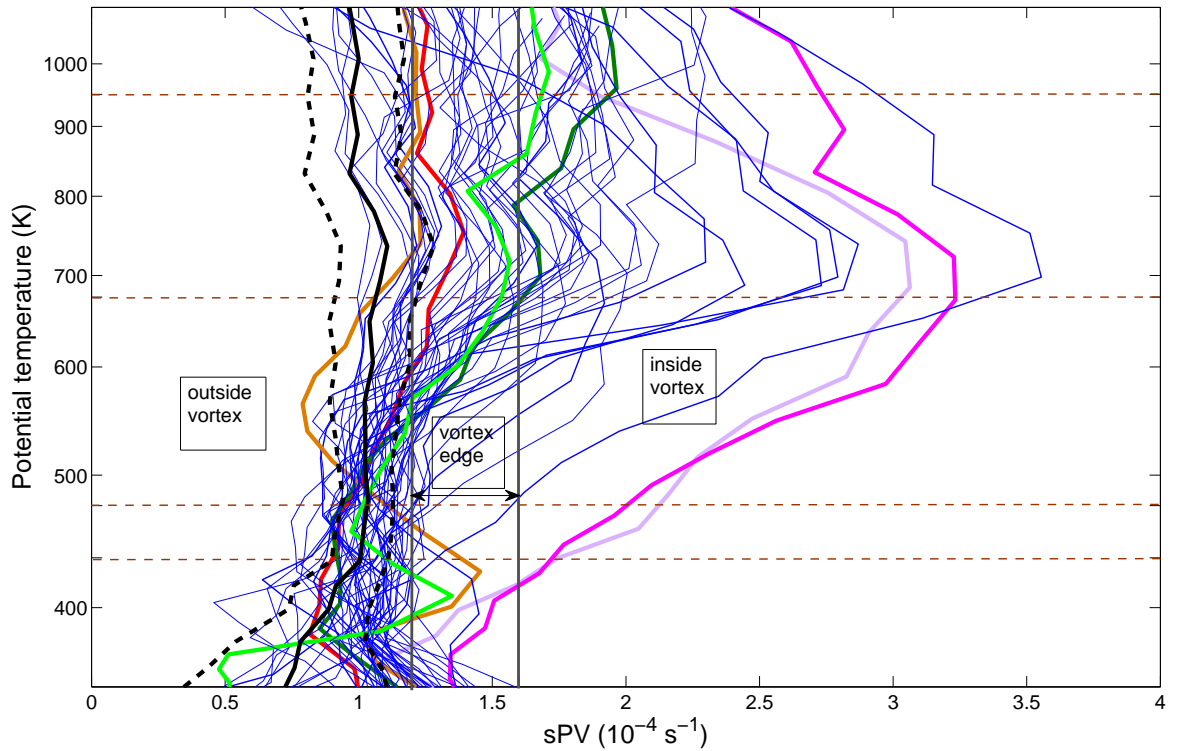


Figure 6.12: sPV over Toronto during the 53 polar intrusion events derived from MERRA (blue and coloured lines). The grey vertical lines indicate the outer and inner polar vortex edges. The horizontal dashed lines are the four vertical levels at which sPV was sampled in the time series. The thick black line and dashed black lines are the mean sPV profile from all non-intrusion days and its standard deviation, respectively. The coloured lines are sPV profiles from specific days that were discussed in Sections 6.5.2 and 6.5.4: mauve=20 January 2003, red=14 May 2003, dark green=14 December 2004, orange=3 March 2005, pink=16 January 2009, and light green=27 October 2010.

et al. [1996] who observed shallow intrusions at mid-latitudes in the lower stratosphere, as well as with the studies by *Orsolini* [1995], *Orsolini et al.* [1997] and *Schoeberl and Newman* [1995] who observed and modelled both shallow and deep polar vortex filaments throughout the stratosphere.

6.6 Summary and conclusions

I have presented the TAO and CARE ground-based FTIR time series of stratospheric HF, HCl, O₃ and N₂O partial columns measured from January 2002 to March 2013, and have used these results, along with the sPV analysis, to identify 53 polar intrusion events over the densely populated Toronto area. All eleven years had at least two days with a polar intrusion event detected in enhanced HF columns, with four events per year being the average. Most of the events were detected in the late fall, winter or early spring, when the polar vortex was formed or distorted, rapidly changing, and frequently shedding filaments. These conditions commonly occur throughout Arctic fall and winter [e.g., *Manney et al.*, 2000]. To our knowledge, this was the first study to use ground-based FTIR column measurements to identify multiple polar intrusions over the course of a decade over a particular mid-latitude region and to examine the impact of intrusions on the stratospheric columns of four different trace gases.

FTIR measurements of HF columns were useful for detecting polar vortex intrusions; the HF stratospheric columns were enhanced during 100% of the lower-stratosphere (435 K and 475 K) polar vortex (sPV > $1.6 \times 10^{-4} \text{ s}^{-1}$) overpasses. When the upper-stratosphere (675 K and 950 K) polar vortex intrusions are also included, 40% of HF stratospheric columns were enhanced, as the upper-stratosphere contributes less overall to the HF columns. When the polar vortex *edge* (sPV > $1.2 \times 10^{-4} \text{ s}^{-1}$) overpasses are also included, the percentage drops to 30%(25%) for the lower(upper)-stratosphere events.

Most of the late-fall, winter, and early-spring variability in the TAO HF time series (Figure 6.7) can be explained by transient polar intrusion events, although the magnitude of the effect varies from year to year. The effect on the O₃ time series (FTIR and OSIRIS) is irregular (Figure 6.7, Table 6.2); most of the time there is a small increase in O₃ during an event, even when there is O₃ depletion inside the vortex. The vortex filaments often do not share the O₃-depleted state of the vortex (e.g., the unprecedented Arctic O₃ loss in 2011 did not cause a decrease in Toronto O₃ columns). Based on our results and the *Marchand et al.* [2003] study, O₃ depletion over Toronto is more likely to occur during a vortex excursion, and these are rarer than filaments.

The vertical profiles of sPV (Figure 6.12) show that the intrusions can occur at varying altitudes, and span various vertical ranges. While the FTIR retrievals cannot resolve those features, the sensitivity in the 12-50 km range is sufficient to see variability in the stratospheric columns caused by these polar intrusion events, including mid-to-upper stratospheric events, which are not measurable with sondes, lidar, aircraft, and *in situ* instruments.

6.6.1 Future work

FTIR spectroscopy is capable of measuring numerous polar vortex tracers and stratospheric gases important for O₃ chemistry over long periods. There are 14 NDACC sites north of 40°N, many of which have been taking observations for more than a decade (e.g., <http://www.acd.ucar.edu/irwg/>). Based on the results of this study, these datasets should also provide evidence of polar intrusion events, and afford an opportunity to study the accuracy of their representation in models.

Chapter 7

Conclusions

The first goal of this research was to improve retrievals – particularly tropospheric retrievals – at TAO. These were done in parallel with the NDACC-IRWG harmonization initiative, which requires all sites to use similar parameters to improve network-wide consistency. Numerous tests of retrieval parameters on eight species (O_3 , CO , C_2H_6 , HCN , CH_4 , N_2O , HF , and HCl) were performed, and a set of retrieval parameters was established that both work for our instrument and geographical location, and comply with the NDACC-IRWG recommendations (Chapter 3). However, retrieval improvements are ongoing, and software updates continue to push this exercise forward. The retrievals presented in this thesis are already becoming obsolete with the release of SFIT4. However, the total and partial column values usually do not change significantly when retrieval parameters are changed (although the profiles, and the columns of the weakly absorbing species may). Nevertheless, the current set of retrievals allowed me to pursue a number of scientific questions.

Two scientific questions were discussed in this thesis: “What are the important sources of Toronto-area air pollution, and can the source contributions be quantified?” and “Are polar vortex dynamics responsible for variability of stratospheric trace gases measured over Toronto?”. The first question was addressed using tropospheric trace gas mea-

surements, and the second question using stratospheric trace gas measurements. These results are summarized separately below.

7.1 Summary and conclusions of the interpretation of tropospheric measurements

We studied the complete time series of TAO lower-tropospheric (0-5 km) measurements of O_3 and CO and saw how they varied seasonally and by wind direction, under what conditions they were correlated with each other, and under what conditions they were correlated with surface measurements. We found that high values of O_3 and CO were associated with all wind directions, although a larger fraction came from the west and from the south, associated with regions having higher fossil fuel emissions. Similarly, we found that O_3 and CO were better correlated when air came from the west ($R=0.32$) and from the south ($R=0.47$), and the partial columns were also better correlated with the surface measurements when air came from the west ($R=0.45$) and from the south ($R=0.38$).

In studying the enhanced summertime tropospheric column observations, we found that between April and October, a quarter of them were associated with surface O_3 exceedances (30% between May and September and 35% between June and August). These pollution events were then studied further with the GEOS-Chem model adjoint to determine their sensitivity to North American sources. What was common to all pollution events was high sensitivity to fossil fuel and isoprene emissions, high temperatures, and high pressure systems. What varied between them were the transport patterns, and thus, the specific regions to which air quality in Toronto exhibited the greatest sensitivity. For example, one case study had significant sensitivity to Washington D.C., another to Nashville and Atlanta, and another to a small Michigan town with significant coal-power generation.

It appears that long-range transport from the midwest and western U.S. (SW, Figure 5.23) region is the third most important region for Toronto O₃ pollution events (after the northeast U.S. (NEUS) and the southern Ontario/Quebec (SOnQu) regions). And for the SW region, Toronto O₃ is sensitive to soil NO_x emissions nearly as much as to fossil fuel emissions (e.g., 2 August 2007).

It appears to be rare that biomass burning contributes to Toronto O₃ pollution events, as we found only one case (21 July 2004) with a sensitivity to biomass burning greater than 2% (meaning that Toronto O₃ would increase by 2% if the biomass burning emissions were increased by a unit amount).

So we were able to obtain information on the sources of Toronto tropospheric O₃ during pollution events by quantifying the sensitivities of Toronto tropospheric O₃ to each source in Chapter 5.

7.1.1 Significance

We found 28 Toronto-area pollution events from 2002-2010 in the FTIR lower-tropospheric O₃ and CO columns (the number limited mainly by measurement frequency), and demonstrated their usefulness in studying air quality. The advantage of column measurements over surface measurements is their sensitivity to long-range background sources, and their usefulness in model validation (as they do not have the representativeness error that point surface measurements do). In addition, the advantage of ground-based FTIR measurements over satellite measurements is their sensitivity to the boundary layer for O₃ and CO. Therefore, it is useful to have FTIR instrumentation in urban locations where air quality affects a large percentage of the population.

7.1.2 Policy recommendations

Given the four-year study of Toronto pollution events conducted in Chapter 5, as well as the literature review, I recommend the following for improving Toronto's air quality:

- Reduce fossil fuel emissions as much as possible. They are responsible for not only most of the NO_x and VOCs in North America, but also indirectly responsible for increasing surface temperatures [*IPCC, WorkingGroup1, 2013*], decreasing frequency of low-pressure systems [*Leibensperger et al., 2008*], and increasing biomass burning [*Gillet et al., 2004; Westerling et al., 2006*]. Fossil fuels are also directly responsible for the very high NO_x conditions that lead to O_3 production's increased sensitivity to hydrocarbons, which occur naturally (e.g., CH_4 and isoprene). Although small NO_x reductions may cause an increase in O_3 when its production is hydrocarbon-limited, a substantial reduction of NO_x emissions would reduce NO_x to the point where it would not be high enough to cause a hydrocarbon-limited regime in the first place.
- Reduce nitrogen fertilizers in agriculture, as these increase soil emissions of NO_x .
- Reduce the Canada Wide Standard and provincial criteria for surface NO_x concentrations. They are currently 100 ppb for the 24-hour running average, and 200 ppb for the 1-hour average, respectively, and these criteria haven't been exceeded in Ontario since 1991, which may cause policy-makers not to make further NO_x emission reductions a priority.

Reduction of fossil fuel emissions can be accomplished in many ways: transit and cycling initiatives, carbon taxes, elimination of governmental oil and gas subsidies, increased subsidies for solar, hydro, and nuclear power generation, energy conservation, increased subsidies for electric vehicles and their development and infrastructure, and elimination of certain farming subsidies for high-carbon footprint foods (e.g., meat and dairy). Without government subsidies for fossil-fuel-related goods, the public would be forced to pay the “real price” for these goods, which would discourage their consumption.

Reduction of nitrogen used in agriculture can also be accomplished by elimination of certain farming subsidies for high-carbon footprint foods (e.g., meat and dairy), as

this would reduce the need for almost 80% of crops, which are grown to feed livestock [www.epa.gov/agriculture/ag101/cropmajor.html]. Nitrogen fertilizers may also be reduced with government subsidies for organic farming.

Finally, *Toronto Public Health* [2014] reports that NO_x air pollution is responsible for about 900 hospitalizations (more than from O_3), and about 200 premature deaths (equal to those from O_3) in Toronto annually. These direct health hazards, combined with the indirect harm that NO_x causes through O_3 production imply that the current standards for surface NO_x concentrations are not strict enough.

7.2 Summary and conclusions of the interpretation of stratospheric measurements

We studied the complete time series of TAO stratospheric (12-50 km) measurements of HF, HCl, O_3 , and N_2O and saw how they varied seasonally and with polar vortex intrusions. Fifty-three intrusion events were found in the FTIR dataset, with at least two each winter/spring. Lower-stratospheric polar vortex intrusions ($\text{sPV} > 1.6 \times 10^{-4} \text{ s}^{-1}$) always caused HF column enhancements, whereas intrusions in the upper stratosphere, and overpasses of just the vortex-edge ($1.2 \times 10^{-4} \text{ s}^{-1} < \text{sPV} < 1.6 \times 10^{-4} \text{ s}^{-1}$) caused HF enhancements less than half of the time. All polar vortex intrusions caused a relative increase in HCl stratospheric columns and a relative reduction in N_2O stratospheric columns. Stratospheric O_3 was usually slightly increased during polar intrusion events, except for six out of the fifty-three polar intrusion events, in which Toronto stratospheric O_3 was reduced. Polar intrusions significantly increased HF variability in the winter/spring, and to a lesser degree the variability of HCl, O_3 , and N_2O .

7.2.1 Significance

Again, we have shown the usefulness of FTIR measurements, this time of TAO HF stratospheric measurements in identifying polar intrusions over a populated area. These measurements, which were sensitive to polar vortex intrusions at higher altitudes than conventional methods, allowed for a long-term, multi-species, mid-latitude polar intrusion study. Some studies have stated that polar intrusions are responsible for reducing mid-latitude stratospheric O_3 by a significant amount [Marchand *et al.*, 2003; Millard *et al.*, 2003], however our findings for Toronto indicate that it is rare to have an O_3 -poor intrusion. Thus, the risk of exposing a large population to high UV radiation is minimal.

7.3 Future work

Suggestions for future work were discussed throughout the thesis at the end of each chapter. In Chapter 2, we suggested improvements to TAO which would improve the quality and quantity of measurements to allow more science to be done with the dataset. In Chapter 3, we explained the current efforts to update and continue to improve TAO retrievals, which is an ongoing process, forced by updates to retrieval software and spectroscopic inputs.

In Chapter 4, we discussed the tropospheric science that could be done with the TAO dataset and the GEOS-Chem model that was beyond the scope of this thesis. This included studies of Toronto C_2H_6 , HCN, CH_4 , N_2O and HCHO. For instance, one could do a Toronto-based biomass burning study using the first two species to try to determine how often biomass burning plumes pass over the city, and their effect on tropospheric O_3 and the region's air quality. With CH_4 and N_2O , one could do a Toronto-based, long-lived greenhouse gas study to try to determine their sources of variability, and to discuss whether the city's trends in those species are consistent with global trends (and why or why not). Finally, HCHO could be used to further understand O_3 photochemistry in

the Toronto region, as it is a product of hydrocarbon oxidation during O_3 production. Correlations between TAO and GEOS-Chem O_3 , CO, and HCHO may provide insight into how much O_3 is produced from direct CO emissions, and how much is produced from higher-order hydrocarbons.

In Chapter 5, we suggested that pollution events beyond 2002-2007 be studied, including how they change over time. Given the improvements to measurement density, reductions in North American NO_x emissions, growth of Canada's oil sands, and climate change since 2007, it would be interesting to continue the air quality study started in this chapter. Finally, in Chapter 6, we suggested the use of all mid-latitude NDACC-IRWG sites to be included in a polar intrusion study. Given the significant polar intrusions during winter 2013-2014, there may be renewed interest in this topic.

Appendix A

Retrieval analysis from M.Sc. report

This appendix is the first part of “Chapter 3: Retrieval Analysis”, taken directly out of my M.Sc. report [Whaley, 2009], for archival purposes. It summarizes the results of microwindow testing for TAO retrievals of O₃, CO, C₂H₆, CH₄, and N₂O.

A.1 Retrieval Parameters

Optimal estimation retrievals require an *a priori* VMR profile and its uncertainty in the form of a covariance matrix S_a ¹. For TAO, the *a priori* profiles were taken mainly from different satellite measurements over Toronto [Wiacek, 2006]:

- The CH₄ and N₂O *a priori* profiles are based on the Michelson Interferometer for Passive Atmospheric Sounding (MIPAS) satellite observations,
- the CO *a priori* profile comes from a combination of the GEOS-Chem model, the Whole-Atmosphere Community Climate Model (WACCM) and the Atmospheric Chemistry Experiment (ACE) satellite observations,
- the O₃ *a priori* profile comes from a combination of the GEOS-Chem model,

¹The *a priori* covariance matrix includes both the uncertainty in the *a priori* profile and the natural variability of the trace gas in the atmosphere.

the Halogen Occultation Experiment (HALOE) satellite observations, and MIPAS satellite observations,

- and the C_2H_6 *a priori* profile is based on the GEOS-Chem model.

In the future, all IRWG stations plan to use *a priori* profiles computed from the WACCM model. But in this study, all retrievals were done with the standard TAO *a priori* profiles from the various sources listed above. The S_a matrices are estimates based on the standard deviations in HALOE profiles over Toronto, as well as various other sources, and rounded up to account for natural climatological variations (see *Wiacek* [2006] for details).

One must also input a desired MW, or set of MWs, when retrieving a gas. The choice of MWs is important because if they are too small then important information may be lost from the wings of the spectral lines, which, as discussed in Section 2.1.1, can reduce the vertical information in the retrieved profile. In turn, this means that broader MWs can increase the number of independent pieces of information (or *degrees of freedom for signal*) [*Barret et al.*, 2002; *Schneider and Hase*, 2008]. However, if they are too large then they may start to include lines from other gases (*interfering species*) and could have more noise. A set of MWs were previously selected for the TAO FTS (see *Wiacek* [2006] and *Taylor* [2008]), however, in some cases these differed from those used by other NDACC-IRWG stations. The NDACC-IRWG has begun an initiative to harmonize the retrieval parameters for all IRWG stations around the world (including TAO) and their recommendations have started with the MWs. Some of these recommended MWs were partly based on work done by a European research project called ‘Time series of Upper Free Troposphere observations from a European ground-based FTIR network’, or UFTIR (<http://www.nilu.no/uftir/>). Presented below is an analysis of the two different sets of MWs: *standard TAO* and *recommended*.

Table A.1: Recommended and standard TAO MWs for the retrieval analysis. Interfering species are given in brackets.

species	recommended MW (cm^{-1})	standard TAO MW (cm^{-1})
CH ₄	2613.70 - 2615.40 (HDO, CO ₂)	
	2650.60 - 2651.30 (HDO, CO ₂)	2650.85 - 2651.25 (HDO)
	2835.50 - 2835.80	2666.95 - 2667.35 (HDO)
	2903.60 - 2904.03 (NO ₂)	2673.90 - 2674.41 (HDO)
	2921.00 - 2921.60 (NO ₂ , HDO, H ₂ O)	
C ₂ H ₆	2976.66 - 2976.95 (H ₂ O, O ₃)	2976.60 - 2977.10 (H ₂ O, CH ₄ , H ₂ CO, O ₃)
	2983.20 - 2983.55 (H ₂ O, O ₃)	2996.70 - 2997.10 (H ₂ O, CH ₄ , H ₂ CO, O ₃)
	2986.50 - 2986.95 (H ₂ O, O ₃)	3000.10 - 3000.60 (H ₂ O, CH ₄ , H ₂ CO, O ₃)
N ₂ O	2481.30 - 2482.60 (CO ₂ , CH ₄ , O ₃ , H ₂ O, HDO)	2481.30 - 2482.60 (CO ₂ , CH ₄ , O ₃)
	2526.40 - 2528.20 (CO ₂ , CH ₄ , O ₃ , H ₂ O, HDO)	
	2537.85 - 2538.80 (CO ₂ , CH ₄ , O ₃ , H ₂ O, HDO)	
	2540.10 - 2540.70 (CO ₂ , CH ₄ , O ₃ , H ₂ O, HDO)	
CO	2057.70 - 2058.00 (CO ₂ , O ₃ , OCS)	2057.684 - 2058.00 (CO ₂ , O ₃)
	2069.56 - 2069.76 (CO ₂ , O ₃ , OCS)	2069.56 - 2069.76 (CO ₂ , O ₃)
	2157.50 - 2159.15 (CO ₂ , O ₃ , OCS, N ₂ O, H ₂ O)	2157.507 - 2159.144 (O ₃ , N ₂ O, H ₂ O)
O ₃	1000.0 - 1005.0 (H ₂ O, CO ₂ , CH ₄ , O ₃ isotopes)	3045.10 - 3045.35 (H ₂ O, CH ₄)

A.2 Microwindow Analysis

Table A.1 lists the new recommended MWs and the standard TAO MWs. In brackets are the interfering species that correspond with the given MW.

The following figures show the results of the CH₄, C₂H₆, N₂O, CO, and O₃ retrievals with original data quality filters in place (Section 3.1.4). The total columns, their percent

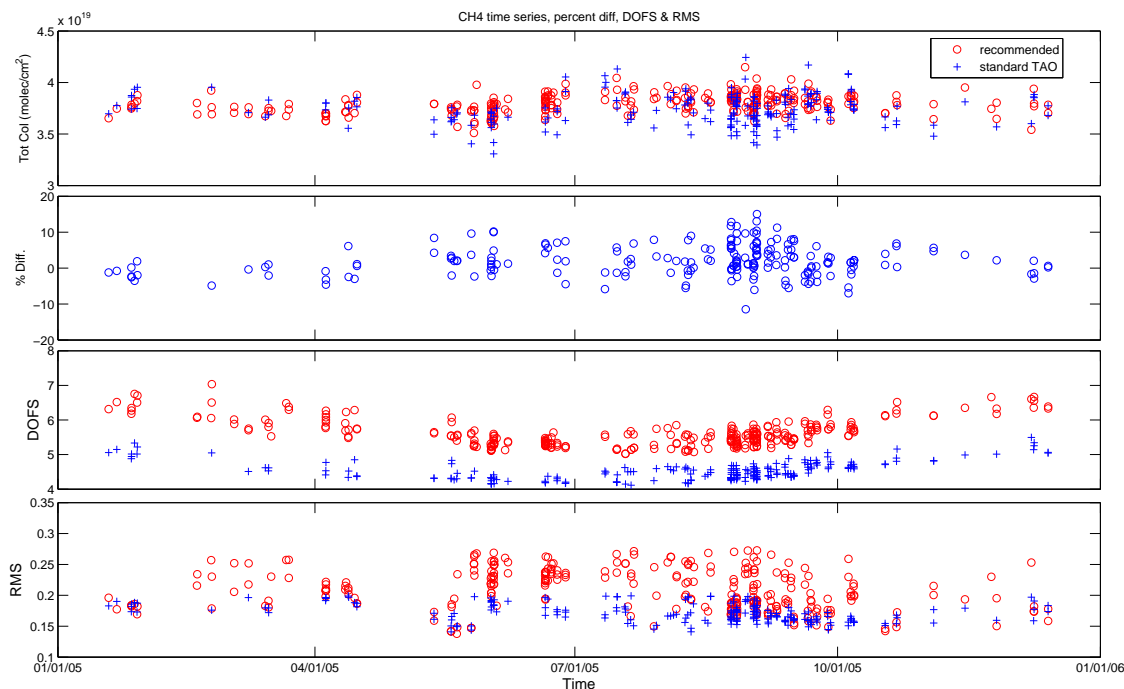


Figure A.1: CH₄ MW analysis. The error bars are not shown for clarity, however they are approximately the same size as the data points.

differences², the degrees of freedom for signal (DOFS), and the RMS fitting residual are all plotted for the year 2005. Data from 2005 were chosen as there were more data that year compared to other years due to a summer FTS intercomparison campaign [*Wunch et al., 2007; Taylor et al., 2007*]. For O₃, the two MWs are so different that they were actually measured with different filters. The recommended MW is in the filter 6 spectral range, (for which there are fewer TAO measurements compared to other filters due to issues with an MCT detector that was later replaced), and the standard TAO MW is in the filter 3 spectral range. Therefore the percent differences could not be computed for O₃ because the data points do not coincide in time.

²Percent differences of the total columns:

$$\%diff = \frac{recommended - standardTAO}{recommended} \times 100\% \quad (\text{A.1})$$

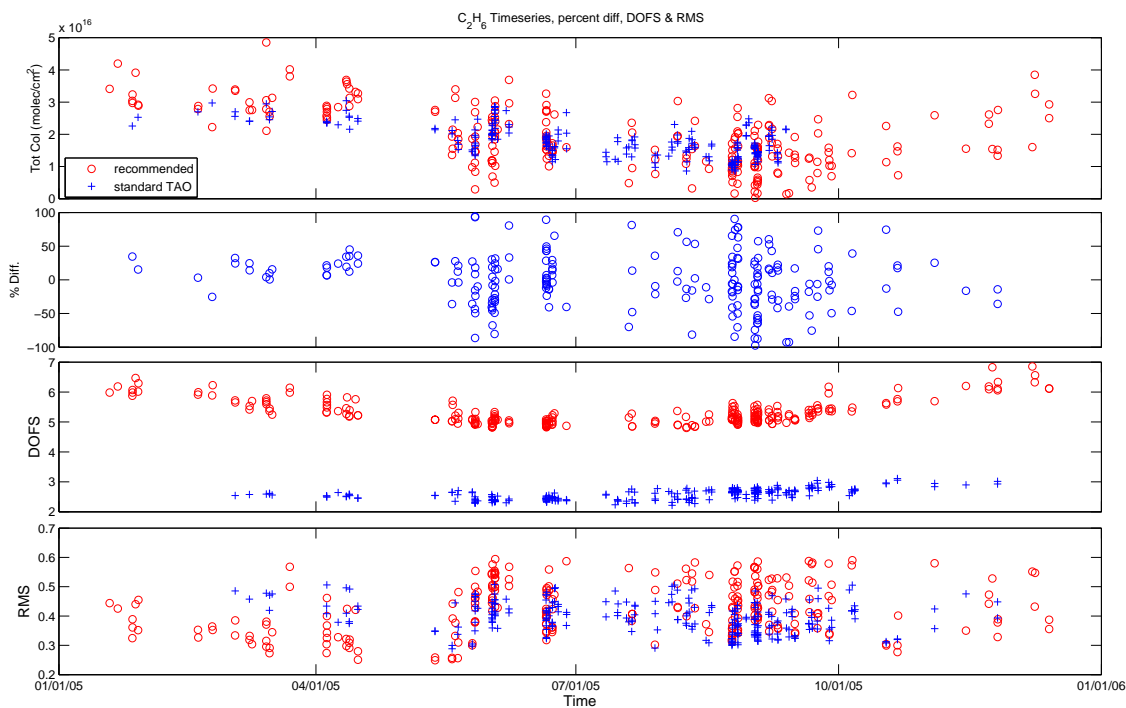


Figure A.2: C_2H_6 MW analysis. The error bars are not shown for clarity, however they are approximately the same size as the data points.

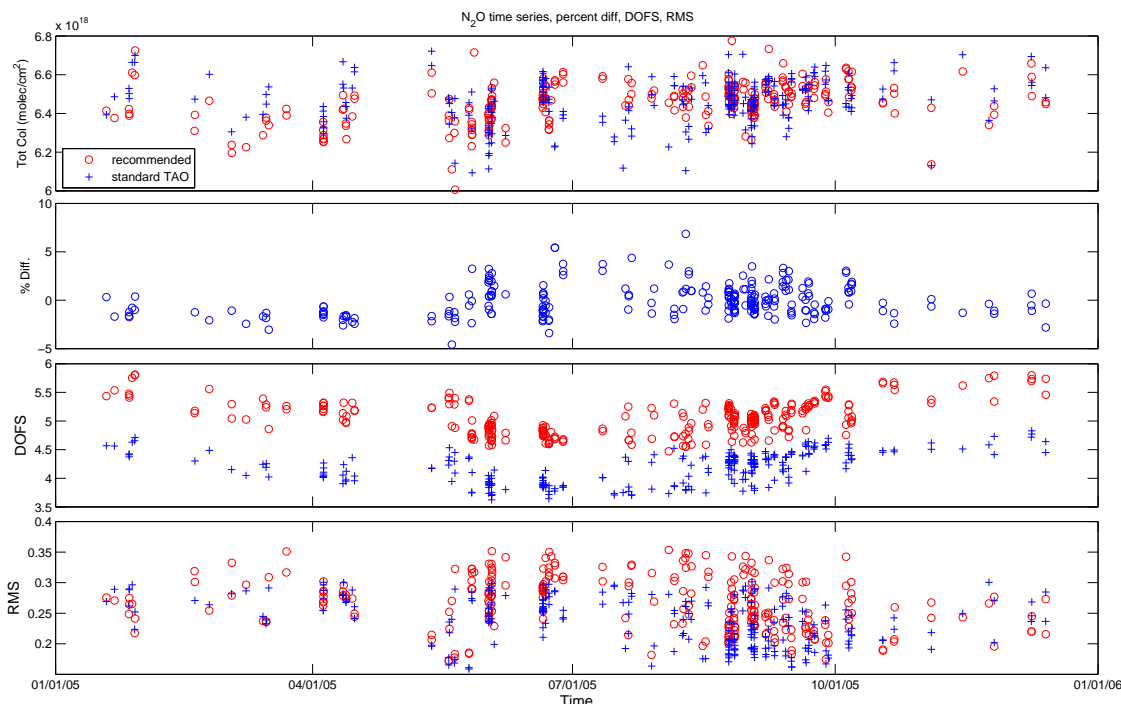


Figure A.3: N_2O MW analysis. The error bars are not shown for clarity, however they are approximately the same size as the data points.

Figures A.1 - A.4 show that in most cases, the new parameters have caused the DOFS to increase, but have also caused the RMS residuals to increase. This is as expected because the recommended MWs are either wider or the number of MWs has increased. This introduces more spectral information and thus higher DOFS, but it also introduces more noise, hence, more scatter in the retrieved values and higher RMS values. A side result of the increased RMS values is that in many cases, more data points have remained after the data quality filtering step (Section 3.1.4). Note that approximately 34 - 38% of the data for each species were filtered out in the data quality step. This may sound like a lot of data being thrown away, however, at TAO, most spectra are acquired in automatic sequences, and sometimes clouds can intermittently block the sun and degrade the measurements. Therefore, the scatter in the time series increases dramatically when

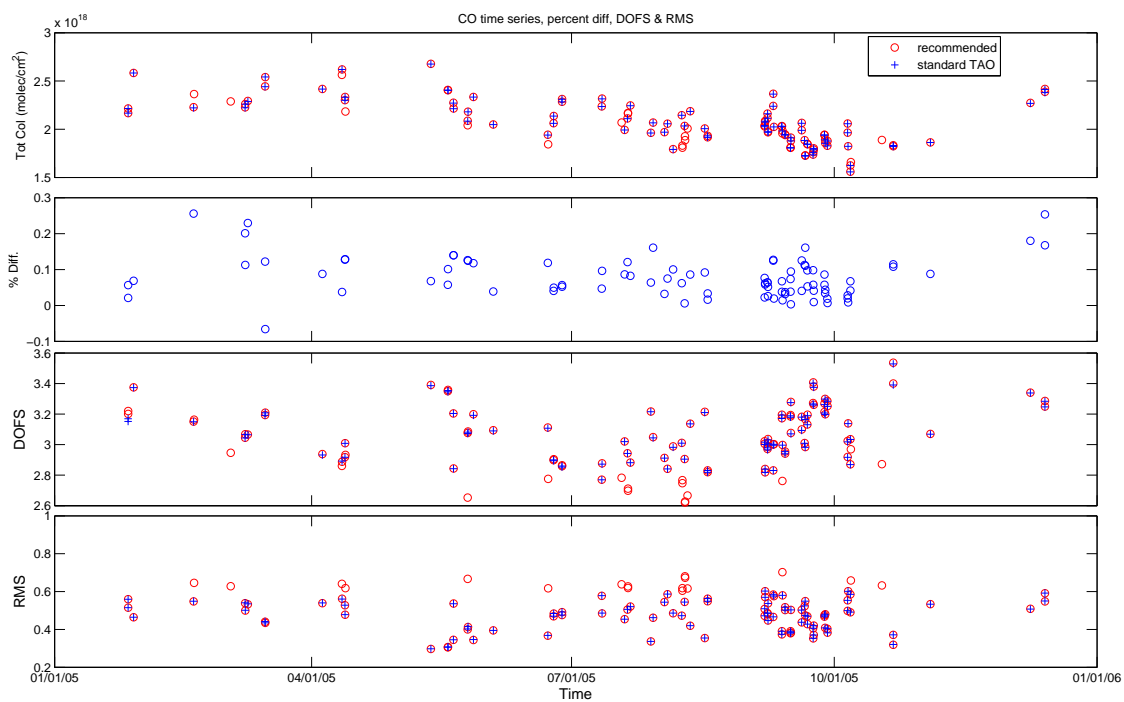


Figure A.4: CO MW analysis. The error bars are not shown for clarity, however they are approximately the same size as the data points.

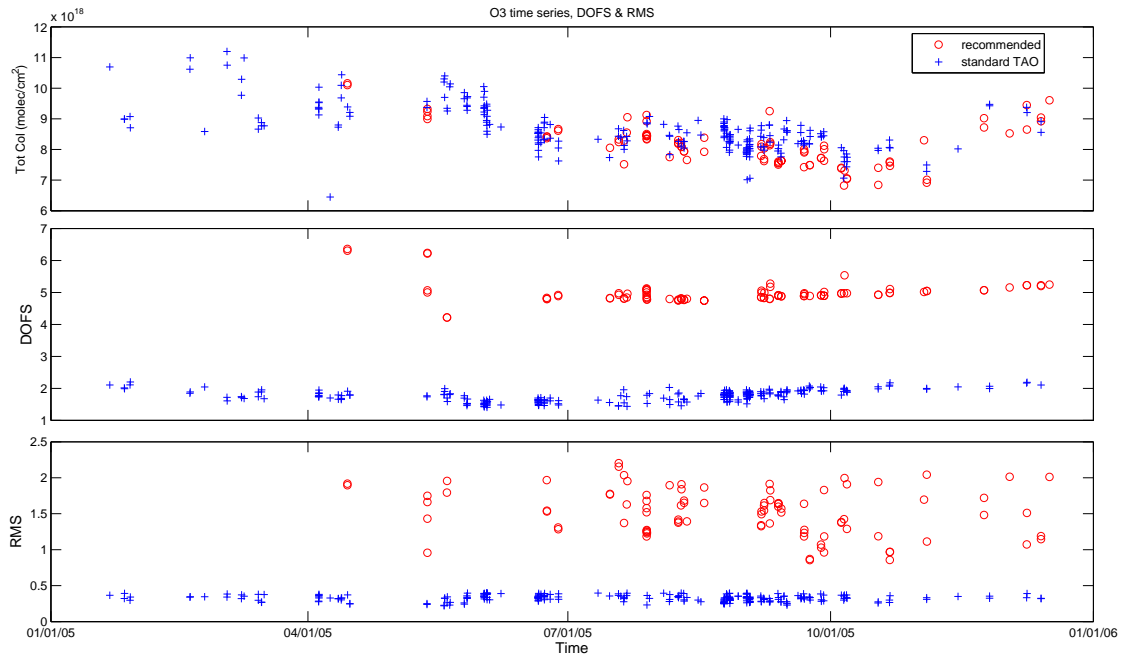


Figure A.5: O₃ MW analysis. The error bars are not shown for clarity, however they are approximately the same size as the data points.

Table A.2: Microwindow analysis: biases

species	mean (%)	median (%)	standard deviation (%)
CH ₄	2.14	1.77	4.28
C ₂ H ₆	-3.69	-0.89	47.04
N ₂ O	-0.03	-0.29	1.66
CO	0.078	0.067	0.056
O ₃	N/A	N/A	N/A

those data points are left in.

The percent differences help us evaluate whether there is a bias for the total columns between the standard TAO and recommended MWs. Table A.2 lists the biases (mean and median percent difference in the total columns and the standard deviation from the mean) that are introduced with the new parameters. For each species, the mean and median biases are small, thus we can conclude that the recommended MWs do not introduce a bias in the retrieved quantities. Note however, that the standard deviation for C₂H₆ is particularly high. This is due to the fact that the C₂H₆ total columns had a lot of scatter. The increased scatter for C₂H₆ may have to do with the data quality filter, which is based on the RMS fitting residual. Since C₂H₆ had such a high RMS residual, this means that more poor quality data were kept.

Figures A.6 - A.15 show some typical spectral fits and their residuals for both the IRWG-recommended MWs and the standard TAO MWs. These are discussed for each species below.

The residuals in Figures A.6 and A.7 for CH₄ are roughly the same size, except for the fifth recommended MW in which the residuals are slightly higher. However, there is slightly less spectral structure seen in the residuals of the recommended MWs, which is a good thing.

The residuals in Figures A.8 and A.9 for C₂H₆ are also approximately the same size

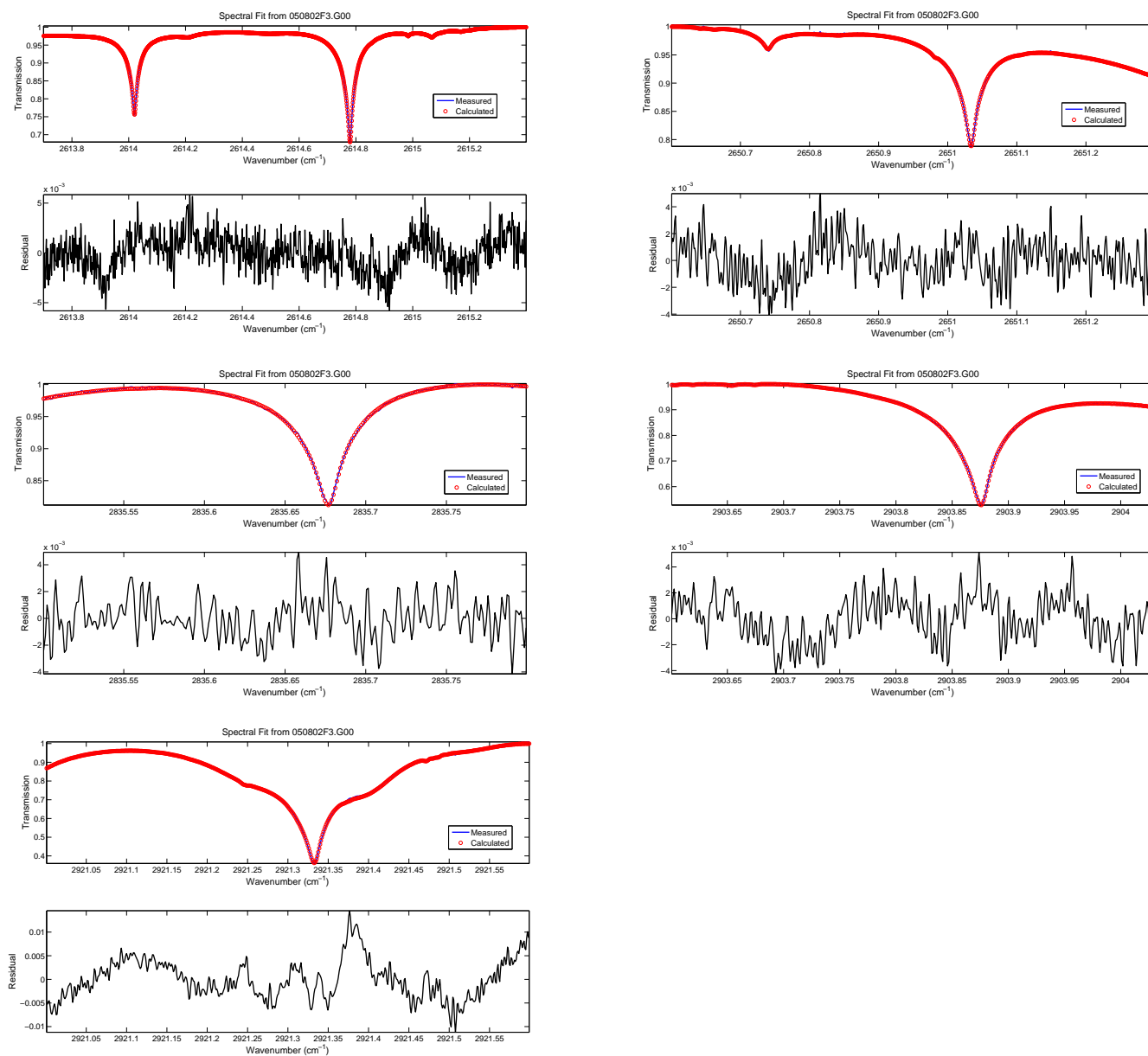
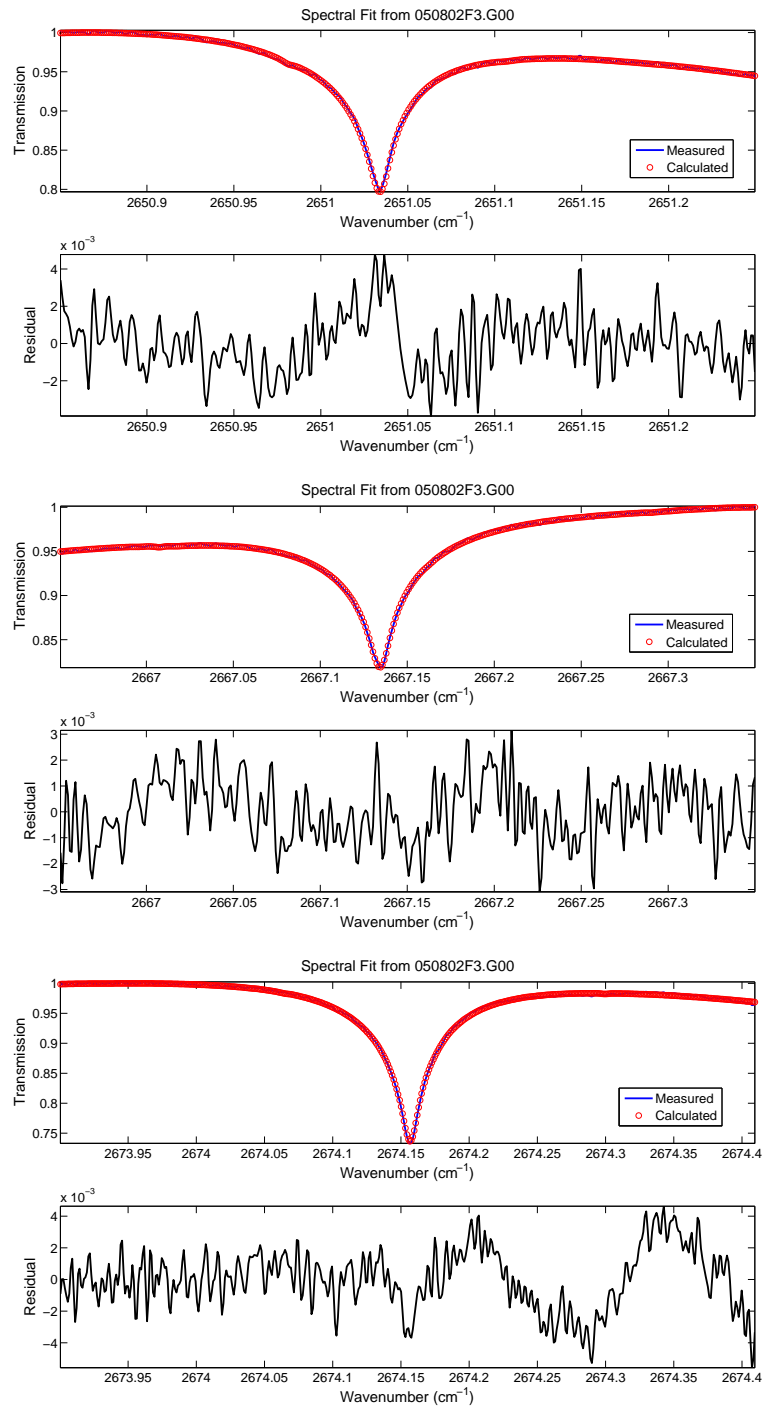


Figure A.6: Typical spectral fits in the IRWG-recommended MWs for CH_4 .

Figure A.7: Typical spectral fits in the standard TAO MWs for CH_4 .

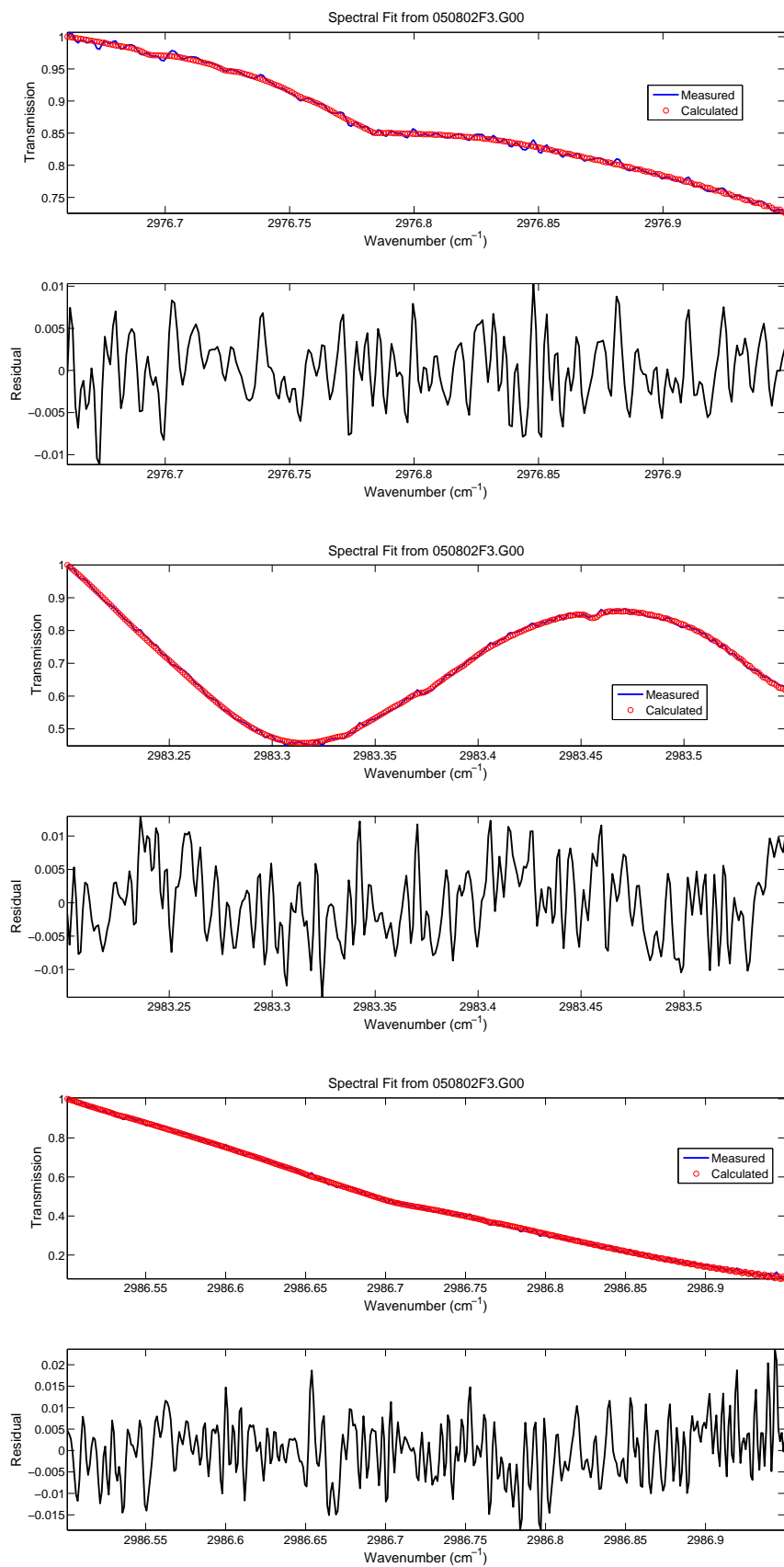
and there is also slightly less spectral structure in the recommended MWs than in the standard TAO ones. Note however, that the C_2H_6 feature is only a tiny dent in the first and last MW in Figure A.8. The general sloping background is due to H_2O and CH_4 [Meier *et al.*, 2004]. This may mean that, even though the fits are nice, there is not as much information in this MW as anticipated.

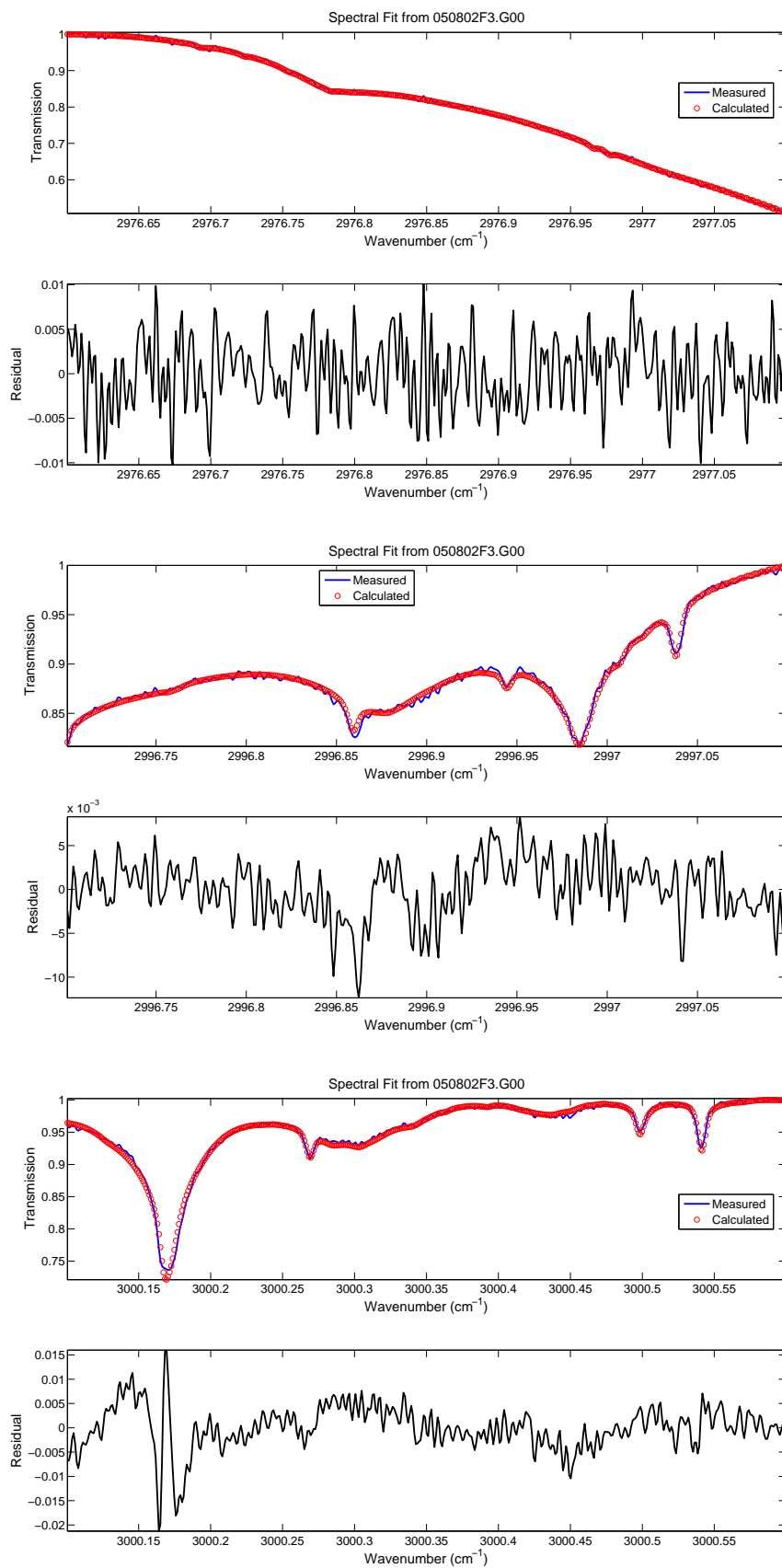
Figures A.10 and A.11 for N_2O also have comparable residuals, however there are four recommended MWs compared to one standard TAO MW, which gives slightly more information (see DOFS in Figure A.3).

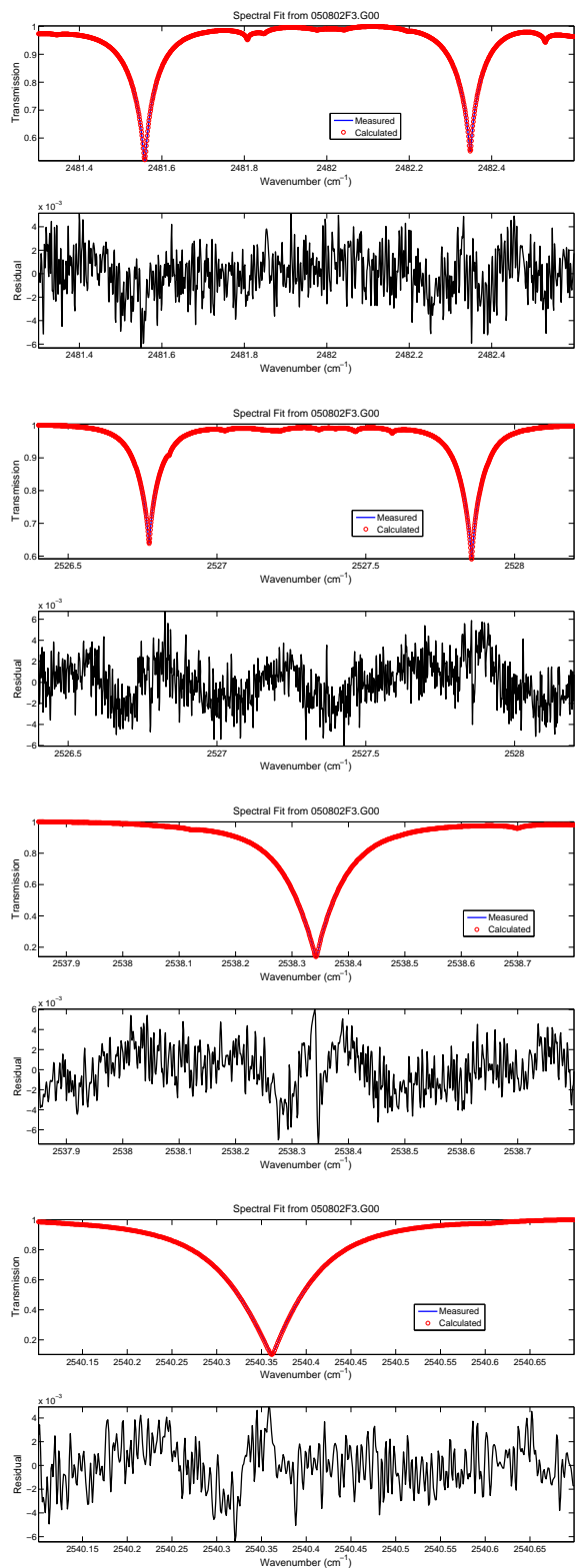
Figures A.12 and A.13 for CO are extremely similar, and poor fits are seen for both sets of MWs. That is, the residuals are quite small (less than 1%), but there is a lot of spectral structure in the residuals. This is however, consistent with CO spectral fits measured at the Eureka IRWG station (80°N , $86^\circ 25'\text{W}$). The CO MWs have quite a bit of interference by O_3 in the first and second MWs, and by N_2O and solar lines in the third MW [Meier *et al.*, 2004]. It is possible that these interfering species are causing the fits to be poor.

Finally Figures A.14 and A.15 for O_3 show that the recommended MW has residuals that are about five times larger than those in the standard TAO MW. There is also more structure in the recommended MW for O_3 . So it is obvious that the increased DOFS in the O_3 retrievals come at the cost of poorer spectral fits. However, the Eureka IRWG station also uses the recommended MW for their retrievals. What they have found is that their residuals are only about 1.5%, compared to TAO's 5%. Also, Eureka's residuals have very little spectral structure, except for the feature located at about 1003.7 cm^{-1} . Therefore, the recommended O_3 MW works well perhaps, for high-latitude sites for which the solar zenith angle (SZA) is larger, than it does for mid-latitude sites like TAO. Further investigation into what other IRWG sites are achieving would be beneficial.

Therefore, in summary the IRWG-recommended MWs work well for CH_4 , N_2O , and CO, as the spectral fits and time series for these species have been good and consistent.

Figure A.8: Typical spectral fits in the IRWG-recommended MWs for C_2H_6 .

Figure A.9: Typical spectral fits in the standard TAO MWs for C_2H_6 .

Figure A.10: Typical spectral fits in the IRWG-recommended MWs for N_2O .

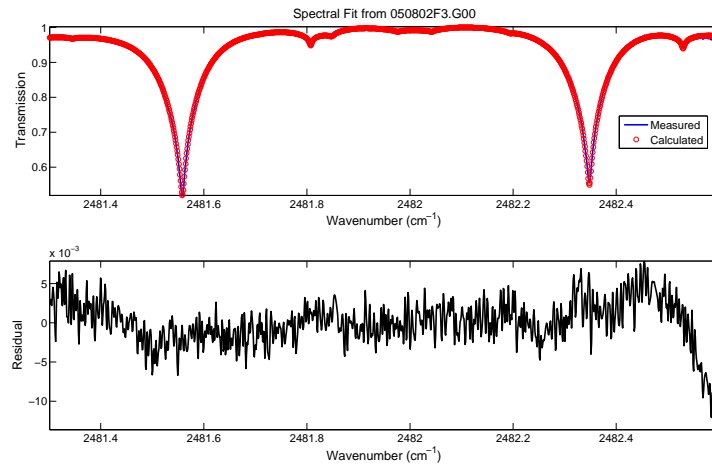


Figure A.11: Typical spectral fit in the standard TAO MW for N_2O .

However, the standard TAO MWs work better for C_2H_6 and O_3 at this time because they give fewer oscillations in the vertical profiles and better spectral fits, respectively. Further investigation into what other IRWG sites are achieving with the recommended MWs should be done to determine if some MWs work better for different latitudes than others. One could also investigate how the retrievals would change if the \mathbf{S}_a matrices were altered. These remain on the agenda for future work.

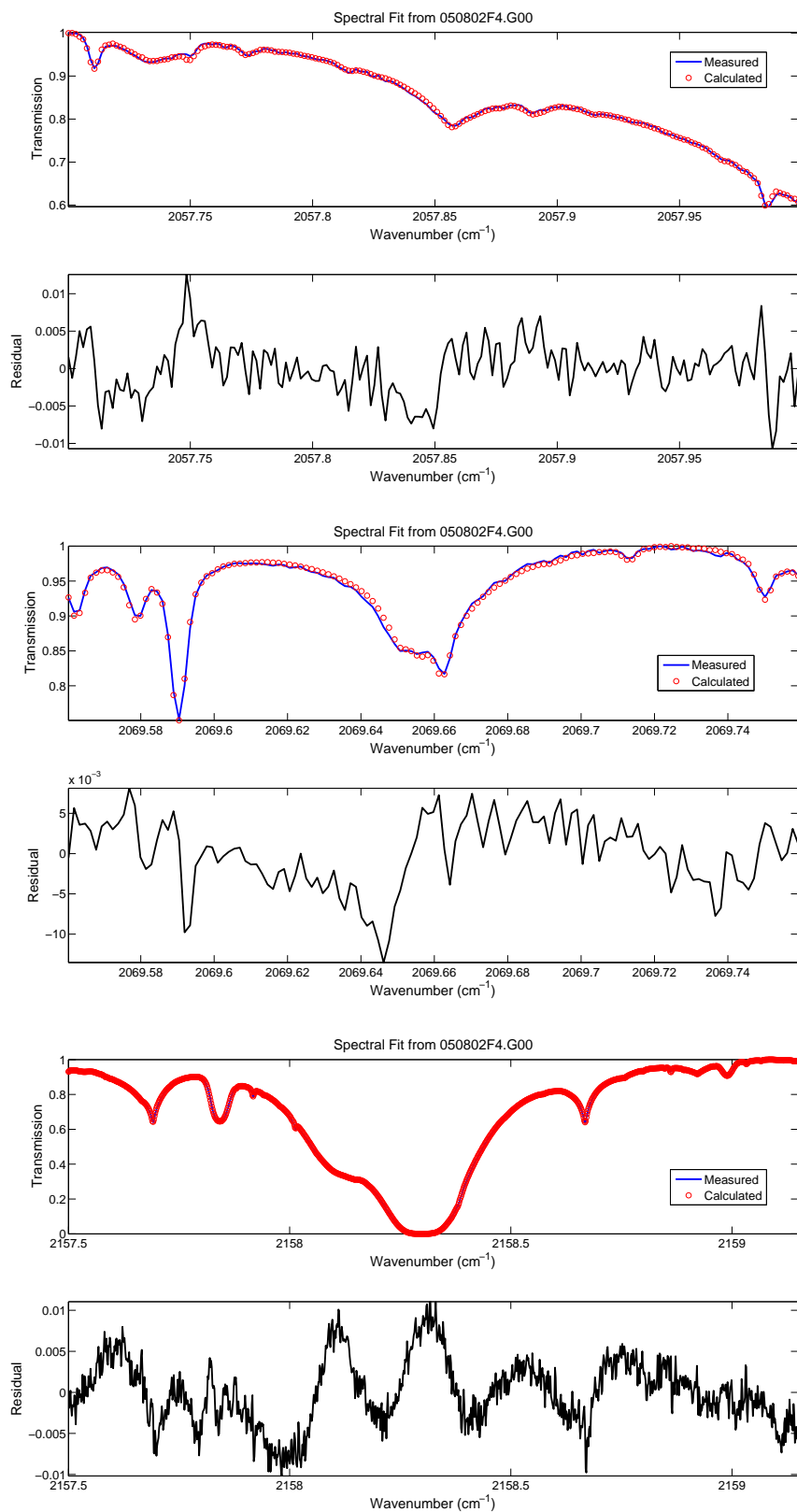


Figure A.12: Typical spectral fits in the IRWG-recommended MWs for CO.

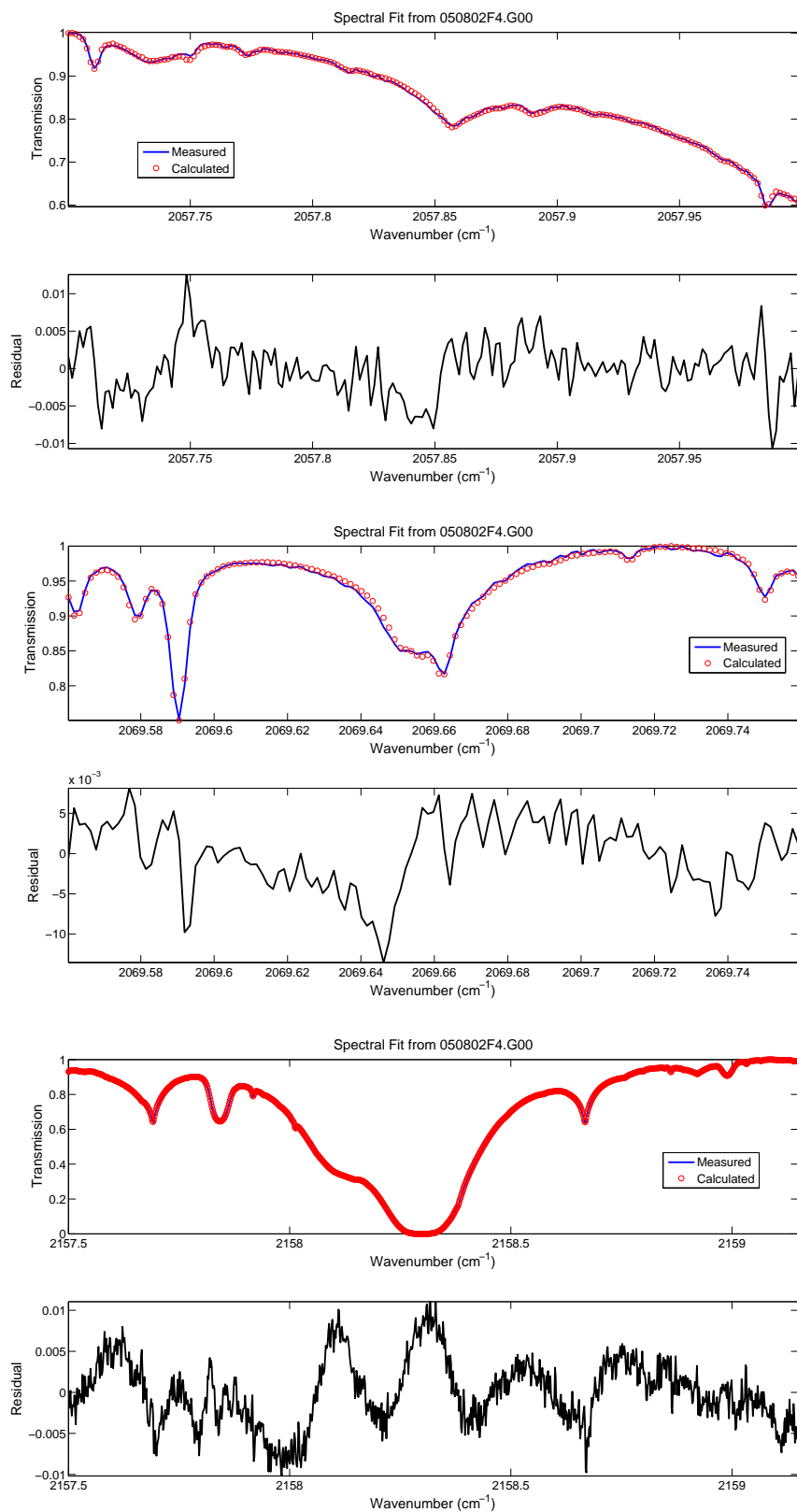
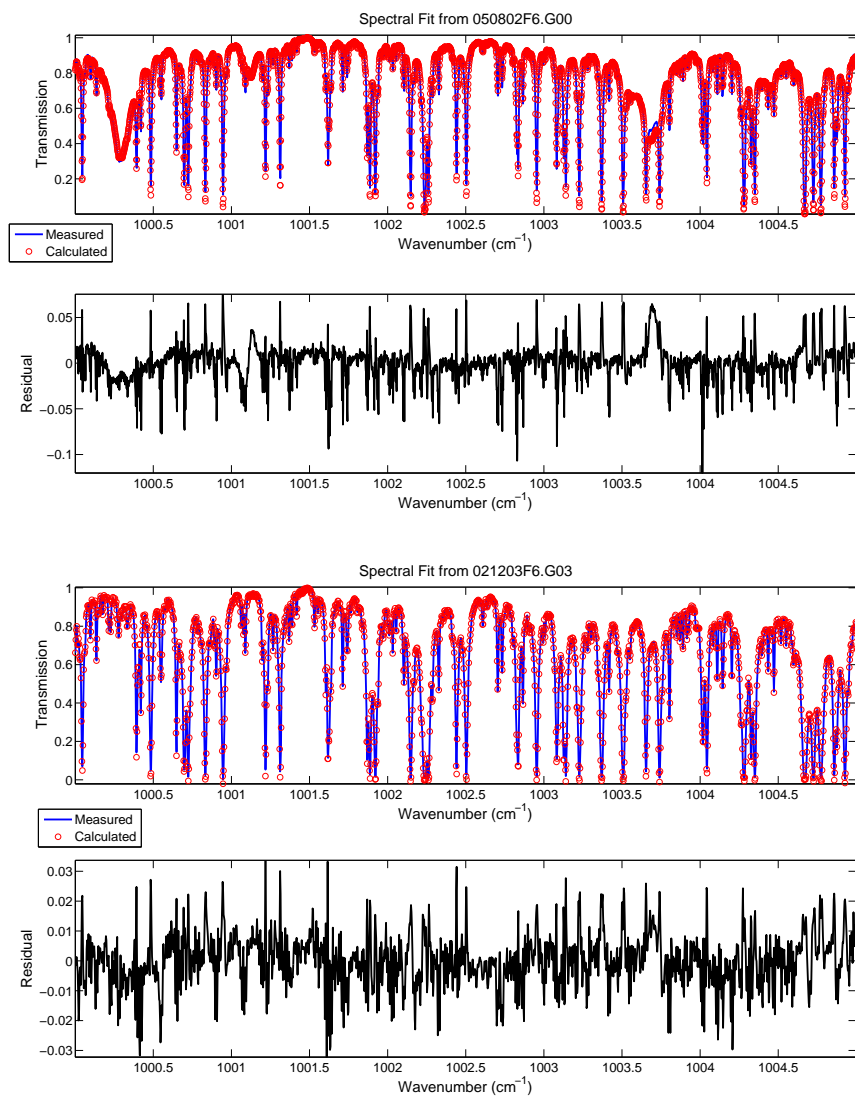


Figure A.13: Typical spectral fits in the standard TAO MWs for CO.

Figure A.14: Two typical spectral fits in the IRWG-recommended MW for O_3 .

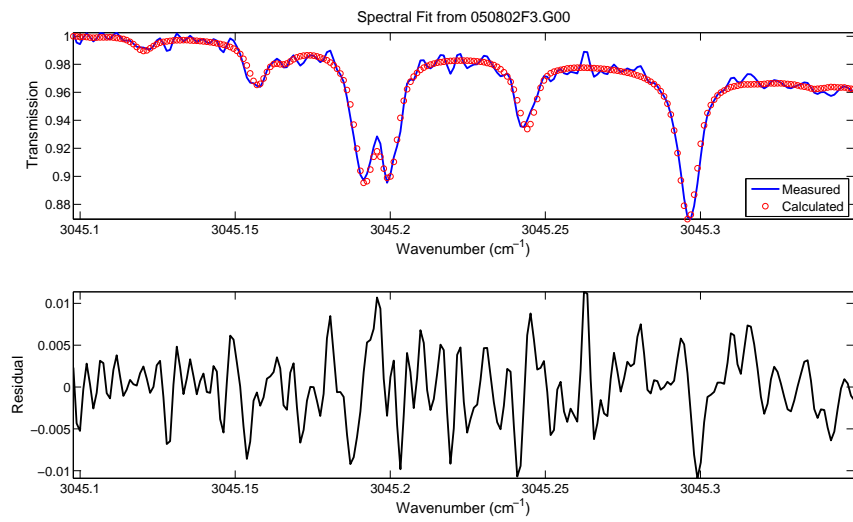


Figure A.15: Typical spectral fit in the standard TAO MW for O₃.

Appendix B

2002-2013 Trends

Table B.1 shows the results of the trend analysis for the total columns of the eight primary species from May 2002 to June 2013. This was done using the method described in *De Mazière et al.* [2005] and *Gardiner et al.* [2008], where a fourth order Fourier series plus a linear trend is fit to the data, and a bootstrap resampling method is used to determine the significance of the trend. Trends which were significant have the 95% confidence bounds given.

Table B.1: Mean annual trends for each species from 2002 to 2013, and, if significant, their 95% confidence limit.

Species	Trend (molecules/cm ² /year)	Trend (%/year)	Confidence Limit (%/year)
O ₃	1.9×10^{16}	0.2	
CO	-3.5×10^{16}	-1.5	-1.6 to -1.3
C ₂ H ₆	2.1×10^{14}	0.9	0.7 to 1.2
HCN	-7.04×10^{11}	-0.015	
CH ₄	7.1×10^{16}	0.19	0.13 to 0.25
N ₂ O	8.5×10^{15}	0.13	0.07 to 0.19
HF	9.4×10^{12}	0.7	0.5 to 0.9
HCl	-2.19×10^{13}	-0.61	-0.8 to -0.4

Bibliography

- Abbot, D. S., P. I. Palmer, R. V. Martin, K. V. Chance, D. J. Jacob, and A. Guenther, Seasonal and interannual variability of North American isoprene emissions as determined by formaldehyde column measurements from space, *Geophys. Res. Lett.*, *30*, 1886–1890, doi:10.1029/2003GL017336, 2003.
- Adams, C., A. E. Bourassa, V. Sofieva, L. Froidevaux, C. A. McLinden, D. Hubert, C. Lambert, E. Sioris, and D. A. Degenstein, Assessment of Odin-OSIRIS ozone measurements from the present using MLS, GOMOS, and ozone sondes, *Atmos. Meas. Tech.*, *7*, 49–64, doi:10.5194/amt-7-49-2014, 2014.
- Adams, C., et al., Severe 2011 ozone depletion assessed with 11 years of ozone, NO₂, and OClO measurements at 80°N, *Geophys. Res. Lett.*, *39*, L05,806, doi:10.1029/2011GL050478, 2012.
- Adams, C., et al., Characterization of Odin-OSIRIS ozone profiles with the SAGE II dataset, *Atmos. Meas. Tech.*, *6*, 1447–1459, doi:10.5194/amt-6-1447-2013, 2013a.
- Adams, C., et al., The spring 2011 final stratospheric warming above Eureka: anomalous dynamics and chemistry, *Atmos. Chem. Phys.*, *13*, 611–624, doi:10.5194/acp-13-611-2013, 2013b.
- Andrews, D. G., *An Introduction to Atmospheric Physics*, Cambridge University Press, New York, 2005.

- Andrews, D. G., J. R. Holton, and C. B. Leovy, *Middle Atmosphere Dynamics*, Academic Press, London, 1987.
- Balis, D., et al., Observed and modelled record ozone decline over the Arctic during winter/spring 2011, *Geophys. Res. Lett.*, *38*, L23,801, doi:10.1029/2011GL049259, 2011.
- Barret, B., M. D. Mazière, and P. Demoulin, Retrieval and characterization of ozone profiles from solar infrared spectra at the Jungfraujoch, *J. Geophys. Res.*, *107*, ACH 19–1ACH 19–15, doi:10.1029/2001JD001298, 2002.
- Batchelor, R. L., K. Strong, R. Lindenmaier, R. L. Mittermeier, H. Fast, J. R. Drummond, and P. F. Fogal, A new Bruker IFS 125HR FTIR spectrometer for the polar environment atmospheric research laboratory at Eureka, Nunavut, Canada: measurements and comparison with the existing Bomem DA8 spectrometer, *J. Atmos. Ocean. Tech.*, *26*, 1328–1340, doi:10.1175/2009JTECHA1215.1, 2009.
- Bauguitte, S., Facility for airborne atmospheric measurements: science instruments, www.faam.ac.uk/index.php/science-instruments/chemistry/64-instruments, 2014.
- Baum, M. M., J. A. Moss, S. H. Pastel, and G. A. Poskrebyshev, Hydrogen cyanide exhaust emissions from in-use motor vehicles, *Environ. Sci. Technol.*, *41*, 857–862, doi:10.1021/es061402v, 2007.
- Beer, R., TES on the Aura mission: Scientific objectives, measurements, and analysis overview, *IEEE Trans. Geosci. Remote Sens.*, *44*, 1102–1105, doi:10.1109/TGRS.2005.863716, 2006.
- Beer, R., T. Glavich, and D. Rider, Tropospheric Emission Spectrometer for the Earth observing system's Aura satellite, *Appl. Opt.*, *40*, 2356–2367, doi:10.1364/AO.40.002356, 2001.

- Bell, J. N. B., and M. Treshow, *Air Pollution and Plant Life. 2nd ed.*, John Wiley and Sons, Inc., Chichester, 2002.
- Bell, R. J., *Introductory Fourier Transform Spectroscopy*, Academic Press, New York, 1972.
- Bernath, P., *Spectra of Atoms and Molecules, 2nd Ed.*, Oxford University Press, New York, 2005.
- Bey, I., D. J. Jacobs, J. A. Logan, and R. M. Yantosca, Asian chemical outflow to the Pacific in spring: origins, pathways, and budgets, *J. Geophys Res*, 106(D19), 23,097–23,113, 2001a.
- Bey, I., et al., Global modeling of tropospheric chemistry with assimilated meteorology: Model description and evaluation, *J. Geophys Res*, 106(D19), 23,073–23,095, 2001b.
- Biraud, S. C., Carbon monoxide mixing ratio system handbook, U.S. Dept. of Energy, ARM Climate Research Facility, 2011.
- Bloom, A., P. Palmer, A. Fraser, D. S. Reay, and C. Frankenberg, Large-scale controls of methanogenesis inferred from methane and gravity spaceborne data, *Science*, 327, 322–325, doi:10.1126/science.1175176, 2010.
- Bowman, K., et al., Tropospheric Emission Spectrometer: Retrieval method and error analysis, *IEEE Trans. Geosci. Remote Sens.*, 44, 1297–1307, doi:10.1109/TGRS.2006.871234, 2006.
- Bowman, K., et al., Earth Observing System Tropospheric Emission Spectrometer data validation report v3.0, *JPL*, pp. D–33,192, 2007.
- Brasseur, G. P., J. J. Orlando, and G. S. Tyndall, *Atmospheric Chemistry and Global Change*, Oxford University Press, New York, 1999.

- Brasseur, G. P., et al., European scientific assessment of the atmospheric effects of aircraft emissions, *Atmos. Environ.*, *32*(13), 2329–2418, doi:10.1016/S1352-2310(97)00486-X, 1998.
- Brewer, A., Evidence for a world circulation provided by the measurements of helium and water vapour distribution in the stratosphere, *Q. J. R. Meteorol. Soc.*, *75*(326), 351363, doi:10.1002/qj.49707532603, 1949.
- Brown, L. R., et al., Methane line parameters in HITRAN, *J. Quant. Spec. Rad. Trans.*, *82*, 219–238, doi:10.1016/S0022-4073(03)00155-9, 2003.
- Butchart, N., The Brewer-Dobson circulation, *Rev. Geophys.*, *52*(2), 157–184, doi:10.1002/2013RG000448, 2014.
- Butchart, N., and E. E. Remsberg, The area of the stratospheric polar vortex as a diagnostic for tracer transport on an isentropic surface, *J. Atmos. Sci.*, *43*, 1319–1339, 1986.
- Chan, D., Y. X. Wang, M. B. McElroy, K. He, R. M. Yantosca, and P. L. Sager, Regional CO pollution and export in China simulated by the high-resolution nested-grid GEOS-Chem model, *Atmos. Chem. Phys.*, *9*, 3825–3839, doi:10.5194/acp-9-3825-2009, 2009.
- Chapman, S., A theory of upper-atmospheric ozone, *Mem. Roy. Met. Soc.*, *3*, 103–125, 1929.
- Chin, M., D. J. Jacob, J. W. Munger, D. D. Parish, and B. G. Doddridge, Relationship of ozone and carbon monoxide over North America, *J. Geophys. Res.*, *99*, 14,565–14,573, doi:10.1029/94JD00907, 1994.
- Chipperfield, M. P., et al., On the use of HF as a reference for the comparison of stratospheric observations and models, *J. Geophys. Res.*, *102*(D11), 12,901–12,919, doi:10.1029/96JD03964, 1997.

- Christensen, T., et al., Vortex-averaged Arctic ozone depletion in the winter 2002/2003, *Atmos. Chem. Phys.*, *5*, 131–138, doi:10.5194/acp-5-131-2005, 2005.
- Coffey, M. T., A. Goldman, J. W. Hannigan, W. G. Mankin, W. G. Schoenfeld, C. P. Rinsland, C. Bernardo, and D. W. T. Griffith, Improved vibration-rotation (0-1) HBr line parameters for validating high resolution infrared atmospheric spectra measurements, *J. Quant. Spec. Rad. Trans.*, *60*, 863–867, doi:10.1016/S0022-4073(98)00088-0, 1998.
- Coffey, M. T., et al., Airborne Fourier transform spectrometer observations in support of EOS Aura validation, *J. Geophys. Res.*, *113*, D16S42, doi:10.1029/2007JD008833, 2008.
- Cohan, D. S., Y. Hu, and A. G. Russell, Alternative approaches to diagnosing ozone production regime, in *Air Pollution Modeling and Its application XVII*, edited by C. Borrego and A.-L. Norman, Springer, New York, 2007.
- Cooper, O. R., R.-S. Gao, D. Tarasick, T. Leblanc, and C. Sweeney, Long-term ozone trends at rural ozone monitoring sites across the United States, 1990-2010, *J. Geophys. Res.*, *117*, D22,307, doi:10.1029/2012JD018261, 2012.
- Crutzen, P. J., and M. O. Andreae, Biomass burning in the tropics: Impact on atmospheric chemistry and biogeochemical cycles, *Science*, *250(4988)*, 1669–1678, doi:10.1126/science.250.4988.1669, 1990.
- Deeter, M. N., H. M. Worden, D. P. Edwards, J. C. Gille, and A. E. Andrews, Evaluation of MOPITT retrievals of lower-tropospheric carbon monoxide over the United States, *J. Geophys. Res.*, *117*, D13,306, doi:10.1029/2012JD017553, 2012.
- Degenstein, D. A., A. E. Bourassa, C. Z. Roth, and E. J. Llewellyn, Limb scatter ozone retrieval from 10 to 60 km using a multiplicative algebraic reconstruction technique, *Atmos. Chem. Phys.*, *9*, 6521–6529, doi:10.5194/acp-9-6521-2009, 2009.

- Dobson, G. M. B., Origin and distribution of the polyatomic molecules in the atmosphere, *Proceedings of the Royal Society of London. Series A, Mathematical and Physical Sciences*, 236(1205), 187–193, 1956.
- Duchatelet, P., E. Mahieu, R. Ruhnke, W. Feng, M. Chipperfield, P. Demoulin, P. Bernath, C. D. Boone, and K. A. Walker, An approach to retrieve information on the carbonyl fluoride (COF₂) vertical distributions above Jungfraujoch by FTIR multi-spectrum multi-window fitting, *Atmos. Chem. Phys.*, 9, 9027–9042, doi:10.5194/acp-9-9027-2009, 2009.
- Duncan, B. N., S. E. Strahan, Y. Yoshida, S. D. Steenrod, and N. Livesey, Model study of the cross-tropopause transport of biomass burning pollution, *Atmos. Chem. Phys.*, 7, 3713–3736, doi:10.5194/acp-7-3713-2007, 2007.
- Dunkerton, T. J., and D. P. Delisi, Evolution of potential vorticity in the winter stratosphere of January-February 1979, *J. Geophys. Res.*, 91(D1), 1199–1208, doi:10.1029/JD091iD01p01199, 1986.
- Durry, G., and A. Hauchecorne, Evidence for long-lived polar vortex air in the mid-latitude summer stratosphere from in situ laser diode CH₄ and H₂O measurements, *Atmos. Chem. Phys.*, 5, 1467–1472, doi:10.5194/acp-5-1467-2005, 2005.
- Emmons, L. K., D. P. Edwards, M. N. Deeter, J. C. Gille, T. Campos, P. Nédélec, P. Novelli, and G. Sachse, Measurements Of Pollution In The Troposphere (MOPITT) validation through 2006, *Atmos. Chem. Phys.*, 9, 1795–1803, doi:10.5194/acp-9-1795-2009, 2009.
- EPA, *Smog Who Does It Hurt? - What You Need to Know About Ozone and Your Health*, U.S. Environmental Protection Agency, Washington, United States, technical Report, 1999.

- EPA, Our nation's air - status and trends through 2010, U.S. Environmental Protection Agency Office of Air Quality Planning and Standards, Research Triangle Park, North Carolina, 2012.
- Eyring, V., et al., Multimodel projections of stratospheric ozone in the 21st century, *J. Geophys. Res.*, *112*, D16,303, doi:10.1029/2006JD008332, 2007.
- Fairlie, T. D. A., R. B. Pierce, W. L. Grose, G. Lingenfelter, M. Loewenstein, and J. R. Podolske, Lagrangian forecasting during ASHOE/MAESA: Analysis of predictive skill for analyzed and reverse-domain-filled potential vorticity, *J. Geophys. Res.*, *102*(D11), 13,169–13,182, doi:10.1029/96JD03507, 1997.
- Fellgett, P., The multiplex advantage, Ph.D. thesis, University of Cambridge, 1951.
- Fiore, A. M., D. J. Jacob, I. Bey, R. M. Yantosca, B. D. Field, A. C. Fusco, and J. G. Wilkinson, Background ozone over the United States in summer: Origin, trend, and contribution to pollution episodes, *J. Geophys. Res.*, *107*(D15), ACH 11–1–ACH 11–25, doi:10.1029/2001JD000982, 2002.
- Fisher, J. A., et al., Source attribution and interannual variability of Arctic pollution in spring constrained by aircraft (ARCTAS, ARCPAC) and satellite (AIRS) observations of carbon monoxide, *Atmos. Chem. Phys.*, *10*, 977–996, doi:10.5194/acp-9-8531-2009, 2010.
- Fishman, J., J. K. Creilson, P. A. Parker, E. A. Ainsworth, G. G. Vining, J. Szarka, F. L. Booker, and X. Xu, An investigation of widespread ozone damage to the soybean crop in the upper Midwest determined from ground-based and satellite measurements, *Atmos. Environ.*, *44*, 2248–2256, doi:10.1016/j.atmosenv.2010.01.015, 2010.
- Gardiner, T., et al., Trend analysis of greenhouse gases over Europe measured by a network of ground-based remote FTIR instruments, *Atmos. Chem. Phys.*, *8*, 6719–6727, doi:10.5194/acp-8-6719-2008, 2008.

- Geddes, J. A., J. G. Murphy, and D. K. Wang, Long term changes in nitrogen oxides and volatile organic compounds in Toronto and the challenges facing local ozone control, *Atmos. Environ.*, *43*, 3407–3415, doi:10.1016/j.atmosenv.2009.03.053, 2009.
- Gillet, N. P., A. J. Weaver, F. W. Zwiers, and M. D. Flannigan, Detecting the effect of climate change on Canadian forest fires, *Geophys. Res. Lett.*, *31*, L18,211, doi:10.1029/2004GL020876, 2004.
- Gilliland, A. B., C. Hogrefe, R. W. Pinder, J. M. Godowitch, K. L. Foley, and S. T. Rao, Dynamic evaluation of regional air quality models: assessing changes in O₃ stemming from changes in emissions and meteorology, *Atmos. Env.*, *42*, 5110–5123, doi:10.1016/j.atmosenv.2008.02.018, 2008.
- Gisi, M., F. Hase, S. Dohe, and T. Blumenstock, Camtracker: a new camera controlled high precision solar tracker system for FTIR-spectrometers, *Atmos. Meas. Tech.*, *4*, 47–54, doi:10.5194/amt-4-47-2011, 2011.
- Godin, S., M. Marchand, A. Hauchecorne, and F. Lefèvre, Influence of Arctic polar ozone depletion on lower stratospheric ozone amounts at Haute-Provence Observatory (43.92°N,5.71°E), *J. Geophys. Res.*, *107*(D20), 8272, doi:10.1029/2001JD00516, 2002.
- Godowitch, J. M., G. A. Pouliot, and S. T. Rao, Assessing multi-year changes in modeled and observed urban NO_x concentrations from a dynamical model evaluation perspective, *Atmos. Env.*, *44*, 2894–2901, doi:10.1016/j.atmosenv.2010.04.040, 2010.
- Griffin, D., et al., Investigation of CO, C₂H₆ and aerosols in a boreal fire plume over eastern Canada during BORTAS 2011 using ground- and satellite-based observations and model simulations, *Atmos. Chem. Phys.*, *13*(D20), 10,227–10,241, doi:10.5194/acp-13-10227-2013, 2013.
- Griffiths, P., and J. D. Haseth, *Fourier Transform Infrared Spectroscopy, 2nd Ed.*, John Wiley and Sons Inc., Hoboken, New Jersey, 2007.

- Guenther, A. B., P. R. Zimmerman, P. C. Harley, R. K. Monson, and R. Fall, Isoprene and monoterpene emission rate variability: model evaluations and sensitivity analyses, *J. Geophys. Res.*, *98*, 12,609–12,617, doi:10.1029/93JD00527, 1993.
- Hannigan, J. W., IRWG uniform retrieval parameter summary, Report distributed among the NDACC-IRWG, 2012.
- Harvey, V. L., R. B. Pierce, T. D. Fairlie, and M. H. Hitchman, A climatology of stratospheric polar vortices and anticyclones, *J. Geophys. Res.*, *107*(D20), 4442, doi:10.1029/2001JD001471, 2002.
- Hase, F., T. Blumenstock, and C. Paton-Walsh, Analysis of the instrumental line shape of high-resolution Fourier transform IR spectrometers with gas cell measurements and new retrieval software, *Appl. Opt.*, *38*(15), 3417–3422, doi:10.1364/AO.38.003417, 1999.
- Hauchecorne, A., S. Godin, M. Marchand, B. Heese, and C. Souprayen, Quantification of the transport of chemical constituents from the polar vortex to midlatitudes in the lower stratosphere using the high-resolution advection model MIMOSA and effective diffusivity, *J. Geophys. Res.*, *107*(D20), 8289–8302, doi:10.1029/2001JD0000491, 2002.
- Henze, D. K., A. Hakami, and J. H. Seinfeld, Development of the adjoint of GEOS-Chem, *Atmos. Chem. Phys.*, *7*, 2413–2433, doi:10.5194/acp-7-2413-2007, 2007.
- Hoskins, B. J., M. E. McIntyre, and A. W. Robertson, On the use and significance of isentropic potential vorticity maps, *Quart. J. R. Met. Soc.*, *111*, 877–946, doi:10.1002/qj.49711147002, 1985.
- Hudman, R. C., L. T. Murray, D. J. Jacob, S. Turquety, S. Wu, D. B. Millet, M. Avery, A. H. Goldstein, and J. Holloway, North American influence on tropospheric ozone and the effects of recent emission reductions: Constraints from ICARTT observations, *J. Geophys. Res.*, *114*(D7), doi:10.1029/2008JD010126, 2009.

- Hudman, R. C., et al., Ozone production in transpacific Asian pollution plumes and implications for ozone air quality in California, *J. Geophys. Res.*, *109*(D23), doi:10.1029/2004JD004974, 2004.
- IGOS, IGOS, the changing atmosphere: An integrated global atmospheric chemistry observation theme for the IGOS partnership, ESA SP-1282. Report GAW No. 159 (WMO TD No. 1235), 2004.
- International Joint Commission, Canada United States Air Quality Agreement progress report 2012, Environment Canada Report, 2012.
- IPCC, WorkingGroup1, Climate change 2013: the physical science basis, *Fifth Assessment report of the Intergovernmental Panel on Climate Change (IPCC)*, Cambridge University Press, 2013.
- Jacob, D., *Introduction to Atmospheric Chemistry*, Princeton University Press, Princeton, 1999.
- Jacob, D. J., and D. A. Winner, Effect of climate change on air quality, *Atmos. Environ.*, *43*, 51–63, doi:10.1016/j.atmosenv.2008.09.051, 2009.
- Jacob, D. J., et al., Origin of ozone and NO_x in the tropical troposphere: A photochemical analysis of aircraft observations over the South Atlantic basin, *J. Geophys. Res.*, *101*, 24,23524,250, doi:10.1029/96JD00336, 1996.
- Jacquinet, P., and C. Dufour, Conditions optiques d'emploi des cellules photoélectriques dans les spectrographes et les interféromètres, *J. Rech. CNRS (Paris)*, *6*, 91–103, 1948.
- Jaeglé, L., et al., Satellite mapping of rain-induced nitric oxide emissions from soils, *J. Geophys. Res.*, *109*(D21), doi:10.1029/2004JD004787, 2004.
- Jaffe, D., I. Bertschi, L. Jaegle, P. Novelli, J. S. Reid, H. Tanimoto, R. Vingarzan, and D. L. Westphal, Long-range transport of Siberian biomass burning emissions and im-

- pact on surface ozone in western North America, *Geophys. Res. Lett.*, *31(16)*, L16,106, doi:10.1029/2004GL020093, 2004.
- Jayanarayanan, K., A. Kleinbohl, M. Sinnhuber, H. Bremer, H. Kullmann, J. Notholt, S. Godin-Beekmann, O. Tripathi, and G. Nikulin, Arctic ozone depletion in 2002-2003 measured by ASUR and comparison with POAM observations, *J. Geophys. Res.*, *116(D22305)*, doi:10.1029/2011JD016020, 2011.
- Jones, N. B., K. Riedel, W. Allan, S. Wood, P. I. Palmer, K. Chance, and J. Notholt, Long-term tropospheric formaldehyde concentrations deduced from ground-based Fourier transform solar infrared measurements, *Atmos. Chem. Phys.*, *9*, 7131–7142, doi:10.5194/acp-9-7131-2009, 2009.
- Kang, D., V. P. Aneja, R. Mathur, and J. D. Ray, Nonmethane hydrocarbons and ozone in three rural southeast United States national parks: A model sensitivity analysis and comparison to measurements, *J. Geophys. Res.*, *108(D19)*, 4604–4621, doi:10.1029/2002JD003054, 2003.
- Keckhut, P., C. David, M. Marchand, S. Bekki, J. Jumelet, A. Hauchecorne, and M. Höpfner, Observation of polar stratospheric clouds down to the Mediterranean coast, *Atmos. Chem. Phys.*, *7*, 5275–5281, doi:10.5194/acp-7-5275-2007, 2007.
- Konopka, P., J.-U. Grooß, S. Bausch, R. Müller, D. S. McKenna, O. Morgenstern, and Y. Orsolini, Dynamics and chemistry of vortex remnants in late arctic spring 1997 and 2000: Simulations with the Chemical Lagrangian Model of the Stratosphere (CLaMS), *Atmos. Chem. Phys.*, *3*, 839–849, doi:10.5194/acp-3-839-2003, 2003.
- Labitzke, K., and M. Kunze, On the remarkable Arctic winter in 2008/2009, *J. Geophys. Res.*, *114*, D00I02, doi:10.1029/2009JD012273, 2009.
- Lee, D. S., et al., Transport impacts on atmosphere and climate: Aviation, *Atmos. Environ.*, *44*, 4678–4734, doi:10.1016/j.atmosenv.2009.06.005, 2010.

- Lee, H.-M., D. K. Henze, B. Alexander, and L. T. Murray, Investigating the sensitivity of surface-level nitrate seasonality in Antarctica to primary sources using a global model, *Atmos. Environ.*, *89*, 757–767, doi:10.1016/j.atmosenv.2014.03.003, 2014.
- Leibensperger, E. M., L. J. Mickley, and D. J. Jacob, Sensitivity of U.S. air quality to mid-latitude cyclone frequency and implications of 1980–2006 climate change, *Atmos. Chem. Phys.*, *8*, 7075–7086, doi:10.5194/acp-8-7075-2008, 2008.
- Leovy, C. B., C.-R. Sun, M. Hitchman, E. E. Remsburg, J. M. R. III, L. L. Gordley, J. C. Gille, and L. V. Lyjak, Transport of ozone in the middle stratosphere: Evidence for planetary wave breaking, *J. Atmos. Sci.*, *42*, 230–244, doi:10.1175/1520-0469(1985)042<0230:TOOITM>2.0.CO;2, 1985.
- Li, Q., P. I. Palmer, H. C. Pumphrey, P. Bernath, and E. Mahieu, What drives the observed variability of HCN in the troposphere and lower stratosphere?, *Atmos. Chem. Phys.*, *9*, 8531–8543, doi:10.5194/acp-9-8531-2009, 2009.
- Lin, C.-Y. C., D. J. Jacob, J. W. Munger, and A. M. Fiore, Increasing background ozone in surface air over the United States, *Geophys. Res. Lett.*, *27*, 3465–3468, doi:10.1029/2000GL011762, 2000.
- Lin, S.-J., and R. B. Rood, Multidimensional flux-form semi-lagrangian transport schemes, *Mon. Wea. Rev.*, *124*, 2046–2070, doi:10.1175/1520-0493(1996)124<2046:MFFSLT>2.0.CO;2, 1996.
- Lindenmaier, R., R. Batchelor, K. Strong, H. Fast, F. Goutail, F. Kolonjari, C. T. McElroy, R. Mittermaier, and K. Walker, An evaluation of infrared microwindows for ozone retrievals using the Eureka Bruker 125HR Fourier transform spectrometer, *J. Quant. Spec. Rad. Trans.*, *111*, 569–585, doi:10.1016/j.jqsrt.2009.10.013, 2010.
- Lindenmaier, R., et al., Unusually low ozone, HCl, and HNO₃ column measurements

- at Eureka, Canada during winter/spring 2011, *Atmos. Chem. Phys.*, *12*, 3821–3835, doi:10.5194/acp-12-3821-2012, 2012.
- Liou, K. N., *An Introduction to Atmospheric Radiation, 2nd Ed.*, Academic Press, San Diego, California, 2002.
- Llewellyn, E. J., et al., The OSIRIS instrument on the Odin spacecraft, *Can. J. Phys.*, *82*, 411–422, doi:10.1139/p04-005, 2004.
- Logan, J., Ozone in rural areas of the United States, *J. Geophys. Res.*, *94(D6)*, 8511–8532, doi:10.1029/JD094iD06p08511, 1989.
- Lorentz, H. A., The absorption and emission of lines of gaseous bodies, HA Lorentz Collected Papers (The Hague, 1934-1939), 1906.
- Mahieu, E., et al., Retrievals of HCN from high-resolution FTIR solar absorption spectra recorded at the Junfraujoch station, poster from the European Geophysical Society, 2007.
- Manney, G. L., R. W. Zurek, A. O'Neill, and R. Swinbank, On the motion of air through the stratospheric polar vortex, *J. Atmos. Sci.*, *51*, 2973–2994, doi:10.1175/1520-0469(1994)051<2973:OTMOAT>2.0.CO;2, 1994.
- Manney, G. L., J. C. Bird, D. P. Donovan, T. J. Duck, J. A. Whiteway, S. R. Pal, and A. I. Carswell, Modeling ozone laminae in ground-based Arctic wintertime observations using trajectory calculations and satellite data, *J. Geophys. Res.*, *103(D5)*, 5797–5814, doi:10.1029/97JD03449, 1998.
- Manney, G. L., H. A. Michelsen, F. W. Irion, M. R. Gunson, G. C. Toon, and A. E. Roche, Lamination and polar vortex development in fall from ATMOS long-lived trace gases observed during November 1994, *J. Geophys. Res.*, *105(D23)*, 29,023–29,038, doi:10.1029/2000JD900428, 2000.

- Manney, G. L., M. J. Schwartz, K. Krüger, M. L. Santee, S. Pawson, J. N. Lee, W. H. Daffer, R. A. Fuller, and N. J. Livesey, Aura Microwave Limb Sounder observations of dynamics and transport during the record-breaking 2009 Arctic stratospheric major warming, *Geophys. Res. Lett.*, *36*, L12,815, doi:10.1029/2009GL038586, 2009.
- Manney, G. L., et al., Solar occultation satellite data and derived meteorological products: Sampling issues and comparisons with Aura Microwave Limb Sounder, *J. Geophys. Res.*, *112*(D24), D24S50, doi:10.1029/2007JD008709, 2007.
- Manney, G. L., et al., Unprecedented Arctic ozone loss in 2011, *Nature*, *478*, 469–475, doi:10.1038/nature10556, 2011.
- Mao, J., et al., Chemistry of hydrogen oxide radicals (HO_x) in the Arctic troposphere in spring, *Atmos. Chem. Phys.*, *10*, 5823–2838, doi:10.5194/acp-10-5823-2010, 2010.
- Mao, J., et al., Ozone and organic nitrates over the eastern United States: Sensitivity to isoprene chemistry, *J. Geophys. Res.*, *118*, 11,256–11,268, doi:10.1002/jgrd.50817, 2013.
- Marchand, M., S. Godin, A. Hauchecorne, F. L. A., and S. Bekki, Influence of polar ozone loss on northern midlatitude regions estimated by a high-resolution chemistry transport model during winter 1999/2000, *J. Geophys. Res.*, *108*(D5), 8326–8337, doi:10.1029/2001JF000906, 2003.
- Mauzerall, D. L., et al., Photochemistry in biomass burning plumes and implications for tropospheric ozone over the tropical South Atlantic, *J. Geophys. Res.*, *103*(D7), 8401–8423, doi:10.1029/97JD02612, 1998.
- McIntyre, M. E., and T. N. Palmer, The “surf zone” in the stratosphere, *J. Atmos. Terr. Phys.*, *9*, 825–849, 1984.

- McLinden, C. A., S. C. Olsen, B. J. Hannegan, O. Wild, M. J. Prather, and J. Sundet, Stratospheric ozone in 3-D models: A simple chemistry and the cross tropopause flux, *J. Geophys. Res.*, *105(D11)*, 14,653–14,665, doi:10.1029/2000JD900124, 2000.
- Meier, A., G. Toon, C. Rinsland, A. Goldman, and F. Hase, Spectroscopic atlas of atmospheric microwindows in the middle infra-red, 2nd ed, IRF Technical Report 048, Swedish Institute for Space Physics, 2004.
- Mellqvist, J., et al., Ground-based FTIR observations of chlorine activation and ozone depletion inside the Arctic vortex during the winter of 1999/2000, *J. Geophys. Res.*, *107(D20)*, 8263–8279, doi:10.1029/2001JD001080, 2002.
- Millard, G. A., A. M. Lee, and J. A. Pyle, A model study of the connection between polar and midlatitude ozone loss in the Northern Hemisphere lower stratosphere, *J. Geophys. Res.*, *108(D5)*, 8323–8332, doi:10.1029/2001JD000899, 2003.
- Millet, D. B., D. J. Jacob, K. F. Boersma, T.-M. Fu, T. P. Kurosu, K. Chance, C. L. Heald, and A. Guenther, Spatial distribution of isoprene emissions from North America derived from formaldehyde column measurements by the OMI satellite sensor, *J. Geophys. Res.*, *113*, D02,307, doi:10.1029/2007JD008950, 2008.
- Millstein, D. E., and R. A. Harley, Impact of climate change on photochemical air pollution in Southern California, *Atmos. Chem. Phys.*, *9*, 3745–3754, doi:10.5194/acp-9-3745-2009, 2009.
- MOE, Ontario Ministry of the Environment air quality in Ontario report for 2010, Queen's Printer for Ontario, 2012.
- MOE, Ontario Ministry of the Environment air quality in Ontario report for 2011, Queen's Printer for Ontario, 2013.

- Monson, R. K., C. H. Jaeger, W. W. A. III, E. M. Drigger, G. M. Silver, and R. Fall, Relationships among isoprene emission rate, photosynthesis and isoprene synthase activity as influenced by temperature, *Plant Physiol.*, *98*, 1175–1180, doi:10.1104/pp.98.3.1175, 1992.
- Moussa, S. G., A. Leithead, J. J. Wentzell, G. Lu, S. Li, J. R. Brook, and J. Liggi, Quantifying the emissions of HCN from on-road vehicles in urban areas, poster presented at 2013 Fall Meeting, AGU, San Francisco, California, 9-13 December, Abstract A31C-0096, 2013.
- Murtagh, D., et al., An overview of the Odin atmospheric mission, *Can. J. Phys.*, *80*, 309–319, doi:10.1139/p01-157, 2002.
- Nash, E. R., P. A. Newman, J. E. Rosenfield, and M. R. Schoeberl, An objective determination of the polar vortex using Ertel's potential vorticity, *J. Geophys. Res.*, *101*(D5), 9471–9478, doi:10.1029/96JD00066, 1996.
- Nassar, R., et al., Validation of Tropospheric Emission Spectrometer (TES) nadir ozone profiles using ozonesonde measurements, *J. Geophys. Res.*, *113*, D15S17, doi:10.1029/2007JD008819, 2009.
- Newman, P. A., et al., Measurements of polar vortex air in midlatitudes, *J. Geophys. Res.*, *101*(D8), 12,879–12,891, doi:10.1029/95JD03387, 1996.
- NOAA, *U.S. Standard Atmosphere, 1976*, U.S. Government Printing Office, Washington D.C., United States, 1976.
- Oltmans, S. J., et al., Trends of ozone in the troposphere, *Geophys. Res. Lett.*, *25*, 139–142, doi:10.1029/97GL03505, 1998.
- Orsolini, Y. J., On the formation of ozone laminae at the edge of the Arctic polar vortex, *Q. J. R. Meteorol. Soc.*, *121*, 1923–1941, doi:10.1002/qj.49712152808, 1995.

- Orsolini, Y. J., and W. B. Grant, Seasonal formation of nitrous oxide laminae in the mid and low latitude stratosphere, *Geophys. Res. Lett*, 27(D8), 1119–1122, doi:10.1029/1999GL011172, 2000.
- Orsolini, Y. J., G. Hansen, U. Hoppe, G. L. Manney, and K. Fricke, Dynamical modelling of wintertime lidar observations in the Arctic: Ozone laminae, and ozone depletion, *Q. J. R. Meteorol. Soc*, 123, 785–800, doi:10.1002/qj.49712353913, 1997.
- Orsolini, Y. J., G. L. Manney, A. Engel, J. Ovarlez, C. Claud, and L. Coy, Layering in stratospheric profiles of long-lived trace species: Balloon-borne observations and modeling, *J. Geophys. Res*, 103(D5), 5815–5825, doi:10.1029/97JD03131, 1998.
- Orsolini, Y. J., G. Hansen, G. L. Manney, N. J. Livesey, and U.-P. Hoppe, Lagrangian reconstruction of ozone column and profile at the Arctic Lidar Observatory for Middle Atmosphere Research (ALOMAR) throughout winter and spring 1997-98, *J. Geophys. Res*, 106(D9), 10,011–10,021, doi:10.1029/2000JD900659, 2001.
- Palmer, P. I., D. J. Jacob, A. M. Fiore, R. V. Martin, K. Chance, and T. P. Kurosu, Mapping isoprene emissions over North America using formaldehyde column observations from space, *J. Geophys. Res*, 108, 4180, doi:10.1029/2002JD002153, 2003.
- Parrington, M., et al., The influence of boreal biomass burning emissions on the distribution of tropospheric ozone over north america and the north atlantic during 2010, *Atmos. Chem. Phys.*, 12(4), 2077–2098, doi:10.5194/acp-12-2077-2012, 2012.
- Parrington, M., et al., Ozone photochemistry in boreal biomass burning plumes, *Atmos. Chem. Phys.*, 13, 7321–7341, doi:10.5194/acp-13-7321-2013, 2013.
- Parrish, D. D., M. Trainer, J. S. Holloway, J. E. Yee, M. S. Warshawsky, F. C. Fehsenfeld, G. L. Forbes, and J. L. Moody, Relationships between ozone and carbon monoxide at surface sites in the North Atlantic region, *J. Geophys. Res.*, 103(D11), 13,357–13,376, doi:10.1029/98JD00376, 1998.

- Paton-Walsh, C., N. M. Deutscher, D. W. T. Griffith, B. W. Forgan, S. R. Wilson, N. B. Jones, and D. P. Edwards, Trace gas emissions from savanna fires in northern Australia, *J. Geophys. Res.*, *115*(D16314), doi:10.1029/2009JD013309, 2010.
- Paton-Walsh, C., C. C. Miller, N. M. Deutscher, D. W. T. Griffith, N. B. Jones, K. Strong, and C. Whaley, Changing total column ethane amounts from NDACC sites, NDACC-IRWG meeting poster, Boulder, CO, USA, May 2011.
- Paulot, F., D. K. Henze, and P. O. Wennberg, Impact of the isoprene photochemical cascade on tropical ozone, *Atmos. Chem. Phys.*, *12*(3), 1307–1325, doi:10.5194/acp-12-1307-2012, 2012.
- Perrin, F. H., Whose absorption law?, *J. Opt. Soc. Am.*, *38*, 72–74, 1948.
- Pierce, R. B., and T. D. A. Fairlie, Chaotic advection in the stratosphere: Implications for the dispersal of chemically perturbed air from the polar vortex, *J. Geophys. Res.*, *98*(D10), 18,589–18,595, doi:10.1029/93JD01619, 1993.
- Pommier, M., C. A. McLinden, and M. Deeter, Relative changes in CO emissions over megacities based on observations from space, *Geophys. Res. Lett.*, *40*, 1–6, doi:10.1002/grl.50704, 2013.
- Ravishankara, A., J. Daniel, and R. Portmann, Nitrous oxide (N₂O): The dominant ozone-depleting substance emitted in the 21st century, *Science*, *326*(123), doi:10.1126/science.1176985, 2009.
- Rienecker, M. M. et al., MERRA: NASA's Modern-Era Retrospective Analysis for Research and Applications, *J. Climate*, *24*, 3624–3648, doi:10.1175/JCLI-D-11-00015.1, 2011.
- Rinsland, C. P., M. A. H. Smith, P. L. Rinsland, A. Goldman, J. W. Brault, and G. M. Stokes, Ground-based infrared spectroscopic measurements of atmospheric hydrogen

- cyanide, *J. Geophys. Res.*, *87(C13)*, 11,119-11,125, doi:10.1029/JC087iC13p11119, 1982.
- Rinsland, C. P., et al., Northern and southern hemisphere ground-based infrared spectroscopic measurements of tropospheric carbon monoxide and ethane, *J. Geophys. Res.*, *103(D21)*, 28,197-28,217, doi:10.1029/98JD02515, 1998.
- Rodgers, C. D., Retrieval of atmospheric temperature and composition from remote measurements of thermal radiation, *Rev. Geophys.*, *14(4)*, 609-624, doi:10.1029/RG014i004p00609, 1976.
- Rodgers, C. D., Characterization and error analysis of profiles retrieved from remote sounding measurements, *J. Geophys. Res.*, *95(D5)*, 5587-5595, doi:10.1029/JD095iD05p05587, 1990.
- Rodgers, C. D., *Inverse Methods For Atmospheric Sounding; Theory and Practice, Series on Atmospheric, Oceanic and Planetary Physics*, vol. 2, World Scientific Publishing Co. Pte. Ltd., New Jersey, 2000.
- Rodgers, C. D., and B. J. Connor, Intercomparison of remote sounding instruments, *J. Geophys. Res.*, *108(D3)*, doi:10.1029/2002JD002299, 2003.
- Rösevall, J. D., D. P. Murtagh, and J. Urban, Ozone depletion in the 2006/2007 Arctic winter, *Geophys. Res. Lett.*, *34*, L21,809, doi:10.1029/2007GL030620, 2007.
- Rösevall, J. D., D. P. Murtagh, J. Urban, W. Feng, P. Eriksson, and S. Brohede, A study of ozone depletion in the 2004/2005 Arctic winter based on data from Odin/SMR and Aura/MLS, *J. Geophys. Res.*, *113*, D13,301, doi:10.1029/2007JD009560, 2008.
- Rothman, L. S., et al., The HITRAN molecular spectroscopic database: edition of 2000 including updates through 2001, *J. Quant. Spec. Rad. Trans.*, *82*, 5-44, 2003.

- Rothman, L. S., et al., The HITRAN 2004 molecular spectroscopic database, *J. Quant. Spec.. Rad. Trans.*, *96*, 139–204, 2005.
- Rothman, L. S., et al., The HITRAN 2008 molecular spectroscopic database, *J. Quant. Spec. Rad. Trans.*, *110*, 533–572, 2009.
- Schneider, M., and F. Hase, Technical note: Recipe for monitoring of total ozone with a precision of around 1 DU applying mid-infrared solar absorption spectra, *Atmos. Chem. Phys.*, *8*, 63–71, doi:10.5194/acp-8-63-2008, 2008.
- Schoeberl, M. R., and P. A. Newman, A multiple-level trajectory analysis of vortex filaments, *J. Geophys. Res.*, *100*(D12), 25,801–25,815, doi:10.1029/95JD02414, 1995.
- Schoeberl, M. R., L. R. Lait, P. A. Newman, and J. E. Rosenfield, The structure of the polar vortex, *J. Geophys. Res.*, *97*(D8), 7859–7882, doi:1029/91JD02168, 1992.
- Schoeberl, M. R., M. Luo, and J. E. Rosenfield, An analysis of the Antarctic Halogen Occultation Experiment trace gas observations, *J. Geophys. Res.*, *100*(D3), 5159–5172, doi:10.1029/94JD02749, 1995.
- Shepard, M. F., S. Barzetti, and D. R. Hastie, The production of NO_x and N₂O from a fertilized agricultural soil, *Atmos. Environ.*, *25A*, 1961–1969, doi:10.1016/0960-1686(91)90277-E, 1991.
- Sillman, S., The use of NO_y, H₂O₂, and HNO₃ as indicators for O₃-NO_x-VOC sensitivity in urban locations, *J. Geophys. Res.*, *100*, 14,175–14,188, doi:10.1029/94JD02953, 1995.
- Singleton, C. S., et al., 2002-2003 Arctic ozone loss deduced from POAM III satellite observations and the SLIMCAT chemical transport model, *Atmos. Chem. Phys.*, *5*, 597–609, doi:10.5194/acp-5-597-2005, 2005.

- Sitch, S., P. M. Cox, W. J. Collins, and C. Huntingford, Indirect radiative forcing of climate change through ozone effects on the land-carbon sink, *Nature Lett.*, *448*, 791–794, doi:10.1038/nature06059, 2007.
- Sonkaew, T., C. von Savigny, K.-U. Eichmann, M. Weber, A. Rozanov, H. Bovensmann, and J. P. Burrows, Chemical ozone loss in Arctic and Antarctic polar winter/spring season derived from SCIAMACHY limb measurements 2002–2009, *Atmos. Chem. Phys. Discuss*, *11*, 6555–6599, doi:10.5194/acpd-11-6555-2011, 2011.
- Søvde, O. A., Y. J. Orsolini, D. R. Jackson, F. Stordal, I. S. A. Isaksen, and B. Rognerud, Estimation of Arctic O₃ loss during winter 2006/2007 using data assimilation and comparison with a chemical transport model, *Q. J. R. Meteorol Soc.*, *137*, 118–128, doi:10.1002/qj.740, 2011.
- Spivakovsky, C. M., et al., Three-dimensional climatological distribution of tropospheric OH: update and evaluation, *J. Geophys. Res.*, *105*(D7), 8931–8980, doi:10.1029/1999JD901006, 2000.
- Strahan, S. E., B. N. Duncan, and P. Hoor, Observationally derived transport diagnostics for the lowermost stratosphere and their application to the GMI chemistry and transport model, *Atmos. Chem. Phys.*, *7*, 2435–2445, doi:10.5194/acp-7-2435-2007, 2007.
- Streets, D., Q. Zhang, L. Wang, K. He, J. Hao, Y. Wu, Y. Tang, and G. Carmichael, Revisiting China’s CO emissions after the Transport and Chemical Evolution over the Pacific (TRACE-P) mission: Synthesis of inventories, atmospheric modeling, and observations, *J. Geophys. Res.*, *111*, D14,306, 2006.
- Sussmann, R., F. Forster, M. Rettinger, and N. Jones, Strategy for high-accuracy-and-precision retrieval of atmospheric methane from the mid-infrared FTIR network, *Atmos. Meas. Tech.*, *4*, 1943–1964, doi:10.5194/amt-4-1943-2011, 2011.

- Sutton, R., H. M. T., R. Swinbank, A. O'Neill, and F. W. Taylor, High-resolution stratospheric tracer fields estimated from satellite observations using lagrangian trajectory calculations, *J. Atmos. Sci*, 51, 2995–3005, 1994.
- Tarasick, D. W., V. E. Fioletov, D. I. Wardle, J. B. Kerr, and J. Davies, Changes in the vertical distribution of ozone over Canada from ozonesondes: 1980–2001, *J. Geophys. Res.*, 110(D2), D02,304, doi:10.1029/2004JD004643, 2005.
- Taylor, J. R., Assessment of trace gas observations from the Toronto Atmospheric Observatory, Ph.D. thesis, Department of Physics, University of Toronto, 2008.
- Taylor, J. R., K. Strong, C. A. McLinden, D. A. Degenstein, and C. S. Haley, Comparison of OSIRIS stratospheric NO₂ and O₃ measurements with ground-based Fourier transform spectrometer measurements at the Toronto Atmospheric Observatory, *Can. J. Phys*, 85, 1301–1316, doi:10.1139/P07-144, 2007.
- Taylor, J. R., D. Wunch, C. Midwinter, A. Wiacek, J. R. Drummond, and K. Strong, An extended intercomparison of simultaneous ground-based Fourier transform infrared spectrometer measurements at the Toronto Atmospheric Observatory, *J. Quant. Spec. Rad. Trans.*, 109, 2244–2260, doi:10.1016/j.jqsrt.2008.03.011, 2008.
- TES Users Guide, Earth Observing System Tropospheric Emission Spectrometer data validation report v3.0, 2013.
- Thompson, A. M., K. E. Pickering, D. P. McNamara, M. R. Schoeberl, R. D. Hudson, J.-H. Kim, E. V. Browell, V. W. J. H. Kirchhoff, and D. Nganga, Where did tropospheric ozone over southern Africa and the tropical Atlantic come from in october 1992? insights from TOMS, GTE/TRACE-A and SAFARI-92, *J. Geophys. Res.*, 101, 24,25124,278, doi:10.1029/96JD01463, 1996.
- Thompson, A. M., J. C. Witte, R. D. Hudson, H. Guo, J. R. Herman, and M. Fujiwara,

- Tropical tropospheric ozone and biomass burning, *Science*, *16*(5511), 2128–2132, doi:10.1126/science.291.5511.2128, 2001.
- Tikhonov, A., On the solution of incorrectly stated problems and a method of regularization, *Dokl. Acad. Nauk SSSR*, *151*, 501–504, 1963.
- Toon, G. C., C. B. Farmer, P. W. Schaper, L. L. Lowes, and R. H. Norton, Composition measurements of the 1989 Arctic winter stratosphere by airborne infrared solar absorption spectroscopy, *J. Geophys. Res.*, *97*, 7939–7961, doi:10.1029/91JD03114, 1992.
- Toon, G. C., J.-F. Blavier, B. Sen, R. J. Salawitch, G. B. Osterman, J. Notholt, M. Rex, C. T. McElroy, and J. M. R. III, Ground-based observations of Arctic O_3 loss during spring and summer 1997, *J. Geophys. Res.*, *104*(D21), 26,497–26,510, doi:10.1029/1999JD900745, 1999.
- Toronto Public Health, Path to healthier air: Toronto air pollution burden of illness update, technical report, Toronto, Canada, 2014.
- Tripathi, O. P., T. Leblanc, I. S. McDermid, L. F., M. Marchand, and A. Hauchecorne, Forecast, measurement, and modeling of an unprecedented polar ozone filament event over Mauna Loa Observatory, Hawaii, *J. Geophys. Res.*, *111*, D20,308, doi:10.1029/2006JD007177, 2006.
- Viatte, C., et al., Tropospheric and total ozone columns over Paris (France) measured using medium-resolution ground-based solar-absorption Fourier-transform infrared spectroscopy, *Atmos. Meas. Tech.*, *4*, 2323–2331, doi:10.5194/amt-4-2323-2011, 2011.
- Vigouroux, C., et al., Evaluation of tropospheric and stratospheric ozone trends over Western Europe from ground-based FTIR network observations, *Atmos. Chem. Phys.*, *8*, 6865–6886, doi:10.5194/acp-8-6865-2008, 2008.

- Vigouroux, C., et al., Ground-based FTIR and MAX-DOAS observations of formaldehyde at Reunion Island and comparisons with satellite and model data, *Atmos. Chem. Phys.*, *9*, 9523–9544, doi:10.5194/acp-9-9523-2009, 2009.
- Vigouroux, C., et al., FTIR time-series of biomass burning products (HCN, C₂H₆, C₂H₂, CH₃OH, and HCOOH) at Reunion Island (21° S, 55° E) and comparisons with model data, *Atmos. Chem. Phys.*, *12*, 10,367–10,385, doi:10.5194/acp-12-10367-2012, 2012.
- Voulgarakis, A., P. J. Telford, A. M. Aghedo, P. Braesicke, G. Faluvegi, N. L. Abraham, K. W. Bowman, J. A. Pyle, and D. T. Shindell, Global multi-year O₃-CO correlation patterns from models and TES satellite observations, *Atmos. Chem. Phys.*, *11*, 5819–5838, doi:10.5194/acp-11-5819-2011, 2011.
- Vukovich, F. M., Regional scale boundary layer ozone variations in the eastern United States and their association with meteorological variations, *Atmos. Environ.*, *29*, 2259–2273, doi:10.1016/1352-2310(95)00146-P, 1995.
- Vukovich, F. M., W. D. B. Jr., B. W. Crissman, and W. J. King, On the relationship between high ozone in the rural surface layer and high pressure systems, *Atmos. Environ.*, *11*(10), 967–983, doi:10.1016/0004-6981(77)90026-9, 1977.
- Walker, T. W., et al., Impacts of midlatitude precursor emissions and local photochemistry on ozone abundances in the arctic, *J. Geophys. Res.*, *117*(D1), doi:10.1029/2011JD016370, 2012.
- Wang, Y., and D. J. Jacob, Anthropogenic forcing on tropospheric ozone and OH since preindustrial times, *J. Geophys. Res.*, *103*, 31,123–31,135, doi:10.1029/1998JD100004, 1998.
- Wang, Y., D. J. Jacob, and J. A. Logan, Global simulation of tropospheric O₃-NO_x-hydrocarbon chemistry, 3. Origin of tropospheric ozone and effects of non-methane hydrocarbons, *J. Geophys. Res.*, *103*, 10,757–10,768, doi:10.1029/98JD00156, 1998.

- Waugh, D. W., et al., Transport out of the lower stratospheric Arctic vortex by rossby wave breaking, *J. Geophys. Res.*, *99*(D1), 1071–1088, doi:10.1029/93JD02556, 1994.
- Weatherhead, E. C., A. J. Stevermer, and B. E. Schwartz, Detecting environmental changes and trends, *Phys. Chem. Earth*, *27*, 99403, doi:10.1016/S1474-7065(02)00019-0, 2002.
- Weatherhead, E. C., et al., Factors affecting the detection of trends: statistical considerations and applications to environmental data, *J. Geophys. Res.*, *103*(D14), 17,149–14,161, doi:10.1029/98JD00995, 1998.
- Westerling, A. L., H. G. Hidalgo, D. R. Cayan, and T. W. Swetnam, Warming and earlier spring increase Western U.S. forest wildfire activity, *Science*, *313*(5789), 940–943, doi:10.1126/science.1128834, 2006.
- Whaley, C., Ground-based tropospheric measurements at the University of Toronto Atmospheric Observatory, MSc Report, Department of Physics, University of Toronto, 2009.
- Whaley, C., et al., Using FTIR measurements of stratospheric composition to identify midlatitude polar vortex intrusions over Toronto, *J. Geophys. Res.*, *118*, 12,766–12,783, 2013.
- WHO, Burden of disease from the joint effects of household and ambient air pollution for 2012, World Health Organization, 2014.
- Wiacek, A., First trace gas measurements using Fourier transform infrared solar absorption spectroscopy at the University of Toronto Atmospheric Observatory, Ph.D. thesis, Department of Physics, University of Toronto, 2006.
- Wiacek, A., and K. Strong, Effects of vertical grid discretization in infrared transmission

- modeling, *J. Quant. Spec. Rad. Trans.*, *109*, 2463–2490, doi:10.1016/j.jqsrt.2008.03.015, 2008.
- Wiacek, A., J. R. Taylor, K. Strong, R. Saari, and T. E. Kerzenmacher, Ground-based solar absorption FTIR spectroscopy: Characterization of retrievals and first results from a novel optical design instrument at a new NDACC complementary station, *J. Atmos. Oceanic Tech.*, *24*, 432–448, doi:10.1175/JTRCH1962.1, 2007.
- WMO, *WMO (World Meteorological Organization): Scientific Assessment of Ozone Depletion: 2006*, WMO Global Ozone Research and Monitoring Project-Report 50, Geneva, Switzerland, 2007.
- WMO, *WMO (World Meteorological Organization): Scientific Assessment of Ozone Depletion: 2010*, Global Ozone Research and Monitoring Project-Report 52, Geneva, Switzerland, 2011.
- Wunch, D., J. R. Taylor, D. Fu, P. F. Bernath, J. R. Drummond, C. Midwinter, K. Strong, and K. A. Walker, Simultaneous ground-based observations of O₃, HCl, N₂O, and CH₄ over Toronto, Canada by three Fourier transform spectrometers with different resolutions, *Atmos. Chem. Phys.*, *7*, 1275–1292, doi:10.5194/acp-7-1275-2007, 2007.
- Wunch, D., P. Wennberg, G. Toon, G. Keppel-Aleks, and Y. Yavin, Emissions of greenhouse gases from a North American megacity, *Geophys. Res. Lett.*, *36*, L15,810, doi:10.1029/2009GL039825, 2009.
- Yang, Q., D. M. Cunnold, Y. Choi, Y. Wang, J. Nam, H.-H. Wang, L. Froidevaux, A. M. Thompson, and P. K. Bhartia, A study of tropospheric ozone column enhancements over North America using satellite data and a global chemical transport model, *J. Geophys. Res.*, *115*, D08,302, doi:10.1029/2009JD012616, 2010.
- Yap, D., N. Reid, G. D. Brou, and R. Bloxam, *Transboundary air pollution in Ontario*, Queen's Printer for Ontario, 2005.

- Yevich, R., and J. A. Logan, An assessment of biofuel use and burning of agricultural waste in the developing world 1095, *Global Biogeochem. Cycles*, *17*(4), 2003.
- Yienger, J. J., and H. Levy III, Empirical model of global soil-biogenic NO_x emissions, *J. Geophys. Res.*, *100*(D6), 11,447–11,464, doi:10.1029/95JD00370, 1995.
- Zhang, L., D. J. Jacob, M. Kopacz, D. K. Henze, K. Singh, and D. A. Jaff, Intercontinental source attribution of ozone pollution at western U.S. sites using an adjoint method, *Geophys. Res. Lett.*, *36*, L11,810, doi:10.1029/2009GL037950, 2009.
- Zhang, L., et al., Transpacific transport of ozone pollution and the effect of recent Asian emission increases on air quality in North America: an integrated analysis using satellite, aircraft, ozonesonde, and surface observations, *Atmos. Chem. Phys.*, *8*, 6117–6136, doi:10.5194/acp-8-6117-2008, 2008.
- Zhang, L., et al., Improved estimate of the policy-relevant background ozone in the United States using the GEOS-Chem global model with $1/2^\circ \times 2/3^\circ$ horizontal resolution over North America, *Atmos. Environ.*, *45*, 6769–6776, doi:10.1016/j.atmosenv.2011.07.054, 2011.
- Zhou, W., D. S. Cohan, and S. L. Napelenok, Reconciling NO_x emissions reductions and ozone trends in the U.S., 2002–2006, *Atmos. Environ.*, *70*, 236–244, doi:10.1016/j.atmosenv.2012.12.038, 2013.
- Zhu, J., and X.-Z. Liang, Impacts of the Bermuda high on regional climate and ozone over the United States, *J. Climate*, *26*, 10181032, doi:10.1175/JCLI-D-12-00168.1, 2012.
- Zishka, K. M., and P. J. Smith, The climatology of cyclones and anticyclones over North America and surrounding ocean environs for January and July, 1950–77, *Month. Weath. Rev.*, *108*(4), 387–401, 1980.